The Oscillating Turbulent Boundary Layer In A Conical Diffuser.

INFORMATION TO USERS

This material was produced from a microfilm copy of the original document. While the most advanced technological means to photograph and reproduce this document have been used, the quality is heavily dependent upon the quality of the original submitted.

The following explanation of techniques is provided to help you understand markings or patterns which may appear on this reproduction.

1. The sign or "target" for pages apparently lacking from the document photographed is "Missing Page(s)". If it was possible to obtain the missing page(s) or section, they are spliced into the film along with adjacent pages. This may have necessitated cutting thru an image and duplicating adjacent pages to insure you complete continuity.

2. When an image on the film is obliterated with a large round black mark, it is an indication that the photographer suspected that the copy may have moved during exposure and thus cause a blurred image. You will find a good image of the page in the adjacent frame.

3. When a map, drawing or chart, etc., was part of the material being photographed the photographer followed a definite method in "sectioning" the material. It is customary to begin photoing at the upper left hand corner of a large sheet and to continue photoing from left to right in equal sections with a small overlap. If necessary, sectioning is continued again — beginning below the first row and continuing on until complete.

4. The majority of users indicate that the textual content is of greatest value, however, a somewhat higher quality reproduction could be made from "photographs" if essential to the understanding of the dissertation. Silver prints of "photographs" may be ordered at additional charge by writing the Order Department, giving the catalog number, title, author and specific pages you wish reproduced.

5. PLEASE NOTE: Some pages may have indistinct print. Filmed as received.

University Microfilms International
300 North Zeeb Road
Ann Arbor, Michigan 48106 USA
St. John's Road, Tyler's Green
High Wycombe, Bucks, England HP10 8HR

THE OSCILLATING TURBULENT BOUNDARY LAYER IN A CONICAL DIFFUSER

by

Michael Edward Tomsho

A Dissertation

Presented to the Graduate Committee

of Lehigh University

in Candidacy for the Degree of

Doctor of Philosophy

in

Mechanical Engineering

Lehigh University

1978

Approved and recommended for acceptance as a dissertation in partial fulfillment of the requirements for the degree of Doctor of Philosophy.

21 Sept 1978
(date)

Forbes T. Brown
Professor in Charge

Accepted Sept. 21, 1978
(date)

Special committee directing
the doctoral work of
Mr. Michael E. Tomsho

Forbes T. Brown
Chairman

Edward K Levy

John C. Chen

W. E. Ackerman

Arnold Rakowitz

ACKNOWLEDGEMENTS

The author wishes to acknowledge the fact that the late Professor Alan H. Stenning initiated and guided the unsteady diffuser flow program for several years at Lehigh University. Professor Stenning was the author's thesis supervisor until his death in 1973. Professor F. T. Brown then assumed that role and he has since provided the necessary review, discussion, advice and encouragement. Dr. A. A. Schachenmann designed the original test facility and performed the initial experiments together with the author. Professor D. O. Rockwell reviewed this work periodically and contributed to its development. Professor J. V. D. Eppes did the photographic documentation. Professor T. E. Jackson and his crew of Mr. Dick Towne and Mr. Tim Nixon provided equipment support.

My wife Ann has acted as typist, graphic artist, editor, critic, sounding board, and cheering section. The transformation of my rough drafts and working curves to the finished document is entirely her doing. Without her this project would neither have been started nor finished.

TABLE OF CONTENTS

LIST OF TABLES

LIST OF FIGURES

NOMENCLATURE

A	-	cross sectional area
AEFF	-	effective flow area
C_F	-	wall friction coefficient
const	-	constant in Law-of-the-Wall formulation
C_p	-	pressure recovery coefficient
D	-	test section diameter
DELTA	-	boundary layer thickness
f	-	dimensionless streamfunction
FREQ	-	frequency
h_1, h_2, h_3	-	metric coefficients
H	-	shape factor
i	-	imaginary unit
$\hat{i}_1, \hat{i}_2, \hat{i}_3$	-	unit vectors
κ	-	constant in Law-of-the-Wall formulation
ℓ	-	characteristic length
ℓ_m	-	mixing length
L	-	reference length (=test section centerline length)
$\mathcal{O}$	-	denotes order of magnitude
P	-	stream pressure
PCL	-	core flow stream pressure
r	-	radial distance from the test section centerline to the point (x,y)

R - test section radius

Re - Reynolds number

$\mathcal{R}_E$ - denotes real component of complex quantity

t - time

T - oscillation period

U_1, U_2, U_3 / U, V, W - streamwise, transverse, and circumferential velocity components, respectively

UCL - core flow velocity

UE - main stream velocity

U^+ - Law-of-the-Wall velocity

U_τ - friction velocity

$U_i' U_j'$ - Reynolds stress component

V - characteristic velocity

V - voltage

X_1, X_2, X_3 / X, Y, θ - streamwise, transverse, and circumferential coordinate distances

XCL - centerline distance from test section inlet (corresponds to x-station in inches)

y^+ - Law-of-the-Wall transverse distance

Greek notation:

κ - diffuser half-angle

$\bar{\alpha}$ - constant in eddy viscosity formulation

β - pressure gradient parameter

γ - intermittency function

δ - boundary layer thickness

$\delta 1$ - displacement thickness

$\delta 2$ - momentum thickness

δ_s - correlating parameter in Thompson profile fitting

η - transformed, transverse distance coordinate

μ - dynamic viscosity

ν - kinematic viscosity

ν_T - eddy viscosity

ξ - transformed, streamwise distance coordinate

ρ - fluid density

σ - stress tensor component

τ - shear stress

τ_ω - wall shear stress

ϕ - phase angle

ψ - streamfunction

ω - radian frequency (2π)(FREQ)

$\bar{\omega}_L$ - reduced frequency $(\omega)(L)/\overline{uc}_L(o)$

$\bar{\omega}_x$ - reduced frequency $(\omega)(x)/\overline{uc}_L(x)$

The following notation applies to all flow properties:

$\bar{u}$ - time-average component

$\langle u \rangle$ - phase-average component

$\tilde{u}$ - oscillatory component

u' - random, fluctuating component

Δu - amplitude (zero-to-peak) of $\tilde{u}$

$\mathcal{U}$ - complex amplitude ($= \Delta u e^{i\phi}$)

u_R - real component of $\mathcal{U}$ ($= \Delta u \cos\phi$)

u_I - imaginary component of $\mathcal{U}$ ($= \Delta u \sin\phi$)

Subscripts:

AX - axisymmetric

2D - rectangular, two-dimensional

(i) - i denotes x-station

Note: The nomenclature employed in Chapter 5 in the description of the theoretical model solution procedure is defined within the text.

ABSTRACT

The turbulent boundary layer in a conical diffuser, with the inlet airflow oscillating sinusoidally, was studied experimentally and theoretically. The diffuser inlet diameter is 100 mm and the flow is characterized by an entrance Reynolds number on the order of 120000. The 3-degree (half-angle) diffuser flow is in the turbulent regime throughout the test section, and no separation occurs. Oscillation frequencies span the range of 5-30 Hz with amplitudes approximately 10 percent of the time-averaged velocities.

Mappings of the oscillatory response were made by a hot wire anemometer, and the signals were processed on-line by a laboratory computer to obtain the phase average of the unsteady velocity field. The oscillatory response pattern of the streamwise velocity component in the outer region of the boundary layer crosses over between amplification and attenuation, and between phase lead and lag, along the test section length, at a rate related to the oscillation frequency. A phase lead is established in the inner region throughout the test section.

In place of a direct attack on the 3-dimensional (x,y,t),

time-dependent boundary layer equations, the equations for the oscillatory component were derived and solved numerically. The oscillatory Reynolds shear stresses are modeled as the product of the time-invariant (time-average) local eddy viscosity and the local oscillatory velocity gradient. The strongly coupled flow requires that the core flow response be used as a boundary condition. The eddy viscosity modeling scheme is capable of simulating the boundary layer response qualitatively in that the inner phase lead is reproduced throughout and the pattern crossovers are established in the outer region. However, the predicted pattern crossover rate and the predicted magnitudes of the pattern excursions exceed the experimental values.

1. INTRODUCTION

Boundary layer development in the presence of periodic oscillations is not uncommon. Two such instances where sophisticated design requires a knowledge of the oscillatory response are the external flow over the surface of a helicopter rotor blade in flight, and the internal flow in the blade passages of rotating turbomachinery. The work of this report was stimulated by an interest in the problems of determining the flow on the blade surfaces and passage walls in turbines and compressors. For internal flow the blockage caused by the boundary layer is determined by the oscillatory response, and the amplitude and phase change of the oscillation in the core flow, along the length of the flow path is, in turn, coupled to the boundary layer blockage pattern.

The results of several studies are available in the literature in which the time-dependent flow field in the blade passages of turbomachinery test equipment was measured experimentally. Evans (1)[1] measured the flow field oscillations between the rotor and stator of a

[1]Underlined numbers in parentheses designate citations in the REFERENCES section.

single stage experimental compressor with a hot wire anemometer. Figure 1.1 shows a portion of the results obtained. The passing of the pressure surface of the rotor blade causes the steep drop in $\tilde{u}$, and the passing suction surface is indicated by the more gradual rise which follows. Evans reported the results of oscillating boundary layer measurements in the same facility (2) which show that there is a shift between the laminar and turbulent regimes during each cycle at the 30 percent chord location. This phenomenon produces a 180 deg phase difference between the boundary layer and core flow oscillations. Similar behavior was reported by Gostelow (3) for measurements in a cascade of aerofoils mounted in a gust tunnel. Hirsch and Kool (4) extended these techniques to measure the 3-dimensional flow field behind an axial compressor stage using a rotating slant wire probe.

Unsteady diffuser flow work was begun at Lehigh Universiety in 1971 under the direction of Prof. A. H. Stenning. In 1973 Stenning and Schachenmann (5) published the results of measurements in a conical diffuser for $10^3 < Re_D < 10^4$. The work reported here is the second phase of a project begun jointly by the author and

Schachenmann to study the dynamic response in oscillatory diffuser flow for $Re_D \sim 150{,}000$. Schachenmann's work was directed primarily at measuring and modeling the core flow response, and he has proposed simplified representations of the required boundary layer input for the limiting cases of very high and very low frequency. He has published the initial set of experimental data and his theoretical results in references (6), (7), (8).

The objective of the follow-on work reported herein is to study in detail the oscillatory response of the turbulent boundary layer developing in the diffuser test section. Very limited experimental information on oscillatory turbulent boundary layers has been made available in the literature to this point in time, and no controlled study for an internal flow in a non-zero pressure gradient has been reported. This study has produced a set of mappings of the boundary layer response for a range of input frequencies. A theoretical model was developed for the purpose of evaluating the performance of a time-invariant eddy viscosity closure scheme. The data are used for comparison with the theoretical predictions.

This study does not address the subjects of separation or transition between the laminar and turbulent regimes. For the boundary layer model the converse situation from that of the Schachenmann study applies, in that the core flow response is required as input to the boundary layer calculation. A complete solution of the oscillatory diffuser flow field would be an iterative process combining a core flow model and a boundary layer simulation, but this was not attempted.

2. BACKGROUND

2.1 GENERAL

The equations of motion governing the oscillating turbulent flow in a conical diffuser are derived in this chapter in order to provide a framework for the report which follows. The phase-averaging procedure is described and the format used in the presentation of the results is discussed. The development of the equations for the modeling study is continued in Chapter 5. The final section in this chapter presents a review of the literature related to this area of study.

2.2 THEORETICAL BACKGROUND

Basic Equations

Coordinate System

The time dependent equations governing the flow can be written (see Ref. (9)), for a general, orthogonal, curvilinear coordinate system, in the following form

continuity

$$\frac{\partial \rho}{\partial t} + \frac{1}{h_1 h_2 h_3}\left[\frac{\partial}{\partial x_1}(h_2 h_3 \rho U_1) + \frac{\partial}{\partial x_2}(h_3 h_1 \rho U_2) + \frac{\partial}{\partial x_3}(h_1 h_2 \rho U_3)\right] \quad (2.1a)$$

x_1-momentum

$$\rho\left[\frac{\partial u_1}{\partial t}+\frac{u_1}{h_1}\frac{\partial u_1}{\partial x_1}+\frac{u_2}{h_2}\frac{\partial u_1}{\partial x_2}+\frac{u_3}{h_3}\frac{\partial u_1}{\partial x_3}\right.$$

$$\left.-u_2\left(\frac{u_2}{h_2h_1}\frac{\partial h_2}{\partial x_1}-\frac{u_1}{h_1h_2}\frac{\partial h_1}{\partial x_2}\right)+u_3\left(\frac{u_1}{h_1h_3}\frac{\partial h_1}{\partial x_3}-\frac{u_3}{h_3h_1}\frac{\partial h_3}{\partial x_1}\right)\right]$$

$$=\frac{1}{h_1h_2h_3}\left[\frac{\partial}{\partial x_1}(h_2h_3\sigma_{11})+\frac{\partial}{\partial x_2}(h_3h_1\overline{\tau_{21}})+\frac{\partial}{\partial x_3}(h_1h_2\overline{\tau_{31}})\right]$$

$$+\frac{\overline{\tau_{12}}}{h_1h_2}\frac{\partial h_1}{\partial x_2}+\frac{\overline{\tau_{31}}}{h_1h_3}\frac{\partial h_1}{\partial x_3}-\frac{\overline{\tau_{22}}}{h_1h_2}\frac{\partial h_2}{\partial x_1}-\frac{\overline{\sigma_{33}}}{h_1h_3}\frac{\partial h_3}{\partial x_1} \qquad (2.1b)$$

x_2-momentum

$$\rho\left[\frac{\partial u_2}{\partial t}+\frac{u_1}{h_1}\frac{\partial u_2}{\partial x_1}+\frac{u_2}{h_2}\frac{\partial u_2}{\partial x_2}+\frac{u_3}{h_3}\frac{\partial u_2}{\partial x_3}\right.$$

$$\left.-u_3\left(\frac{u_3}{h_3h_2}\frac{\partial h_3}{\partial x_2}-\frac{u_2}{h_2h_3}\frac{\partial h_2}{\partial x_3}\right)+u_1\left(\frac{u_2}{h_2h_1}\frac{\partial h_2}{\partial x_1}-\frac{u_1}{h_1h_2}\frac{\partial h_1}{\partial x_2}\right)\right]$$

$$=\frac{1}{h_1h_2h_3}\left[\frac{\partial}{\partial x_1}(h_2h_3\overline{\tau_{12}})+\frac{\partial}{\partial x_2}(h_3h_1\overline{\tau_{22}})+\frac{\partial}{\partial x_3}(h_1h_2\overline{\tau_{32}})\right]$$

$$+\frac{\overline{\sigma_{23}}}{h_2h_3}\frac{\partial h_2}{\partial x_3}+\frac{\overline{\tau_{12}}}{h_2h_1}\frac{\partial h_2}{\partial x_1}-\frac{\overline{\tau_{33}}}{h_2h_3}\frac{\partial h_3}{\partial x_2}-\frac{\overline{\tau_{11}}}{h_2h_1}\frac{\partial h_1}{\partial x_2} \qquad (2.1c)$$

x_3-momentum

$$\rho\left[\frac{\partial u_3}{\partial t}+\frac{u_1}{h_1}\frac{\partial u_3}{\partial x_1}+\frac{u_2}{h_2}\frac{\partial u_3}{\partial x_2}+\frac{u_3}{h_3}\frac{\partial u_3}{\partial x_3}\right.$$

$$\left.-u_1\left(\frac{u_1}{h_1h_3}\frac{\partial h_1}{\partial x_3}-\frac{u_3}{h_3h_1}\frac{\partial h_3}{\partial x_1}\right)+u_2\left(\frac{u_3}{h_3h_2}\frac{\partial h_3}{\partial x_2}-\frac{u_2}{h_2h_3}\frac{\partial h_2}{\partial x_3}\right)\right]$$

$$=\frac{1}{h_1h_2h_3}\left[\frac{\partial}{\partial x_1}(h_2h_3\overline{\tau_{13}})+\frac{\partial}{\partial x_2}(h_3h_1\overline{\tau_{23}})+\frac{\partial}{\partial x_3}(h_1h_2\overline{\tau_{33}})\right]$$

$$+\frac{\overline{\tau_{31}}}{h_1h_3}\frac{\partial h_3}{\partial x_1}+\frac{\overline{\tau_{23}}}{h_3h_2}\frac{\partial h_3}{\partial x_2}-\frac{\overline{\tau_{11}}}{h_3h_1}\frac{\partial h_1}{\partial x_3}-\frac{\overline{\tau_{22}}}{h_3h_2}\frac{\partial h_2}{\partial x_3}. \qquad (2.1d)$$

For the following assumption:

► incompressible flow regime (div $\bar{V} = 0$)

the components of the stress tensor are given by

$$\sigma_{11} = -P + 2\mu\left(\frac{1}{h_1}\frac{\partial u_1}{\partial x_1} + \frac{u_2}{h_1 h_2}\frac{\partial h_1}{\partial x_2} + \frac{u_3}{h_3 h_1}\frac{\partial h_1}{\partial x_3}\right)$$

$$\sigma_{22} = -P + 2\mu\left(\frac{1}{h_2}\frac{\partial u_2}{\partial x_2} + \frac{u_3}{h_2 h_3}\frac{\partial h_2}{\partial x_3} + \frac{u_1}{h_1 h_2}\frac{\partial h_2}{\partial x_1}\right)$$

$$\sigma_{33} = -P + 2\mu\left(\frac{1}{h_3}\frac{\partial u_3}{\partial x_3} + \frac{u_1}{h_3 h_1}\frac{\partial h_3}{\partial x_1} + \frac{u_2}{h_2 h_3}\frac{\partial h_3}{\partial x_2}\right)$$

$$\sigma_{12} = \mu\left[\frac{h_2}{h_1}\frac{\partial}{\partial x_1}\left(\frac{u_2}{h_2}\right) + \frac{h_1}{h_2}\frac{\partial}{\partial x_2}\left(\frac{u_1}{h_1}\right)\right]$$

$$\sigma_{13} = \mu\left[\frac{h_1}{h_3}\frac{\partial}{\partial x_3}\left(\frac{u_1}{h_1}\right) + \frac{h_3}{h_1}\frac{\partial}{\partial x_1}\left(\frac{u_3}{h_3}\right)\right]$$

$$\sigma_{23} = \mu\left[\frac{h_3}{h_2}\frac{\partial}{\partial x_2}\left(\frac{u_3}{h_3}\right) + \frac{h_2}{h_3}\frac{\partial}{\partial x_3}\left(\frac{u_2}{h_2}\right)\right]. \qquad (2.2a\text{-}f)$$

The axisymmetric coordinate system within which the diffuser flow field is described is shown in Figure 2.1. The x_1-coordinate lies along a generatrix of the inside surface of the conical flow passage, the x_2-coordinate is normal to this surface, and x_3 is the angular distance in the circumferential direction, mutually perpendicular to the x_1 and y_1 axes. The following notation applies:

$$x_1 = x, \quad U_1 = U$$
$$x_2 = y, \quad U_2 = V$$
$$x_3 = \theta, \quad U_3 = W.$$

The distance r , in the plane of the flow cross-section, from the passage centerline to a specified point (x, y, θ), is given by

$$r = R(x) - y \cos \alpha \tag{2.3}$$

where

$$R(x) = R(0) + x \sin \alpha \tag{2.4}$$

α = const. (conical diffuser half-angle).

Ideally, the flow in a conical passage has spherical symmetry with the origin located at the vertex of the cone. The axisymmetric coordinate system used here approximates the spherical flow surfaces by conical sections; however, the deviations are negligibly small for the small angle of divergence of the test section studied. The metric coefficients (h_1, h_2, and h_3) are specified in the definition of arc length, ds , given by

$$ds^2 = h_1^2 dx^2 + h_2^2 dy^2 + h_3^2 d\theta^2.$$

so that

$$\begin{aligned} h_1 &= 1 \\ h_2 &= 1 \\ h_3 &= r. \end{aligned} \tag{2.5}$$

(Note that this system accommodates streamwise divergence and transverse curvature. For the more general case of streamwise curvature and transverse curvature, the angle α is a function of x , and $d\alpha/dx = -1/R$, where

$\mathcal{R}$ is the streamwise radius of curvature (10). It follows that $h_1 = 1. + y/\mathcal{R}$ for the general case.)

Substituting equations 2.2 and 2.5 into equation 2.1, and applying the assumptions listed:

- ▶ axisymmetric flow $(\partial/\partial\theta = 0)$
- ▶ incompressible, constant properties $(\rho, \mu = \text{const})$

gives the following results:

continuity

$$\frac{\partial}{\partial x}(ru) + \frac{\partial}{\partial y}(rV) = 0 \qquad (2.6a)$$

x-momentum

$$\rho\left[\frac{\partial u}{\partial t} + u\frac{\partial u}{\partial x} + V\frac{\partial u}{\partial y} - \frac{w^2}{r}\frac{\partial r}{\partial x}\right] = -\frac{\partial P}{\partial x} + \mu\left[\frac{1}{r}\frac{\partial}{\partial x}\left(2r\frac{\partial u}{\partial x}\right) + \frac{1}{r}\frac{\partial}{\partial y}\left(r\left(\frac{\partial u}{\partial y} + \frac{\partial v}{\partial x}\right)\right) - \frac{2}{r^2}\left(u\frac{\partial r}{\partial x} + v\frac{\partial r}{\partial y}\right)\frac{\partial r}{\partial x}\right] \qquad (2.6b)$$

y-momentum

$$\rho\left[\frac{\partial V}{\partial t} + u\frac{\partial V}{\partial x} + V\frac{\partial V}{\partial y} - \frac{w^2}{r}\frac{\partial r}{\partial y}\right] = -\frac{\partial P}{\partial y} + \mu\left[\frac{1}{r}\frac{\partial}{\partial x}\left(r\left(\frac{\partial u}{\partial y} + \frac{\partial v}{\partial x}\right)\right) + \frac{1}{r}\frac{\partial}{\partial y}\left(2r\frac{\partial v}{\partial y}\right) - \frac{2}{r^2}\left(u\frac{\partial r}{\partial x} + v\frac{\partial r}{\partial y}\right)\frac{\partial r}{\partial y}\right] \qquad (2.6c)$$

θ-momentum

$$\rho\left[\frac{\partial w}{\partial t}+u\frac{\partial w}{\partial x}+v\frac{\partial w}{\partial y}+\frac{uw}{r}\frac{\partial r}{\partial x}+\frac{vw}{r}\frac{\partial r}{\partial y}\right]$$
$$=\mu\left[\frac{1}{r}\frac{\partial}{\partial x}\left(r^2\frac{\partial}{\partial x}\left(\frac{w}{r}\right)\right)+\frac{1}{r}\frac{\partial}{\partial y}\left(r^2\frac{\partial}{\partial y}\left(\frac{w}{r}\right)\right)\right.$$
$$\left.+\frac{\partial}{\partial x}\left(\frac{w}{r}\right)\frac{\partial r}{\partial x}+\frac{\partial}{\partial y}\left(\frac{w}{r}\right)\frac{\partial r}{\partial y}\right]. \qquad (2.6d)$$

Phase-averaging

The standard procedure used to permit calculations for turbulent flow involves decomposing the flow properties and separating the random fluctuating component due to the turbulence from the time-averaged component. The equations of motion are then expanded to incorporate this decomposition, and a final time-averaging is done term by term. For steady flow, the x-component of velocity can be written as the sum of a time-averaged component and a fluctuating component,

$$u(x,y,t)=\bar{u}(x,y)+u'(x,y,t) \qquad (2.7)$$

where

$$\bar{u}(x,y)=\lim_{T\to\infty}\frac{1}{T}\int_0^T u(x,y,t)\,dt. \qquad (2.8)$$

The T denotes the time period over which the average is taken.

If the flow is non-steady, the decomposition takes the form of the sum of an ensemble-averaged component and a

fluctuating component,

$$u(x,y,t) = \langle u(x,y,t) \rangle + u'(x,y,t) \tag{2.9}$$

where

$$\langle u(x,y,t) \rangle = \lim_{N \to \infty} \frac{1}{N} \sum_{n=1}^{N} u(x,y,t)_n . \tag{2.10}$$

The n denotes the nth data record, and N is the total number of data records used in determining the average. If the non-steady flow properties vary <u>periodically</u> with time, the ensemble-averaging process (which experimentally would require a large number of data records) can be replaced by phase-averaging (which is accomplished experimentally with a single data record containing a large number of complete cycles of the oscillation),

$$\langle u(x,y,t) \rangle = \lim_{N \to \infty} \frac{1}{N} \sum_{n=0}^{N} u(x,y,t+nT) \tag{2.11}$$

where T is the period of the oscillation. The phase-averaging process is illustrated in Figure 2.2.

The decomposition (2.9) is applied, followed by phase-averaging each of the terms of equations (2.6). The rules listed below are used when phase-averaging combinations of the components in the terms of the equations:

$$\langle f' \rangle = 0$$
$$\langle \langle f \rangle g' \rangle = 0$$
$$\langle f' g' \rangle \neq 0.$$

The θ -momentum equation is eliminated by the following assumption:

► zero swirl velocity $(\langle w \rangle = 0)$,

and equations (2.6) become

continuity

$$\frac{\partial}{\partial x}\left(r\langle u \rangle\right) + \frac{\partial}{\partial y}\left(r\langle v \rangle\right) = 0 \qquad (2.12a)$$

x-momentum

$$\frac{\partial \langle u \rangle}{\partial t} + \langle u \rangle \frac{\partial \langle u \rangle}{\partial x} + \langle v \rangle \frac{\partial \langle u \rangle}{\partial y}$$
$$= \frac{-1}{\rho}\frac{\partial \langle p \rangle}{\partial x} + \nu\left[\frac{1}{r}\frac{\partial}{\partial x}\left(r\frac{\partial \langle u \rangle}{\partial x}\right) + \frac{1}{r}\frac{\partial}{\partial y}\left(r\frac{\partial \langle u \rangle}{\partial y}\right)\right.$$
$$\left. -\left(\frac{\sin\alpha}{r}\right)^2\langle u \rangle + \left(\frac{\sin 2\alpha}{2r^2}\right)\langle v \rangle\right]$$
$$-\frac{1}{r}\frac{\partial}{\partial x}\left(r\langle u'^2 \rangle\right) - \frac{1}{r}\frac{\partial}{\partial y}\left(r\langle u'v' \rangle\right) + \left(\frac{\sin\alpha}{r}\right)\langle w'^2 \rangle \qquad (2.12b)$$

y-momentum

$$\frac{\partial \langle v \rangle}{\partial t} + \langle u \rangle \frac{\partial \langle v \rangle}{\partial x} + \langle v \rangle \frac{\partial \langle v \rangle}{\partial y}$$
$$= -\frac{1}{\rho}\frac{\partial \langle p \rangle}{\partial y} + \nu\left[\frac{1}{r}\frac{\partial}{\partial x}\left(r\frac{\partial \langle v \rangle}{\partial x}\right) + \frac{1}{r}\frac{\partial}{\partial y}\left(r\frac{\partial \langle v \rangle}{\partial y}\right)\right.$$
$$\left. + \left(\frac{\sin 2\alpha}{2r^2}\right)\langle u \rangle - \left(\frac{\cos\alpha}{r}\right)^2\langle v \rangle\right]$$
$$-\frac{1}{r}\frac{\partial}{\partial x}\left(r\langle u'v' \rangle\right) - \frac{1}{r}\frac{\partial}{\partial y}\left(r\langle v'^2 \rangle\right) - \left(\frac{\cos\alpha}{r}\right)\langle w'^2 \rangle. \qquad (2.12c)$$

Base Flow Equations

Oscillatory Component Equations

The phase-averaged flow properties of (2.12) are further decomposed into a time-average component and an oscillatory component,

$$\langle u(x,y,t)\rangle = \bar{u}(x,y) + \tilde{u}(x,y,t) \qquad (2.13)$$

where $\bar{u}$ is defined by (2.8).

Time-averaging the terms of (2.12) after substitution of the decomposition (2.13) produces the base flow equations. The following rules and nomenclature apply:

$$\overline{\tilde{u}} = 0, \qquad \overline{\bar{u}\tilde{v}} = 0$$

$$\langle \tilde{u}\tilde{v}\rangle = \overline{\tilde{u}\tilde{v}} + \widetilde{\tilde{u}\tilde{v}}$$

$$\overline{\overline{\tilde{u}\tilde{v}} + \widetilde{\tilde{u}\tilde{v}}} = \overline{\tilde{u}\tilde{v}}$$

$$\langle \tilde{u}\tilde{v}\rangle - \overline{\tilde{u}\tilde{v}} = \widetilde{\tilde{u}\tilde{v}}.$$

Subtracting the base flow from (2.12) gives the oscillatory component equations.

The equations can now be written in two sets,

Boundary layer (time-averaged base flow):

continuity

$$\frac{\partial}{\partial x}\left(r\bar{u}\right)+\frac{\partial}{\partial y}\left(r\bar{v}\right)=0 \tag{2.14a}$$

x-momentum

$$\bar{u}\frac{\partial\bar{u}}{\partial x}+\bar{v}\frac{\partial\bar{u}}{\partial y}=-\frac{1}{\rho}\frac{\partial\bar{p}}{\partial x}$$
$$+\nu\left[\frac{1}{r}\frac{\partial}{\partial x}\left(r\frac{\partial\bar{u}}{\partial x}\right)+\frac{1}{r}\frac{\partial}{\partial y}\left(r\frac{\partial\bar{u}}{\partial y}\right)-\left(\frac{\sin\alpha}{r}\right)^{2}\bar{u}\right.$$
$$\left.+\left(\frac{\sin 2\alpha}{2r^{2}}\right)\bar{v}\right]-\frac{1}{r}\frac{\partial}{\partial x}\left(r\,\overline{u'^{2}}\right)-\frac{1}{r}\frac{\partial}{\partial y}\left(r\,\overline{u'v'}\right)$$
$$+\left(\frac{\sin\alpha}{r}\right)\overline{w'^{2}}-\frac{1}{r}\frac{\partial}{\partial x}\left(r\overline{\tilde{u}^{2}}\right)-\frac{1}{r}\frac{\partial}{\partial y}\left(r\overline{\tilde{u}\tilde{v}}\right)+\left(\frac{\sin\alpha}{r}\right)\overline{\tilde{w}^{2}} \tag{2.14b}$$

y-momentum

$$\bar{u}\frac{\partial\bar{v}}{\partial x}+\bar{v}\frac{\partial\bar{v}}{\partial y}=-\frac{1}{\rho}\frac{\partial\bar{p}}{\partial y}$$
$$+\nu\left[\frac{1}{r}\frac{\partial}{\partial x}\left(r\frac{\partial\bar{v}}{\partial x}\right)+\frac{1}{r}\frac{\partial}{\partial y}\left(r\frac{\partial\bar{v}}{\partial y}\right)+\left(\frac{\sin 2\alpha}{2r^{2}}\right)\bar{u}-\left(\frac{\cos\alpha}{r}\right)^{2}\bar{v}\right]$$
$$-\frac{1}{r}\frac{\partial}{\partial x}\left(r\,\overline{u'v'}\right)-\frac{1}{r}\frac{\partial}{\partial y}\left(r\,\overline{v'^{2}}\right)-\left(\frac{\cos\alpha}{r}\right)\overline{w'^{2}}$$
$$-\frac{1}{r}\frac{\partial}{\partial x}\left(r\overline{\tilde{u}\tilde{v}}\right)-\frac{1}{r}\frac{\partial}{\partial y}\left(r\overline{\tilde{v}^{2}}\right)-\left(\frac{\cos\alpha}{r}\right)\overline{\tilde{w}^{2}} \tag{2.14c}$$

(Note: The shaded circle symbols denote terms retained in a subsequent boundary layer approximation analysis.)

Boundary layer (oscillatory component):

continuity

$$\frac{\partial}{\partial x}(r\tilde{u}) + \frac{\partial}{\partial y}(r\tilde{v}) = 0 \qquad (2.15a)$$

x-momentum

$$\frac{\partial \tilde{u}}{\partial t} + \left[\bar{u}\frac{\partial \tilde{u}}{\partial x} + \bar{v}\frac{\partial \tilde{u}}{\partial y}\right] + \left[\tilde{u}\frac{\partial \bar{u}}{\partial x} + \tilde{v}\frac{\partial \bar{u}}{\partial y}\right]$$

$$= -\frac{1}{\rho}\frac{\partial \tilde{p}}{\partial x}$$

$$+\nu\left[\frac{1}{r}\frac{\partial}{\partial x}\left(r\frac{\partial \tilde{u}}{\partial x}\right) + \frac{1}{r}\frac{\partial}{\partial y}\left(r\frac{\partial \tilde{u}}{\partial y}\right) - \left(\frac{\sin\alpha}{r}\right)^2\tilde{u} + \left(\frac{\sin 2\alpha}{2r^2}\right)\tilde{v}\right]$$

$$-\frac{1}{r}\frac{\partial}{\partial x}\left(r\widetilde{u'^2}\right) - \frac{1}{r}\frac{\partial}{\partial y}\left(r\widetilde{u'v'}\right) + \left(\frac{\sin\alpha}{r}\right)\widetilde{w'^2}$$

$$-\frac{1}{r}\frac{\partial}{\partial x}\left(r\tilde{\tilde{u}}^2\right) - \frac{1}{r}\frac{\partial}{\partial y}\left(r\tilde{\tilde{u}}\tilde{\tilde{v}}\right) + \left(\frac{\sin\alpha}{r}\right)\tilde{\tilde{w}}^2 \qquad (2.15b)$$

y-momentum

$$\frac{\partial \tilde{v}}{\partial t} + \left[\bar{u}\frac{\partial \tilde{v}}{\partial x} + \bar{v}\frac{\partial \tilde{v}}{\partial y}\right] + \left[\tilde{u}\frac{\partial \bar{v}}{\partial x} + \tilde{v}\frac{\partial \bar{v}}{\partial y}\right]$$

$$= -\frac{1}{\rho}\frac{\partial \tilde{p}}{\partial y}$$

$$+\nu\left[\frac{1}{r}\frac{\partial}{\partial x}\left(r\frac{\partial \tilde{v}}{\partial x}\right) + \frac{1}{r}\frac{\partial}{\partial y}\left(r\frac{\partial \tilde{v}}{\partial y}\right) + \left(\frac{\sin 2\alpha}{2r^2}\right)\tilde{u} - \left(\frac{\cos\alpha}{r}\right)\tilde{v}\right]$$

$$-\frac{1}{r}\frac{\partial}{\partial x}\left(r\widetilde{u'v'}\right) - \frac{1}{r}\frac{\partial}{\partial y}\left(r\widetilde{v'^2}\right) - \left(\frac{\cos\alpha}{r}\right)\widetilde{w'^2}$$

$$-\frac{1}{r}\frac{\partial}{\partial x}\left(r\tilde{\tilde{u}}\tilde{\tilde{v}}\right) - \frac{1}{r}\frac{\partial}{\partial y}\left(r\tilde{\tilde{v}}^2\right) - \left(\frac{\cos\alpha}{r}\right)\tilde{\tilde{w}}^2 \qquad (2.15c)$$

(Note: The significance of the shaded circle symbols is defined with equations 2.14)

Core Flow

The core flow equations are developed by the same process of phase-averaging, decomposition, and separation of the time-averaged and oscillatory components. The phase-average momentum equation is given as follows:

$$\frac{\partial \langle u_{CL} \rangle}{\partial t} + \langle u_{CL} \rangle \frac{\partial}{\partial x} \langle u_{CL} \rangle = -\frac{1}{\rho} \frac{\partial}{\partial x} \langle p_{CL} \rangle . \qquad (2.16)$$

Decomposition to $\langle u_{CL} \rangle = \overline{u_{CL}} + \widetilde{u_{CL}}$, time-averaging, and separating the base flow and oscillatory component gives,

Core flow (time-average):

$$\overline{u_{CL}} \frac{\partial \overline{u_{CL}}}{\partial x} + \frac{1}{2} \frac{\partial}{\partial x} \left(\overline{\widetilde{u_{CL}} \widetilde{u_{CL}}} \right) = -\frac{1}{\rho} \frac{\partial \overline{p_{CL}}}{\partial x} \qquad (2.17)$$

Core flow (oscillatory component):

$$\frac{\partial \widetilde{u_{CL}}}{\partial t} + \left[\overline{u_{CL}} \frac{\partial \widetilde{u_{CL}}}{\partial x} + \widetilde{u_{CL}} \frac{\partial \overline{u_{CL}}}{\partial x} \right] + \frac{1}{2} \frac{\partial}{\partial x} \left(\langle \widetilde{u_{CL}} \widetilde{u_{CL}} \rangle - \overline{\widetilde{u_{CL}} \widetilde{u_{CL}}} \right)$$
$$= -\frac{1}{\rho} \frac{\partial \widetilde{p_{CL}}}{\partial x} . \qquad (2.18)$$

Boundary Layer Equations/Small Amplitude Linearization

In the boundary layer, because the gradients of the flow properties perpendicular to the solid surface are much larger than the gradients parallel to the surface, some of the terms in equations (2.14) and (2.15) can be neglected. The order of magnitude $(\mathcal{O})$ of $\bar{u}$ is $\overline{u_{CL}}$,

$x = \mathcal{O}(L)$, and $r = \mathcal{O}(L)$, so that $\partial(r\bar{u})/\partial x = \mathcal{O}(\overline{uc}L)$. L is a reference dimension which is defined as the test section length. The continuity equation (2.14a) then requires that $\partial(r\bar{v})/\partial y = \mathcal{O}(\overline{uc}L)$. Since $y = \mathcal{O}(\delta)$, this gives $\bar{v} = \mathcal{O}(\overline{uc}L \times \delta/L)$.

In the time-average x-momentum equation (2.14b) all of the terms which are marked with shaded circles are of the order $\mathcal{O}(\overline{uc}L^2/L)$. Those which are unmarked are at least 100 times smaller in magnitude and they are omitted in the boundary layer approximation. The pressure variable, P , is the order of magnitude of $(\rho)(\overline{uc}L^2)$ and $\nu = (\overline{uc}L)(L)/Re_L$. It can be shown that, in the boundary layer, the inertia force per unit volume, $\mathcal{O}(\rho\,\overline{uc}L^2/L)$, and the viscous force per unit volume, $\mathcal{O}(\rho\nu\,\overline{uc}L/\delta^2)$, are of the same order of magnitude. It follows then that

$$\mathcal{O}\left[\rho\frac{\overline{uc}L^2}{L}\left(\frac{1}{\rho\overline{uc}L^2}\frac{\delta^2}{L}\right)\right] = \mathcal{O}\left[\rho\frac{\nu\overline{uc}L}{\delta^2}\left(\frac{1}{\rho\overline{uc}L^2}\frac{\delta^2}{L}\right)\right]$$

or

$$\mathcal{O}\left[\left(\frac{\delta}{L}\right)^2\right] = \mathcal{O}\left[\frac{\nu}{\rho\overline{uc}L} = \frac{1}{Re_L}\right]. \tag{2.19}$$

The viscous shear stress term $\nu\left(\frac{1}{r}\frac{\partial}{\partial y}\left(r\frac{\partial\bar{u}}{\partial y}\right)\right) =$ $\mathcal{O}(\overline{uc}L^2/L) \times (L^2/\delta^2\,Re_L)$ which, by using (2.19), is $\mathcal{O}(\overline{uc}L^2/L)$, and the term is thus retained.

The terms $\sin\alpha$ and $\cos\alpha$ are respectively $\mathcal{O}(0.1)$ and $\mathcal{O}(1.0)$ for small α. It is assumed that $u_\gamma (= \mathcal{O}(.1\,\overline{UE}))$ is the relevant scale for the turbulent motion (see(11)) so that $\overline{u_i' u_i'} = \mathcal{O}(.01\,\overline{UE})$. The oscillatory velocity $\tilde{u} = \mathcal{O}(.1\,\overline{UE})$ and, assuming that the continuity equation (2.15a) applies over the transverse scale δ, the oscillatory component $\tilde{v} = \mathcal{O}(.1\,\overline{UE}\,\delta/L)$. The component $\tilde{w}$ is assumed to be no larger in magnitude than $\tilde{v}$.

Applying these definitions to the time-average y-momentum equation (2.14c) gives the result that all of the terms are at least an order of magnitude smaller than $-\frac{1}{\rho}\partial\bar{P}/\partial y \left(= \mathcal{O}(\overline{UC}L^2/L \times L/\delta)\right)$, so that, in the boundary layer,

$$\frac{\partial \bar{P}}{\partial y} = 0. \tag{2.20}$$

In the phase-average equations of motion, oscillatory components are assumed to be $\mathcal{O}$(.1 x time-average component), e.g. $\tilde{u} = \mathcal{O}(.1\overline{UE})$, $\widetilde{u_i' u_i'} = \mathcal{O}(.001\,\overline{UE})$, and $\widetilde{\tilde{u}\tilde{v}} = \mathcal{O}(.001\,\overline{UE}^2\delta/L)$. The terms marked with a shaded circle in equations (2.15) are retained and the others are omitted in the boundary layer equations. The y-momentum equation (2.15c) becomes

$$\frac{\partial \tilde{P}}{\partial y} = 0. \tag{2.21}$$

The core flow equations, (2.17) and (2.18), are treated similarly so that terms which are quadratic in the oscillatory component $\widetilde{UCL}$ are omitted.

The equations of motion are now given as,

Base Flow, Boundary Layer and Core Flow:

continuity

$$\frac{\partial}{\partial x}(r\bar{u})+\frac{\partial}{\partial y}(r\bar{v})=0 \tag{2.22a}$$

momentum

$$\bar{u}\frac{\partial\bar{u}}{\partial x}+\bar{v}\frac{\partial\bar{u}}{\partial y}=-\frac{1}{\rho}\frac{d\bar{P}}{dx}+\nu\left[\frac{1}{r}\frac{\partial}{\partial y}\left(r\frac{\partial\bar{u}}{\partial y}\right)\right] - \frac{1}{r}\frac{\partial}{\partial y}(r\overline{u'v'}) \tag{2.22b}$$

core flow

$$\overline{UCL}\frac{d\overline{UCL}}{dx} = -\frac{1}{\rho}\frac{d\bar{P}}{dx} \tag{2.22c}$$

Oscillatory Component, Boundary Layer and Core Flow:

continuity

$$\frac{\partial}{\partial x}(r\tilde{u})+\frac{\partial}{\partial y}(r\tilde{v})=0 \tag{2.23a}$$

momentum

$$\frac{\partial\tilde{u}}{\partial t}+\left[\bar{u}\frac{\partial\tilde{u}}{\partial x}+\bar{v}\frac{\partial\tilde{u}}{\partial y}\right]+\left[\tilde{u}\frac{\partial\bar{u}}{\partial x}+\tilde{v}\frac{\partial\bar{u}}{\partial y}\right] = -\frac{1}{\rho}\frac{\partial\tilde{P}}{\partial x}(x,t)+\nu\left[\frac{1}{r}\frac{\partial}{\partial y}\left(r\frac{\partial\tilde{u}}{\partial y}\right)\right]-\frac{1}{r}\frac{\partial}{\partial y}\left[r(\langle u'v'\rangle-\overline{u'v'})\right] \tag{2.23b}$$

core flow

$$\frac{\partial\widetilde{UCL}}{\partial t}+\left[\overline{UCL}\frac{\partial\widetilde{UCL}}{\partial x}+\widetilde{UCL}\frac{\partial\overline{UCL}}{\partial x}\right]=-\frac{1}{\rho}\frac{\partial\tilde{P}}{\partial x}. \tag{2.23c}$$

Presentation of the Oscillatory Response

The experimental and theoretical oscillatory response of the boundary layer will, in general, be presented in terms of the amplitude ratio and phase difference of $\tilde{u}$ with respect to a reference oscillation. Figure 2.3 is an illustration of the measured response in the boundary layer at a single x-station. The $\tilde{u}$ oscillation is superimposed on the time-average $\bar{u}$ profile. The line segments indicate the amplitude, Δu , and the position of the data point shows the phase relationship to the centerline oscillation which is represented at the outermost point. These data translate into the amplitude ratio and phase difference patterns shown in Figure 2.4. The amplitude amplification in the outer region, and attenuation close to the wall is shown. A phase lead pattern is established across the boundary layer with a maximum in the region closest to the wall.

2.3 HISTORICAL BACKGROUND

The oscillatory laminar boundary layer has been studied extensively from a theoretical point of view. The first important paper was that of Lighthill (12) who treated the case of a boundary layer flow around a circular cylinder. Lighthill developed a low and a high frequency model, and he predicted a crossover frequency at each point on the body surface. Nickerson (13) refined Lighthill's low frequency analysis. The asymptotic solutions of several authors, which are essentially extensions of Lighthill's solutions, are discussed by Pedley(14). Details of the high frequency solution are reported by Lin (15).

Experimental data were obtained by Hill and Stenning (16) for laminar flat plate (Blasius) flow, and for diffusing (Howarth) flow. They developed an improved model for the intermediate frequency range which is based on the shear wave (high frequency) solution and accounts for first order convective effects by a successive approximation procedure. Recently, Patel (17) has measured laminar boundary layer response with a traveling wave imposed on the freestream velocity, and he has developed an analysis which is similar to the

Lighthill theory.

Several studies of the oscillatory response in fully-developed, turbulent channel or pipe flows have been reported. Hussain and Reynolds (18) compared the measurements of the interaction between weak, orgainzed waves generated upstream by a vibrating ribbon and the background turbulence, in a 2-dimensional channel, with predictions from modified Orr-Sommerfield equations. The same apparatus with a new cylindrical pulser was used by Acharya and Reynolds (19) to measure the channel response to oscillations on the order of 3% of the average velocity. They tested several levels of Reynolds stress modeling with limited success, concluding that adequate modeling of the pressure strain correlations is a crucial step.

Brown, et al, (20) compared predictions of a high frequency model with high frequency data for the attenuation and velocity of wave propagation in small diameter ($\sim$10 mm) fluid lines with imposed oscillations. A time-invariant eddy viscosity modeling of the Reynolds stresses worked well in this regime. A low frequency model and a transition band prediction were also developed but not tested. Margolis and Brown (21)

reported the completion of the experimental work showing good agreement between low frequency data and a quasi-steady, friction factor-based model. Unexpected and dramatic peaks in attenuation and phase velocity were found within the predicted transition band.

Theoretical modeling of the oscillating turbulent boundary layer has progressed from the use of integral methods, e.g. McDonald and Shamroth (22), to the use of differential methods with multi-equation turbulence models. Singleton, et al (23) adapted a differential method originally developed for 3-dimensional, steady flow. A one-equation Reynolds stress closure model was used to predict zero and positive pressure gradient flows. An algebraic eddy viscosity (zero-equation model) modified for unsteady flow was tested by Cebeci (24) and the results agreed reasonably well with the flat plate data of Karlsson (see below, and (27)). Cousteix, et al (25) have compared the results of four different types of models with detailed measurements they have made in a zero pressure gradient boundary layer flow at 43 Hz and amplitudes up to 37%. The models included: (1) integral method, (2) mixing length, (3) k-ϵ /mixing length, and (4) k-ϵ /low Re (see

Chapter 5 for a classification of these methods). Theory vs data comparisons were generally satisfactory with the more sophisticated models giving more detailed information. Patel (26) has extended his earlier laminar work (see above and (17)) to the turbulent boundary layer regime. He devised low and high frequency models, following the strategy used by Lighthill on laminar layers, and compared his results to response data for a traveling wave oscillation. The original detailed oscillating turbulent boundary layer data was reported by Karlsson (27) in 1959, and it was the only data available until very recently. His flat plate data spanned a frequency range of .33-48.0 Hz. for $\overline{UE}$ ~ 5 m/sec, and measurements were made at one x-station.

Heat transfer measurements for a flat plate oscillating turbulent boundary layer were reported by Miller (28). An excellent review on transition in oscillating boundary layers was written by Loehrke, et al (29). Two of several reviews of unsteady fluid dynamics, which include oscillatory shear flows, have been authored by McCroskey (30) and Brocher (31).

3. EXPERIMENTAL EQUIPMENT AND PROCEDURE

3.1 INTRODUCTION

A periodic velocity oscillation is introduced into the flow at the inlet of the conical flow passage where the wall boundary layer is very thin. The objective is to measure and compare the amplitudes and phase orientations of the corresponding oscillations produced in the boundary layer as it develops in the test section. A hot wire anemometer system produces an analog (voltage) output which is related to the velocity in the flow field at the point where the wire probe is positioned. The output signal is decomposed into its time average, oscillatory, and fluctuating components. The probe can be traversed in the streamwise and transverse directions to accomplish a full mapping of the test section flow field. The velocity data are further processed as necessary in order to present a characterization of the oscillatory response of the test section flow.

Subsection 3.2 presents a description of the equipment used, outlines the test procedure, and discusses problems associated with the data acquisition phase. Subsection 3.3 follows a similar format for the data reduction phase.

Preliminary test data and results are presented in this Chapter where appropriate, and the main body of the test results, together with discussion, are presented in Chapter 4.

3.2 DATA ACQUISITION

Equipment

Air Flow Circuit

The air flow test circuit is shown in Figure 3.1. Air is supplied by an 18-bladed, 11.2 kW centrifugal fan. The air is drawn in from the ground floor of the building through a residential furnace filter and sliding throttle valve, and is delivered to the third floor laboratory through 304.8 mm (12.0 in.) diameter, sheet metal ducting. The air is taken into a plenum box which is 750 x 750 x 750 mm. The plenum exit is located 3500 mm upstream of the test section inlet. A sliding valve is located in the roof of the plenum box which is used to bleed air out of the flow circuit to control the velocity at the test section inlet. At the exit of the plenum there is a 152.4 mm (6 in.) length of plexiglass duct 152.4 mm in diameter with a screen filter insert which serves to back pressure the box for better flow uniformity. The plexiglass plenum outlet tube is connected to the wave-maker valve assembly by 304.8 mm (12 in.) diameter sheet metal ducting.

The wave-maker valve is 2585 mm upstream of the test section inlet. The assembly includes the three-plate valve with a plywood-flanged, 304.8 mm diameter plexiglass duct section on both the upstream and downstream sides. Located at the exit of the assembly is a screen and plywood insert whose pattern was tailored to produce uniform flow in the test section.

One sheet metal duct and one plexiglass duct, both 304.8 mm diameter connect the wave-maker valve assembly to a machined, steel nozzle which contracts to 101.6 mm (4.0 in.) at its exit. Just upstream of the nozzle a honeycomb insert 76.2 mm (3 in.) long with 3.2 mm(1/8 in.) hexagonal cells is used to insure non-swirling flow in the test section. A plexiglass cylindrical tube, 101.6 mm (4 in.) in length, connects the nozzle exit to the test section inlet.

Test Section

The test section is a conical diffuser constructed of fiberglass and epoxy resin (see Figure 3.2). The inlet diameter is 101.6 mm (4.0 in.). The outlet diameter is 165.4 mm (6.51 in.), and the length is 609.6 mm (24.0 in.) The diffuser angle included between the centerline and one wall (half-angle) is 3^{o}. The centerline distance is divided into 25 x-stations (0-24) which are spaced

25.4 mm (1 in.) apart. X-station=0 is located at the point where the 3° divergence begins, and there is a constant diameter section which extends 32 mm upstream of this location. X-station=24 is 6 mm from the end of the diffuser duct. The inside walls of the test section are very smooth to eliminate any effects of wall roughness on the boundary layer behavior. Five wall pressure taps are located in a row at x-stations 0,6,12,18 and 24.

The experimental results are represented within a cylindrical coordinate system as shown in Figure 3.2. The x-coordinate is parallel to the test section centerline. The y-coordinate defines the transverse direction in the boundary layer and it lies in a plane perpendicular to the centerline. $R(x)$ is the local radius of the test section, and $r(=R-y)$ is the distance from the centerline to the point (x,y). This coordinate system differs from that described in Chapter 2 within which the equations of motion are derived. Spatial locations differ between the two systems on the order of 1.25 mm at the outer edge of the boundary layer for the 3-degree diffuser angle.

Wave-maker Valve

The sliding plate, wave-maker valve is constructed of three aluminum sections and two plywood flanges as shown in Figure 3.3 The upstream, stationary plate has a pattern of twelve, 19.0 x 50.8 mm slots (16% open area). The center, sliding plate has an identical pattern of slots. The downstream, stationary plate serves to retain the center plate on its sliding track and its flow area is 100% open except for two horizontal guide strips each 12.7 mm in height. Teflon strips are inserted between the sliding track and the top and bottom of the sliding plate to act as bearing surfaces. The sliding plate attaches by connecting rod to an adjustable camshaft assembly. Adjusting the cam controls the length of stroke and the open slot area remaining at T.D.C, which in turn controls the amplitude of the oscillation. The camshaft is belt driven from a Master, 0.37 kW shunt wound, D.C. motor. The motor is connected to the power source through a Minarik, Model SH-56, Motor Speed Control which is used to set the frequency of the oscillation. Photographs of the valve assembly are shown in Figure 3.4 and a schematic of the drive and control components is shown in Figure 3.5.

Instrumentation

The instrumentation for data aqquisition is shown in Figure 3.5. Instantaneous velocity data is obtained using a DISA, constant temperature hot wire anemometer system comprised of the following units:

55D01 Anemometer

55D10 Linearizer

55F35 Right Angle Probe

55H21 Probe Support

The probe wire is platinum plated tungsten 5 μm(.0002 in.) in diameter, and 1.25 mm (.050 in.) in length. The anemometer/linearizer voltage output is proportional to the total velocity sensed at the probe tip. The total velocity is the sum of the time-average, oscillatory, and fluctuating components.

The total signal is inserted into a DISA, 55D30, D.C. voltmeter to obtain a readout proportional to the time-average velocity component, $\overline{U}$. A DISA, 55D35, r.m.s. voltmeter reading is proportional to $\sqrt{\overline{(u'+\tilde{u})^2}}$. A Digital Equipment Corporation PDP 8/E, laboratory computer extracts the oscillatory component, $\tilde{U}$, from the total signal by phase-averaging.

Prior to processing by the laboratory computer the D.C. component is subtracted out of the anemometer/linearizer

output by a zero-suppressor. This is done to accommodate the ± 1 V. limits for the analog input of the DEC computer. The zero-suppressor offsets the D.C. level of the input signal and passes through the A.C. signal components unchanged. The resulting A.C. signal is displayed on an oscilloscope for monitoring purposes and is then processed into the computer.

For the phase averaging operation, the DEC computer also requires a triggering signal input which fires once during each cycle of the wave-maker valve oscillation at the same phase angle position each time. This signal is generated by a photocell circuit located at the wave-maker valve camshaft drive. A notched disk rotates with the camshaft and allows the light from a flashlight bulb to energize the photocell once during each full cycle. The photocell circuit then generates a square wave signal which is used for triggering the sampling sequence of the computer-phase averaging operation. The frequency of the photocell output (wave-maker valve frequency) is monitored on a Hewlett Packard, Model 5216A, Electronic Counter.

The phase averaging process is defined in detail in Chapter 2. The laboratory computer essentially samples, digitizes, and stores a large number of data records from the zero-suppressor output. Each record is one full oscillation of the input waveform (wave-maker valve oscillation) in length, all begun at exactly the same phase angle position. The computer then averages the data records, which, in principal, for a sufficiently large number of records will produce the pure oscillatory component of the input signal. In practice, the D.C. component is not entirely removed by the zero-suppressor, and the fluctuating component is not entirely removed in the phase averaging process. The extraction of the oscillatory component from the total signal is completed by numerically processing the digitized data.

The analog input to the computer is routed through an 8-channel multiplexer to an analog-to-digital (ATD) converter. The computer's sampling, calculation, and display functions are controlled by a user supplied program written in BASIC language. The control program is stored permanently on magnetic tape compatible with the computer's tape drive systems. The input parameters of sampling rate (SR), number of samples per sweep set (NPPSWP), and the number of sweep sets (NSWEEP) are

calculated to correspond to the wave-maker valve frequency. SR (no. sec. between samples) x NPPSWP = the length of one data record. NSWEEP = the total number of records used in the average.

The analog signal levels are continuously digitized in the ATD converter. When the sampling sequence is initiated, the trigger signal causes the ATD to be sampled every SR msec for NPPSWP times. The array of sampled signal levels is retained in storage. The first trigger signal following the completion of the initial sweep set initiates the second set, followed by the third, fourth, etc. The signal levels from the second sweep set are added to the respective entries in the sampling array already in storage. Each point value in succeeding sweep sets is added to its respective sum in the array. The signal from the photocell circuit causes the (Schmitt) trigger in the lab computer to start the sampling sequence for each sweep set at exactly the same phase angle position of the wave-maker valve oscillation.

When the specified number of sweep sets are completed, each of the NPPSWP sums are divided by NSWEEP. The array of the results is the point-by-point phase average of the input wave form.

The phase average is displayed on an oscilloscope, and it is output to punched paper tape and to printed format by teletype.

Traversing Mechanism

The hot wire probe is positioned in the flow through the open outlet of the test section. A traversing carriage which supports the probe rests on the tracks of an optical bench which is positioned parallel to the test section axis downstream of the exit. The probe support is fitted into a 6.4 mm diam. pipe mounting tube. The total length from the probe tip to the end of the mounting tube is approximately 900 mm. The mounting tube is bolted into a fixture on the traversing carriage. The probe is traversed parallel to the axis by sliding the carriage along the tracks of the optical bench. A pointer fixed to the carriage marks the position of the probe (x-coordinate) on a scale fixed to the optical bench.

The mounting tube fixture is traversed perpendicular to the test section axis by turning a lead screw on the carriage. The position of the probe (y-coordinate) is monitored by a dial indicator with divisions of .025 mm (.001 in.). The traversing mechanism with the mounting tube and probe, and the test section are shown in the photograph of Figure 3.2. An overview of the airflow circuit and instrumentation is shown in Figure 3.6.

Numerical Fourier Decomposition

The punched paper tape output of the DEC laboratory computer, together with a control tape are read into the university's CDC 6400 computer and the information is transferred to an internal temporary file via a computer center user library program. A computer calculation procedure then transfers the raw data on the temporary file to punched cards and printed output. The residual non-oscillatory component in the data is removed, and the data are converted from voltage to velocity units. A second computer calculation procedure decomposes the phase-average waveform into its sinusoidal harmonic components by a numerical Fourier analysis.

Data Acquisition - Procedure

The data acquisition procedure is given in the following steps:

PRIOR TO THE TEST RUN

(1) Warm up the electronic units for a minimum of 4 hrs.

(2) Clean and inspect hot wire probe.

(3) Check system for leaks, lubrication, etc.

(4) Check calibration of voltmeters and oscilloscope.

(5) Check operation of triggering signal circuit.

(6) Align probe support tube. Adjust X and Y coordinate indicators.

(7) Run air flow through the test circuit to bring the components up to operating temperature.

(8) Calibrate anemometer and linearizer.

(9) Set, record, and settle out the test section inlet conditions.

DURING THE TEST RUN:

(1) The test section inlet conditions are set immediately following the anemometer system calibration. The linearizer voltage output (time-average) and the air stream temperature and pressure at the test section inlet are recorded. All test variables are monitored continuously throughout the run and the calibration of the anemometer system is checked periodically. A change in temperature of $2^{o}C$ requires a re-calibration of the anemometer system.

(2) For each data point, record the anemometer time-averaged signal component and X and Y coordinate distances. Process the oscillatory component of the anemometer output online through the laboratory computer obtaining punched paper tape and teletype, printed output.

FOLLOWING THE TEST RUN:

(1) Recheck all of the instrumentation for calibrations and zero settings.

(2) Submit the paper tape output of the lab computer, together with a control tape, for conversion to punched card and printed output by the university's CDC 6400 computer.

(3) Submit the punched card data decks with a numerical Fourier decomposition computer calculation procedure to obtain the sinusoidal harmonic components of the phase-averaged wave form at each data point.

(4) Transfer the time-averaged data to punched card format for further data reduction.

Data Acquisition - Discussion

Test Section Conditions - Resonant Frequencies

The resonant frequencies of the test section cavity were determined by introducing an acoustic wave with a signal generator/amplifier/loudspeaker system and measuring the response by traversing with a condenser microphone. Standing waves were found to occur at

170 Hz (fundamental), 340 Hz (2nd harmonic), 510 Hz, etc. Original plans to use an air supply fan with a blade-passing frequency of 345 Hz had to be altered since this unit caused an excitation of the 2nd harmonic resonance. The replacement fan blade passing frequency of 525 Hz, although close to the third harmonic, did not produce a detectable standing wave in the test section. Also, the wave-maker valve frequencies, which were in the range of 5-35 Hz, were not in close proximity to the resonance points.

There will be, superimposed on the boundary layer response, an extraneous disturbance caused by acoustic feedback from the test section exit. The effect on the results is expected to be insignificant with the possible exception of x-station 24. No attempt was made to measure or to eliminate the problem.

Test Section Conditions - Flow Uniformity

A considerable amount of work was required to produce uniform flow in the test section. The flow symmetry under steady flow conditions is shown for the time- averaged velocity, $\overline{U}$, and the turbulence intensity, U_{rms}, in

Figure 3.7. The symmetry of the oscillatory velocity component, $\tilde{U}$, over the flow cross section is illustrated in Figure 3.8. The diffuser angle, plenum box configuration, the orientation and sizes of the ducting and the wave-maker valve design, were dictated, in part, by the flow uniformity requirements. Final adjustments were made by tailoring a plywood and screening insert at the exit of the wave-maker valve assembly section.

Hot Wire Anemometer Measurement

The accuracy with which the time-average or steady flow velocities ($\overline{U}$) in the test section can be measured depends primarily upon the accuracy with which the linearizer output can be made to match the true value of a reference velocity over the range expected in the tests. Additional considerations include the probe spatial resolution, calibration drift, effects of wall proximity, and the directional sensitivity of the wire.

The reference airflow used for calibration was the centerline flow at the exit of the test section. During calibration a pitot-static probe and the hot wire probe are positioned side by side in the reference flow field. A mercury-in-glass thermometer is located in the flow

upstream of the test section. The true velocity is determined from the pitot-static and temperature data.

A constant temperature anemometer is essentially a Wheatstone bridge with the hot wire probe acting as one of the bridge arm resistances. An operating temperature is chosen for the wire depending on the oxidation limits of the material (e.g.~315 C. for a tungsten wire). The resistance of the active (probe) branch of the bridge when the probe is at operating temperature can be calculated. The resistance in the passive branch is set to match the desired active branch resistance. When the anemometer is operating in still air it will supply just enough voltage across the wire to raise its temperature to the point where the bridge is balanced. When the hot probe is placed in an air stream, the flow will tend to cool the wire and to change its resistance. The anemometer circuit keeps the bridge in balance by varying the voltage across the probe to maintain the selected operating temperature. The voltage across the probe (V) is a function only of the velocity of the air stream (U) if the temperature remains constant at the calibration value.

According to King's law (see Bradshaw(32)), which is

derived from a semi-empirical relationship for forced convection heat transfer from a wire in a crossflow,

$$V^2 = V_o^2 + C_1 U^n$$

where

$$V_o = V \text{ at } U = 0.$$

Solving for the velocity, U, gives

$$U = C_2 \left[\left(\frac{V}{V_o} \right)^2 - 1 \right]^{\frac{1}{n}}$$

The anemometer output voltages ($V \rightarrow V_{IN}$, $V_o \rightarrow V_{IN_o}$) are put into a linearizer (non-linear amplifier) which produces an output of the form,

$$V_{OUT\ (LINEARIZER)} = C_3 \left[\left(\frac{V_{IN}}{V_{IN_o}} \right)^2 - 1 \right]^m .$$

The system is calibrated over a selected range of reference velocities. The exponent m is adjusted at the control panel so that V_{OUT} is a linear function of U (i.e. $m = 1/n$). The air velocity across the wire is then directly proportional to the anemometer system output,

$$U = C_4 \times V_{OUT\ (LINEARIZER)}$$

and the proportionality constant can be calculated from the calibration data.

A linearizer calibration plot is shown in Figure 3.9. The reference velocities spanned a range of 25.0-5.5 m/sec,

and velocity measurements were made over a range of 30.48-1.5 m/sec. It is permissible to make moderate extrapolations of the calibration of a hot wire against a Pitot tube (see(32). Sect. 8.3) except for speeds less than .3 m/sec where linearity cannot be maintained and special calibration methods must be used. The position and slope of the line in Figure 3.9 are both important for absolute velocity measurements. Bradshaw (32) maintains that the uncertainty in the slope can be expected to be on the order of ±10%. With care in calibration the linearizer output could be made to match the reference velocity over the calibration range to the accuracy with which the voltmeter could be read. The finest division on the voltmeter scale was 0.002 V.D.C. (0-10 V.D.C. range); however, during calibration the uncertainty in the reading is estimated to be ± 0.03 V.D.C. because of the motion of the scale. This band translates to ± .18 m/sec for the scale factor being used, and the overall uncertainty in $\overline{U}$ is estimated at ± 15% near the wall to ± 2% in the core flow.

The hot wire probe tip is constructed to minimize its interference with the flow field. The probe prongs are 0.5 mm diameter and they are tapered to the point where

the wire is welded. The prongs extend 5 mm at a right angle from the probe support body. The platinum plated, tungsten wire is 5μ m diameter and 1.25 mm in length. The question of adequate spatial resolution arises where very small scale turbulence measurements are being made and the eddy wave lengths may be of the same order as the wire length. The wavelength of the 30 Hz oscillation used in these tests is many times greater than the 1.25 mm wire length.

During operation of a hot wire anemometer the calibration can "drift" from its original setting for a number of reasons. Dirt buildup was minimized in these tests by the installation of three filter screens at three different locations in the airflow circuit. The probe wire was washed before each test by brushing carefully with acetone. An inspection under a microscope followed the cleaning. Another cause of drift is a change in temperature of the test section airflow. The absolute level of the calibration is affected to a much greater degree than the linearity by changing temperature so that this is more important when measuring $\overline{U}$ than when measuring $\widetilde{U}$. The airflow temperature indicator was closely monitored during the course of a test and a recalibration was performed for a change of more

than $2^{o}C$.

Tests with a $5\mu m$ wire in fully developed channel flow (33) indicated that increased heat transfer from the wire due to the proximity of the channel wall gave inaccurately high velocity readings for $y+ < 5$. This effect appears in the steady flow data for $5 < y+ < 15$, and it is shown in the Law-of-the-Wall plots in Chapter 4.

The hot wire probe senses the vector sum of the x, y and θ velocity components. The test circuit was designed to provide non-swirling flow ($\overline{W} = 0$). It was shown in Chapter 2 that $\overline{V}$ and $\tilde{V}$ are on the order of 10 to 100 times smaller than $\bar{u}$ and $\tilde{u}$ respectively. Comparisons in steady and oscillatory flow with the probe in several different orientations showed no significant effect of the y and θ velocity components on the data for $\bar{u}$ and $\tilde{u}$.

Phase-Averaging

The accuracy of the oscillatory data depends primarily on the accuracy of the slope of the linearizer calibration curve, the frequency response of the instrumentation train, and the phase-averaging procedure. The accuracy of the linearizer calibration was discussed in the previous section. An amplitude measurement for a

single boundary layer y-station utilizes only a small segment of the linearizer curve ($\Delta u \backsim \bar{u}/10$); however, each y-station is located on a different part of the curve and amplitude ratios are calculated with respect to the centerline oscillation. If the assumed calibration curve is flatter than the true curve, the reported amplitudes would be inaccurately high; and if the curve is too steep, the amplitude data would be low. Amplitude ratios are affected similarly but to a lesser degree.

The limit of the true phase-averaging (requiring an infinite number of data samples) can be approached in practice by increasing the number of samples used to a point where any changes in the average become insignificant. At the centerline of the duct, where the turbulence level is low, the oscillatory component is easily extracted as shown in Figure 3.10. There is little change in increasing the number of samples above 200, and the amplitudes of the higher harmonics are less than 5 percent of the fundamental. Figures 3.11 and 3.12 show more obvious effects for y-stations at the edge and in the middle of the boundary layer, respectively. A larger number of samples is required to eliminate the fluctuating component. Figure 3.13 shows the amplitudes of the fundamental and the higher harmonics corresponding

to the previous two figures. At .91$\bar{\delta}$ the Fourier fundamental can adequately define the oscillatory component using $\sim$ 500 samples as shown by the approach to a constant amplitude. The picture at .48$\bar{\delta}$ is not so clear. Using less than 500 samples is obviously inadequate. Above 500 samples an amplitude band is defined that is ± 8% of the average. The higher harmonics are 5 percent or less of the fundamental.

The hot wire anemometer is adjusted during calibration so that negligible phase shift or amplitude modulation occurs out to 3 kHz. The zero suppressor and lab computer components were checked and adjustments made in operation to minimize errors.

Based on an anlysis of the errors associated with specific operations, as discussed above, and an examination of the results of a number of sensitivity and repeatability checks, the estimated maximum uncertainty, with 95% confidence, in the oscillation amplitude is ± 10%, and for the phase difference is ± 7 deg. The

uncertainty is greater near the wall and smaller in the core flow. The higher harmonics are considered to be insignificant, and the response is adequately defined by the Fourier fundamental.

X and Y Coordinate Distances

The x-distance alignment is accomplished by positioning the traverse mechanism such that the probe tip contacts an alignment fixture which is inserted into the test section with its front surface coincident with x-station 0. A graduated-scale which is fastened to the base of the optical bench track is then adjusted to line up the zero with a pointer attached to the traversing carriage. The x-distance accuracy is a function of how well the pointer can be visually lined up with the scale divisions.

The measurement of the distance of the hot wire probe tip from the wall is made difficult by the conical geometry of the test section.

A determination of one reference distance at each x-station is made in the following way: A strip of tape of known thickness, which is an electrical conductor, is installed along the length of the inside of the test section where the traversing will take place.

A dummy probe of the same dimensions as the probe to be used in the data run is placed in the probe support and aligned. The probe is traversed in toward the wall to a point where it is just touching the tape. Contact is detected by an ohmmeter connected to the circuit from the probe electrical connector through the prong tips and through the conductor tape. At this point the probe distance from the wall is equal to the thickness of the tape. A dial indicator reading on the traversing mechanism is recorded and matched to the y-distance. The finest scale divisions on the dial indicator are 0.001 in. When the tape is removed and the run-probe is installed and aligned, the initial y-distance can then be determined using the dial indicator reading recorded as described above. As a final check before a data run, the probe distance from the wall is checked visually at x-station-24. Subsequent y-positions are set by the dial indicator on the traverse mechanism.

At each x-station, an error in the initial y-distance

calibration will be propagated unchanged to all subsequent y-distances. Based on the repeatability of the calibration and the matchup of time averaged boundary layer profiles it is estimated that the uncertainty band in the y-distance is ±0.125 mm.

3.3 DATA REDUCTION

Data Reduction - Procedure

Time Average (and Steady Flow) Velocity

From the time average and steady flow velocity data the boundary layer thickness parameters $\overline{\delta 1}$ and $\overline{H}$ are calculated, and the wall friction coefficient, $\overline{C}_F$, determined. These parameters serve to characterize the base flow, and the information is required in the theoretical study which follows. Law-of-the-wall and velocity-defect-law profiles were developed to further define the base flow. Boundary layer equilibrium parameters were determined. The core flow streamwise velocity gradient, $d\overline{UCL}/dx$ was calculated numerically in order to define the pressure gradient conditions.

Oscillatory Velocity Data

The primary reduction of the oscillatory velocity data was accomplished in smoothing the phase averaged wave forms by numerical Fourier analysis as described above in the data acquisition procedure. The response patterns

in the boundary layer are presented in terms of amplitude ratios and phase differences with respect to reference oscillations on the diffuser centerline.

Data Reduction - Discussion

Boundary Layer Thickness Parameters

The axisymmetric boundary layer displacement thickness, $\overline{\delta 1}_{AX}$, is defined as follows:

$$\rho \overline{UCL} \times 2\pi R \times \overline{\delta 1}_{AX} = 2\pi \int_0^{\delta} \rho (\overline{UCL} - \bar{u})(R-y)dy$$

The right hand side (RHS) is the deficit in mass flow rate through a cross section of the diffuser caused by the retardation of the flow in the boundary layer. This is equated (LHS) to the mass flow rate of the fluid with a uniform velocity, $\overline{UCL}$, through a cross section of area $2\pi R \overline{\delta 1}_{AX}$. The $2\pi R \overline{\delta 1}_{AX}$ can be considered to be the part of the cross sectional area which is blocked off due to the boundary layer resistance. The effective flow area, AEFF, is then

$$AEFF = \pi R^2 - 2\pi R \overline{\delta 1}_{AX}$$

and the volume flow rate, Q, at a cross section of the diffuser is

$$Q = \overline{UCL} \times AEFF$$

The axisymmetric momentum thickness, $\overline{\delta 2}_{AX}$, is defined by

$$\rho \times \overline{UCL}^2 \times 2\pi R \times \overline{\delta 2}_{AX} = 2\pi \int_0^{\delta} \rho \, \overline{u}(\overline{UCL} - \overline{u})(R-y)\,dy$$

where the right hand side is the deficit in momentum flux through a cross section caused by the boundary layer velocity gradient.

The boundary layer displacement thickness, $\overline{\delta 1}_{AX}$, the momentum thickness, $\overline{\delta 2}_{AX}$, and the shape factor, $\overline{H}$, are calculated for the axisymmetric coordinate system of the test section, as follows:

$$\overline{\delta 1}_{AX} = \int_0^{\delta} \left(1 - \frac{\overline{u}}{\overline{UCL}}\right)\left(1 - \frac{y}{R}\right) dy \qquad (3.1)$$

$$\overline{\delta 2}_{AX} = \int_0^{\delta} \frac{\overline{u}}{\overline{UCL}}\left(1 - \frac{\overline{u}}{\overline{UCL}}\right)\left(1 - \frac{y}{R}\right) dy \qquad (3.2)$$

$$\overline{H} = \overline{\delta 1}_{AX} / \overline{\delta 2}_{AX} \qquad (3.3)$$

Note that in the definition (3.1) the $\overline{\delta 1}_{AX}$ is not physically the distance that the annular blocked area extends inward along a radius from the wall of the test section. The equation which does define this physical distance is given by

$$\rho \times \overline{UCL} \times 2\pi\left(R - \frac{\delta 1}{2}\right) \times \delta 1 = 2\pi \int_0^{\delta} \rho\left(\overline{UCL} - \overline{u}\right)(R-y)\,dy$$

and

$$\delta 1 - \frac{\delta 1^2}{2R} = \int_0^{\delta} \left(1 - \frac{\overline{u}}{\overline{UCL}}\right)\left(1 - \frac{y}{R}\right) dy$$

so that

$$\overline{\delta 1}_{AX} = \delta 1 - \frac{\delta 1^2}{2R}$$

For the case where $R \gg \delta$, the boundary layer geometry may be approximated to be 2-dimensional, and:

$$\delta 1_{2D} = \int_0^{\delta} \left(1 - \frac{\overline{u}}{\overline{UCL}}\right) dy$$

The experimental velocity profiles are numerically integrated to obtain the boundary layer thickness parameters. This involves curve fitting and smoothing the data points. The primary requirement is that the methods are consistent where comparisons are to be made. The difficulty lies in making the calculations very close to the wall where data points are few and the velocity gradient very steep.

One of the most extensive projects for reducing boundary layer data was carried out by Coles for the 1968 Stanford University, Boundary Layer Conference (see (34)). Coles published results using two methods. The first involved a parabolic curve fitting of sets of three points with smoothing by overlap-averaging. In the second, the data were fitted by a Law-of-the-Wake profile and this curve was integrated analytically from the wall to $y^+ = 50$, beyond which the integration scheme continued numerically by the first method. The first method of Coles was followed in this study for the calculation of the axisymmetric thickness parameters for both the time averaged and steady flow data. A variation on the second method using the Law-of-the-Wall was used to calculate the 2-D thickness parameters required for profile fitting in the theoretical study.

In the curve fitting, overlap averaging method, a polynomial of degree 2 is fitted through three data points. The required integrals are evaluated for the intervals between points #1 and #2 (= $A_{12}(I)$), and between points #2 and #3 (=$A_{23}(I)$). The whole process is then moved outward away from the wall by one data point so that the new set of three points includes the previous #2 and #3 points (now #1 and #2) and one additional point. The integrals are again evaluated for the intervals between points and the values for the repeated interval are averaged

$$A = \frac{A_{23}(I) + A_{12}(I+1)}{2} .$$

The calculation begins at the wall (y=0, U=0) so that the interval between the wall and the first data point is not repeated and averaged. The same is true of the last interval which is bounded by the first data point at which $\overline{U}=\overline{UCL}$.

In the profile fitting method, the data points are fitted with the Law-of-the-Wall profile:

sublayer

$0 \leq y^+ < 4 \qquad u^+ = y^+ \qquad (3.4)$

buffer

$4 \leq y^+ < 30 \qquad u^+ = C_0 + C_1(\ln y^+) + C_2(\ln y^+)^2 + C_3(\ln y^+)^3 \qquad (3.5)$

fully turbulent

$30 \leq y^+ \qquad u^+ = \frac{1}{0.41}\ln y^+ + 5.00 \qquad (3.6)$

where $u^+ = \overline{u}/u_\tau$ $y^+ = y u_\tau/\nu$, and $u_\tau = \overline{UCL}\sqrt{c_f/2}$.

The constants in the buffer profile are determined by matching slopes and ordinates with the sublayer on one end and the log region on the other. The determination of C_F from the data is discussed below.

The Law-of-the-Wall profile is integrated analytically from the wall (y=y+=0) to the first data point in the fully turbulent region. From this point on, the integration is continued using the curve fitting, overlap-averaging method described above.

Boundary Layer Wall Friction

The shear stress at the wall of the test section is expressed in terms of a friction coefficient, $\overline{C}_F$,

$$\tau_w = \overline{C}_F \rho \frac{\overline{UCL}^2}{2} . \qquad (3.7)$$

The friction coefficient was obtained from the boundary layer velocity data by use of the Law-of-the-Wall. The Law-of-the-Wall profile in the logarithmic region is given by equation (3.5). After substitution and rearrangement, this equation becomes

$$\frac{\overline{U}}{\overline{UCL}} = \sqrt{\frac{\overline{CF}}{2}} \left[\frac{1}{0.41} \ln\left(\frac{y \overline{UCL}}{\nu} \sqrt{\frac{\overline{CF}}{2}} \right) + 5.0 \right] . \qquad (3.8)$$

For each data point $(y, \overline{U}, \overline{UCL})$ a solution is obtained for $\overline{C}_F$. The method for selecting $\overline{C}_F$ is illustrated

in Figure 3.14. The coordinates are the $\overline{U}/\overline{UCL}$ and $\ell n((y)(\overline{UCL})/\nu)$ of equation (3.8), and the loci of constant $\overline{C}_F$ are the solid straight lines in the logarthmic region of the boundary layer. The curved portion of the solid, constant $\overline{C}_F$ curves are plots of equation (3.4), representing the sublayer region of the Law of the Wall. The logarithmic, or fully turbulent region, of the boundary layer is defined where the data points fall along a straight line parallel to a line of constant $\overline{C}_F$. The value of $\overline{C}_F$ in this region is the correct solution for the profile data points. As an example, for the data shown, for x-station 22, $\overline{C}_F$=.00105. This method was proposed by Clauser (35) and has been used extensively for calculating $\overline{C}_F$ from boundary layer velocity profiles. The results of a sensitivity study indicated that the uncertainty associated with the calculation of $\overline{C}_F$ is ± 5%.

Numerical Differentiation

The time-averaged centerline velocity data are numerically differentiated in order to characterize the diffuser performance in terms of the pressure gradient profile

$$\frac{dP}{dx} = -\rho \overline{UCL} \frac{d\overline{UCL}}{dx} .$$

In the theoretical study it was required to obtain streamwise derivatives for the time average boundary layer

thickness parameters and for the oscillatory component of the centerline velocity. The numerical differentiation procedure involves fitting a smooth curve to the data points and obtaining the derivatives from the equation of the curve.

The time-average, centerline velocity data were fitted by a least squares, polynomial regression. The procedure is to minimize the sum of the squares of the differences between data and curve fit by adjusting the polynomial coefficients. The curve fits for a range of polynomial degrees were computer plotted against the data for visual examination. Centerline velocity data were obtained at four additional points, extending 100 mm both upstream and downstream of the test section, to insure the smoothness of the curve fit at the inlet and exit. A choice of the degree of the polynomial which gave the best fit was based on visual examination and a comparison of tabulated curve fit values of $\overline{UCL}$, $d\overline{UCL}/dx$, and $d^2\overline{UCL}/dx^2$, and the apparent concavity and location of an inflexion point in the data.

4. EXPERIMENTAL RESULTS

4.1 TEST VARIABLES

Definition

The test variables which were controlled during the study are the following:

- Test section geometry:
  - Inlet diameter (D(0))
  - Diffuser half-angle (α)
  - Centerline length (L)
- Inlet centerline velocity ($\overline{UCL}(0)$)
- Inlet oscillation amplitude ($\Delta UCL(0)$)
- Oscillation frequency (FREQ).

The non-dimensional test parameters listed below are derived from the test variables, and they are used to characterize the test conditions reported. These parameters represent ratios of forces acting on the fluid particles in oscillatory viscous flow. They are useful in discussing the response patterns, and they are the measures of dynamic similarity which allow the results to be compared with those from other studies:

- Inlet Reynolds number ($Re_D = (\overline{UCL}(0))(D(0))/\nu$)
- Pressure Gradient parameter ($\beta = (\delta 1/\tau_w)(dP/dx)$)

- Oscillation amplitude ratio $(\Delta u_{CL}(x)/\overline{u_{CL}}(x))$
- Reduced frequency $(\overline{\omega}_x = 2\pi(FREQ)(x)/\overline{u_{CL}}(x))$.

The experimental tests were run in two separate sets. The first set was conducted jointly with A. A. Schachenmann. The data from this set will be referred to as Data Set-1 (DS-1). The tests run and the conditions for each run are listed in Table 5.1. The DS-1 results have been reported by Schachenmann (6). These were used primarily to show the response of the diffuser core flow to the oscillations. Boundary layer response was measured at five x-stations (0,6,12,18,24) in the test section.

The tests from which have come the results of Data Set-2 (DS-2) are an extension of DS-1 and they were performed by the author. The tests and conditions are listed in Table 5.2, and the results are reported and discussed herein. The primary objective of the DS-2 tests was to determine the boundary layer response. Modifications made in the testing equipment and procedure allowed the measurement of the oscillatory response at thirteen x-stations in the test section. The DS-2 results give a complete picture of the velocity response in a conical diffuser to oscillations in the core flow. It was desired to test as wide a range as possible of each parameter which might affect the response, and it

was desired to vary each parameter independently as far as was possible. The extent to which these goals were met is discussed in the following paragraphs.

Test Section Geometry

A single test section geometry was used for all of the tests of DS-1 and DS-2. An inlet diameter of 101.6 mm (4.0 in.) was chosen to provide, together with the inlet velocity, a Reynolds number, Re_D, on the order of magnitude of 150,000 which is comparable to a portion of the Re_D range for turbomachinery blade passages. The 3^o diffuser half-angle gave a stable, attached flow throughout the test section. The angle was selected in order to avoid the transitory or continuously separated flow regimes. A 6^o diffuser was tested and found to be unsatisfactory. The walls of the test section were made hydrodynamically smooth so that wall roughness was eliminated as a variable.

Inlet Centerline Velocity

Inlet centerline velocity, $\overline{UCL}(0)$, ranged from 18.29-30.48 m/sec (60-100 ft/sec). It was desired that a fully turbulent boundary layer be already established in the flow at x-station 0. A constant diameter duct section 134 mm in length was built into the airflow circuit upstream of x-station 0 to accommodate the laminar to

turbulent transition. Pen recorder traces of the boundary layer velocity profiles, taken during preliminary testing, indicated that 18.3 m/sec was a safe lower limit to assure that the turbulent flow regime was established at the test section inlet. The maximum capacity of the fan was 42.1 m/sec. Upon establishing the fact that the dependence of the oscillatory response on Re_D could not be shown within the limited range available with the test facility, most of the DS-2 tests were run at $\overline{UCL}(0)$ = 18.3 m/sec. These velocity levels represent a Mach number range of, .05-.12, which is well within the incompressible regime.

The streamwise pressure gradient in the test section is characterized by the dimensionless parameter $\beta = (\bar{\delta}1/\tau_w)(dP/dx)$. This quantity can be shown to be a measure of the ratio of local pressure and shearing forces. The values of β range from .14 to 17.07 over the test section length. This range can be described as a mild pressure gradient and the flow is one of decreasing severity.

Oscillation Amplitude

The inlet oscillation amplitude (zero-to-peak) was varied in the range of 2-10% of the inlet centerline velocity. The maximum for each run was limited to the

point where excessive vibrations occurred in the valve mechanism. The lower limit corresponds to the higher frequencies.

Oscillation Frequency

The oscillation frequencies ranged from 5 Hz to 30 Hz. At 5 Hz the sinusoidal quality of the oscillation at the test section inlet began to show some deterioration. The maximum of 35 Hz was the mechanical limit of the valve mechanism.

The reduced frequency parameter $\overline{\omega}_x = \frac{(2\pi)(FREQ)(x)}{\overline{UCL}(x)}$ physically expresses a ratio of local oscillatory acceleration to convective acceleration in the flow field (see Section 4.3). Characteristic values for the tests $\overline{\omega}_L = (2\pi)(FREQ)(L)/\overline{UCL}(0)$ ranged from 0.5 to 7.3, while local values, $\overline{\omega}_x$, spanned .09 to 11.7.

Six categories of tests were run for DS-2: (1) Steady flow, boundary layer velocity profile tests; (2) time-mean, boundary layer velocity profile tests; (3) 7-8 point, boundary layer oscillatory velocity tests taken at 13 x-stations; (4) 20-point, boundary layer oscillatory velocity tests, taken at 5 x-stations; (5) boundary condition tests of velocity oscillations, taken on the test section centerline, at 13 x-stations; and

(6) initial condition tests of velocity oscillations, taken at 20 points through the boundary layer, at x-station 4.

4.2 EXPERIMENTAL STEADY FLOW

Characterization

Centerline Velocity

The centerline velocity profiles through the test section, and the streamwise velocity gradient profiles for $\overline{UCL}(0)$ = 18.3 and 30.5 m/sec are shown in Figure 4.1. Note that in the conical geometry the velocity gradient increases in magnitude very sharply from the inlet to approximately x-station 3. At this point the boundary layer growth begins to counteract the wall divergence, and the centerline velocity profile then progressively flattens out through the remaining length of the test section. On the centerline the turbulence intensity ratio $\sqrt{\overline{u'^2}} / \overline{UCL}(0)$ was on the order of 1%.

Boundary Layer

Steady flow, boundary layer velocity profiles at thirteen x-stations are shown for $\overline{UCL}(0)$ = 18.29 m/sec in Figure 4.2, and for $\overline{UCL}(0)$ = 30.48 m/sec in Figure 4.3. The normalized profiles, $\overline{U}/\overline{UCL}$ vs Y, are virtually identical for the two inlet velocities. The classic shape of a turbulent boundary layer developing in an adverse

pressure gradient is illustrated. The velocity has a very steep gradient just adjacent to the wall. The fluid near the wall is retarded to a progressively greater degree, with respect to the free stream velocity, at each x-station further downstream in the test section. At x-station 18 the profile begins to show the approach to separation as it develops a shape with two inflection points. The boundary layer thickness, $\overline{\delta}$, ranges from 5 mm to 45 mm for $\overline{UCL}(0)$ = 18.29 m/sec, and 30.48 m/sec.

The profiles of axisymmetric displacement thickness, $\overline{\delta 1}_{AX}$, shape factor, H, and wall friction coefficient, $\overline{C}_F$, are shown for $\overline{UCL}(0)$ = 18.29 m/sec and 30.48 m/sec in Figures 4.4 and 4.5 respectively. Since the normalized boundary layer velocity profiles for the two inlet velocities match so closely, the profiles for the thickness parameters, $\overline{\delta 1}_{AX}$ and H, are also nearly identical. The value for H reaches 2.3 at the end of the test section giving a measure of the approach of the flow to separation. The skin friction decreases as the boundary layer thickens. A comparison of the wall shear stress profiles for the two inlet velocities is shown in Figure 4.6.

More detailed information is provided for the primary base flow of $\overline{UCL}(0)$ = 18.29 m/sec:

For descriptive reasons a turbulent boundary layer is generally divided into two regions, inner and outer (see Figure 4.7), because the mechanism of the flow near the wall is distinctly different from that near the free stream boundary. In the inner layer the presence of the solid boundary is felt through the fluid viscosity. The outer layer flow is intermittent. The turbulent eddies form a distinct, but continuously and randomly moving boundary with the irrotational free stream flow. At a given point location in the outer layer, the flow varies with time between free stream irrotational flow and turbulent eddy flow.

The inner layer is viewed, with even greater resolution, as being itself composed of three distinct regions. Viscous forces dominate in the viscous sublayer adjacent to the wall. The flow here is not identical to laminar flow but it has a highly ordered, time-dependent turbulent structure in which turbulent filaments are periodically ejected outward from the sublayer. The buffer layer is a transition between the sublayer and the fully turbulent region. The flow pattern

in the fully turbulent region is a very complicated, apparently random, turbulent motion over the entire plane of flow.

The universal nature of the inner region is illustrated by the Law of the Wall. The Law of the Wall describes the velocity profile of the inner layer in terms of the wall shear stress, τ_w. A characteristic velocity (friction velocity), u_τ, is defined by,

$$\rho u_\tau^2 = \tau_w, \quad \text{or} \quad u_\tau = \sqrt{\tau_w/\rho}. \tag{4.1}$$

A characteristic length is given by ν/u_τ.

The x-momentum equation for a two dimensional, incompressible turbulent boundary layer is given by

$$\bar{u}\frac{\partial \bar{u}}{\partial x} + \bar{v}\frac{\partial \bar{u}}{\partial y} = -\frac{1}{\rho}\left(\frac{d\bar{P}}{dx} + \frac{\partial \tau}{\partial y}\right)$$

where τ is the laminar plus turbulent shear stress

$$\tau = \mu\frac{\partial \bar{u}}{\partial y} - \rho\overline{u'v'}.$$

The original derivation of the Law of the Wall was applied to a zero pressure gradient flow, $d\bar{P}/dx = 0$, so that, in the very thin film of the viscous sublayer, where $\bar{u} \to 0$, $\bar{v} \to 0$ as the wall is approached,

$$\tau \approx \text{const} = \tau_w$$

and

$$\nu\frac{\partial \bar{u}}{\partial y} - \overline{u'v'} = \frac{\tau}{\rho} \approx \frac{\tau_w}{\rho} = u_\tau^2,$$

also, as $y \to 0$ then $\overline{u'v'} \to 0$, and

$$u_\tau^2 = \nu(\partial \bar{u}/\partial y).$$

Integrating this equation and introducing the characteristic velocity and length scales to non dimensionalize both sides gives

$$u^+ = y^+ \qquad 0 \leq y^+ < 4 \quad \underline{\text{viscous sublayer}}. \qquad (4.2)$$

where

$$u^+ = \bar{u}/u_\tau$$
$$y^+ = y/(\nu/u_\tau).$$

The assumption $\tau \approx \tau_w$ is carried over to the <u>fully turbulent region</u> where $\nu \frac{\partial \bar{u}}{\partial y}$ is small compared to $-\rho \overline{u'v'}$ and therefore

$$u_\tau^2 = -\overline{u'v'}. \qquad (4.3)$$

The turbulent shear stress term on the RHS of the equation above can be modeled by a Boussinesq eddy viscosity equation (a detailed discussion of this level of turbulence modeling is included in Chapter 5)

$$-\overline{u'v'} = \overline{\nu}_T \, \partial \bar{u}/\partial y.$$

The eddy viscosity, $\overline{\nu}_T$, is proportional to the product of a characteristic turbulence velocity and a characteristic turbulence length,

$$\overline{\nu}_T \propto \ell_T \times V_T.$$

On a flat plate the eddy viscosity has been shown to vary linearly with distance y from the wall.

Using $y \propto \ell_T$ and $u_\tau \propto v_T$ gives

$$\nu_T = \kappa y u_\tau$$

where

$$\kappa = \text{constant}$$

Substituting into (4.3) gives

$$u_\tau^2 = \kappa y u_\tau (\partial \bar{u}/\partial y).$$

Integration and nondimensionalizing yields

$$u^+ = (1/\kappa) \ln y^+ + \text{const} \qquad \begin{matrix} y^+ \geq 30 \\ \underline{\text{fully turbulent}} \\ \underline{\text{region}}. \end{matrix} \quad (4.4)$$

The <u>buffer</u> profile is a third degree curve fit in $(\ln y^+)$ which matches the ordinate and slope of the $u^+ = f(y^+)$ profile of the sublayer on one end, and of the fully turbulent region on the other,

$$u^+ = C_0 + C_1(\ln y^+) + C_2(\ln y^+)^2 + C_3(\ln y^+)^3 \qquad \begin{matrix} 4 \leq y^+ < 30 \\ \underline{\text{buffer}}. \end{matrix} \quad (4.5)$$

A composite of the Law-of-the-Wall profiles for the thirteen x-stations of the $\overline{UCL}(0)$ = 18.29 m/sec run, DS-2/Run 1 is presented in Figure 4.8. The wall shear stress, τ_w, at each x-station was determined as described in Section 3.3, and the solid curves are the corresponding Law-of-the-Wall profiles as described above. The extent of the fully turbulent region of the boundary layer is shown where the data points coincide with the straight line, logarithmic portion of the curve. The growth of

the outer region is shown as the data points progressively deviate to a greater extent from the curve at each successive x-station. Deviation of the data point nearest the wall from the profile curve is believed to be caused by experimental error. The wall proximity produces effects which result in an inaccurately high velocity reading from the hot wire anemometer. This source of error is discussed in Chapter 3.

A universality of the outer region of a turbulent boundary layer exists only for special cases where the ratio of pressure forces to shear forces, as expressed by the parameter β, remains constant at every point in the flow. Only a few of these self-preserving or equilibrium flows have been measured experimentally: $\beta = 0$, flat plate; $\beta =$ 1.8 and 8.0, Clauser (1954); $\beta = -0.35$ and -0.53, Herring and Norbury (1967) (see (36), p. 122). The x-dependence of β for the non-self-preserving flow of DS-2/Run 1 is illustrated in Figure 4.10. It can be shown that a self-preserving boundary layer will have a universal <u>velocity defect profile</u>,

$$\frac{\bar{u} - \overline{u_{CL}}}{u_\tau} \text{ vs } f(y/\delta).$$

The function f will differ for each type of self-preserving layer, but, when the proper conditions are met, f is not a function of length Reynolds number or of surface roughness. The dissimilarity of a streamwise series of

velocity-defect profiles is then a measure of the deviation of the flow development from equilibrium. The profiles for the 13 x-stations of DS-1/Run 1 are shown in Figure 4.11. The effect on the development of a non-equilibrium pressure gradient profile is clearly seen in the changing shape of the defect profiles.

Diffuser Flow

The test section pressure recovery for $\overline{UCL}(0)=18.29$ m/sec is characterized in Figure 4.11. The pressure recovery coefficient is defined as

$$C_p = P(XCL) - P(0)/\tfrac{1}{2}\rho\,\overline{UCL}^2(0).$$

From the Bernoulli equation, in the inviscid, 1-D core flow,

$$P(XCL) - P(0) = \tfrac{1}{2}\rho\,\overline{UCL}^2(0) - \tfrac{1}{2}\rho\,\overline{UCL}^2(XCL).$$

Pressure recovery calculated from $\overline{UCL}$ data is shown as a solid curve in Figure 4.11.

Alternatively (see Chapter 3),

$$AEFF = \pi R^2 - 2\pi R\,\bar{\delta}1_{AX}$$
$$\overline{UCL} = Q/AEFF.$$

As a test of the consistency of the experimental results, $C_{\bar{p}}$ was calculated from $\bar{\delta}1_{AX}$ data (open symbols). Volume flow rate, Q, was not measured directly but was calculated from $\overline{UCL}$ and AEFF data at x-station 0.

The diffuser inlet blockage parameter, $B(o)$, is defined as

$$B(0) = \frac{A^{(0)} - AEFF^{(0)}}{A^{(0)}} = 1 - \frac{AEFF^{(0)}}{A(0)}.$$

$B(0) = .0191$ for the $\overline{UCL}(0)=18.29$ m/sec test.

4.3 EXPERIMENTAL OSCILLATING FLOW

Results

Karlsson Data

The Karlsson (27) data for an oscillating turbulent boundary layer on a flat plate are shown in Figures 4.12 and 4.13. The main stream flow is given by

$$U_E(t) = \overline{U_E} + \Delta U_E \cos \omega t.$$

The response of the velocity in the boundary layer is shown as a function of the main stream amplitude and frequency for a single x-station. The amplitude and phase in the figures are referenced to the local, main stream values.

The boundary layer exhibits a surprising variety of responses for the frequency range of 0.33 to 7.65 Hz, and free stream amplitudes, $\Delta U_E/\overline{U_E}$, on the order of 10 percent. The amplitude ratio profiles, $\Delta U/\Delta U_E$ vs $y/\bar{\delta}$, clearly show that as frequency is increased the oscillation penetrates unchanged deeper into the boundary layer. An amplification peak moves progressively from the outer region of the boundary layer closer to the wall as the frequency is increased over the range. The phase angle profile shows a lead (with respect to the local

centerline oscillation) in the outer region for the lowest frequency. This gradually changes to a lag for 1.33 Hz, and then changes to a zero phase angle for higher frequencies. Very near the wall $\Delta U/\Delta U_E \rightarrow 0$, and there is a phase lead over the entire frequency range. One test at a high frequency of 48 Hz showed that the oscillation penetrated unchanged all the way to the data point nearest the wall.

Data Set-1

The Karlsson study, like the experimental studies of Cousteix (25) and Patel (26) show the response of the turbulent boundary layer to main stream oscillations which are independent of that response. For the internal flow of a diffuser, the boundary layer response is strongly coupled to the main stream oscillations. The main stream oscillation pattern cannot be considered as an independent forcing function which is simply defined as was done for the Karlsson tests. For an internal flow, the inlet velocity, oscillation frequency, oscillation amplitude and passage geometry are the independent test variables. The main stream (core flow) pattern is measured together with the boundary layer response.

A sample of the DS-1 results is presented in Figures

4.14a and 4.14b to provide an historical perspective. Because of the coupling discussed above, a mapping of the whole test section is required to define the response. The variation in the response patterns along the test section length for a constant frequency can be seen. There is an obvious amplitude amplification at x-station 6 and switches between weak amplifications and attenuations at x-stations 12, 18, and 24. There are phase lag patterns in the outer region of the boundary layer at x-stations 6 and 12, no discernible pattern at 18, and a phase lead bulge in the inner half of the layer at 24. The shortcoming of the DS-1 boundary layer results is that the evolution of the response pattern in the test section could not be determined since the mappings were done at an insufficient number of x-stations.

Data Set-2

The principal portion of the DS-2 results are presented in Figures 4.15a and b to 4.20a and b. These are boundary layer response mappings done at 50 mm intervals along the test section length. The inlet velocity was held constant at 18.3 m/sec for these six runs and the oscillation frequency was varied from 5 Hz to 30 Hz.

At 5 Hz, near the inlet of the test section, the oscillation amplitude is attenuated in the inner half of the boundary layer, i.e. the amplitude ratio, $\Delta U(x,y)/\Delta UCL(x)$, is less than 1.0. There is zero amplitude, of course, at the wall. In the outer half of the boundary layer, a pattern of amplification develops, beginning at x-station 12 and increasing to an amplitude ratio maximum of approximately 1.55 at x-station 22. The phase difference exhibits a similar pattern of development. A phase lead maximum occurs at the data point just adjacent to the wall (the oscillation is damped out right at the wall so that no phase angle relationship exists). The closest data to the wall are at $0.1\bar{\delta}$. At this y-location the phase lead increases from +8 at x-station 2, to +65 degrees at x-station 24. Across the boundary layer thickness, the phase angle relationship is nearly linear, from a maximum lead at the wall, to zero at the outer edge of the boundary layer.

The mappings for 10 Hz in Figures 4.16a and b show a pattern development similar to the 5 Hz data. It is obvious, however, that the 5 Hz type of pattern has moved upstream in the test section, and that a crossover of the pattern occurs further downstream. The increase in

amplitude ratio over the outer region of the boundary layer begins at x-station 2 and continues downstream to a maximum amplification at x-station 14. The amplitude ratio then begins to swing back in the opposite direction until it crosses over from amplification to attenuation at x-station 22. A similar response is shown for the phase angle. The maximum phase lead pattern occurs at x-station 8. Beyond this, the phase pattern swings back in the opposite direction until it crosses over from lead to lag, in the outer region, between x-stations 12 and 14. In the inner region of the boundary layer, it appears that there exists always a phase lead.

The response patterns move still further upstream for the 15 Hz case as shown in Figures 4.17a and b. The amplitude ratio shows an amplification peak near x-station 6, crosses over between x-stations 12 and 14, and shows an attenuation peak at x-station 22. Phase lead in the outer region persists only until a crossover occurs at x-station 6. There is a phase lag peak between x-stations 14 and 16, and a second crossover near x-station 24.

Beyond 15 Hz, the patterns can be easily identified only in the upstream one-half or one-third of the test section.

In the downstream portion of the test section, the response patterns at first appeared to vary randomly between amplification and attenuation, and phase lead and lag. A closer look established the fact that the number of crossovers in the patterns increased with frequency so that even the 50 mm mapping intervals used in DS-2 did not provide sufficient resolution.

At 20 Hz the amplitude ratio pattern crosses over three times and the phase difference pattern four times. There are four each for the 25 Hz patterns and five each for 30 Hz. The response patterns are illustrated and discussed in detail in a later subsection of this chapter.

The core flow response corresponding to the six tests just presented is shown in Figures 4.21a and b. In these figures the response is shown relative to the inlet, centerline oscillation. It is evident that the core flow response is coupled to the boundary layer response. For the amplitude ratio, a best-fit curve is drawn through the data points and this is superimposed onto a second curve representing the slope of the time-average, core flow velocity decay.

The phase difference patterns exhibit a number of crossovers corresponding to the amplitude ratio patterns for the same tests. Data points from several test runs at similar conditions are included in Figures 4.21a and b to illustrate repeatability.

Within the boundary layer, repeatability is illustrated in Figures 4.22a and b. The test runs shown were widely separated in time, and the procedure and equipment were modified to some extent between DS-1 and DS-2. The fact that the response patterns from each of the tests are nearly identical is an argument for the validity of the data.

A more detailed look at the data across the boundary layer is presented in Figures 4.23a through 4.23b. These are plots of the phase averaged data for the oscillatory component ($=\tilde{u}(x,y,t)$) vs time, in one cycle. Two x-stations (8 and 22) are shown for the 20 Hz runs. The linearity of the oscillatory response is illustrated in the figures. The data points are well represented by the solid line,

fundamental sinusoidal Fourier curves at all the y-locations shown. The scatter in the data points is caused by the fraction of the random turbulence velocity component remaining in the data when a finite number of cycles is used in the phase averaging process. This subject is discussed in detail in Chapter 3. The response at all locations is defined by a sinusoidal oscillation, of the identical frequency as the input frequency, which is symmetrically superimposed on the local time-average velocity.

Discussion

Effect of Frequency

The oscillatory response pattern across the outer region of the boundary layer crosses between amplification and attenuation, and between phase lead and lag along the test section length at a rate related to the oscillation frequency. The pattern crossovers can be seen most clearly in the data plots of Figures 4.24a through f. These Figures show the amplitude ratio and phase difference (with respect to the inlet centerline oscillation) plotted vs x-station location. The core flow response is shown as a solid line, and the boundary layer data are plotted with curves showing the best smooth approximation to the points.

The pattern crossover rate, and consequently the number of crossovers which occur in the test section length, can be related in an approximate way to the oscillation frequency and the effective residence time of the fluid in traveling from the inlet to the exit. The mechanism postulated is one in which the strongly coupled internal flow is characterized by a profile of cross-sectionally averaged velocities and a single residence time, and in which the pattern cross-overs are related to the number of oscillation cycles seen by the fluid within the test section. As an example, if the boundary layer velocity at $y/\delta = 0.5$ is chosen as a characteristic fluid velocity for the cross section at each x-station, the characteristic residence time for a particle of fluid obtained by integrating over the test section length is 0.067 sec. The number of cycles which the fluid will see during its time in the test section can be obtained by dividing the residence time by the oscillation period (T = 1/FREQ). The results of such a calculation are shown tabulated below:

		X-Station 0 - 24		
FREQ (1/sec)	T (sec)	Residence time (sec)	No. calculated cycles	No. measured pattern cycles
5	.200	.067	.33	.3
10	.100		.66	.6
15	.067		.99	.9
20	.050		1.33	1.7
25	.040		1.66	1.9
30	.033	↓	2.02	2.2

The calculated number of cycles corresponds roughly with the number of cycles in the response pattern.

In addition, it can be seen from the figures that the crossovers are more closely spaced in the downstream portion of the test section where the velocities are reduced. The calculated residence time for the upstream half of the test section (x-stations 0-12) is 0.025 sec. This means that the fluid would see slightly less than one-third of the total number of cycles in the first half of the test section and approximately two-thirds in the remaining half. Again, this corresponds roughly with the measured pattern crossover behavior.

In the boundary layer, the phase difference patterns lead the amplitude ratio patterns by 90 degrees. Illustration A, shown below, demonstrates the relationship.

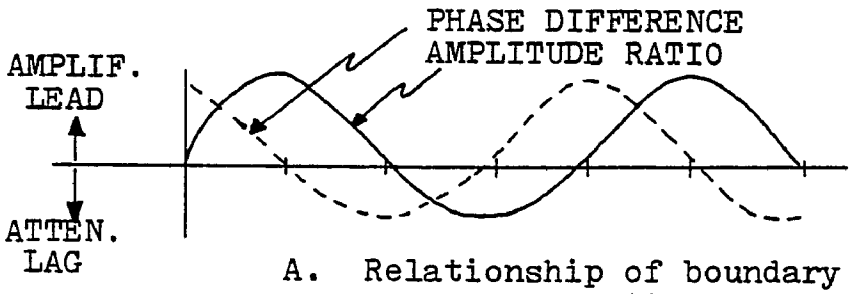

A. Relationship of boundary layer response patterns

As the phase pattern crosses from lead to lag the amplitude pattern passes through a maximum. During the half cycle that the phase is lagging, the amplitude is being attenuated. When the phase crosses from lag to lead the amplitude passes through its minimum. During the half cycle that the phase is leading, the amplitude is being amplified.

The boundary layer patterns are 180 degrees out-of-phase with the core flow patterns. Illustration B, shown below, shows the relationship.

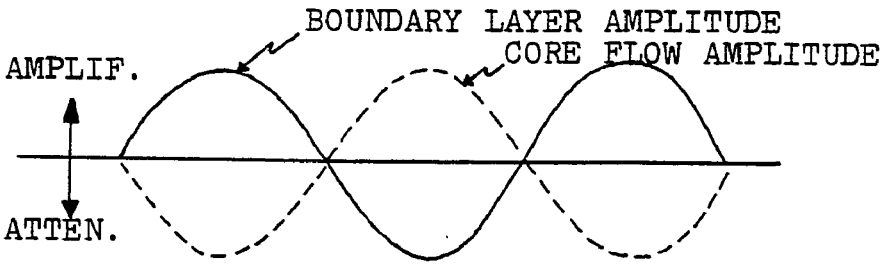

B. Relationship of boundary layer to core flow response

The Figures 4.24a to 4.24f clearly show the crossover pattern that is established with respect to the streamwise direction as discussed above. The scatter in the data, however, obscures the details of the pattern with respect to the y-direction in the boundary layer. All of the data shown ($0.2 \leqslant y/\delta \leqslant 0.6$) are in the outer or intermittent region. It does appear that the crossover patterns at all the levels shown in the boundary layer have approximately the same wavelength; however, it is not clear whether the patterns cross over in-phase, as shown in illustration C below, or out-of-phase, as shown in illustration D.

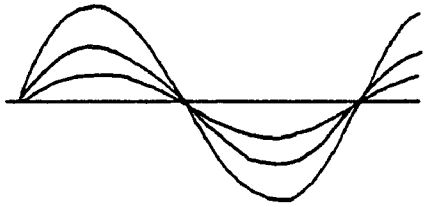

C. In-phase patterns

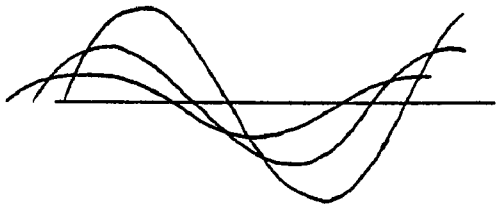

D. Out-of-phase patterns

The out-of-phase crossover pattern is evident in the upstream portion of the test section especially for the first crossover, whereas, in the downstream portion, where for higher frequencies the oscillations are closer together, the pattern approaches the in-phase type.

It is also not clear from the data shown whether a specified y-location maintains its relative position in

magnitude as it swings through the changeovers as shown in illustration E below, or whether the relative positions vary on the changeovers as shown in illustration F.

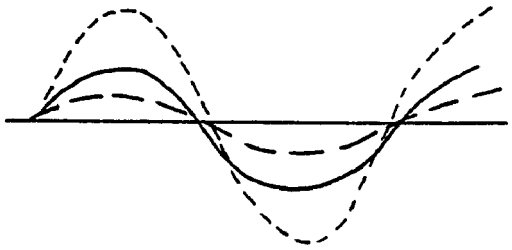

E. Relative position maintained

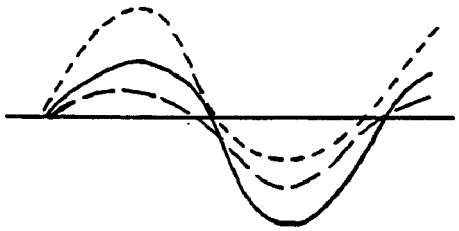

F. Relative position varies

These properties of the response patterns will be further discussed together with the presentation of the theoretical results in Chapter 6.

The data near the edge of the boundary layer ($y/\overline{\delta}$ = .6, .8, 1.0, C.L.) for the 10 Hz case are shown in Figure 4.25. The $0.6\overline{\delta}$ location exhibits the maximum magnitude in amplitude over the length of the test section, and the maximum magnitude in phase difference in the downstream half. The $0.8\overline{\delta}$ and $1.0\overline{\delta}$ curves show a progressive approach towards the core flow response.

The data point nearest the wall in all cases is at $0.1\overline{\delta}$. In all but a few cases the phase at this location is leading with respect to the local centerline. Data from the inner region of the boundary layer are

shown in detail in Figure 4.25b for the 15 Hz case (DS-2/Run 13). The viscous sublayer extends from the wall out to approximately $.01\bar{\delta}$. No data were obtained in this region. The buffer region lies approximately between $.01\bar{\delta}$ and $.06\bar{\delta}$, and the fully turbulent region extends from $.06\bar{\delta}$ to $.20\bar{\delta}$. The oscillation amplitude can be seen to be damped out only very close to the wall, in the sublayer. The data show the phase lead pattern which is established in the inner region.

Between the outer edge of the boundary layer and the near wall region the amplitude ratio and phase difference patterns change dramatically with frequency and location in the test section. The mechanisms which produce the boundary layer patterns are not well enough understood to present a complete explanation.

The relationships of the free stream forces acting across the boundary layer can be illustrated by considering the components of the two-dimensional, unsteady boundary layer equation,

$$\frac{\partial\langle u\rangle}{\partial t}+\langle u\rangle\frac{\partial\langle u\rangle}{\partial x}+\langle v\rangle\frac{\partial\langle u\rangle}{\partial y}=\frac{\partial}{\partial t}\langle UE\rangle+\langle UE\rangle\frac{\partial\langle UE\rangle}{\partial x}+\frac{\partial}{\partial y}(\langle\tau\rangle/\rho).$$

For an imposed oscillation of the form,

$$\langle UE\rangle=\overline{UE}+\Delta UE\sin(\omega t),$$

then

$$\frac{\partial}{\partial t}\langle u_E\rangle = \Delta u_E\,\omega \sin(\omega t + 90)$$

$$\langle u_E\rangle \frac{\partial\langle u_E\rangle}{\partial x} = A + B\sin(\omega t) + C\sin^2(\omega t)$$

where

$$A = \overline{u_E}\,\partial\overline{u_E}/\partial x$$
$$B = \overline{u_E}\,\partial\Delta u_E/\partial x + \Delta u_E\,\partial\overline{u_E}/\partial x$$
$$C = \Delta u_E\,\partial\Delta u_E/\partial x .$$

The force exerted by $\partial\langle u_E\rangle/\partial t$ always leads oscillations in $\langle u_E\rangle$ by 90°. The unsteady component of $\langle u_E\rangle\partial\langle u_E\rangle/\partial x$ will be in phase with $u_E(t)$ for a favorable pressure gradient ($B=+$) and 180° out of phase for an adverse pressure gradient ($B=-$). In laminar flow the opposing forces are the inertia terms and the viscous term $\partial/\partial y(\nu\partial\langle u\rangle/\partial y)$. The response in turbulent flow is complicated by the addition of a time-dependent Reynolds stress term $\partial/\partial y(\langle u'v'\rangle)$. The response patterns are a function of relative amplitudes and phase angles of all of the terms at a point in the flow. For turbulent flow, since the eddy structure does not adjust instantaneously to imposed perturbations, the upstream history effect is important.

Reduced Frequency

The dynamic similarity parameter in oscillatory flow is the reduced frequency, $\bar{\omega}$. Following Owczarek (37), a similarity parameter is defined as the ratio of a general force, F, to an inertia force,

$$\frac{F}{\rho V^2 \ell^2}$$

where V and ℓ are a characteristic velocity and length, respectively. The acceleration, a, in oscillatory motion is proportional to the product of the square of the frequency and the amplitude. The amplitude can be expressed as a length proportional to ℓ,

$$\frac{F}{\rho V^2 \ell^2} \longrightarrow \frac{ma}{\rho V^2 \ell^2} \longrightarrow \frac{(\rho \ell^3)(FREQ^2 \ell)}{\rho V^2 \ell^2} \longrightarrow \frac{FREQ^2 \ell^2}{V^2}.$$

The reduced frequency parameter is taken as the square root of this ratio

$$\bar{\omega}_\ell = \frac{(2\pi)(FREQ)(\ell)}{V}.$$

Physically $\bar{\omega}$ expresses a ratio of local oscillatory acceleration to convective acceleration in the flow field.

Figure 4.26 shows the variation in $\bar{\omega}_x = (2\pi)(FREQ)(x)/UCL(x)$, with x-station for all the frequencies tested. The similarity of the oscillatory response is shown as a function of $\bar{\omega}_x$ for y/δ = 0.6 in Figure 4.27. The 5 Hz test

covers a range of $\overline{\omega}_x$ from 0 to 1.95 and the 30 Hz test covers a range up to 11.69. Similarity of the response is approached at the higher frequencies, 20-30 Hz, while the curves for 5, 10 and 15 Hz show dissimilar patterns. An upstream history argument can be made to explain these results. Figure 4.26 indicates that each of the frequency runs has a different $\overline{\omega}_x$ development pattern, but that the curves become more closely spaced for the higher frequencies. The response similarity matchup follows the trend of the $\overline{\omega}_x$ development matchup.

A comparison of two test runs with <u>identical</u> $\overline{\omega}_x$ development is shown in Figures 4.28a and b. For one run, FREQ = 10 Hz and Re_D = 120,000, and for the other, FREQ = 16.6 Hz and Re_D = 200,000. The oscillatory response is virtually identical across the entire test section length.

<u>Effect of Oscillation Amplitude</u>

Oscillation amplitude $\Delta UCL(0)/\overline{UCL}(0)$ was varied only in the range of 0-10% for all of the test runs of DS-2. Within this range, the effect of varying amplitude is shown by the data plots of Figures 4.29 and 4.30. Three sets of test data are plotted, for amplitudes of 2.7%, 5.6%, and 8.6%, and no systematic variation in the response can be seen.

Effect of Re_D and Pressure Gradient

The ranges of Re_D (120,000 to 200,000), and the resulting pressure gradient (single test section geometry with diffuser half-angle = 3 degrees) were not sufficient to resolve specifically the dependence of the oscillatory response on these parameters. The extent to which these effects were tested was discussed in the previous section on reduced frequency.

Comparison of Time-average and Steady Flow

Steady flow boundary layer data (no oscillations imposed) are compared with time-averaged data (with oscillations imposed) in Figure 4.31. The base flow in all cases was for Re_D = 120,000 and $\overline{UCL}(0)$ = 18.29 m/sec. The time-average data was taken from two runs in which the oscillation amplitude was at the high end of the range used in DS-2: $\Delta UCL(0)/\overline{UCL}(0)$ = 9.2% for 15 Hz, and $\Delta UCL(0)/\overline{UCL}(0)$ = 10.6% for 5 Hz. Within the range of the variables tested, the thickness parameters, $\overline{\delta 1}$ and H, and the wall friction coefficient, $\overline{C}_F$, for the steady and time-average flows are virtually identical. This property of the oscillatory response will be utilized in uncoupling the base flow and oscillatory components in the theoretical study.

5. EDDY VISCOSITY MODELING

5.1 PHILOSOPHY

The modeling of the core response in the previous study of oscillating diffuser flow by Schachenmann (6) required the boundary layer response as input. Schachenmann proposed simplified representations for the limiting cases of very high frequency and very low frequency. The detailed boundary layer data acquired in the current study makes more practicable an attempt at modeling the boundary layer response directly. The converse situation from that of the Schachenmann study applies, in that the core flow response is required as input to the boundary layer calculation. A complete solution of the oscillatory diffuser flow field would be an iterative process combining a core flow model and a boundary layer model.

In place of a direct attack on the three-dimensional (x,y,t), time-dependent, boundary layer equations, the equations for the oscillatory component are derived and solved numerically. The oscillatory flow cannot be completely uncoupled from the time-averaged flow however, as the convective terms in the momentum equations are mixed products of oscillatory and time-averaged components.

Based on the experimental evidence that the base flow is essentially unaffected by the oscillation, the time-average boundary layer solution is obtained separately by a profile fitting technique and the results are input to the oscillatory calculation. This separate solution method serves to isolate the performance of the turbulence modeling within the oscillatory flow. The response is obtained using a well-tested finite differencing and solution technique.

The goal of the theoretical study was to test the validity of the use of a specific eddy viscosity model in an oscillatory flow situation. The oscillatory Reynolds shear stresses are modeled as the product of the time-invariant (time-averaged) local eddy viscosity and the local oscillatory velocity gradient. A complete linearized model would add to this the product of the local eddy viscosity perturbations (ensemble-averaged) and the local time invariant (time-averaged) velocity gradient. This second component has been shown to be of comparable magnitude as the first in pipe flow (20), so its neglect should be expected to be serious. It is omitted, nevertheless, because of difficulties it would introduce, with the hope that the comparison of the data with the results of the model will at least enhance qualitative understanding of the behavior.

5.2 DERIVATION OF THE EQUATIONS

The boundary layer equations for the time-average base flow and for the oscillatory flow component were derived in Chapter 2. Combining the core flow, (2.22c) and (2.23c), and momentum equations, (2.22b) and (2.23b), gives the following set:

.Boundary Layer Equations - Base Flow:

continuity

$$\frac{\partial}{\partial x}(r\bar{u}) + \frac{\partial}{\partial y}(r\bar{v}) = 0 \qquad (5.1a)$$

momentum

$$\bar{u}\frac{\partial \bar{u}}{\partial x} + \bar{v}\frac{\partial \bar{u}}{\partial y} = \overline{uc}_L \frac{d\overline{uc}_L}{dx} + \frac{1}{r}\frac{\partial}{\partial y}\left(r\nu\frac{\partial \bar{u}}{\partial y}\right) - \frac{1}{r}\frac{\partial}{\partial y}\left(r\overline{u'v'}\right) \qquad (5.1b)$$

.Boundary Layer Equations - Oscillatory Component:

continuity

$$\frac{\partial}{\partial x}(r\tilde{u}) + \frac{\partial}{\partial y}(r\tilde{v}) = 0 \qquad (5.2a)$$

momentum

$$\frac{\partial \tilde{u}}{\partial t} + \left[\bar{u}\frac{\partial \tilde{u}}{\partial x} + \bar{v}\frac{\partial \tilde{u}}{\partial y}\right] + \left[\tilde{u}\frac{\partial \bar{u}}{\partial x} + \tilde{v}\frac{\partial \bar{u}}{\partial y}\right] = \frac{\partial \widetilde{uc}_L}{\partial t} + \left[\overline{uc}_L \frac{\partial \widetilde{uc}_L}{\partial x} + \widetilde{uc}_L \frac{\partial \overline{uc}_L}{\partial x}\right] + \frac{1}{r}\frac{\partial}{\partial y}\left(r\nu\frac{\partial \tilde{u}}{\partial y}\right) - \frac{1}{r}\frac{\partial}{\partial y}\left[r\left(\langle u'v'\rangle - \overline{u'v'}\right)\right] \qquad (5.2b)$$

The oscillating flow properties can be represented by a cosine series:

$$\tilde{u}(x,y,t) = \sum_{n=1}^{\infty} \Delta u_n(x,y)\cos\left(\omega_n t + \phi_n(x,y)\right). \qquad (5.3)$$

Following the simplification which was imposed in defining the response measured experimentally, the theoretical response is limited to the fundamental by setting n=1,

$$\tilde{u}(x,y,t) = \Delta u \cos(\omega t + \phi). \qquad (5.4)$$

It is convenient to the solution procedure to substitute the exponential form for the RHS of (5.4),

$$\begin{aligned} \Delta u \cos(\omega t + \phi) &= \mathcal{R}_E \{\Delta u e^{i(\omega t + \phi)}\} \\ &= \mathcal{R}_E \{\Delta u e^{i\phi} e^{i\omega t}\} \\ &= \mathcal{R}_E \{\mathcal{U} e^{i\omega t}\}. \end{aligned} \qquad (5.5)$$

The quantity $\mathcal{U}$ is a complex amplitude,

$$\begin{aligned} \mathcal{U} &= \Delta u e^{i\phi} \\ &= \Delta u \cos\phi + i \Delta u \sin\phi \\ &= u_R + i u_I \end{aligned} \qquad (5.6)$$

and

$$\Delta u = \sqrt{u_R^2 + u_I^2} \qquad (5.7)$$

$$\phi = \tan^{-1}\left(\frac{u_I}{u_R}\right). \qquad (5.8)$$

The convention is used that since the real component (5.5) is a solution to the linear equations (5.2), the complex function $\mathcal{U} e^{i\omega t}$ is also a solution, and it is this quantity that is substituted into (5.2). The time dimension is eliminated from the solution by canceling the common factor $e^{i\omega t}$ giving

Oscillatory Component:

continuity

$$\frac{\partial}{\partial x}(r\mathcal{U})+\frac{\partial}{\partial y}(r\mathcal{V})=0 \qquad (5.9a)$$

momentum

$$i\omega\mathcal{U}+\left[\bar{u}\frac{\partial \mathcal{U}}{\partial x}+\bar{v}\frac{\partial \mathcal{U}}{\partial y}\right]+\left[\mathcal{U}\frac{\partial \bar{u}}{\partial x}+\mathcal{V}\frac{\partial \bar{u}}{\partial y}\right]$$
$$=i\omega\mathcal{U}_{CL}+\frac{\partial}{\partial x}(\bar{u}_{CL}\mathcal{U}_{CL})$$
$$+\frac{1}{r}\frac{\partial}{\partial y}\left(r\nu\frac{\partial \mathcal{U}}{\partial y}\right)+\frac{1}{r}\frac{\partial}{\partial y}\left[r\{u'v'\}\right] \qquad (5.9b)$$

where $\mathcal{V}$ is the complex amplitude of $\tilde{v}$ and $\{u'v'\}$ is the complex amplitude of $[\langle u'v'\rangle-\overline{u'v'}]$.

By use of equation (5.6), the oscillatory component equations are separated into a real and an imaginary set as follows:

continuity

$$\frac{\partial}{\partial x}(rU_R)+\frac{\partial}{\partial y}(rV_R)=0 \qquad (5.10a)$$

$$\frac{\partial}{\partial x}(rU_I)+\frac{\partial}{\partial y}(rV_I)=0 \qquad (5.11a)$$

momentum

$$\left[\bar{u}\frac{\partial U_R}{\partial x}+\bar{v}\frac{\partial U_R}{\partial y}\right]+\left[\frac{\partial \bar{u}}{\partial x}U_R+\frac{\partial \bar{u}}{\partial y}V_R\right]$$
$$=-\omega(U_{CL_I}-U_I)+\frac{\partial}{\partial x}(\overline{u_{CL}}\,U_{CL_R})$$
$$+\frac{1}{r}\frac{\partial}{\partial y}\left[r\left(\nu\frac{\partial U_R}{\partial y}-(u'v')_R\right)\right] \qquad (5.10b)$$

$$\left[\bar{u}\frac{\partial U_I}{\partial x}+\bar{v}\frac{\partial U_I}{\partial y}\right]+\left[\frac{\partial \bar{u}}{\partial x}U_I+\frac{\partial \bar{u}}{\partial y}V_I\right]$$
$$=\omega(U_{CL_R}-U_R)+\frac{\partial}{\partial x}(\overline{u_{CL}}\,U_{CL_I})$$
$$+\frac{1}{r}\frac{\partial}{\partial y}\left[r\left(\nu\frac{\partial U_I}{\partial y}-(u'v')_I\right)\right] \qquad (5.11b)$$

5.3 SOLUTION OF THE TIME-AVERAGE FLOW

Profile Fitting

The time-average, boundary layer flow field is determined and represented mathematically by the use of a profile fitting procedure which matches Thompson (38) two-parameter velocity profiles to experimentally determined thickness parameters. The solution of the oscillatory component flow requires that $\bar{u}$, $\partial\bar{u}/\partial x$, and $\partial\bar{u}/\partial y$ be defined ($\bar{v}$ is eliminated in a transformation of the two dependent velocity variables $\bar{u}$ and $\bar{v}$ to a single stream function variable, ψ, through the continuity equation). The Thompson profile uses the Law-of-the-Wall formulation for the inner region of the boundary layer, and a blending of the Law-of-the-Wall velocity and the free stream velocity by an intermittency function for the outer region,

$$\bar{u} = \gamma(\bar{u}_{LAW\text{-}WALL}) + (1-\gamma)\overline{UCL}. \qquad (5.12)$$

Figure 4.7 illustrates the composite form of the velocity profile. A turbulent boundary layer is composed of an inner region, whose structure is influenced by the interaction of turbulence eddies, the fluid viscosity and the wall, and an outer region, in which the turbulence eddies intermittently interrupt the main stream flow. The inner region velocity can, with a few exceptions, be universally described (independent of the streamwise location) by the

Law of the Wall:

sublayer

$0 \leq y^+ < 4 \qquad u^+ = y^+ \qquad (5.13a)$

buffer (5.13b)

$4 \leq y^+ < 30 \qquad u^+ = C_0 + C_1(\ln y^+) + C_2(\ln y^+)^2 + C_3(\ln y^+)^3$

logarithmic

$30 \leq y^+ \qquad u^+ = \frac{1}{0.41} \ln y^+ + 5.00 \qquad (5.13c)$

where $u^+ = \bar{u}_{LAW\ WALL}/u_\tau$, $y^+ = y u_\tau/\nu$, and $u_\tau = \overline{UCL}\sqrt{C_F/2}$,

so that $\bar{u}_{LAW\ WALL} = (\overline{UCL}\sqrt{\frac{C_F}{2}}) \times (u^+(y^+)) \qquad (5.14)$

For the outer region the characteristic velocity is chosen to be the free stream velocity, $\overline{UCL}$. The characteristic length is a boundary layer thickness parameter, δ_s, which is defined in the description of the intermittency function, γ. A correlation for γ was made by Sarnecki(39) from a large collection of mean velocity profile data. A mathematical formulation, developed by McD Galbraith and Head (40) to produce a smooth curve for $\partial\bar{u}/\partial y$, is given by

$0 < Y/\delta_s \leq 0.05 \qquad \gamma = 1$

$0.05 < Y/\delta_s \leq 0.3 \qquad \gamma = 1 - 2.64214(Y/\delta_s - 0.05)^2$

$0.3 < Y/\delta_s \leq 0.7 \qquad \gamma = 4.4053(Y/\delta_s - 0.5)^3 - 1.8503(Y/\delta_s - 0.5) + 0.5$

$0.7 < Y/\delta_s \leq 0.95 \qquad \gamma = 2.64214(0.95 - Y/\delta_s)^2$

$0.95 < Y/\delta_s \leq 1 \qquad \gamma = 0. \qquad (5.15)$

The intermittency function γ vs Y/δ_s is shown in Figure 5.1. The correlating parameter δ_s has no physical significance. The boundary layer thickness, $\bar{\delta}$, is taken as the value of Y where $\bar{u}/\overline{UCL} = 0.995$.

Dividing equation (5.12) by $\overline{UCL}$ gives

$$\frac{\bar{u}}{\overline{UCL}} = \gamma\left(\frac{\bar{u}_{LAW\ WALL}}{\overline{UCL}}\right) + (1-\gamma). \qquad (5.16)$$

The Law-of-the-Wall velocity can be expressed in terms of $\overline{C_F}$ and δ_s :

$$\frac{\bar{u}_{LAW\ WALL}}{\overline{UCL}} = \sqrt{\frac{\overline{C_F}}{2}}\left[u^+(Y^+)\right] \qquad (5.17)$$

where

$$u^+ = (5.13) \qquad (5.18)$$

$$Y^+ = \left(\frac{Y u_\tau}{\nu}\right) = \left(\frac{\overline{UCL}}{\nu}\sqrt{\frac{\overline{C_F}}{2}}\,Y\right) = \left(RE_{\delta_s}\sqrt{\frac{\overline{C_F}}{2}}\,\frac{Y}{\delta_s}\right)$$

and

$$RE_{\delta_s} = \frac{(\overline{UCL})(\delta_s)}{\nu}. \qquad (5.19)$$

The velocity profile (5.16) can now be written in terms of the two parameters, $\overline{C_F}$ and δ_s (or $R_{E\delta s}$),

$$\frac{\bar{u}}{\overline{UCL}} = \mathcal{F}\left(C_F, RE_{\delta_s}\right). \qquad (5.20)$$

The profile fitting procedure involves the systematic adjustment of $\overline{C_F}$ and δ_s (or $RE_{\delta s}$) until the thickness parameters, $H = \delta 1_{2D}/\delta 2_{2D}$ and $RE_{\delta 2} = (\overline{UCL})(\delta 2_{2D})/\nu$, of the Thompson profile, match the experimental data. For each $\overline{C_F}$ iteration the $RE_{\delta s}$ is adjusted until the H's are matched, and then $\overline{C_F}$ is adjusted until finally the

$Re_{\delta 2}$ and H's are matched.

For a velocity profile representation which is to be input to a numerical boundary layer calculation, the requirements are that the points be closely spaced and numerically smooth so that differentiation to obtain $\partial\bar{u}/\partial y$ and $\partial\bar{u}/\partial x$ is possible. Sixty-one points are calculated in each profile, 4 in the sublayer, 9 in the buffer, 8, closely spaced, near the outer edge of the boundary layer, and the remainder are equidistantly spaced in between. A time-average velocity profile is generated at each x-location where a numerical solution for the oscillatory flow is performed. The thickness parameters H and $Re_{\delta 2}$ for locations between the data stations are obtained from polynomial curve fits to the thickness profiles. The curve fitting procedure is outlined in Chapter 3.

The Thompson profiles are shown matched with the data in Figures 5.2 and 5.3 for $\overline{UCL}(0)$ = 18.3 m/sec. The match-up between the two is excellent for the 18.3 m/sec case except for the data point nearest the the wall which falls below the Thompson profile. The experimental profile defined by this last data point is steeper near the wall than the Thompson fit. The same problem was

apparent in the 30.5 m/sec case but to a lesser degree.

The fitting procedure was checked by testing a range of Law-of-the-wall constants (κ and const.) and a range of y^+ limits on the sublayer, buffer, and fully turbulent regions. Since it appears that the match-up improves at the x-stations further downstream, a modification to the Law of the wall proposed by Simpson (41) was tested:

for $Re_{\delta 2} < 6000$,

$$\kappa = 0.40(Re_{\delta 2}/6000)^{-\frac{1}{8}}$$

$$\text{const} = Re_{\delta 2}^{\frac{1}{8}}(7.90 - 0.737 \ln Re_{\delta 2}).$$

None of the modifications tested served to eliminate the mismatch at the first data point.

The possibility exists that the data value may be erroneously high because of increased heat transfer from the hot wire when it is in close proximity to the wall as suggested in an article by Oka and Kostic (33). Figure 4.8 lends support to this argument where it can be seen that the data points closest to the wall, at all the x-stations, fall above the Law-of-the-wall profiles, indicating too high a value. Excellent agreement between the Law-of-the-wall $\overline{C_f}$ and the Thompson $\overline{C_f}$ supports the validity of the profile fitting procedure.

The profile fits are started at x-station 4 and the

prediction calculations were begun at the same location. Difficulty with Thompson profile matching upstream of x-station 4 indicated that the boundary layer development was unsettled in this region. A detailed look at the Law-of-the-wall $\overline{C_F}$ calculation is given in Figure 5.4. It can be seen that the $\overline{C_F}$ calculation profiles for x-stations 0 and 2 differ significantly from those further downstream. At x-station 0 there is no identifiable constant $\overline{C_F}$ region. The profile at x-station 2 dips downward a second time in the outer region of the boundary layer. The convergent nozzle entry and the abrupt change to a diffusing passage produce a disturbed flow, and a standard pattern is established beginning at x-station 4.

Calculation of the Spatial Derivatives

The y-derivative of the streamwise velocity is generated analytically as follows:

$$\frac{\partial \bar{u}}{\partial y} = \overline{uCL} \times \frac{\partial}{\partial y}\left(\frac{\bar{u}}{\overline{uCL}}\right). \qquad (5.21)$$

where

$$\frac{\partial}{\partial y}\left(\frac{\bar{u}}{\overline{uCL}}\right) = \gamma \frac{\partial}{\partial y}\left(\frac{\bar{u}_{LAW\ WALL}}{\overline{uCL}}\right) + \left(\frac{\bar{u}_{LAW\ WALL}}{\overline{uCL}} - 1\right)\frac{\partial \gamma}{\partial y}. \qquad (5.22)$$

A sample of the smooth y-derivative profiles which are obtained is shown in Figure 5.5.

The x-derivative is calculated by a difference method. Thompson profiles are generated at $\Delta x/2$ upstream, and $\Delta x/2$ downstream of the specified x-station. The x-derivative for each y-point location in the boundary layer is then given by

$$\frac{\partial \bar{u}}{\partial x} = \frac{\bar{u}_{\text{DOWN-STREAM}} - \bar{u}_{\text{UP-STREAM}}}{\Delta x} \qquad (5.23)$$

It is important that the magnitude of Δx be chosen such that it is sufficiently small for the linear approximation to be valid over the interval, and yet sufficiently large for round-off errors to be insignificant. A numerical check was performed on the variables used in the profile fitting calculation to assess the validity of a range of values for Δx. A linear extrapolation for the values of $\overline{UCL}$, H and $\overline{\delta 2}$, using a range of Δx's was compared with the true curve fit value. For example,

$$H(x+\Delta x)\ \begin{pmatrix}\text{linear}\\ \text{extrapolation}\end{pmatrix} = H\ (\text{x-station}) + \left(\frac{dH}{dx}\right)(\Delta x)$$

$$H(x+\Delta x)\ \begin{pmatrix}\text{curve fit}\\ \text{value}\end{pmatrix} = H\ (\text{x-station}+\Delta x \text{ -curve fit}).$$

The linear extrapolations were found to be in good agreement with the curve fit values for $\Delta x \leqslant 2.54$ mm (0.10 in.) and this value was used at all x-locations. Sample profiles of $\partial \bar{u}/\partial x$ are shown in Figure 5.6.

5.4 SOLUTION OF THE OSCILLATORY FLOW

Modeling of the Turbulence Stresses

Closure Methods

If the solution for $\tilde{U}$ and $\tilde{V}$ from equations (5.10) and (5.11) is to proceed, it is necessary to construct additional equations relating the oscillatory turbulence stress, $-\rho(\widetilde{u'v'})$, to the $\tilde{U}$ and $\tilde{V}$ velocity components. This is the classic closure problem which heretofore has primarily been addressed to solution of steady turbulent boundary layer development.

The following classification of closure methods for time average boundary layer development is used by Reynolds(42).

1. Zero-equation models: models using no turbulence transport equations.
2. One-equation models: models involving a transport equation for a turbulence velocity scale.
3. Two-equation models: models incorporating an additional transport equation for a turbulence length scale.
4. Stress-equation models: models involving transport equations for all components of the turbulent stress tensor.
5. Large-eddy simulations: computations of the three dimensional time-dependent large eddy structure,

and a low level model for the small scale turbulence.

Large-eddy simulations are in their infancy. These methods are not for practical calculations. Their primary value may be in their use as mathematical turbulence experiments replacing very difficult physical experiments. Stress equation models are the most elaborate that have been seriously tested over a range of flows. They are currently under intense development. The basic transport equations for the components of the turbulent stress tensor are derived directly from the Navier-Stokes equations. Triple correlations of turbulence velocity components appear, however, and higher order modeling is required which results in a set of 5-7 transport equations for the turbulent quantities.

There are several variations of closure models which fall in the two-, one-, and zero-equation categories. The role of the zero-equation model, which is used in this study, can be illustrated by specific examples of two-, one-, and zero-equation models which are related in that they each employ the "eddy viscosity" constitutive equation to define the Reynolds stress terms

$$-\rho \overline{u'v'} = \rho \bar{\nu}_T \frac{\partial \bar{u}}{\partial y} . \qquad (5.24)$$

This gradient-diffusion model for momentum transport by the turbulence eddies was first proposed by Boussinesq in 1877. It is analogous to the Newtonian model for momentum transport by molecular motion in a laminar fluid flow, $\tau_{xy} = \rho\nu\, \partial\bar{u}/\partial y$. The eddy viscosity, $\overline{\nu}_T$, is proportional to the product of a characteristic turbulence velocity and characteristic turbulence length,

$$\overline{\nu}_T \propto \ell_T \times V_T. \qquad (5.25)$$

This formulation follows from the fact that the property of fluid viscosity is proportional to a product of . molecular mean free path and molecular speed.

The "k-ϵ" method is a two equation model which is being developed mainly on a research level. The eddy viscosity is a function of the turbulence kinetic energy, $k = (\overline{u'^2} + \overline{v'^2} + \overline{w'^2})$, and the length-containing parameter, ϵ, which is equal to the dissipation rate of k ,

$$\overline{\nu}_T = c\, k^2/\epsilon$$

The method has potential for broad application since it retains the transport mechanism for the Reynolds stresses by incorporating the differential equations for k and ϵ with the solution of the mean field equations of motion.

A one-equation member of this family uses what is known

as the Prandtl-Kolmogovov eddy viscosity

$$\overline{\nu}_T = C\sqrt{k}\,\ell$$

The transport equation for k is derived from the Navier-Stokes equations just as it is for the two-equation model. The length scale, ℓ, is algebraically related to the mean field parameters just as it is for the zero-equation model.

For the zero-equation modeling, which is used in this study, the eddy viscosity is related to the mean flow algebraically. Algebraic eddy viscosity models are generally of a composite nature with the outer region functions based on the free stream velocity and/or the boundary layer thickness parameters, and the inner region functions based on wall parameters such as the wall shear stress, $\overline{C_F}$, and the fluid viscosity, ν.

Of the several different types of algebraic eddy viscosity equations, one of the most important is Prandtl's Mixing Length Hypothesis (MLH). The turbulence length scale of equation (5.25) becomes a mixing length, ℓ_m, which is defined as the effective distance an eddy travels in the transverse direction before losing its identity. The turbulence velocity scale is given by

$$\overline{\nu}_T = \ell_m \left| \frac{\partial \bar{u}}{\partial y} \right| \qquad (5.26)$$

and

$$\overline{\nu}_T = C\, \ell_m^2 \left| \frac{\partial \bar{u}}{\partial y} \right| . \qquad (5.27)$$

The mixing length, ℓ_m, is then defined in terms of the mean flow parameters. Many models have been formulated and tested and modifications for wall proximity, pressure gradient, low R_E, etc. have been incorporated. Prandtl's MLH is used in both the inner and outer boundary layer regions, with different formulations in each, by Patankar and Spalding (43) and Crawford and Kays (44). The Cebeci and Smith model (36), which is used in this study, employs the MLH model for the boundary layer inner region, and a non-MLH model for the outer region. Mellor and Herring (45) are an example of workers who have used a non-MLH model in both the inner and outer regions.

Oscillatory Component of the Turbulence Stresses

The phase-averaged Reynolds stresses and eddy viscosity formulation are given by

$$-\rho\langle u'v' \rangle = \rho\langle \nu_T \frac{\partial \bar{u}}{\partial y} \rangle \qquad (5.28)$$

The RHS is decomposed into time-average and oscillatory components as follows:

$$-\rho\langle u'v' \rangle = \rho(\bar{\nu}_T + \tilde{\nu}_T)\frac{\partial}{\partial y}(\bar{u} + \tilde{u}) \qquad (5.29)$$

$$= \rho\left(\bar{\nu}_T \frac{\partial \bar{u}}{\partial y} + \bar{\nu}_T \frac{\partial \tilde{u}}{\partial y} + \tilde{\nu}_T \frac{\partial \bar{u}}{\partial y} + \tilde{\nu}_T \frac{\partial \tilde{u}}{\partial y}\right)$$

Subtracting out the time-average components from both the LHS and RHS, and neglecting the second order oscillatory term gives

$$-\rho\left(\langle u'v'\rangle - \overline{u'v'}\right) = \rho\left(\bar{\nu}_T \frac{\partial \tilde{u}}{\partial y} + \tilde{\nu}_T \frac{\partial \bar{u}}{\partial y}\right). \qquad (5.30)$$

The model tested in this study is the "fixed eddy viscosity" model obtained by neglecting the second term in the parentheses on the RHS,

$$-\rho\left(\langle u'v'\rangle - \overline{u'v'}\right) \cong \rho\left(\bar{\nu}_T \frac{\partial \tilde{u}}{\partial y}\right). \qquad (5.31)$$

The eddy viscosity model is a concept which has worked surprisingly well considering the simplicity of the representation and the complexity of the mechanism. If the eddy viscosity is viewed as being a property solely of the local turbulence field, then retaining only the $\bar{\nu}_T$ term as in (5.31) implies that the turbulence velocity and length scales (see (5.25)) remain constant in the presence of bulk flow oscillations. The oscillatory component of the Reynolds stress would therefore be in phase with $\partial\tilde{u}/\partial y$. This model would seem reasonable for the case where the oscillation frequency was so high that the turbulence scales would not have time to respond. Retaining the $\tilde{\nu}_T$ term allows for an oscillatory response in the turbulence scales. The objective

here is to test the validity of (5.31). The implications of the extension to (5.30) are discussed in Chapter 6.

Two additional, special case models are used for comparisons. The quasi-laminar model assumes that the oscillatory component of the Reynolds stress has no effect on the development of the oscillatory boundary layer flow field. In this case,

$$-\rho\left(\langle u'v'\rangle - \overline{u'v'}\right) = 0. \tag{5.32}$$

The quasi-steady model would apply as $\omega \to 0$. In this case the instantaneous boundary layer properties are the steady flow values which correspond to the instantaneous main stream properties. Phase lag is zero across the boundary layer.

The Cebeci-Smith Eddy Viscosity

The Cebeci-Smith eddy viscosity is formulated in the following manner:

outer region

$$\bar{\nu}_T = (\bar{\alpha})(\overline{uc}_L)(\delta 1_{2D})(\gamma) \tag{5.33}$$

where the "constant", $\bar{\alpha}$, is a function of the momentum thickness Reynolds number, $Re_{\delta 2}$, and γ is an intermittency function proposed by Klebanoff (1954);

inner region

$$\bar{\nu}_T = (l_m)\left(l_m \left|\frac{\partial \bar{u}}{\partial y}\right|\right) \tag{5.34}$$

where the mixing length, l_m, is a function of the distance from the wall, the fluid viscosity, and the wall friction, and a modification is incorporated for the flow field pressure gradient. The condition used to define the boundary between the inner and outer regions is the continuity of the eddy viscosity. The $\bar{\nu}_T$(inner) formulation is used in the region from the wall to the point where $\bar{\nu}_T$(inner) = $\bar{\nu}_T$(outer). At this point the switch is made to the $\bar{\nu}_T$(outer) formulation. The coefficient $\bar{\alpha}$ is modified for the effect of low Re through the relationship of the eddy viscosity formulation with Coles (see (36) pp. 221-227) Law-of-the-Wake velocity profile:

$$\bar{\alpha} = \bar{\alpha}_o \left(\frac{1 + \Uparrow_o}{1 + \Uparrow}\right) \tag{5.35}$$

where

$$\overline{\alpha}_o = 0.0168$$
$$\Pi_o = 0.55$$
$$\Pi = 0.55\left[1 - \exp.(-0.243 Z_1^{\frac{1}{2}} - 0.298 Z_1)\right]$$
$$Z_1 = \frac{Re_{\delta 2}}{425.} - 1.$$

The Π parameter formulation is taken from the equation, determined experimentally with flat plate, turbulent boundary layer data, for the Law-of-the-Wake velocity profile,

$$\frac{\overline{u}}{u_\tau} = \left(\frac{1}{\kappa}\right) ln\left(\frac{y u_\tau}{\nu}\right) + C + \frac{\Pi}{\kappa}\left(w\left(\frac{y}{\delta}\right)\right)$$

where

$$w = 2 \sin^2\left[\left(\frac{\pi}{2}\right)\left(\frac{y}{\delta}\right)\right] .$$

The intermittency function, γ, is a mathematical approximation describing the data of Klebanoff (46),

$$\gamma = \left[1. + 5.5(y/\delta)^6\right]^{-1} \qquad (5.36)$$

The Cebeci-Smith development of a mixing length formulation can be shown as follows:

The Escudier (47) formula for the inner region is given by

$$l_{m_{ESc}} = \kappa y$$

where

$$\kappa = 0.40.$$

The van Driest (48) formula incorporates a modification

for the effect of the wall in damping out the turbulent eddy motion:

$$\ell m_{VD} = \kappa y \left[1 - e^{-y/A}\right]$$

where

$$A = (A^+)(\nu/u_\tau)$$
$$A^+ = 26.$$

The Cebeci-Smith formula is based on the van Driest, and it incorporates a further modification for the flow field pressure gradient

$$\ell m_{cs} = \kappa y \left[1 - e^{-y/A}\right] \tag{5.37}$$

where

$$A = (A^+)(\nu/u_\tau)(1/N)$$
$$N = \sqrt{1 - y_s^+ P_x^+}$$
$$y_s^+ = 11.8$$
$$P_x^+ = \frac{(\nu)(\overline{uCL})}{(u_\tau^3)} \frac{\partial \overline{uCL}}{\partial x}$$

Further modifications have been developed and tested by Cebeci and Smith, and others, for compressible flow, mass transfer, heat transfer etc.

For use with axisymmetric geometry the following modifications are made to the $\overline{\nu}_T$ (inner) formulation

$$\overline{\nu}_{T\,\text{inner}}_{\text{axisymmetric}} = \ell m^2 \left(\frac{r}{R}\right) \left|\frac{\partial \bar{u}}{\partial y}\right|$$

$$\ell m = \kappa \left(R \ell n \left(\frac{r}{R}\right)\right) \left[1. - \exp\left(-\frac{R \ell n \frac{r}{R}}{A}\right)\right]. \tag{5.38}$$

Eddy viscosity profiles are shown plotted vs y/δ in Figure 5.7.

Classification

The equations (5.10) and (5.11) together with the Reynolds stress model (5.31) comprise a linear, coupled, parabolic equation set. Boundary conditions for the transverse coordinate direction are prescribed at the edge of the boundary layer and at the wall. Initial conditions are input for one streamwise x-station and the solution is developed by a marching procedure in the direction of the flow.

Transformation and Nondimensionalizing

Transformations of both the dependent and independent variables are performed as follows for the purpose of simplifying the solution procedure (see (36) p. 260):

$$x, y \longrightarrow \xi, \eta$$
$$u, v \longrightarrow \psi \longrightarrow f.$$

A two-step transformation is performed on the independent variables x and y. The first is the Mangler transformation which puts the equations into an almost two-dimensional form,

$$d\bar{x} = (R(x)/L)^{2k} dx, \quad dy = (r(x,y)/L)^{k} dy, \quad (5.39a)$$

where L is a reference length and k =1 for axisymmetric geometry, k = 0 for 2-D, rectangular geometry. The second is the Levy-Lees transformation which serves to remove

the singularity at $\bar{x}=0$, and stretches the coordinates in the $\bar{x}$ and $\bar{y}$ directions, so that the boundary layer thickness does not change dramatically over the length of the calculation:

$$d\xi = (\rho_{CL})(\mu_{CL})(\overline{uCL})\,d\bar{x},\quad d\eta = \frac{(\rho)(\overline{uCL})}{\sqrt{2\xi}}\,d\bar{y} \qquad (5.39b)$$

where $\rho = \rho_{CL}$ = const and $\mu = \mu_{CL}$ = constant for this study.

A combination of (5.39a) and (5.39b) gives the transformation,

$$d\xi = \rho\mu\,\overline{uCL}\,(R(x)/L)^{2k}\,dx \qquad (5.40a)$$

$$d\eta = \left[\rho\,\overline{uCL}/\sqrt{2\xi}\right](r(x,y)/L)^{k}\,dy. \qquad (5.40b)$$

Following (5.40), the partial derivative operators are given by

$$\frac{\partial}{\partial x}\Big|_y = \rho\mu\,\overline{uCL}\left(\frac{R(x)}{L}\right)^{2k}\left[\frac{\partial}{\partial\xi}\Big|_\eta + \frac{\partial\eta}{\partial\xi}\Big|_y \frac{\partial}{\partial\eta}\Big|_\xi\right] \qquad (5.41a)$$

$$\frac{\partial}{\partial y}\Big|_x = \frac{\rho\,\overline{uCL}}{\sqrt{2\xi}}\left(\frac{r(x,y)}{L}\right)^{k}\frac{\partial}{\partial\eta}\Big|_\xi. \qquad (5.41b)$$

The dependent variables, U_R and V_R (and U_I, V_I), can be combined into a single streamfunction variable, ψ_R (and ψ_I), by virtue of the streamfunction's relationship to the continuity equation. The streamfunction is a mathematical device which serves to express a velocity vector field in terms of a scalar function. Streamlines can be viewed as intersections of a two parameter family of surfaces (streamsurfaces),

$$\psi(x_1, x_2, x_3) = \text{const A}$$
$$\lambda(x_1, x_2, x_3) = \text{const B.}$$

A velocity vector in the flow field is then expressed as

$$\vec{V} = f(x_1, x_2, x_3)(\vec{\nabla\psi} \times \vec{\nabla\lambda})$$

where it can be shown that $f = 1/\rho$ satisfies the necessary conditions of mass continuity. An axisymmetric flow field can be constructed by making the λ surfaces meridional planes on each of which λ = const θ. Then,

$$\nabla\psi = \frac{\partial\psi}{\partial x}\hat{i}_x + \frac{\partial\psi}{\partial y}\hat{i}_y$$
$$\nabla\lambda = \frac{1}{r}\hat{i}_\theta ,$$

and

$$u\hat{i}_x + v\hat{i}_y = \frac{1}{\rho}\left(\frac{1}{r}\frac{\partial\psi}{\partial y}\hat{i}_x - \frac{1}{r}\frac{\partial\psi}{\partial x}\hat{i}_y\right),$$

from which follows the streamfunction relationships,

$$\rho u = \frac{1}{r}\frac{\partial\psi}{\partial y}$$
$$\rho v = -\frac{1}{r}\frac{\partial\psi}{\partial x}.$$

For use with the oscillatory component equations the streamfunction relationships take the following form,

$$\rho u_R = \frac{1}{r^k}\frac{\partial\psi_R}{\partial y} \quad , \quad \rho u_I = \frac{1}{r^k}\frac{\partial\psi_I}{\partial y} \qquad (5.42a)$$

$$\rho v_R = -\frac{1}{r^k}\frac{\partial\psi_R}{\partial x} \quad , \quad \rho v_I = -\frac{1}{r^k}\frac{\partial\psi_I}{\partial x} \qquad (5.42b)$$

(Note: the following information which is presented in terms of the real component of the variables applies as well to the imaginary component). A dimensionless stream function, f, is now defined such that

$$\frac{\partial f_R}{\partial\eta} = f_R' = \frac{u_R}{\overline{uCL}(x)}$$

and

$$f_R = \psi_R / (\sqrt{2\xi}\, L^k) \tag{5.43}$$

The following substitutions are developed from equations (5.41) and (5.43)

$$\left.\frac{\partial \psi_R}{\partial \eta}\right|_{\xi} = \sqrt{2\xi}\, L^k f_R' \tag{5.44a}$$

$$\left.\frac{\partial \psi_R}{\partial \xi}\right|_{\eta} = \sqrt{2\xi}\, L^k \left(\frac{f_R}{2\xi} + \frac{\partial f_R}{\partial \xi}\right). \tag{5.44b}$$

The transformation of equations (5.10) and (5.11) is accomplished by first making the substitutions of the streamfunction relationships (5.42), then applying the derivative operators given in (5.41), and finally, using the substitution (5.44). The time-average terms in equations (5.10) and (5.11) are transformed in an identical manner with the appropriate changes in notation. The shear stress terms in equations (5.10), (5.11) take the following form upon substitution of the eddy viscosity model (5.31),

$$\frac{1}{r}\frac{\partial}{\partial y}\left[r\left(\nu \frac{\partial u_R}{\partial y} - (u'v')_R\right)\right] = \frac{1}{r}\frac{\partial}{\partial y}\left[r\left(\nu + \bar{\nu}_T\right)\frac{\partial u_R}{\partial y}\right]$$

$$= \frac{1}{r}\frac{\partial}{\partial y}\left[r\nu\left(1 + \frac{\bar{\nu}_T}{\nu}\right)\frac{\partial u_R}{\partial y}\right]. \tag{5.45}$$

Following the transformation and non-dimensionalizing, the equations of motion for the oscillatory boundary layer flow take the following form:

$$(bf_R'')' + Cf_R'' + (B - 2\bar{f}'\bar{\beta})f_R' + Df_R + f'_{E_R}(\beta_R + 2\bar{\beta}) - 2\bar{\omega}(f'_{E_I} - f'_I) = A\frac{\partial f'_R}{\partial \xi} - E\frac{\partial f_R}{\partial \xi} \qquad (5.46a)$$

$$(bf_I'')' + Cf_I'' + (B - 2\bar{f}'\bar{\beta})f_I' + Df_I + f'_{E_I}(\beta_I + 2\bar{\beta}) + 2\bar{\omega}(f'_{E_R} - f'_R) = A\frac{\partial f'_I}{\partial \xi} - E\frac{\partial f_I}{\partial \xi}. \qquad (5.46b)$$

A, B, C, D, and E are coefficients involving the time-average flow quantities which will be input to the calculation procedure having been determined from the measured base flow as described above,

$$A = [2\xi \bar{f}']$$

$$B = [-2\xi \frac{\partial \bar{f}'}{\partial \xi}]$$

$$C = [\bar{f} + 2\xi \frac{\partial \bar{f}}{\partial \xi}]$$

$$D = [\bar{f}'']$$

$$E = [2\xi \bar{f}''] . \qquad (5.47)$$

The b term incorporates the effect of transverse curvature and the turbulence eddy viscosity,

$$b = \left(\frac{r}{R}\right)^{2k}\left(1 + \frac{\bar{\nu}_I}{\bar{\nu}}\right). \qquad (5.48)$$

The β terms represent the streamwise pressure gradient,

$$\bar{\beta} = \frac{2\xi}{\overline{UCL}} \frac{\partial \overline{UCL}}{\partial \xi}, \quad \beta_R = \frac{2\xi}{UCL_R} \frac{\partial UCL_R}{\partial \xi}, \text{ etc,} \tag{5.49}$$

and $\overline{\overline{\omega}}$ contains the oscillation frequency in a transformed term similar to the reduced frequency,

$$\overline{\overline{\omega}} = \left(\frac{\omega \xi}{\overline{UCL}}\right)\left(\frac{1}{\rho \mu \overline{UCL}}\right)\left(\frac{L}{R}\right)^{2k} \tag{5.50}$$

The prime symbol represents differentiation with respect to η, and $\bar{f}' = \bar{u}/\overline{UCL}$, $f'_{E_R} = UCL_R/\overline{UCL}$.

Boundary Conditions

Three boundary conditions each on f_R and f_I are required at η-boundaries:

$$\frac{\tilde{u}}{\overline{UCL}} = \frac{\tilde{v}}{\overline{UCL}} = 0 \qquad \text{for } y = 0,$$

Therefore:

B.C.(1) $$f'_R = f'_I = 0 \qquad \text{for } \eta = 0. \tag{5.51a}$$

$$\frac{\tilde{u}}{\overline{UCL}} = \frac{\widetilde{UCL}}{\overline{UCL}}, \frac{\tilde{v}}{\overline{UCL}} = 0 \qquad \text{for } r \to 0,\ y \to R/\cos\alpha$$

Therefore:

B.C.(2) $$f'_R = f'_{E_R}, f'_I = f'_{E_I} \quad \text{for } \eta \to \left[\frac{\rho \overline{UCL}}{\sqrt{2\xi}}\left(\frac{R}{L}\right)^k\right]\frac{R}{2\cos\alpha} \tag{5.51b}$$

$$\psi_R = -\int_0^x R^k \rho V_R(x,0)\,dx \qquad \text{for } y = 0,$$

$$\psi_I = -\int_0^x R^k \rho V_I(x,0)\,dx$$

With zero mass transfer through the wall,

$V_R(x,0) = V_I(x,0) = 0$,

Therefore:

B.C.(3) $$f_R = f_I = 0 \qquad \text{for } \eta = 0. \tag{5.51c}$$

Finite Differencing

The transformed equations (5.46) are each converted to three first-order differential equations by the following substitutions,

$$FR = f_R \qquad FI = f_I$$

$$UR = f_R' = \frac{\partial f_R}{\partial \eta} \qquad UI = f_I' = \frac{\partial f_I}{\partial \eta}$$

$$VR = f_R'' = \frac{\partial^2 f_R}{\partial \eta^2} \qquad VI = f_I'' = \frac{\partial^2 f_I}{\partial \eta^2}.$$

The resulting system of six equations to be solved is given by

$$UR = FR' \tag{5.52a}$$

$$VR = UR' \tag{5.52b}$$

$$(bVR)' + CVR + (B - 2\bar{f}'\bar{\beta})UR + DFR + UER(\beta_R + \bar{\beta}) - 2\bar{\omega}(UEI - UI) = A\frac{\partial UR}{\partial \xi} - E\frac{\partial FR}{\partial \xi} \tag{5.52c}$$

$$UI = FI' \tag{5.53a}$$

$$VI = UI' \tag{5.53b}$$

$$(bVI)' + CVI + (B - 2\bar{f}'\bar{\beta})UI + DFI + UEI(\beta_I + \bar{\beta}) + 2\bar{\omega}(UER - UR) = A\frac{\partial UI}{\partial \xi} - E\frac{\partial FI}{\partial \xi}. \tag{5.53c}$$

The numerical method used to solve the boundary layer equations is the Keller Box scheme (49), (50).

A sketch of the finite difference net with a detailed view of one net rectangle is shown in Figure 5.8. The spacings in the η -direction and the ξ direction are respectively h and k , and the following definitions apply:

$$\eta_j = \eta_{j-1} + h_j \qquad 0 \leq j \leq J$$
$$\xi_n = \xi_{n-1} + k_n \qquad 0 \leq n \leq N.$$

The Box scheme involves writing the equations (5.52) and (5.53) in difference form for the mesh rectangle (box) in the stack of rectangles (boxes) between the known values at ξ_{n-1} and the unknown values at ξ_n. The difference equations are written using the values at the corners of the boxes producing a set of 6J equations (j=1,J) for the 6J + 6 unknowns (FR_j^n, UR_j^n, VR_j^n, FI_j^n, UI_j^n, VI_j^n, j = 0,J) in terms of the known values at ξ_{n-1}. The six additional equations required are supplied by the boundary conditions. The differencing for equations (5.52c) and (5.53c) is done in two steps. First the equations are written for the point $(\xi_{n-\frac{1}{2}}, \eta_j)$ by applying the following types of operations:

$$[W]_j^{n-\frac{1}{2}} = \frac{1}{2}(W_j^n + W_j^{n-1})$$
$$\left[\frac{\partial W}{\partial \xi}\right]_j^{n-\frac{1}{2}} = \left(\frac{W_j^n - W_j^{n-1}}{k_n}\right).$$

All of the terms to be evaluated at ξ_n are arranged on the left hand side (LHS) and all those evaluated at ξ_{n-1}

on the right hand side (RHS). The real-component difference equation for (5.47c) becomes

$$\left([b_j^n]VR_j^n\right)'+[C_j^n]VR_j^n+[G_j^n]UR_j^n+[H_j^n]FR_j^n+PRR^n+[2\bar{\omega}^n]UI_j^n=SR_j^{n-1} \quad (5.54)$$

where

$$G_j^n=\left[(B-2\bar{f}'\bar{\beta})_j^n-\frac{1}{k_n}(A_j^n+A_j^{n-1})\right]$$

$$H_j^n=\left[D_j^n+\frac{1}{k_n}(E_j^n+E_j^{n-1})\right]$$

$$PRR_j^n=\left[UER^n(\beta_R+\bar{\beta})^n-2\bar{\omega}^n UEI^n\right]$$

$$SR_j^{n-1}=-\left([b_j^{n-1}]VR_j^{n-1}\right)'-[C_j^{n-1}]VR_j^{n-1}-[G_j^{n-1}]UR_j^{n-1}-[H_j^{n-1}]FR_j^{n-1}-PRR^{n-1}-[2\bar{\omega}^{n-1}]UI_j^{n-1}$$

$$G^{n-1}=\left[(B-2\bar{f}'\bar{\beta})_j^{n-1}+\frac{1}{k_n}(A_j^n+A_j^{n-1})\right]$$

$$H^{n-1}=\left[D_j^{n-1}-\frac{1}{k_n}(E_j^n+E_j^{n-1})\right]$$

$$PRR^{n-1}=\left[UER^{n-1}(\beta_R+\bar{\beta})^{n-1}-2\bar{\omega}^{n-1}UEI^{n-1}\right]$$

$$UER=f'E_R,\quad UEI=f'E_I.$$

The second step centers the equation on the point $(\xi^{n-\frac{1}{2}}, \eta_{j-\frac{1}{2}})$ by applying the following operations to the terms on both sides of equation (5.54):

$$[W]_{j-\frac{1}{2}}^n=\tfrac{1}{2}\left(W_j^n+W_{j-1}^n\right)$$

$$[W]_{j-\frac{1}{2}}^{n-1}=\tfrac{1}{2}\left(W_j^{n-1}+W_{j-1}^{n-1}\right)$$

$$\left[\frac{\partial W}{\partial \eta}\right]_{j-\frac{1}{2}}^n=\left(\frac{W_j^n-W_{j-1}^n}{h_j}\right)$$

In notational form equation (5.54), centered at $(\xi^{n-\frac{1}{2}}, \eta_{j-\frac{1}{2}})$ becomes

$$\frac{b_j^n VR_j^n - b_{j-1}^n VR_{j-1}^n}{h_j} + \left[C_{j-1/2}^n\right] VR_{j-1/2}^n + \left[G_{j-1/2}^n\right] UR_{j-1/2}^n$$
$$+ \left[H_{j-1/2}^n\right] FR_{j-1/2}^n + \left[PRR^n\right] + \left[2\bar{\omega}^n\right] UI_{j-1/2}^n$$
$$= SR_{j-1/2}^{n-1} . \qquad (5.55)$$

Equations (5.52a), (5.52b) and (5.53a), (5.53b) are centered at $(\xi_n, \eta_{j-1/2})$ in the mesh box. Upon rearrangement, the difference equations become

$$FR_j - FR_{j-1} - (h_j/2)(UR_j + UR_{j-1}) = r_{R_j} \qquad (5.56a)$$

$$[\theta_j] FR_j + [\phi_j] VR_j + [\psi_j] UR_j$$
$$- [\bar{\theta}] FR_{j-1} - [\bar{\phi}] VR_{j-1} - [\bar{\psi}] UR_{j-1} = s_{R_j} \qquad (5.56b)$$

$$UR_j - UR_{j-1} - (h_j/2)(VR_j + VR_{j-1}) = t_{R_j} \qquad (5.56c)$$

$$FI_j - FI_{j-1} - h_j/2\,(UI_j + UI_{j-1}) = r_{I_j} \qquad (5.57a)$$

$$[\theta_j] FI_j + [\phi_j] VI_j + [\psi_j] UI_j - [\bar{\theta}_j] FI_{j-1}$$
$$- [\bar{\phi}_j] VI_{j-1} - [\bar{\psi}_j] UI_{j-1} = s_{I_j} \qquad (5.57b)$$

$$UI_j - UI_{j-1} - h_j/2\,(VI_j + VI_{j-1}) = t_{I_j} \qquad (5.57c)$$

where

$$[\theta_j] = [\bar{\theta}_j] = [(h_j/2) H_{j-1/2}]$$

$$[\phi_j] = [b_j + (h_j/2) C_{j-1/2}]$$

$$\bar{\phi}_j = [-2 b_{j-1/2} + \phi_j]$$

$$[\psi_j] = [\bar{\psi}_j] = [(h_j/2) G_{j-1/2}]$$

$$r_{R_j} = r_{I_j} = 0$$

$$A_{R_j} = h_j SR_{j-1/2}^{n-1} - [h_j PRR_n] - [h_j \bar{\omega}^n](UI_j + UI_{j-1})$$

$$A_{I_j} = h_j SI_{j-1/2}^{n-1} - [h_j PII_n] - [-h_j \bar{\omega}^n](UR_j + UR_{j-1})$$

$$t_{R_j} = t_{I_j} = 0.$$

The n superscripts have been dropped from the unknowns on the LHS of the equations.

Numerical Method

Outline of the Solution

The equations (5.56) and (5.57) form two coupled sets of (Real and Imaginary components) of 3J ($j = 1, J$) equations each, for 3J+3 unknowns (FR, VR, UR $j = 0, J$). The coupling between the two sets is in the term A_R which contains the unknown UI, and the term A_I which contains the term UR. An iterative scheme is used to converge on a solution which satisfies both sets. The set of equations, for the Real component, is given in matrix form below, where the unknown variables on the LHS are all to be evaluated at ξ_n, and the variables in the r_j, A_j, t_j vectors on the RHS are known from their evaluation at ξ_{n-1}:

$$
\begin{array}{l}
j=J \\
\begin{pmatrix} 1 & 0 & -\frac{h_J}{2} \\ \theta_J & \phi_J & \psi_J \\ 0 & -\frac{h_J}{2} & 1 \end{pmatrix}
\begin{Bmatrix} FR_J \\ VR_J \\ UR_J \end{Bmatrix}
- \begin{pmatrix} 1 & 0 & \frac{h_J}{2} \\ \bar{\theta}_J & \bar{\phi}_J & \bar{\psi}_J \\ 0 & \frac{h_J}{2} & 1 \end{pmatrix}
\begin{Bmatrix} FR_{J-1} \\ VR_{J-1} \\ UR_{J-1} \end{Bmatrix}
= \begin{Bmatrix} r_J \\ s_J \\ t_J \end{Bmatrix} \\
\qquad\qquad \text{B.C.} \\
\vdots \\
j=j \\
\begin{pmatrix} 1 & 0 & -\frac{h_j}{2} \\ \theta_j & \phi_j & \psi_j \\ 0 & -\frac{h_j}{2} & 1 \end{pmatrix}
\begin{Bmatrix} FR_j \\ VR_j \\ UR_j \end{Bmatrix}
- \begin{pmatrix} 1 & 0 & \frac{h_j}{2} \\ \bar{\theta}_j & \bar{\phi}_j & \bar{\psi}_j \\ 0 & \frac{h_j}{2} & 1 \end{pmatrix}
\begin{Bmatrix} FR_{j-1} \\ VR_{j-1} \\ UR_{j-1} \end{Bmatrix}
= \begin{Bmatrix} r_j \\ s_j \\ t_j \end{Bmatrix} \\
\vdots \\
j=1 \\
\begin{pmatrix} 1 & 0 & -\frac{h_1}{2} \\ \theta_1 & \phi_1 & \psi_1 \\ 0 & -\frac{h_1}{2} & 1 \end{pmatrix}
\begin{Bmatrix} FR_1 \\ VR_1 \\ UR_1 \end{Bmatrix}
- \begin{pmatrix} 1 & 0 & \frac{h_1}{2} \\ \bar{\theta}_1 & \bar{\phi}_1 & \bar{\psi}_1 \\ 0 & \frac{h_1}{2} & 1 \end{pmatrix}
\begin{Bmatrix} FR_0 \\ VR_0 \\ UR_0 \end{Bmatrix}
= \begin{Bmatrix} r_1 \\ s_1 \\ t_1 \end{Bmatrix}
\begin{array}{l} \text{B.C.} \\ \\ \text{B.C.} \end{array}
\end{array}
\qquad (5.58)
$$

Boundary conditions provide values for the three values circled in (5.58) thereby making the equation sets consistent;

$$
\begin{aligned}
&UR_J = UER(\xi), \quad UI_J = UEI(\xi) \\
&FR_0 = FI_0 = 0 \\
&UR_0 = UI_0 = 0.
\end{aligned}
\qquad (5.58a)
$$

The UER, UEI vs ξ must be provided as input to the calculation.

The next step is to put the equation set into a form with a tridiagonal coefficient matrix for solution. The two terms on the LHS of equation (5.58) are combined, and further rearrangement gives

$$\begin{pmatrix} A_1 & C_1 & & & \\ B_2 & A_2 & C_2 & & \\ & B_3 & A_3 & C_3 & \\ & & \ddots & \ddots & \ddots \\ & & B_{J-1} & A_{J-1} & C_{J-1} \\ & & & B_J & A_J \end{pmatrix} \begin{Bmatrix} \begin{Bmatrix} VR_0 \\ FR_1 \\ VR_1 \end{Bmatrix} \\ \begin{Bmatrix} UR_1 \\ FR_2 \\ VR_2 \end{Bmatrix} \\ \vdots \\ \begin{Bmatrix} UR_{J-2} \\ FR_{J-1} \\ VR_{J-1} \end{Bmatrix} \\ \begin{Bmatrix} UR_{J-1} \\ FR_J \\ VR_J \end{Bmatrix} \end{Bmatrix} = \begin{Bmatrix} \begin{Bmatrix} r_1 \\ s_1 \\ t_1 \end{Bmatrix} \\ \begin{Bmatrix} r_2 \\ s_2 \\ t_2 \end{Bmatrix} \\ \vdots \\ \begin{Bmatrix} \\ \\ \end{Bmatrix} \\ \begin{Bmatrix} r_J + \frac{h_J}{2} UER \\ s_J - \psi_J UER \\ t_J - UER \end{Bmatrix} \end{Bmatrix} \tag{5.59}$$

where

$$A_1 = \begin{pmatrix} 0 & 1 & 0 \\ -\bar{\phi}_1 & \theta_1 & \phi_1 \\ -\frac{h_1}{2} & 0 & -\frac{h_1}{2} \end{pmatrix}$$

$$A_j \; (j=2,J) = \begin{pmatrix} -\frac{h_j}{2} & 1 & 0 \\ -\bar{\psi}_j & \theta_j & \phi_j \\ -1 & 0 & -\frac{h_j}{2} \end{pmatrix}$$

$$B_j \; (j=2,J) = \begin{pmatrix} 0 & -1 & 0 \\ 0 & -\bar{\theta}_j & -\bar{\phi}_j \\ 0 & 0 & -\frac{h_j}{2} \end{pmatrix}$$

$$C_j \; (j=1,J-1) = \begin{pmatrix} -\frac{h_j}{2} & 0 & 0 \\ \psi_j & 0 & 0 \\ 1 & 0 & 0 \end{pmatrix}$$

The linear system of equations (5.59) is represented by

$$A\{Z_j\} = \{r_j\}$$

where

A is the coefficient matrix

$$\{Z_1\} = \begin{Bmatrix} VR_0 \\ FR_1 \\ VR_1 \end{Bmatrix}$$

$$\{Z_j\} = \begin{Bmatrix} UR_{j-1} \\ FR_j \\ VR_j \end{Bmatrix} \quad \text{for } j = 2, J$$

$$\{r_j\} = \begin{Bmatrix} r_j \\ s_j \\ t_j \end{Bmatrix}.$$

The system (5.59) is solved for $\{Z_j\}$ at each $\Leftrightarrow$-step by a block-tridiagonal factorization procedure (see (36) p. 273) as follows:

1. Factor the coefficient matrix: $A = \mathcal{L}\mathcal{U}$
2. Calculate the elements in $\mathcal{L}$ and $\mathcal{U}$
3. Let $\mathcal{U}\{Z_j\} = \{W_j\}$, $\mathcal{L}\{W_j\} = \{r_j\}$
4. Solve for $\{W_1\}$
5. Solve for $\{W_j\}$, $j = 2, J$ in terms of $\{W_{j-1}\}$ using $\mathcal{L}\{W_j\} = \{r_j\}$
6. Solve for $\{Z_j\}$ in terms of $\{W_j\}$ using $\mathcal{U}\{Z_j\} = \{W_j\}$.

The details of each step are presented here.

1. Factor A:

$$A = \mathcal{L}\mathcal{U}$$

$$\begin{pmatrix} A_1 & C_1 & & & & \\ B_2 & A_2 & C_2 & & & \\ & B_3 & A_3 & C_3 & & \\ & & & & B_{J-1} & A_{J-1} & C_{J-1} \\ & & & & & B_J & A_J \end{pmatrix} = \begin{pmatrix} \bar{\alpha}_1 & 0 & 0 & & & \\ B_2 & \bar{\alpha}_2 & 0 & & & \\ 0 & B_3 & \bar{\alpha}_3 & & & \\ & & & B_{J-1} & \bar{\alpha}_{J-1} & 0 \\ & & & & B_J & \bar{\alpha}_J \end{pmatrix} \begin{pmatrix} I & \bar{\Gamma}_1 & 0 & 0 & & \\ 0 & I & \bar{\Gamma}_2 & 0 & & \\ 0 & 0 & I & \bar{\Gamma}_3 & & \\ & & & & I & \bar{\Gamma}_{J-2} & 0 \\ & & & & 0 & I & \bar{\Gamma}_{J-1} \\ & & & & 0 & 0 & I \end{pmatrix} \tag{5.60}$$

where

$$I = \begin{pmatrix} 1 & 0 & 0 \\ 0 & 1 & 0 \\ 0 & 0 & 1 \end{pmatrix}$$

2. Calculate the $\bar{\alpha}_j$'s in $\mathcal{L}$ and the $\bar{\Gamma}_j$'s in $\mathcal{U}$, both of which are 3 x 3 matrices:

$$\bar{\Gamma}_j = \begin{pmatrix} \Gamma_{11} & 0 & 0 \\ \Gamma_{21} & 0 & 0 \\ \Gamma_{31} & 0 & 0 \end{pmatrix}, \qquad \bar{\alpha}_j = \begin{pmatrix} \alpha_{11} & \alpha_{12} & \alpha_{13} \\ \alpha_{21} & \alpha_{22} & \alpha_{23} \\ \alpha_{31} & \alpha_{32} & \alpha_{33} \end{pmatrix}.$$

The following relationships are derived from (5.60)

$$\bar{\alpha}_1 = A_1 \tag{5.61a}$$

$$\bar{\alpha}_j \bar{\Gamma}_j = C_j \qquad j = 1, J-1 \tag{5.61b}$$

$$\bar{\alpha}_j = A_j - B_j \bar{\Gamma}_{j-1} \qquad j = 2, J \tag{5.61c}$$

The $\overline{\alpha}_1$ is calculated directly from (5.61a), $\overline{\Gamma}_1$ from (5.61b), $\overline{\alpha}_2$ from (5.61c), $\overline{\Gamma}_2$ from (5.61b), etc. The following results are obtained:

$$\overline{\alpha}_1 = \begin{pmatrix} 0 & 1 & 0 \\ -\overline{\phi}_1 & \theta_1 & \phi_1 \\ -\frac{h_1}{2} & 0 & -\frac{h_1}{2} \end{pmatrix}$$

$$\overline{\Gamma}_1 = \begin{pmatrix} \left(-\frac{1}{2b_{j-1/2}}\left[\psi_1 + \theta_1\left(\frac{h_1}{2}\right) + \phi_1\left(\frac{2}{h_1}\right)\right]\right) & 0 & 0 \\ \left(-\frac{h_1}{2}\right) & 0 & 0 \\ \left(-\Gamma_{11_1} - \frac{2}{h_1}\right) & 0 & 0 \end{pmatrix}$$

$$\overline{\alpha}_j \underset{(j=2,J)}{=} \begin{pmatrix} \left(-\frac{h_j}{2} + \Gamma_{21\,j-1}\right) & 1 & 0 \\ \left(\psi_j - \theta_j\,\Gamma_{21_{j-1}} - \Gamma_{31_{j-1}}\left(-2b_{j-1/2} + \phi_j\right)\right) & \theta_j & \phi_j \\ \left(-1 + \frac{h_j}{2}\,\Gamma_{31_{j-1}}\right) & 0 & -h_j/2 \end{pmatrix}$$

$$\overline{\Gamma}_j \underset{(j=2,J)}{=} \begin{pmatrix} \left(\frac{\left(\frac{h_j}{2}\right)^2\theta_j + \left(\frac{h_j}{2}\right)\psi_j + \phi_j}{\Delta_j}\right) & 0 & 0 \\ \left(-\frac{h_j}{2} - \alpha_{11_j}\,\Gamma_{11_j}\right) & 0 & 0 \\ \left(\frac{2}{h_j}\left[\alpha_{31_j}\,\Gamma_{11_j} - 1\right]\right) & 0 & 0 \end{pmatrix}$$

where

$$\Delta_j = \left[-\left(\frac{h_j}{2}\right)(\alpha_{11})_j\,\theta_j + \left(\frac{h_j}{2}\right)(\alpha_{21})_j + (\alpha_{31})_j\,\phi_j\right]$$

$$b_{j-1/2} = \tfrac{1}{2}\,(b_j + b_{j-1})$$

$$b = (5.48)$$

3. Let $\mathcal{U}\{Z_j\} = \{W_j\}$

$$\therefore\ \mathcal{L}\{W_j\} = \{r_j\}$$

$$\begin{pmatrix} \bar{\alpha}_1 & & & \\ B_2 & \bar{\alpha}_2 & & \\ & B_3 & \bar{\alpha}_3 & \\ & & & B_J\ \ \bar{\alpha}_J \end{pmatrix} \left\{ \begin{matrix} \{W_{11}\} \\ \{W_{21}\} \\ \{W_{31}\} \\ \vdots \\ \{W_{1j}\} \\ \{W_{2j}\} \\ \{W_{3j}\} \\ \vdots \\ \{W_{1J}\} \\ \{W_{2J}\} \\ \{W_{3J}\} \end{matrix} \right\} = \left\{ \begin{matrix} \{r_j\} \\ \{\Delta_j\} \\ \{t_j\} \\ \vdots \\ \{r_J + \frac{h_J}{2}\,UER\} \\ \{\Delta_J - \varphi_J\,UER\} \\ \{t_J - UER\} \end{matrix} \right\} \qquad (5.62)$$

4. Solve for $\{W_1\}$

$$\{W_1\} = \left\{ \begin{matrix} \left(-\frac{1}{2\,b_{j-1/2}}\left[\Delta_1 - \theta_1 r_1 + \left(\frac{2}{h_1}\right)\phi_1 t_1\right]\right) \\ (r_1) \\ -\frac{2}{h_1}\left[t_1 + \frac{h_1}{2}\,W_{11}\right] \end{matrix} \right\}$$

5. Solve for $\{W_j\}$ in terms of $\{W_{j-1}\}$,

$$\underset{(j=2,J)}{\{W_j\}} = \begin{Bmatrix} \left(\frac{1}{\Delta_j}\left[\frac{h_j}{2}(n_j - \theta_j m_j) + \phi_j P_j\right]\right) \\ (m_j - \alpha_{11j} W_{1j}) \\ \left(\frac{2}{h_j}\left[\alpha_{31j} W_{1j} - P_j\right]\right) \end{Bmatrix}$$

where

$$m_j = (r_j + W_{2j-1})$$

$$n_j = (q_j - \theta_j W_{2j-1} - (-2b_{j-1/2} + \phi_j) W_{3j-1})$$

$$P_j = (t_j + (\tfrac{h_j}{2}) W_{3j-1})$$

6. Solve $\mathcal{U}\{Z_j\} = \{W_j\}$ for $\{Z_j\}$
starting with $\{Z_J\}$

$$\begin{pmatrix} I & \bar{\Gamma}_1 & & & & \\ & I & \bar{\Gamma}_2 & & & \\ & & I & \bar{\Gamma}_3 & & \\ & & & & \bar{\Gamma}_{J-2} & \\ & & & & I & \bar{\Gamma}_{J-1} \\ & & & & & I \end{pmatrix} \begin{Bmatrix} \begin{Bmatrix} VR_0 \\ FR_1 \\ VR_1 \end{Bmatrix} \\ \begin{Bmatrix} UR_1 \\ FR_2 \\ VR_2 \end{Bmatrix} \\ \vdots \\ \begin{Bmatrix} UR_{J-2} \\ FR_{J-1} \\ VR_{J-1} \end{Bmatrix} \\ \begin{Bmatrix} UR_{J-1} \\ FR_J \\ VR_J \end{Bmatrix} \end{Bmatrix} = \begin{Bmatrix} \{W_1\} \\ \{W_2\} \\ \vdots \\ \{W_J\} \end{Bmatrix}$$

$j = J$ $\qquad \{Z_J\} = \{W_J\}$

$$\begin{Bmatrix} UR_{J-1} \\ FR_J \\ VR_J \end{Bmatrix} = \begin{Bmatrix} W_{1J} \\ W_{2J} \\ W_{3J} \end{Bmatrix}$$

$j = (J-1), 2 \qquad \{Z_j\} = \{W_j\} - \bar{\Gamma}_j \{Z\}_{j+1}$

$$\begin{Bmatrix} UR_{j-1} \\ FR_j \\ VR_j \end{Bmatrix} = \begin{Bmatrix} W_{1j} \\ W_{2j} \\ W_{3j} \end{Bmatrix} - \begin{pmatrix} \Gamma_{11_j} & 0 & 0 \\ \Gamma_{21_j} & 0 & 0 \\ \Gamma_{31_j} & 0 & 0 \end{pmatrix} \begin{Bmatrix} UR_j \\ FR_{j+1} \\ VR_{j+1} \end{Bmatrix}$$

$$\begin{aligned} UR_{j-1} &= W_{1j} - \Gamma_{11_j}\, UR_j \\ FR_j &= W_{2j} - \Gamma_{21_j}\, UR_j \\ VR_j &= W_{3j} - \Gamma_{31_j}\, UR_j \end{aligned}$$

$j = 1$

$$\begin{aligned} VR_0 &= W_{1_1} - \Gamma_{11_1}\, UR_1 \\ FR_1 &= W_{2_1} - \Gamma_{21_1}\, UR_1 \\ VR_1 &= W_{3_1} - \Gamma_{31_1}\, UR_1 . \end{aligned}$$

Computer Program

The computer program requires as input the test section geometry, air flow properties, and the amplitude ratio and phase response profiles at the initial x-station as starting conditions. Boundary conditions for the oscillatory response must be defined as input and they are imposed at $y/\delta = 1.2$. At the initial x-station and each successive x-station the time-average flow quantities $\bar{u}$, $\partial\bar{u}/\partial y$, $\partial\bar{u}/\partial x$, and $\overline{\nu}_T$ vs y must be calculated internally or be provided as input. The flexibility is built in to allow for the input B.C.'s, I.C.'s and base flow parameters to be represented in functional form or discrete points. Axisymmetric or 2-D rectangular geometry may be specified, and the $\overline{\nu}_T$ input dictates the flow regime to be either laminar or turbulent.

The information input at the initial x-station is transformed into the difference equations of the form of 5.56 and 5.57 onto the working ξ-η grid. The solution proceeds step=by-step in the ξ-direction as described above. At each ξ-step the UI^n profile in the $\mathcal{A}R$ term of 5.56 is first approximated by the UI^{n-1} profile. The real components FR^n, VR^n, and UR^n profiles are initially determined and the UR^n's are used in the $\mathcal{A}_I$ term to

calculate initial values for the FI^n, VR^n, and UI^n profiles. A second iterate is performed in which the current values for $UI^{n(1)}$ are used in the ΔR term of 5.56 and the dependent variable profiles are again calculated. A convergence test is performed following each successive iterate after the initial calculation until

$$\frac{VI_1^{n(i)} - VI_1^{n(i-1)}}{VI_1^{n(i)}} < 0.0001.$$

The calculation continues in this manner for the full length of the boundary layer development.

A non-uniform grid is employed for the η-direction. Grid points are closely spaced near the wall where the flow gradients are steepest. The initial eta-step, h_1, and a multiplier, K, are input, and the following relationships are used to define the grid spacing:

$$h_1 = h_1(\text{input})$$
$$h_2 = K h_1$$
$$h_3 = K h_2 = K^2 h_1$$
$$h_j = h_1 \frac{(K^j - 1)}{(K-1)}.$$

The total number of grid points, J, for a specified η_J ($y_J = 1.2\,\delta$) is given by

$$J = \frac{\ell n \left[1 + (K-1)\frac{\eta_J}{h_1}\right]}{\ell n [K]}.$$

The Box scheme is second-order accurate in the η - spacing (49), (50). This means that the error between the calculated and true solution, $\mathcal{E}$, inherent in the finite differencing procedure (discretization error) is represented by

$$\mathcal{E} = \mathcal{O}(\Delta\eta^2).$$

The formal derivation of the error estimate is given in (50). The sensitivity of the solution to the η - spacing was tested for h_1 = .0025 (Δy =.001-.003 mm) and .10(Δy =.050-.125 mm), and $K_.$=1.10 for the 10 Hz case. Convergence was acceptable for h_1=.100. This scheme places $\sim$2 points in the sublayer, $\sim$8 in the buffer, $\sim$10 in the fully turbulent region, and $\sim$15 in the outer region. The transformation $y \rightarrow \eta$ causes η_J to change very little over the calculation length, so that the number of grid points remains nearly constant, changing slightly near the end of the test section.

Sensitivity tests were run for a range of values for ξ -spacing (Δx = 50 mm, 25 mm, 6.4 mm). Satisfactory convergence was obtained for Δx= 6.4 mm.

6. THEORETICAL RESULTS

6.1 NUMERICAL VALIDATION

Oscillating Laminar Boundary Layer

The mathematical model was first tested against the data of Hill and Stenning (16) for oscillatory laminar boundary layer. The data were obtained in the boundary layer on the inside wall of a 140 mm diameter cylindrical wind tunnel. The flow oscillations were produced by a sliding plate valve. The data were obtained at a single streamwise location in the wind tunnel; the free stream velocity was varied over a range of 1.8 - 3.0 m/sec; the oscillation amplitude was on the order of 10 percent of the time average velocity, and the frequency was varied such that $0.10 < \bar{\omega}_x < 10.0$. Experiments were run for both Blasius flow ($dP/dx = 0$) and Howarth flow ($dP/dx > 0, UE(x) = UE(0) - (Const)\,x$). The comparisons with predictions are shown here for the Blasius flow.

Relying on the fact that the boundary layer oscillatory response for a laminar boundary layer with zero pressure gradient is primarily a function of the dimensionless frequency parameter, $\bar{\omega}_x = (2\pi)(FREQ)(x)/UE(x)$, the data profiles were rearranged from a fixed x-location/varying

frequency presentation, to a fixed frequency/increasing x-location presentation. In this manner the theory and data could be compared for a developing boundary layer.

The developing Blasius time-average boundary layer possesses a similarity solution. The equations of motion are transformed and solved analytically in such a way that the velocity profiles can be represented in a universal form which is independent of the x-location,

$$\frac{u}{u_E} = f'(\eta)$$

where

$$f = \frac{\psi}{\sqrt{\nu x / u_E}}$$

$$\eta = \frac{y}{\sqrt{\nu x / u_E}}$$

$$f' = df/d\eta.$$

The functions f, f' and $f'' = d^2f/d\eta^2$ are well known universal functions of η. The required base flow input to the oscillatory solution is determined as follows:

$$y = \eta\left(\sqrt{\nu x / \overline{u_E}}\right)$$

$$\bar{u}/\overline{u_E} = f'$$

$$\partial\bar{u}/\partial y = \overline{u_E}\sqrt{\frac{\overline{u_E}}{\nu x}}\, f''$$

$$\partial\bar{u}/\partial x = -\frac{\overline{u_E}}{2x}\eta f''.$$

An example of the velocity profile development is shown in Figure 6.1 for five x-locations which cover a distance of approximately 750 mm.

The comparisons were made for three frequencies 0.28 Hz, 1.0 Hz, and 3.5 Hz. The x-station 0 in all cases was located 700 mm from the flat plate leading edge. The 0.28 Hz test covered a range of $\overline{\omega}_x$ from 0.40 to 0.83 and a development length of 750 mm. The 1.0 Hz test covered $\overline{\omega}_x$ from 1.47 to 2.65 over a length of 560 mm, and the 3.5 Hz test spanned 4.98 to 9.26 in $\overline{\omega}_x$ over 600 mm. It was felt that comparisons over these ranges of variables would provide a measure of validation for the numerical accuracy of the theory under the simplifying conditions of zero pressure gradient and laminar flow (the conical diffuser experiments span a range of 0-11.0 in $\overline{\omega}_x$ over a length of 610 mm). The initial conditions were input from curve fits to the data at x-station 0, and the boundary condition was of the following form,

$$U = \overline{UE} + \Delta U \cos \omega t.$$

The x-station locations shown in Figure 6.1 corresponds to the 0.28 Hz case. A comparison of these low frequency data with a quasi-steady response is shown in Figure 6.2. The velocity profile is assumed to adjust instantaneously to variations in the free stream velocity. The phase difference, with respect to the free stream oscillation, is zero in this model, and the amplitude is determined by the difference in

magnitude of the steady flow profiles which would develop for the maximum and minimum free stream velocity. The data show a pattern of larger amplitudes over the middle region of the boundary layer when compared to the quasi-steady model. An amplification pattern ($\Delta u/\Delta u_E > 1.0$) is measured in the outer half of the boundary layer at x-stations 3 and 4. A phase lead pattern is established in the inner half of the boundary layer.

Comparisons of the same data with the boundary layer predictions are shown in Figure 6.3. The model successfully reproduces the outer amplification pattern and the inner phase lead pattern over the full length of boundary layer development. The predicted amplification pattern penetrates deeper into the boundary layer with increasing $\overline{\omega}_x$. The inner phase lead is slightly overpredicted at x-station 5.

The predictions were also well matched with the data for the 1.0 Hz and 3.5 Hz cases. Figure 6.4 shows the amplification pattern continuing its move closer to the wall with increasing $\overline{\omega}_x$, and a phase lag pattern is established in the outer region of the boundary layer. At 3.5 Hz the boundary layer oscillation is very nearly

locked into the core flow oscillation in the outer region showing only a very slight amplification and phase lead at this location. No attempt was made to determine if the model would predict the crossover from phase lead to lag in the outer region between $\overline{\omega}_x = 0.83$ and 1.47. This test would require a development length of 1850 mm which is equivalent to $Re_x \approx 500{,}000$.

6.2 COMPARISON WITH EXPERIMENTAL RESULTS

Theoretical predictions for the oscillatory response of a turbulent boundary layer in a conical diffuser were compared with the experimental results of Data Set-2. The data for the lowest frequency run, 5 Hz, are first compared with a quasi-steady model as shown in Figure 6.6. The quasi-steady response was developed from the steady flow velocity profiles measured for the $\overline{UCL}(0) = 18.29$ and 30.43 m/sec tests. This represents an amplitude $\Delta UCL(0)/\overline{UCL}(0)$ of 25%. As was shown in the laminar comparison, the developing amplification pattern in the outer region cannot be predicted by a quasi-steady model. Quasi-steady phase difference is zero across the boundary layer.

The initial conditions for the oscillatory boundary layer model are defined from curve fits to the measured

response of $\tilde{U}$ at x-station 4 (DS-2/Run 16). For use in the calculation, the curve fitting is actually done for the U_R and U_I components of $\tilde{U}$, and the two are combined to show amplitude ratio and phase difference for presentation of the results. The I.C.'s for the 10 Hz case are shown in Figure 6.7. The boundary conditions at the core flow/boundary layer interface are developed from the measured centerline response (DS-2/Run 15), and these profiles were presented in Chapter 4, Figures 4.21a and b.

The comparisons of the data and the boundary layer predictions for the 5 Hz case are shown in Figures 6.8a and b. In the outer half of the boundary layer a predicted pattern of amplitude amplification begins to develop just downstream of x-station 12, and this is matched by the measured response. The theory and experiment remain in good agreement out to x-station 18, at which point the predicted amplification pattern begins to show a greater magnitude when compared with the data. From x-station 18 to 24 the amplification pattern continues to increase in magnitude for both theory and data; however, the theory increases at a faster rate, and it reaches a maximum value of $\Delta U/\Delta UCL = 2.5$ at x-station 24 compared to $\Delta U/\Delta UCL = 1.55$ at the same

x-station for the data.

A similar comparison holds for the 5 Hz phase difference pattern. The initial phase lead pattern, which is established across the boundary layer, increases in magnitude with each succeeding downstream x-station, and the theory and data are well matched to x-station 18. At this point the theory pattern in the outer region begins to swing back, crosses from lead to lag at x-station 22, and the lag pattern continues to increase in magnitude for x-station 24. In the inner region a phase lead is predicted throughout the test section with a maximum just adjacent to the wall. The experimental results show a phase lead pattern which continues to increase in magnitude throughout the entire test section with a maximum lead pattern at x-station 24.

At 10 Hz the comparisons presented in Figures 6.9a and b show both the theory and data with a phase lead pattern across the boundary layer out to x-station 10, followed by a phase lag pattern which begins developing in the outer region at x-station 12. At x-station 14 it is apparent that the theory has increased the magnitude of the lag pattern at a faster rate than the data. This mismatch continues to x-station 20 at which point the

theory shows an abrupt crossover from a lag pattern to a lead pattern in the outer region, and at x-station 24 a second abrupt crossover has occurred, this time from lead to lag. As in the 5 Hz case, the phase difference remains positive just adjacent to the wall throughout the test section.

The faster pattern crossover rate of the prediction in comparison with the data is evident also in the plots of amplitude ratio (Figure 6.9b). The theory begins a faster swing in the direction from an amplification pattern towards an attenuation pattern at x-station 16. Two predicted crossovers occur between x-stations 16 and 24 while the data show only one.

The comparisons for 15, 20, 25 and 30 Hz are presented in Figures 6.10a,b through 6.13a and b. In all of the cases the theory matches the initial trend of the data pattern development in the upstream part of the test section. In the vicinity of x-stations 10-12 the theory patterns begin to indicate a faster crossover movement than the data patterns. In the downstream part of the test section the comparisons of theory and data present a chaotic picture since both represent patterns of crossovers between amplification and attenuation and

phase lead and lag, but the theory crossovers occur at a faster rate than the data. For the theory, as for the data, the pattern crossovers take place in the outer region of the boundary layer. In the inner region the predicted phase is always leading the local centerline oscillation and the amplitude is progressively attenuated until it is completely damped out at the wall.

The predicted outer region patterns are shown most clearly in the plots of Figures 6.14a through f. These figures show the amplitude ratio and phase difference (with respect to the inlet centerline oscillation) plotted vs x-station location. Figures 6.14a through f compare respectively with the data plots of Figures 4.24a through f. The core flow response (boundary condition) is shown as a solid line and the boundary layer results are plotted with coded curves. The pattern crossovers with respect to the local centerline oscillation were discussed above and these are indicated wherever the boundary layer curves cross the core flow response curve.

At 5 Hz (Figure 6.14a) the predicted maximum phase lead pattern in the outer region occurs near x-station 16 and it is obvious that the phase angle magnitudes are

greater compared with the data at this location. The predicted phase pattern then swings smoothly back in the direction of decreasing phase lead, and crosses over from lead to lag at x-station 22-24. The amplitude ratio plot shows the overshoot in predicted amplification at x-stations 22-24.

The predicted amplitude and phase patterns for 10 Hz each cross over between amplification and attenuation and phase lead and lag 3 times compared to 1-2 times for the data. The theory predicts the number of crossovers to be 4, 5, 6 and 7 for 15, 20, 25, and 30 Hz respectively, while the data show 2, 3, 4, and 5 in the same order. The magnitudes at the peaks of the crossover excursions are greater for the theory in comparison with the data and this is especially evident in the phase difference patterns.

6.3 DISCUSSION

The theory, using a fixed eddy viscosity modeling scheme for the oscillatory Reynolds stresses, is capable of simulating the boundary layer response qualitatively. The model is constrained by the boundary conditions which insure that the core flow oscillation is matched at $y = 1.2\bar{\delta}$, and which insure that $\tilde{U}=\tilde{V}=0$ at $y = 0$. In

the inner region of the boundary layer a phase lead pattern is predicted for all x-stations, and this appears to be consistent with the data and with the mechanism as it is understood. In the outer region the predicted response patterns follow the trend of the data patterns initially, and they develop the crossovers, with respect to the streamwise direction, between amplification and attenuation and phase lead and lag as do the data. The predicted pattern crossover rate is higher than the data and the predicted magnitudes of the pattern excursions exceed the data.

There are several qualitative aspects of the oscillatory response which can be seen more clearly in the theory plots since the disorder caused by the data scatter is no longer present. The predicted crossover patterns are more closely spaced in the downstream portion of the test section in agreement with the data. A mechanism was described in discussing the experimental results in which the response was envisioned as being driven from a specific location within the boundary layer. The number of cycles in the crossover pattern was said to be related to the effective residence time of the boundary layer in the test section and the period, T, of the oscillation.

$$\text{Residence time} = \text{Number of cycles} \times T$$

The effective residence time can be calculated by integrating a streamwise velocity profile constructed using the local velocities at the controlling regions in the boundary layer. If this mechanism is followed, the fact that the predicted crossover rate is higher than the data suggests that the model operates as if the response were controlled deeper within the boundary layer where the velocity is lower and consequently the effective residence time is higher. An illustration was given in Chapter 4 for the experimental results in which the residence time calculated from a streamwise velocity profile at $y/\overline{\delta} = 0.5$ gave roughly the number of crossover cycles which were measured experimentally. The same calculation applied to the theory suggests that the characteristic velocity profile, which would correspond to the predicted number of crossovers and effective residence time, is located roughly at $y/\overline{\delta}=0.10$. The results are tabulated below:

		X-station 4 - 24	
FREQ (1/sec)	T (sec)	No. predicted cycles	Residence time (sec)
5	.200	.6	
10	.100	1.3	
15	.067	1.8	
20	.050	2.3	~ .12
25	.040	2.7	
30	.033	3.6	

The calculated residence time for x-station 4-12 in the test section is .028 sec. This means that the fluid would effectively see 1/4 of the total number of cycles in this portion of the test section and approximately 3/4 in the remaining portion, and this corresponds roughly with the predicted patterns.

The predicted phase difference patterns lead the amplitude ratio patterns by 90 degrees, in agreement with the data. The crossover patterns in the upstream portion of the test section have different wavelengths and they initially cross over in an out-of-phase band. In the downstream portion of the test section the pattern movement becomes locked in across the boundary layer. The pattern wavelengths become equal and the crossovers occur in phase. Also, in the downstream portion of the test section, the response pattern retains its relative shape across the boundary layer as it swings through its crossovers. It can be seen that, of the outer region curves shown, the $0.6\bar{\delta}$ maintains the maximum magnitude position.

The predicted crossover patterns at the outer edge of the boundary layer, for the 10 Hz case are shown in Figure 6.15. The boundary conditions (core flow response) are imposed

at $1.2\bar{\delta}$. The $0.8\bar{\delta}$ and $1.0\bar{\delta}$ curves show a progressive transition from the point of maximum pattern magnitude near $0.6\bar{\delta}$ to the core response boundary condition.

The boundary layer locations shown in Figures 6.14a through f are all located in the outer or intermittent region, except the $0.1\bar{\delta}$, which is located in the fully turbulent region. The inner region response for 5 Hz is shown in Figure 6.16. The $0.1\bar{\delta}$ location is in the fully turbulent region, $0.040\bar{\delta}$ is in the buffer, and $0.005\bar{\delta}$ is in the sublayer. The shape of the crossover pattern is retained throughout the inner region; however, there is a phase lead in the buffer and sublayer for all the x-stations. The predicted response for the 10 Hz sublayer shows a phase crossover to lag at x-station 24. This is the only such occurence in all of the theoretical results, and this anomaly may be related to an error in the experimentally defined core flow response at the exit of the test section.

Figure 6.17 shows a comparison of the response patterns as a function of $\bar{\omega}_x$ for $y/\bar{\delta} = 0.6$. Figure 6.17 is comparable to the data plot of Figure 4.27. The theory patterns exhibit greater similarity than the data. It was argued that the measured similarity was a function

of the degree to which the $\overline{\omega}_x$ vs X relationships were similar, implying an upstream history effect. This effect is not apparent in the theory patterns perhaps reflecting the limitation of Reynolds stress modeling which cannot accommodate upstream history.

As a final comparison, the results of using a quasi-laminar model (5.32) are shown in Figure 6.18 for the 5 Hz case. In comparison with the fixed-eddy viscosity patterns (Figure 6.14a) it can be seen that the elimination of the oscillatory Reynolds stress term produces greater excursions in magnitude and an even faster rate of pattern crossover.

In the complex, strongly coupled flow which is established in the diffuser test section, it appears that an oscillatory response is required of the modeled turbulence field properties. The fixed eddy viscosity model can only produce oscillations in $\widetilde{u'v'}$ which are in phase with $\partial\tilde{u}/\partial y$. The definition of the model is repeated here for illustration:

$$-\rho(\langle u'v'\rangle - \overline{u'v'}) \cong \rho\,\bar{\nu}_T\,\frac{\partial\tilde{u}}{\partial y}. \qquad (5.31)$$

The neglected term $\rho(\tilde{\nu}_T\,\partial\bar{u}/\partial y)$ can, in principle, provide a dynamic $\langle\nu_T\rangle$. Brown has obtained theoretical results (unpublished) as follow-on to the work reported

in (20) and (21). He has derived an oscillatory eddy viscosity by linearizing a time-average formulation which excludes any dependence on remote quantities such as the wall shear stress. This model would be valid for the quasi-steady case in which the frequency approaches zero. The phase shifts required to reproduce a measured oscillatory response for finite frequencies in pipe flow were examined. It was found that $\tilde{\nu}_T$ lags significantly behind $\partial\tilde{u}/\partial y$ for intermediate frequencies, and that the lag increases monotonically with increasing frequency. The time-invariant eddy viscosity behavior was approached for high frequencies. Brown's work is an indication of the nature of the refinements required to pursue this direction in Reynolds stress modeling.

Cebeci (24) has extended his eddy viscosity model for use in time-dependent boundary layer solutions. The (now instantaneous) formulation is identical to the time-average version used in this study (5.33 to 5.38) with the addition of an unsteady term P_t^+ in the mixing length equation (5.37),

$$A = 26\nu\, u_\tau^{-1}\left[1-11.8(P_t^+ + P_x^+)\right]^{-1/2}$$

where

$$P_t^+ = \frac{\nu}{u_\tau^2}\,\frac{\partial u_E}{\partial t}.$$

Cebeci reports promising results in limited comparison with data.

7. CONCLUSIONS AND RECOMMENDATIONS

The conclusions drawn from the study are listed as follows:

(1) Imposing a velocity oscillation on the turbulent boundary layer flow developing in a conical diffuser produces a complex response pattern in the outer region of the boundary layer which crosses over between amplification and attenuation, and phase lead and lag, along the test section length, at a rate related to the oscillation frequency. A phase lead is established in the inner region throughout the test section.

(2) The response at each point in the boundary layer is adequately defined by the fundamental waveform. Phase-averaging with a large number of cycles showed that higher harmonic components are insignificant.

(3) The core flow response pattern, along the test section length, is of the same shape as that across the boundary layer; however, the two are 180 degrees out of phase. The phase difference pattern in the boundary layer is 90 degrees out of phase with the amplitude pattern.

(4) The oscillation has no measureable effect on the time-average boundary layer development for the frequency range 5-30 Hz and an oscillation amplitude, $\Delta UCL/\overline{UCL}$, on the order of 10 percent.

(5) The time-invariant eddy-viscosity model for the oscillatory Reynolds stresses gives predicted response patterns which cross over between amplification and attenuation, and phase lead and lag, at a higher rate and with greater excursions in magnitude than the data patterns. The model can only produce oscillations in $\widetilde{u'v'}$ which are in phase with $\partial\tilde{u}/\partial y$. This response is not adequate in the strongly coupled flow in the diffuser test section. It appears that an oscillatory response is required of the turbulence field properties which are modeled by the eddy viscosity. The neglected term in the Reynolds stress formulation, $\rho(\tilde{\nu}_T \partial\bar{u}/\partial y)$, can, in principle, provide a dynamic $\langle\nu_T\rangle$. It is not certain, however, whether this concept can be used with success in oscillatory flow or whether more sophisticated turbulence modeling is required.

The following recommendations are offered:

(1) The conical diffuser is a useful tool for exploring dynamic effects over wide ranges of the test

variables. Mappings which include the 30-300 Hz range may show some interesting behavior when the frequency of the imposed oscillation matches with a dominant frequency in the turbulence field spectrum. Non-linear effects can be explored with oscillation amplitudes in the 10-50% range.

(2) A more detailed experimental study is needed to uncover the mechanisms which control the boundary layer response. It is suggested that a simpler geometry, such as a circular pipe, be used for fundamental studies. Direct measurements of the oscillatory Reynolds stresses and other turbulence properties can be made with multi-wire probe systems.

(3) The eddy viscosity concept is worth pursuing for use in oscillatory flow because of its simplicity. As a next step, it is suggested that an examination be made of the response required in the oscillatory eddy viscosity term, $\tilde{\nu}_T$, to reproduce the experimental data. This would provide guidance for an extension of the modeling, and an insight into the regions where the concept remains valid.

TABLE 4.1 . DATA SET 1. Experimental Test Parameters.

Run No.	$\overline{UCL}(0)$ (m/sec)	FREQ. (Hz)	Amplitude Ratio $\frac{\Delta UCL(0)}{\overline{UCL}(0)}$	Re_D $\frac{\overline{UCL}(0) \times D(0)}{\nu}$	Reduced Frequency $\overline{\omega}_L = \frac{2\pi \times FREQ \times L}{\overline{UCL}(0)}$	Description
1	18.29	0	--	118350	0	Steady Flow
2	30.48	0	--	196000	0	
3	18.29	5	.1040	119000	1.05	10 pt. Boundary Layer Traverses; 5 X-Stations
4	↓	15	.0311	117500	3.14	
5		20	.0271	117500	4.19	
6		20	.0858	120000	4.19	
7		25	.0182	116500	5.20	
8		35	.0149	116600	7.33	
9	30.48	5	.0290	197000	0.63	
10	↓	8	.0423	196000	1.00	
11		8	.0706	194000	1.00	
12		15	.0476	193500	1.89	
13		15	.0496	197500	1.89	
14		25	.0211	193000	3.14	
15	42.06	5	.0432	270000	0.46	

TABLE 4.2 DATA SET 2. Experimental Test Parameters.

Run No.	$\overline{UCL}(0)$ (m/sec)	FREQ. (Hz)	Amplitude Ratio $\frac{\Delta UCL(0)}{\overline{UCL}(0)}$	Re_D $\frac{\overline{UCL}(0) \times D(0)}{\nu}$	Reduced Frequency $\overline{(\omega)}_L = \frac{2\pi \times FREQ \times L}{\overline{UCL}(0)}$	Description
1	18.29	0	--	116667	0	Steady Flow
2	30.48	0	--	194931	0	
3	18.29	5	.1060	116085	1.05	Time-Mean Boundary Layer
4	↓	15	.0920	118343	3.14	
5	18.29	5	.0469	117401	1.05	7-8 pt. Boundary Layer Traverses 13 X-Stations
6		10	.0568	116320	2.09	
7		15	.0590	115087	3.14	
8		20	.0565	114768	4.19	
9		25	.0457	113402	5.24	
10	↓	30	.0352	113560	6.28	
11	30.48	16.63	.0485	197675	2.09	
12	18.29	10	.0602	124628	2.09	20 pt. Boundary Layer Traverses 5 X-Stations
13		15	.0768	121852	3.14	
14	↓	20	.0428	121050	4.17	

TABLE 4.3 DATA SET 2. Experimental Test Parameters.

Run No.	$\overline{UCL}(0)$ (m/sec)	FREQ. (Hz)	Amplitude Ratio $\frac{\Delta UCL(0)}{\overline{UCL}(0)}$	Re_D $\frac{\overline{UCL}(0) \times D(0)}{\nu}$	Reduced Frequency $\overline{\omega}_L = \frac{2\pi \times FREQ \times L}{\overline{UCL}(0)}$	Description
15	18.29	5	.0577	124815	1.05	Boundary Condition Run
		10	.0688		2.09	
		15	.0578		3.14	Centerline
		20	.0402		4.19	
		25	.0270		5.24	13 X-Stations
		30	.0210		6.28	
16	18.29	5	.0507	120945	1.05	Initial Condition Run
		10	.0642		2.09	
		15	.0508		3.14	20 pt. Boundary Layer Traverse
		20	.0293		4.19	
		25	.0195		5.24	
		30	.0173		6.28	X-Station = 004

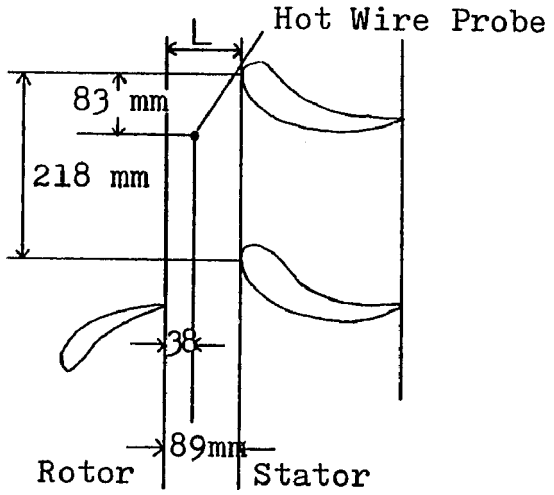

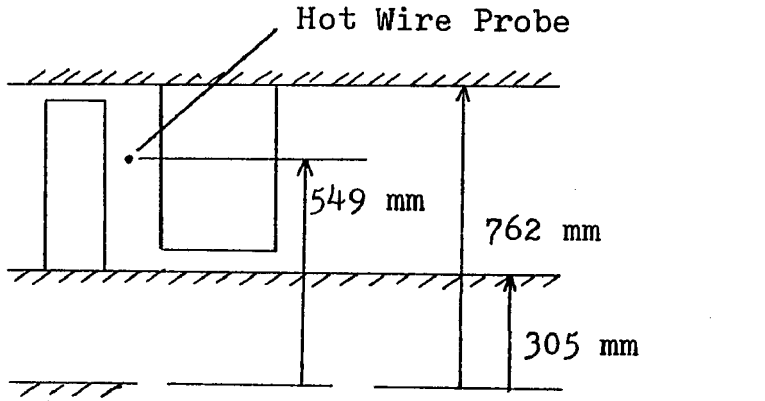

Single Stage, Experimental Compressor:
24 Bladed rotor
15 Blade stator row

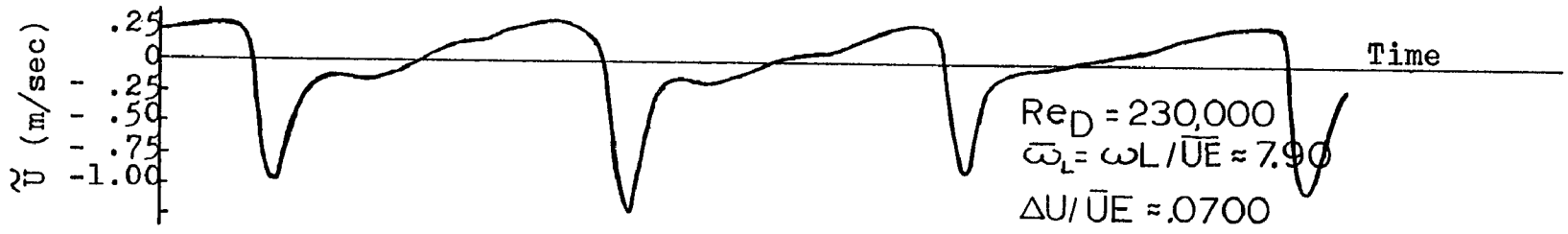

Figure 1.1 Recent work of Evans (1) showing data for velocity oscillations in the mean flow direction in the blade passage of a turbo-compressor. FREQ = 260 Hz, $\overline{UE}$ = 18.29 m/sec, L = 89 mm.

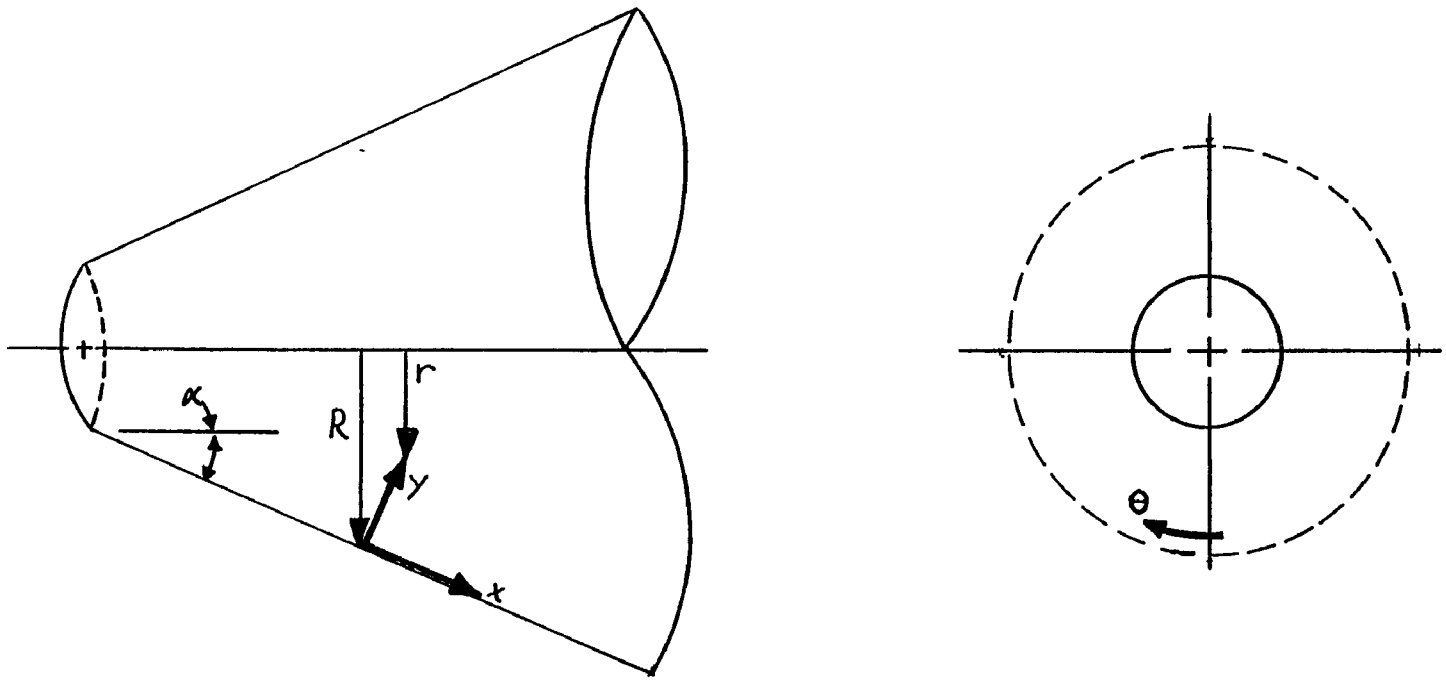

Figure 2.1 Boundary layer theory coordinate system.

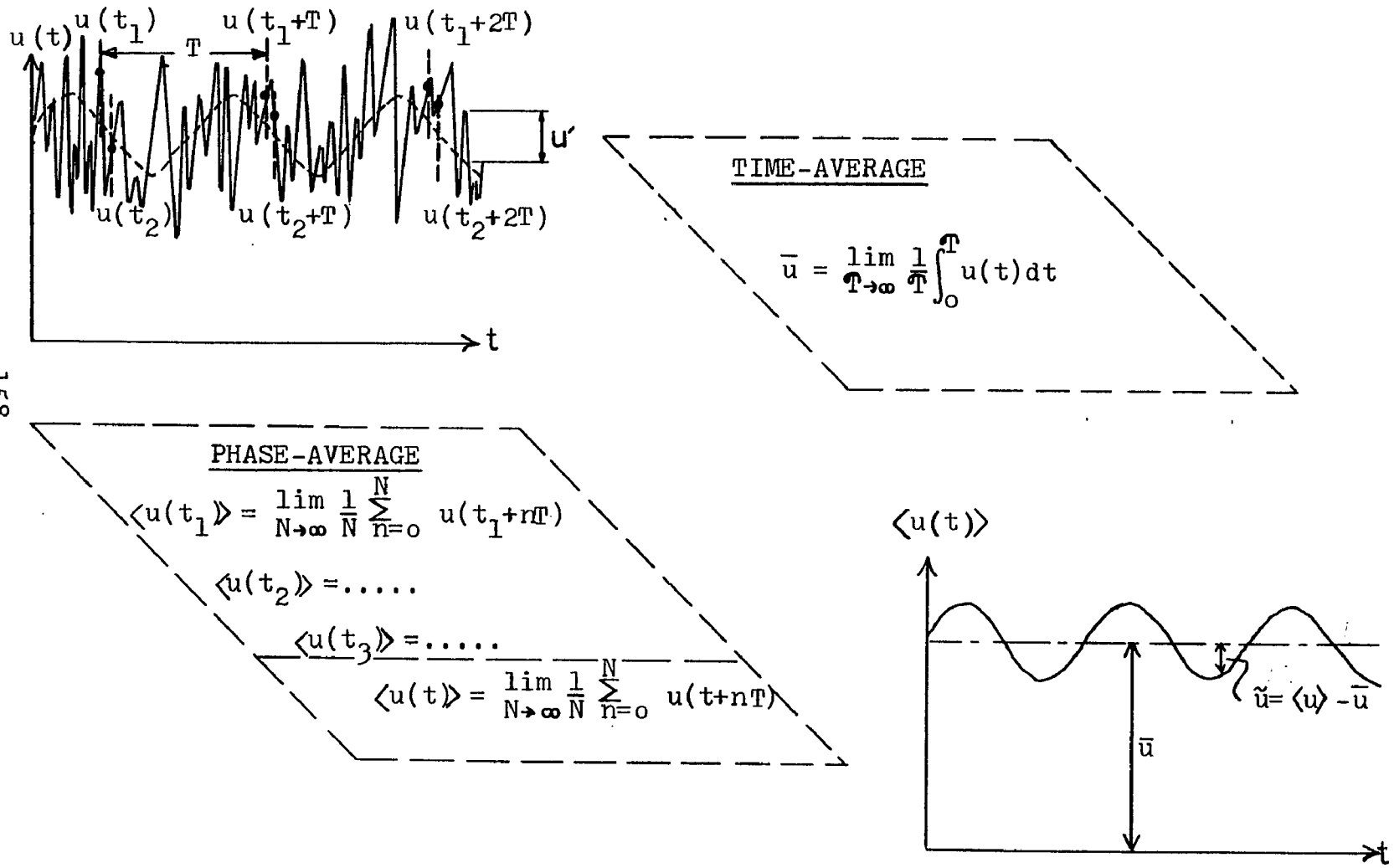

Figure 2.2 Phase-averaging and time-averaging processes. The time dependent, streamwise velocity is used for illustration.

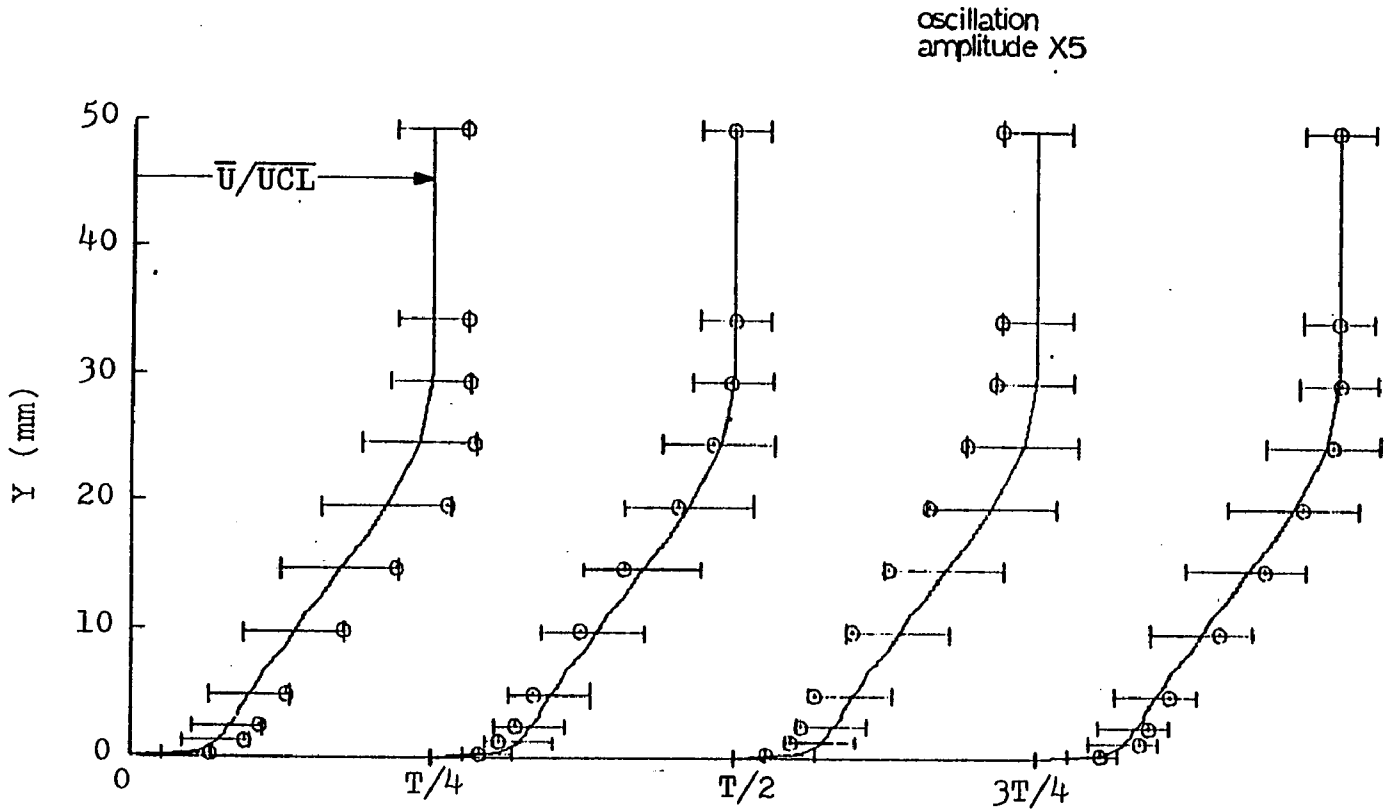

Figure 2.3 Boundary layer oscillatory response shown relative to the local (x-station), centerline, velocity oscillation.
Re_D=197,000, $\bar{\omega}_L$=0.63, FREQ=5 Hz, $\Delta UCL(0)/\overline{UCL}(0)$=.0290,
X-station 18 (DS-1/Run 9).

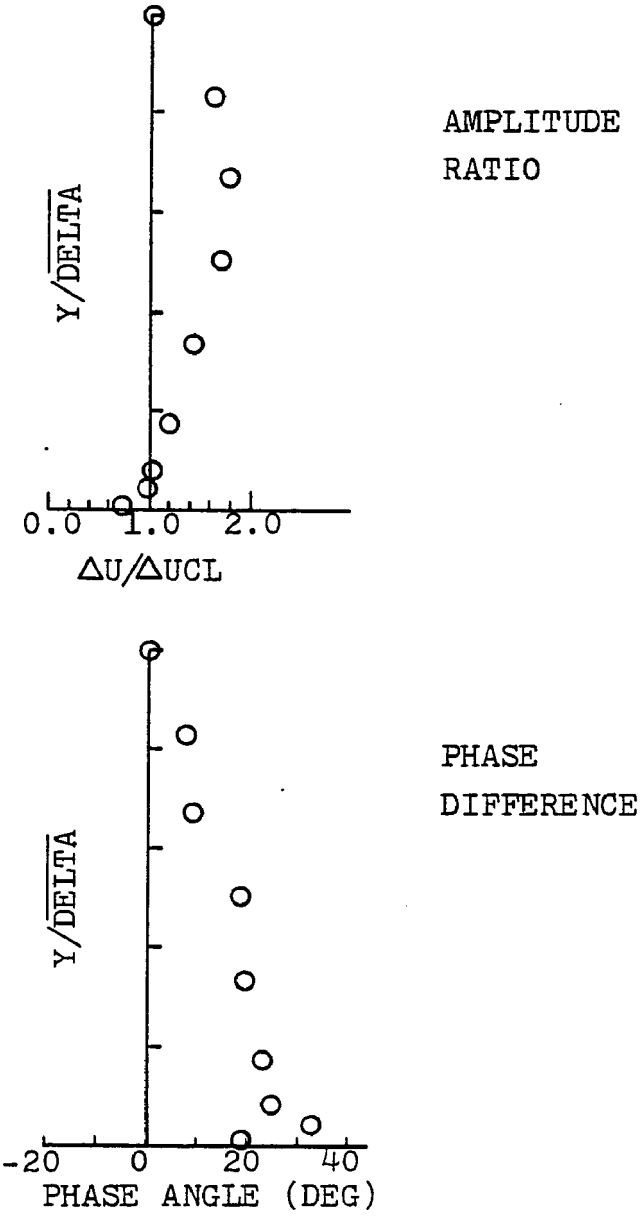

Figure 2.4 Boundary layer oscillatory response shown relative to the local (x-station), centerline, velocity oscillation.
Re_D=197,000, $\bar{\omega}$=0.63, FREQ=5 Hz,
$\Delta UCL(0)/\overline{UCL}(0)$=.0290, x-station 18(DS-1/Run 9).

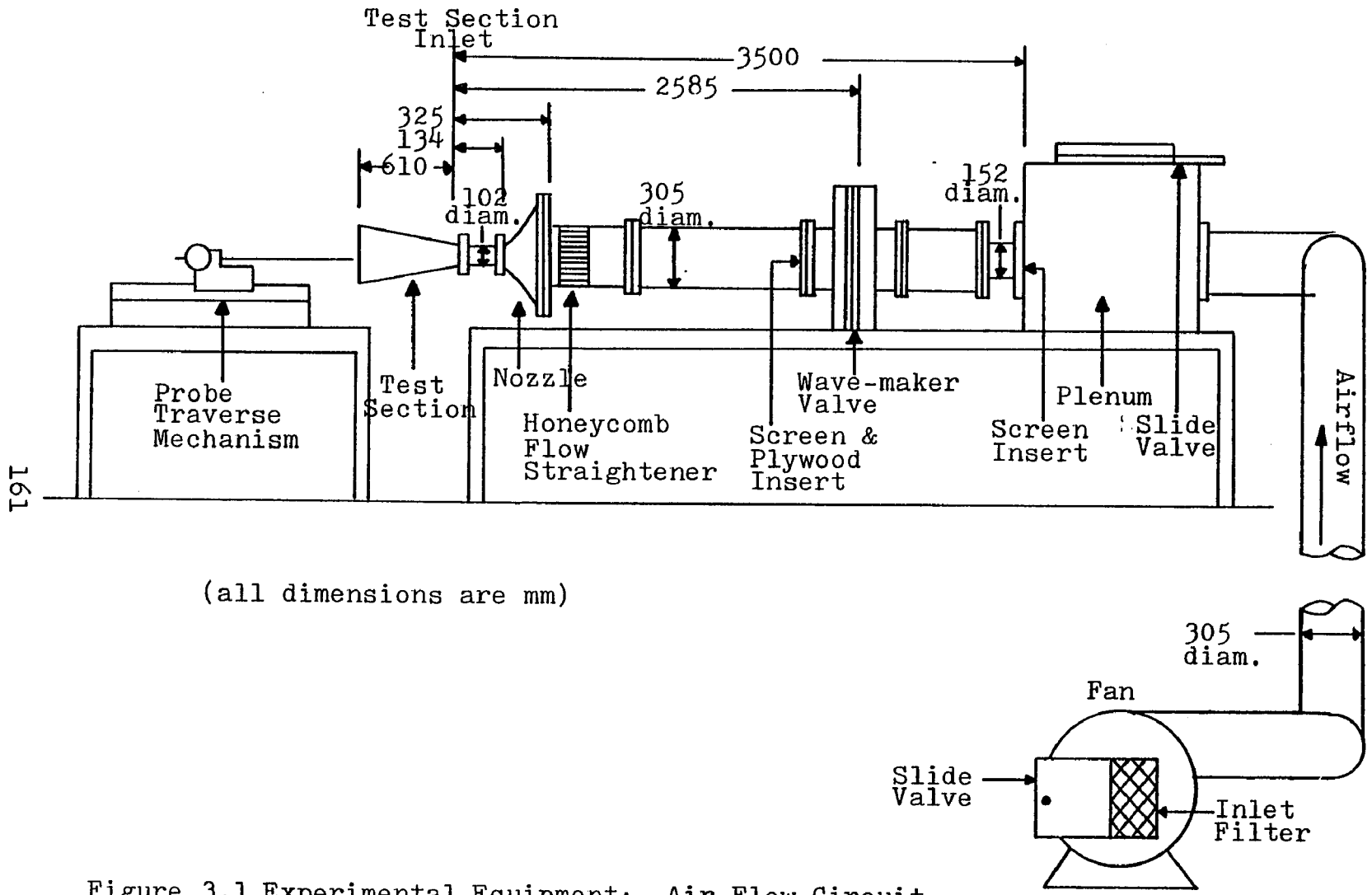

Figure 3.1 Experimental Equipment: Air-Flow Circuit.

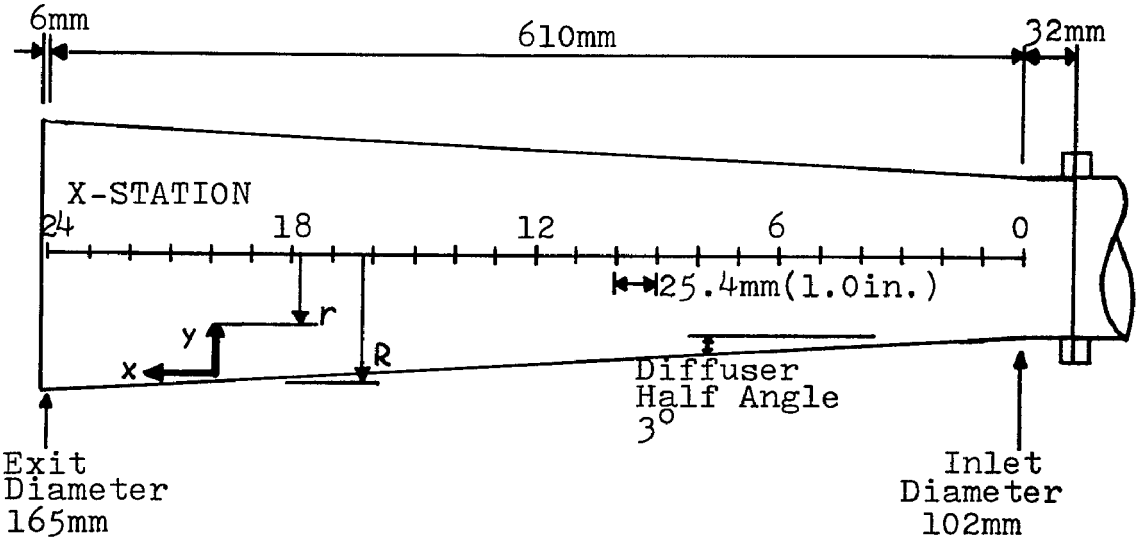

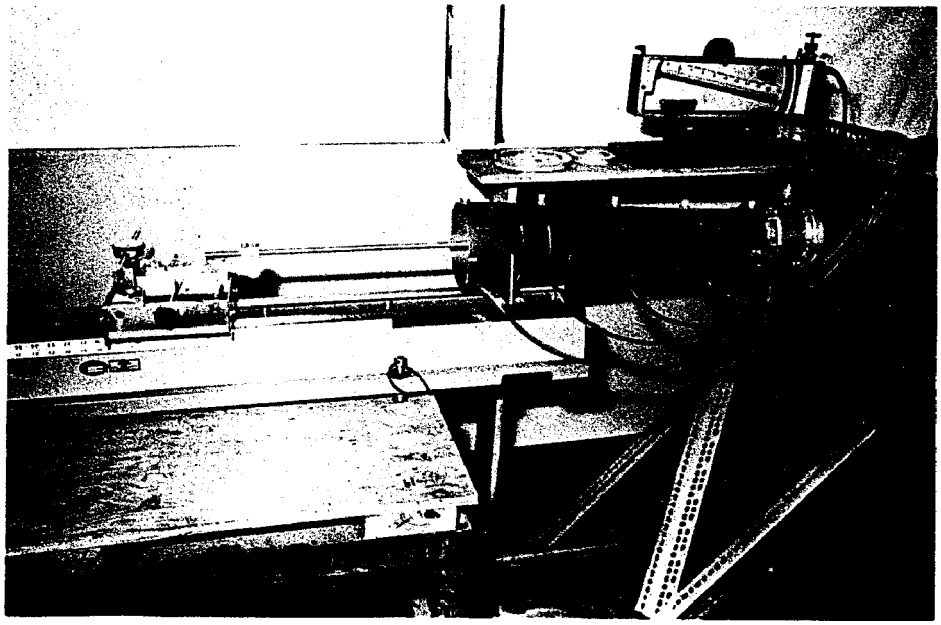

Figure 3.2 Test Equipment: Test Section

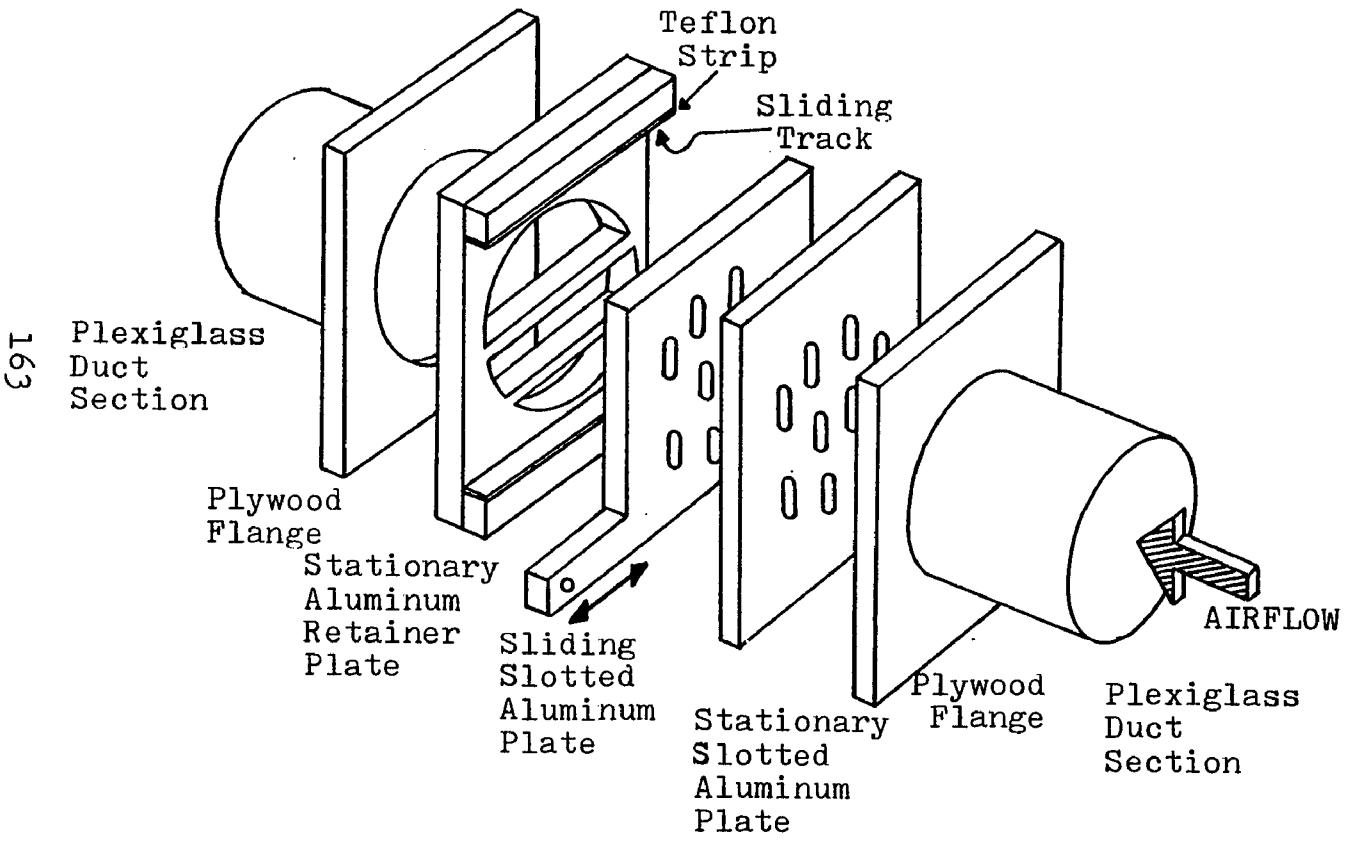

Figure 3.3 Test Equipment: Wave-maker Valve Detail.

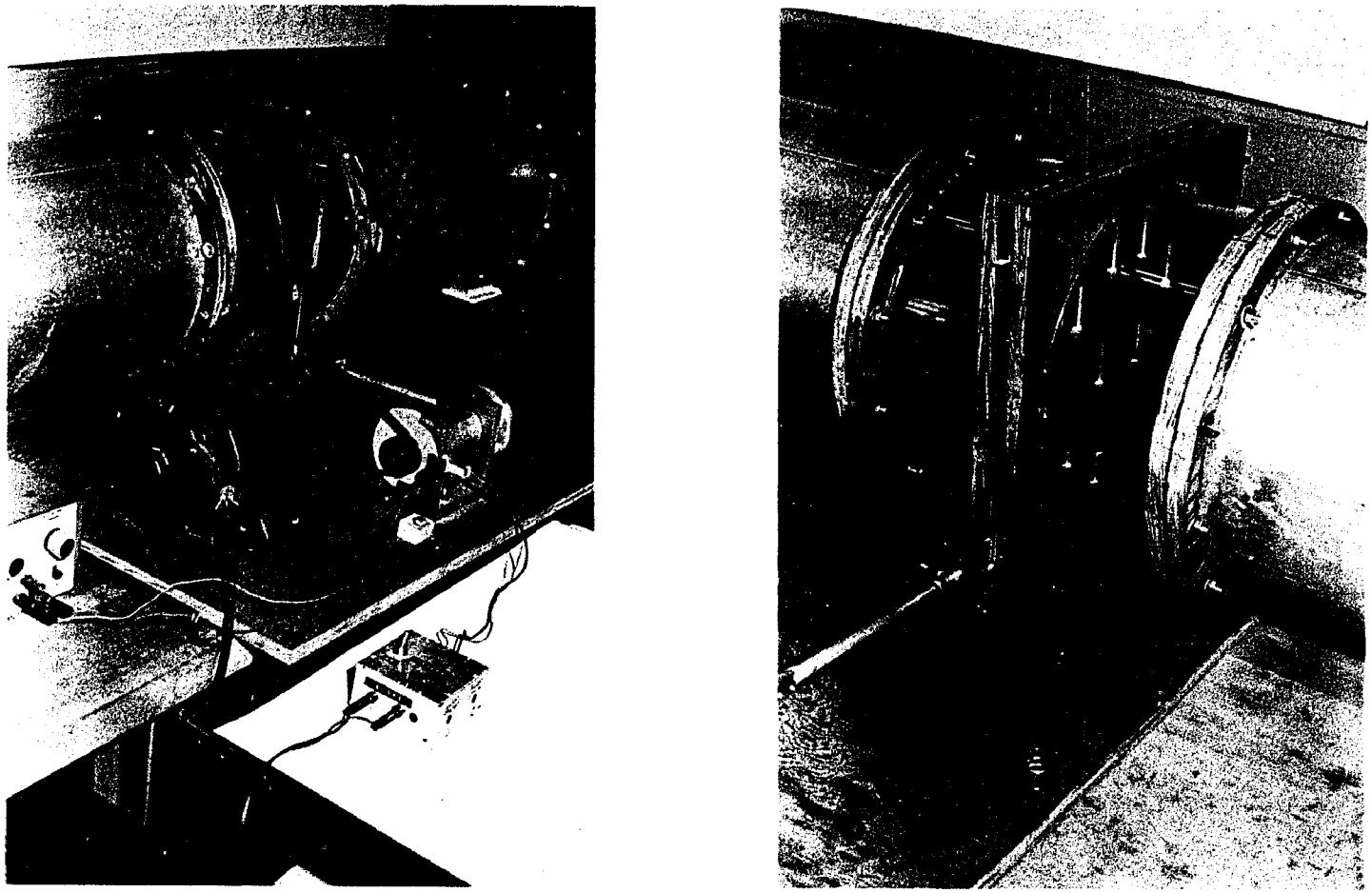

Figure 3.4 Test Equipment: Wave-maker valve with drive train and frequency sensing components.

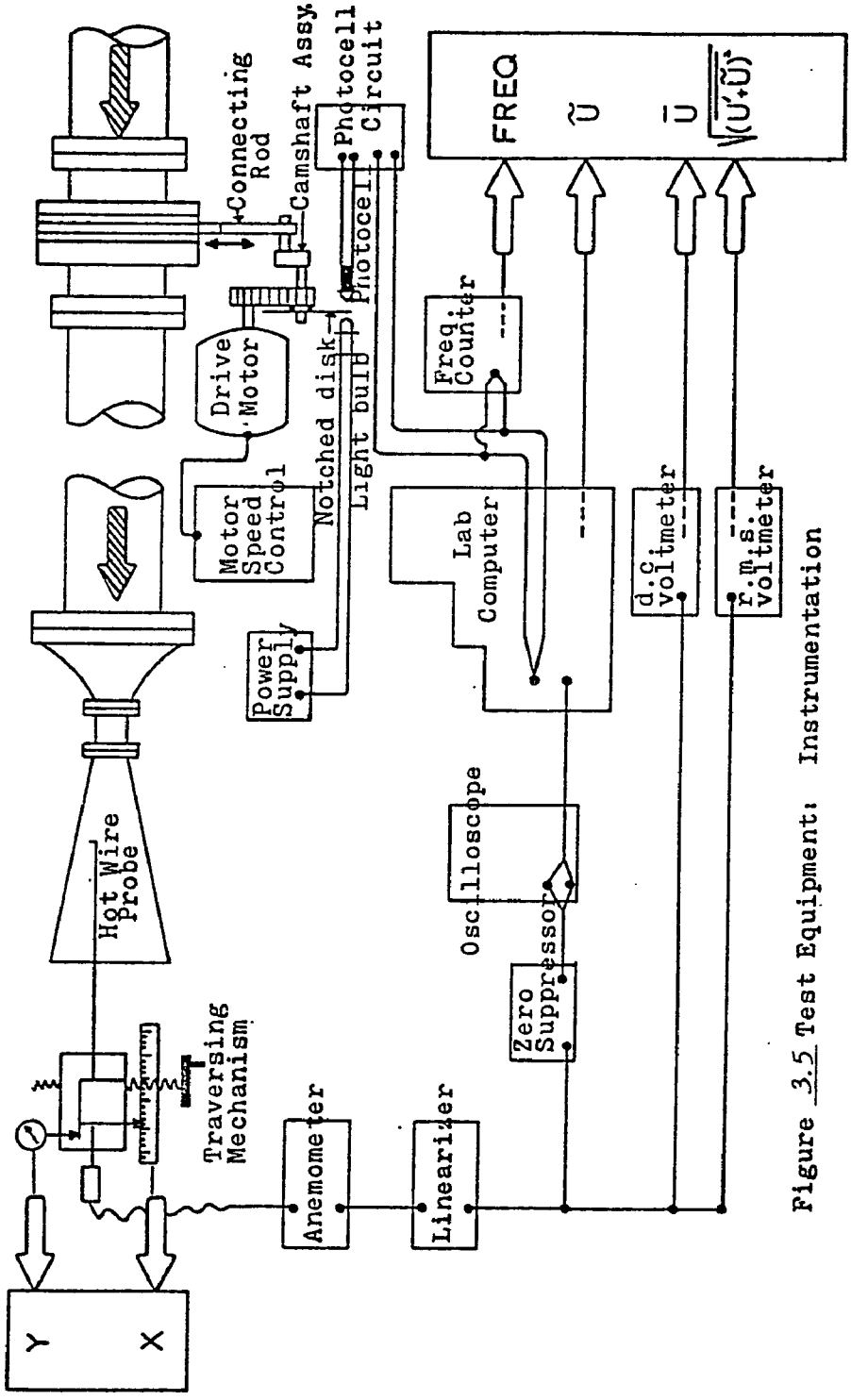

Figure 3.5 Test Equipment: Instrumentation

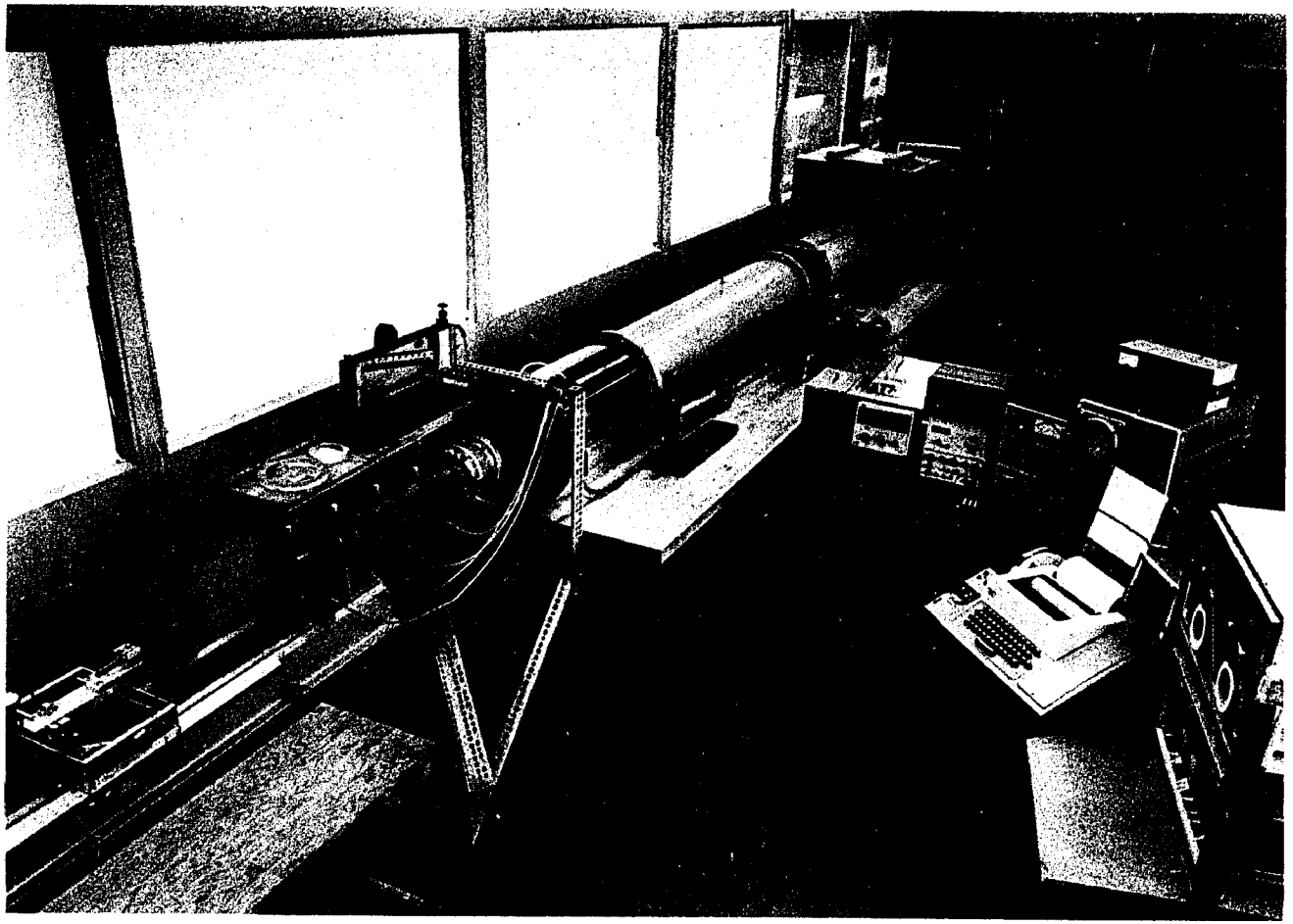

Figure 3.6 Test Equipment: Overview - Airflow circuit and Instrumentation

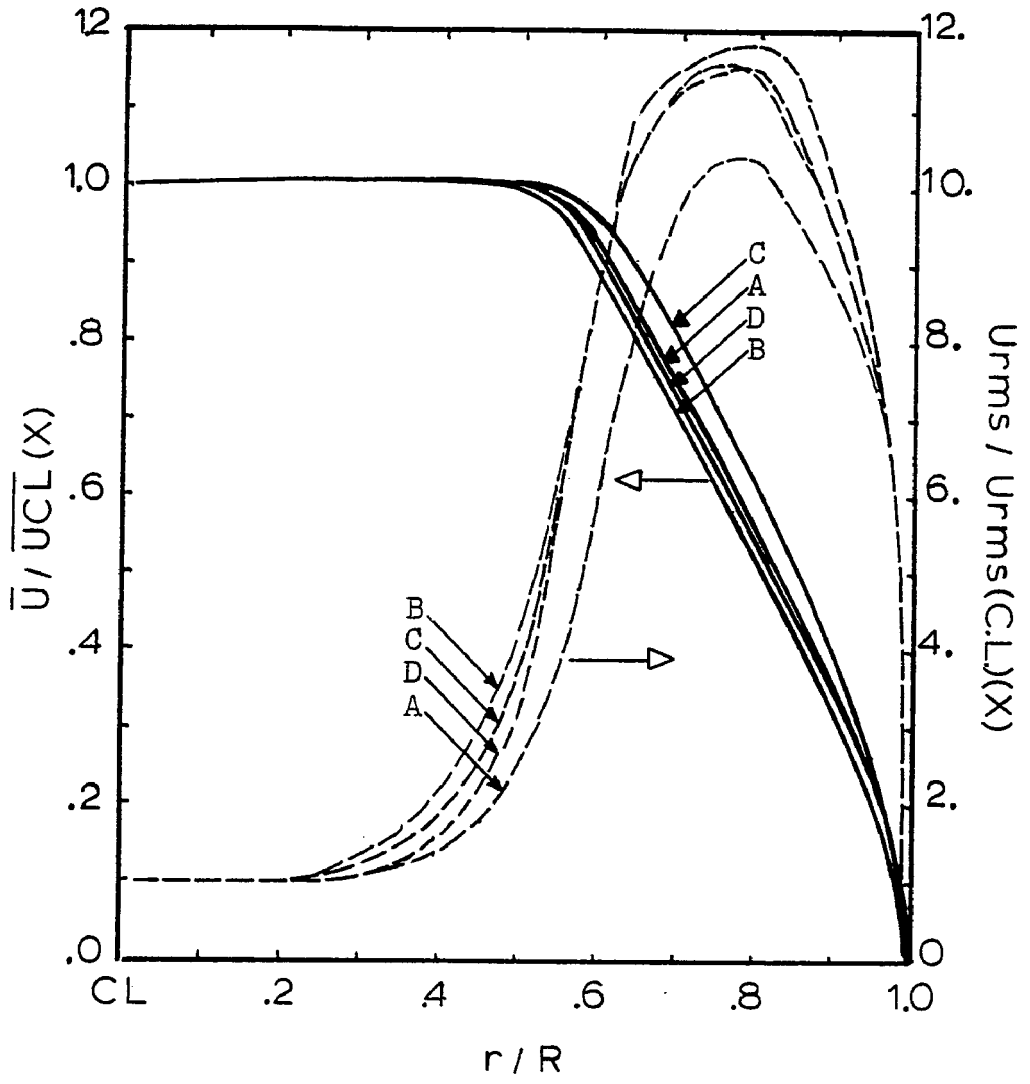

Figure 3.7 Steady flow symmetry measured at the test section exit:

XCL = 578 mm (22.75 in.)

R = 81 mm

$\overline{UCL}(X)$ = 10 m/sec

$Urms(CL)(X)/\overline{UCL}(X)$ = 1.25%

CL-to-top(A), CL-to-bottom(B), CL-to-left(C), CL-to-right(D).

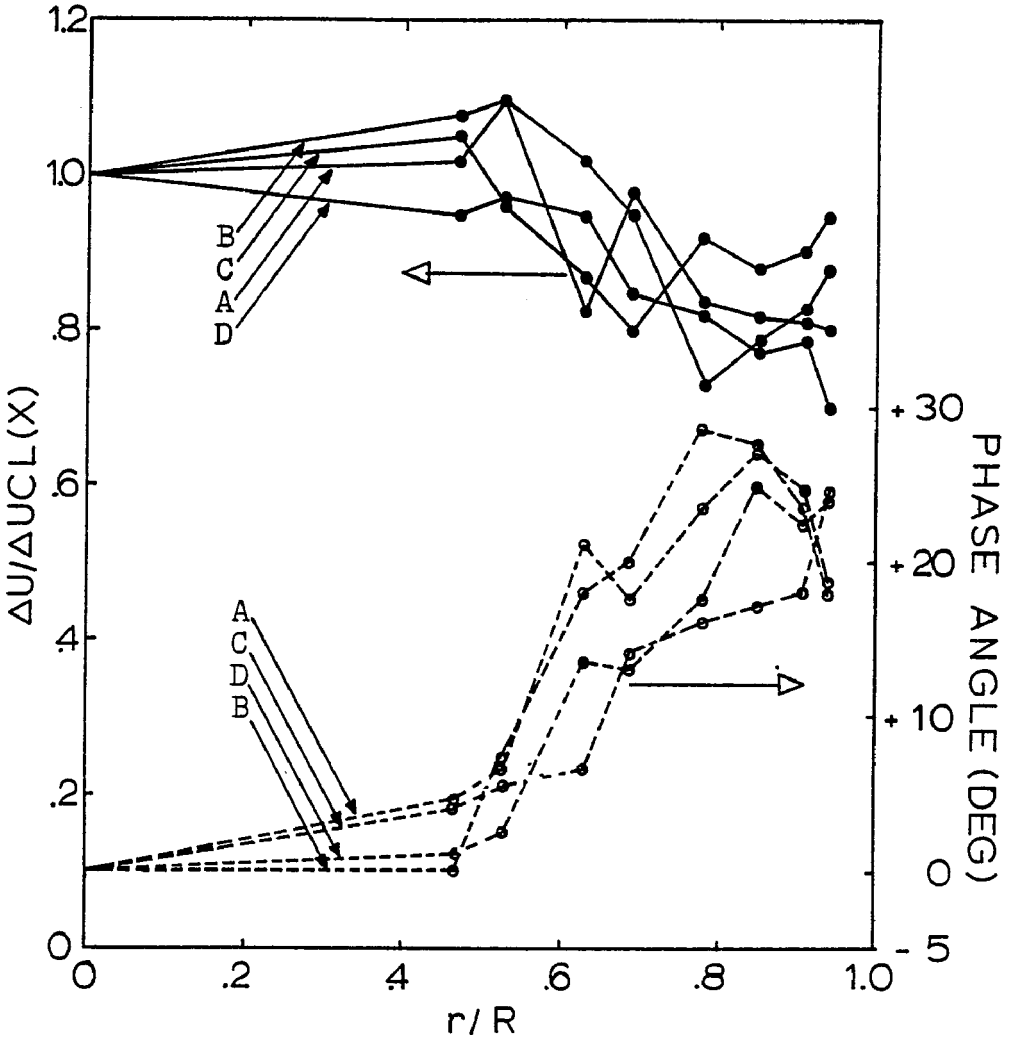

Figure 3.8 Oscillatory symmetry measured at the test section exit

XCL = 578 mm (22.75 in.)
R = 81 mm
$\overline{UCL}(X)$ = 10 m/sec
$\Delta UCL(X)/\overline{UCL}(X)$ = .028
FREQ = 20 Hz

CL-to-top(A), CL-to-bottom(B), CL-to-left(C), CL-to-right(D).

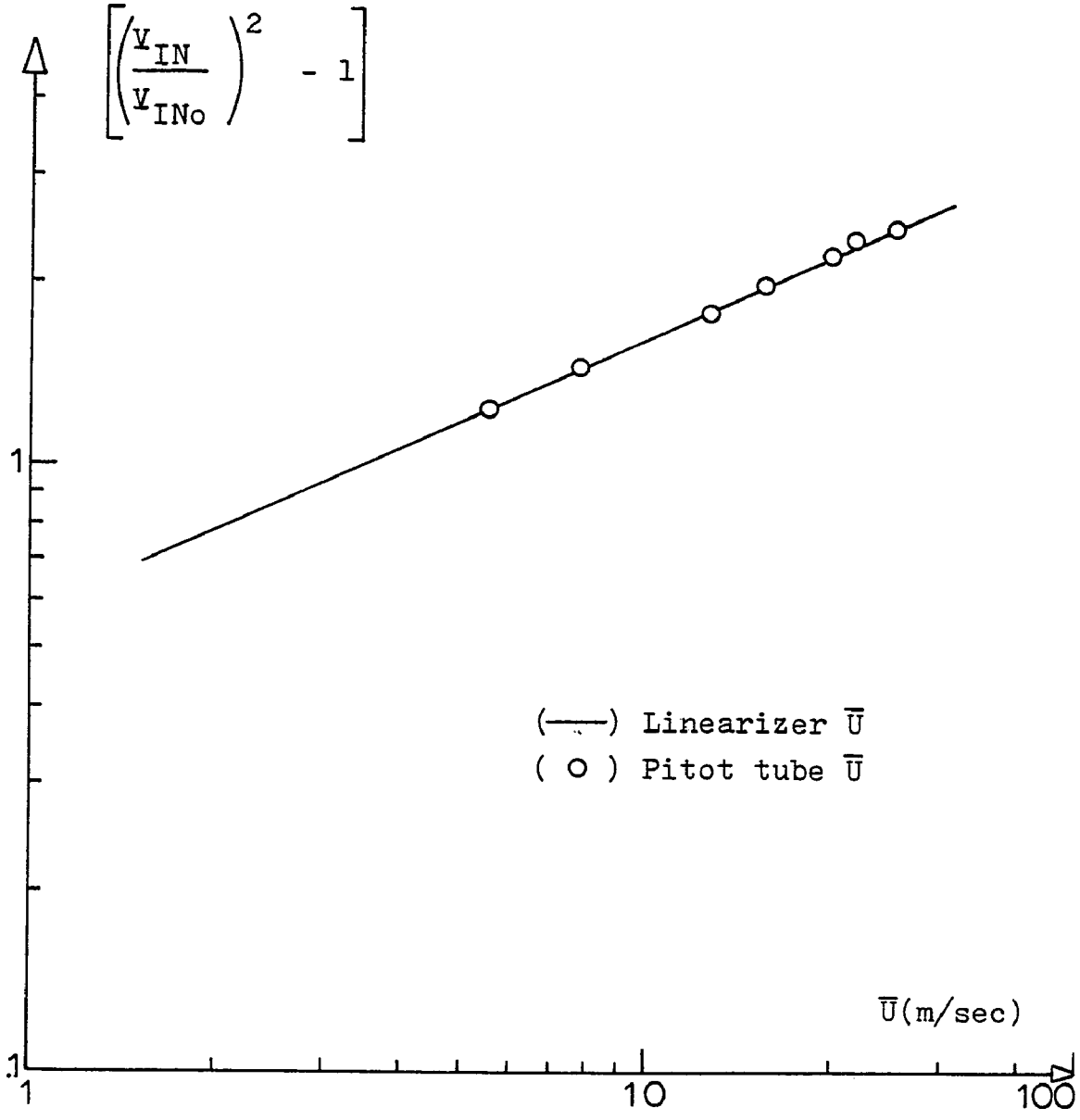

Figure 3.9 Linearizer Calibration.

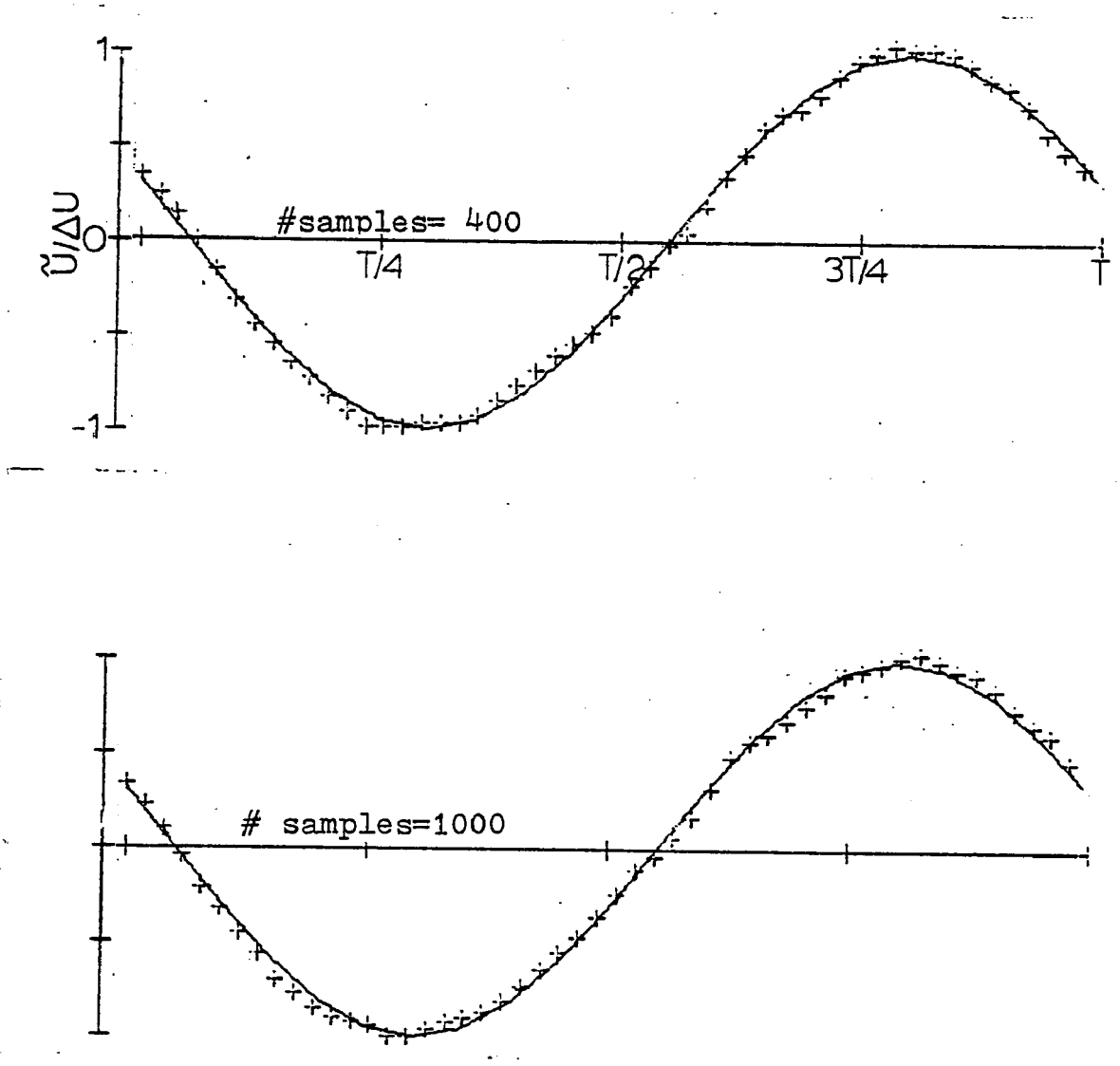

Figure 3.10 The effect of the number-of-samples-taken on the phase-averaged velocity.
DIFFUSER CENTERLINE (XCL=578 mm (22.75 in.)).
Each data point is a phase-average for that location in the cycle. The fundamental wave shape, derived by Fourier analysis from the data, is shown drawn through the points.

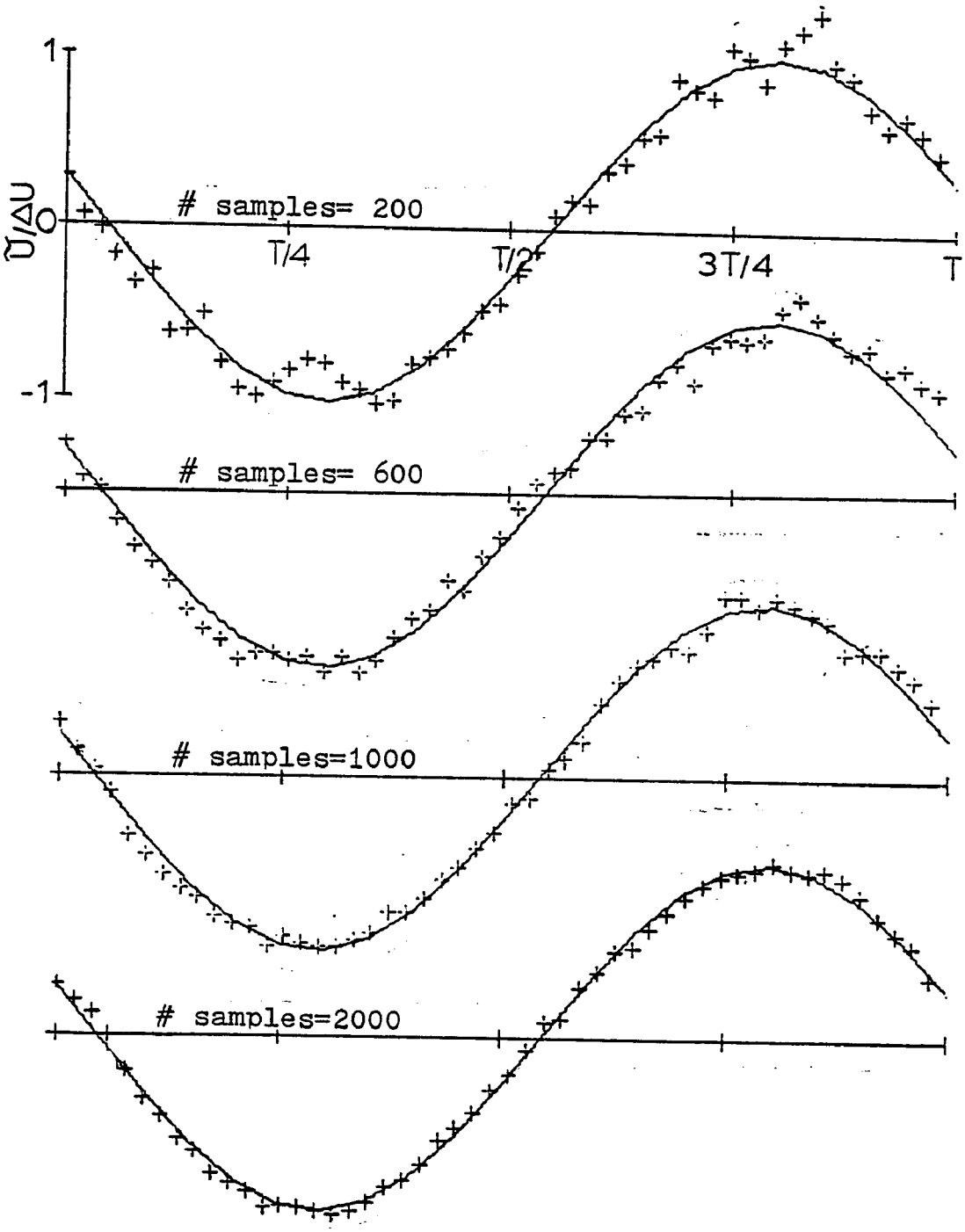

Figure 3.11 The effect of the number-of-samples-taken on the phase-averaged velocity.
OUTER EDGE OF THE BOUNDARY LAYER (XCL=578 mm, y/δ=0.91).
Each data point is a phase-average for that location in the cycle. The fundamental wave shape, derived by Fourier analysis from the data, is shown drawn through the points.

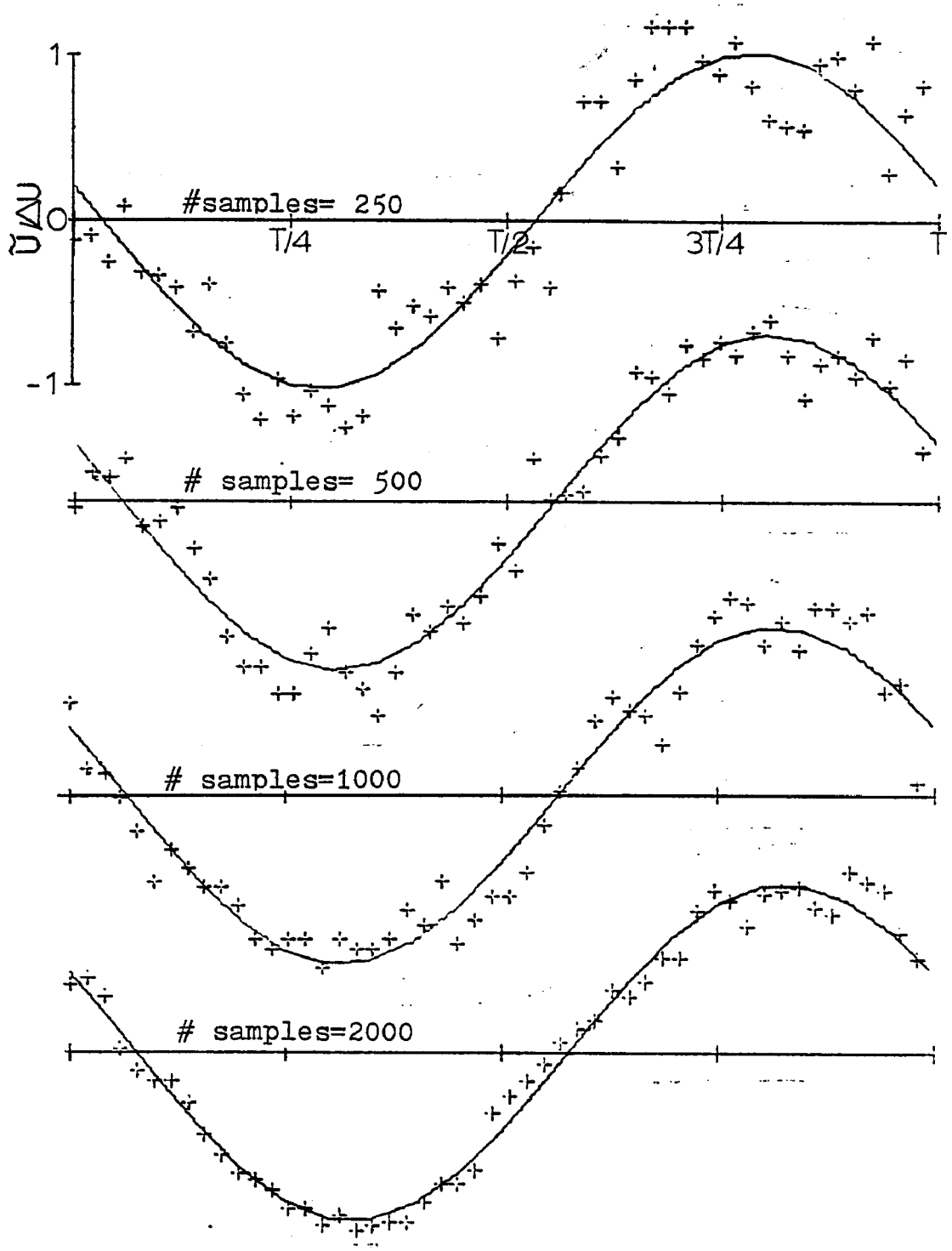

Figure 3.12 The effect of the number-of-samples-taken on the phase-averaged velocity
MID-BOUNDARY LAYER (XCL=578 mm, $U/\sqrt{\delta}$=0.48)
Each data point is a phase-average for that location in the cycle. The fundamental wave shape, derived by Fourier analysis from the data, is shown drawn through the points.

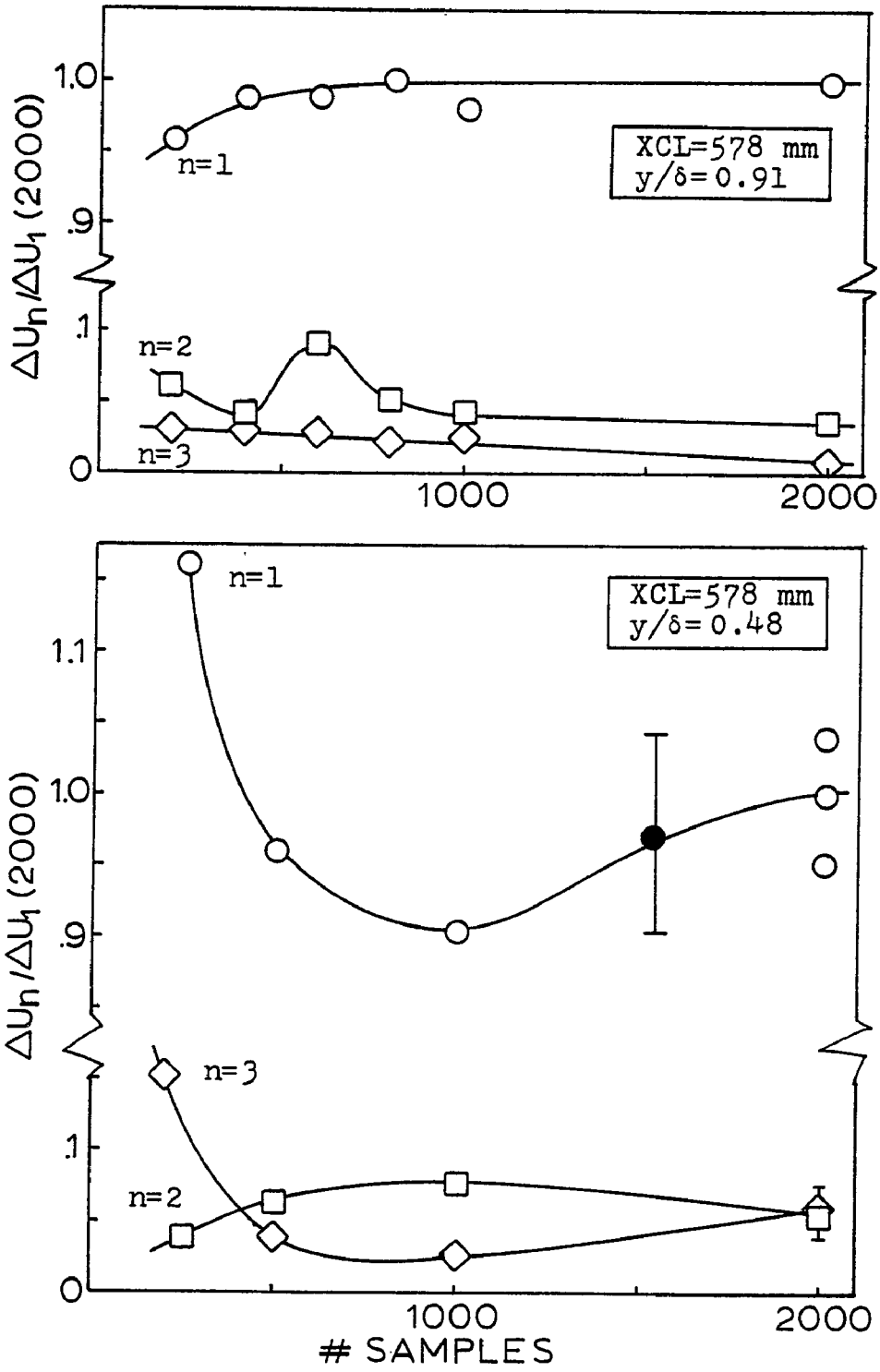

Figure 3.13 Effect of the number-of-samples taken on the phase-average amplitudes. FREQ=20 Hz.

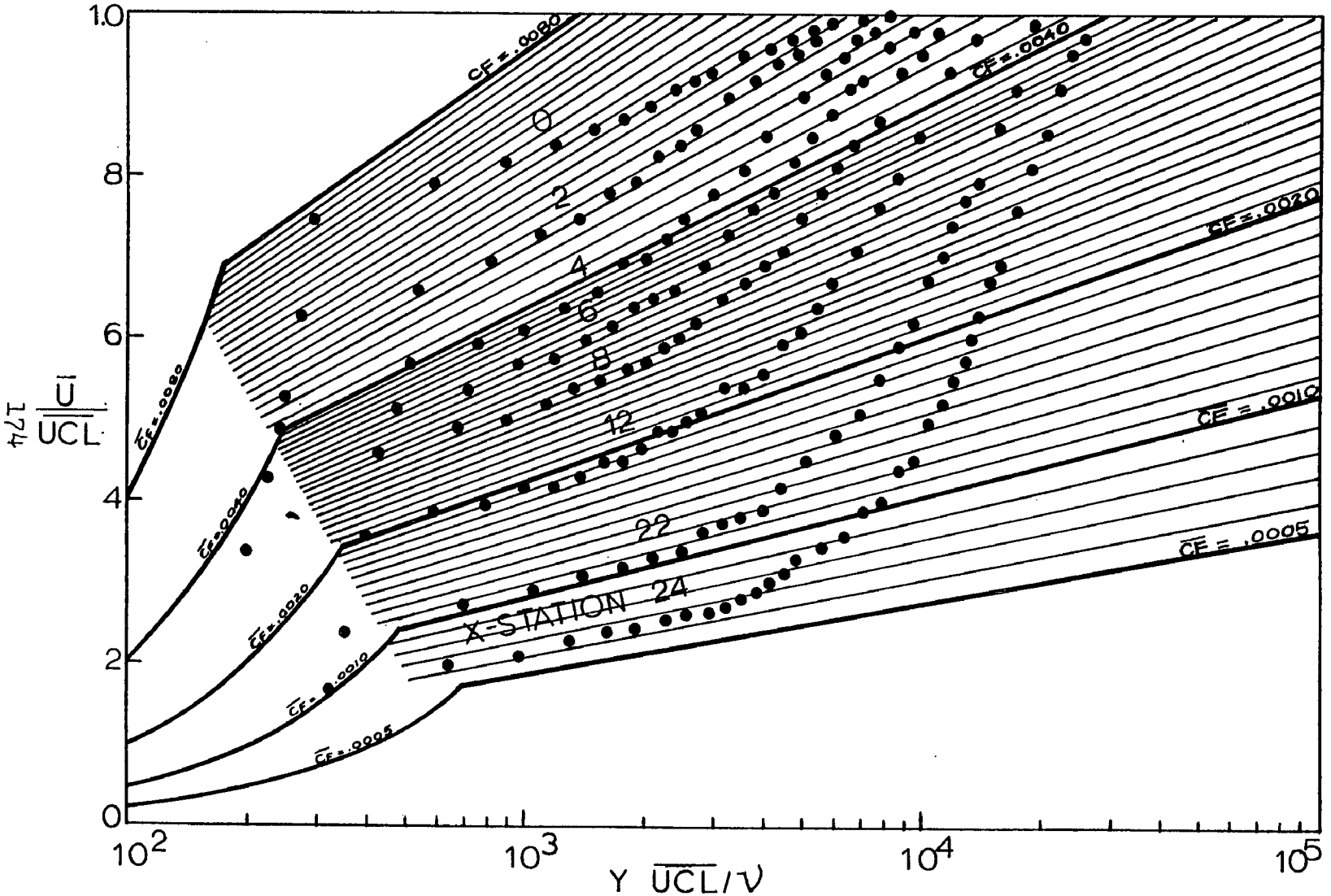

Figure 3.14 Law-of-the-Wall solution for the time-average skin friction coefficient, $\overline{C_F}$.

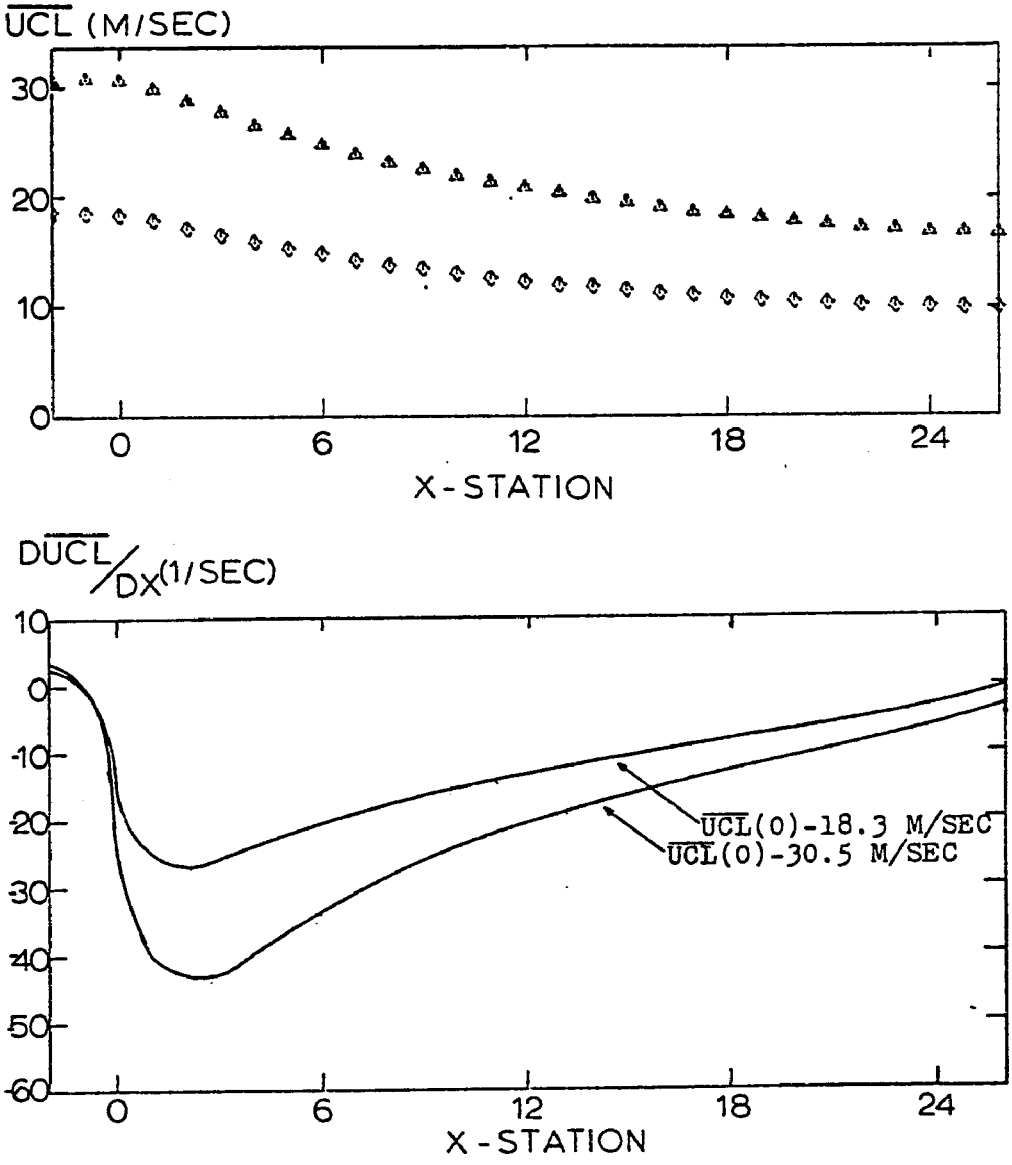

Figure 4.1 Centerline, steady flow velocity and velocity gradient.

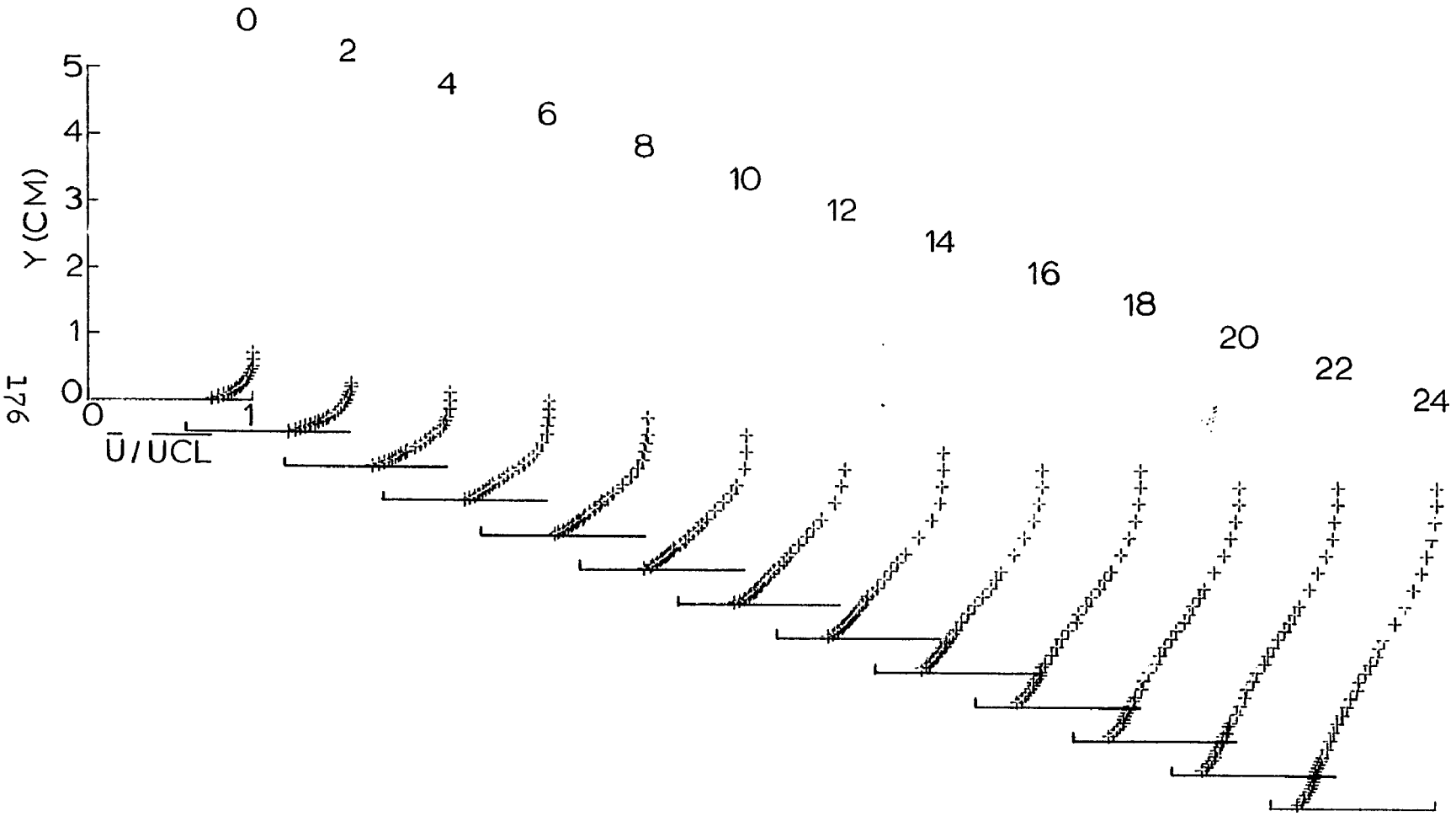

Figure 4.2 Steady Flow boundary layer velocity profiles. $\overline{UCL}(0)$ = 18.29 M/SEC

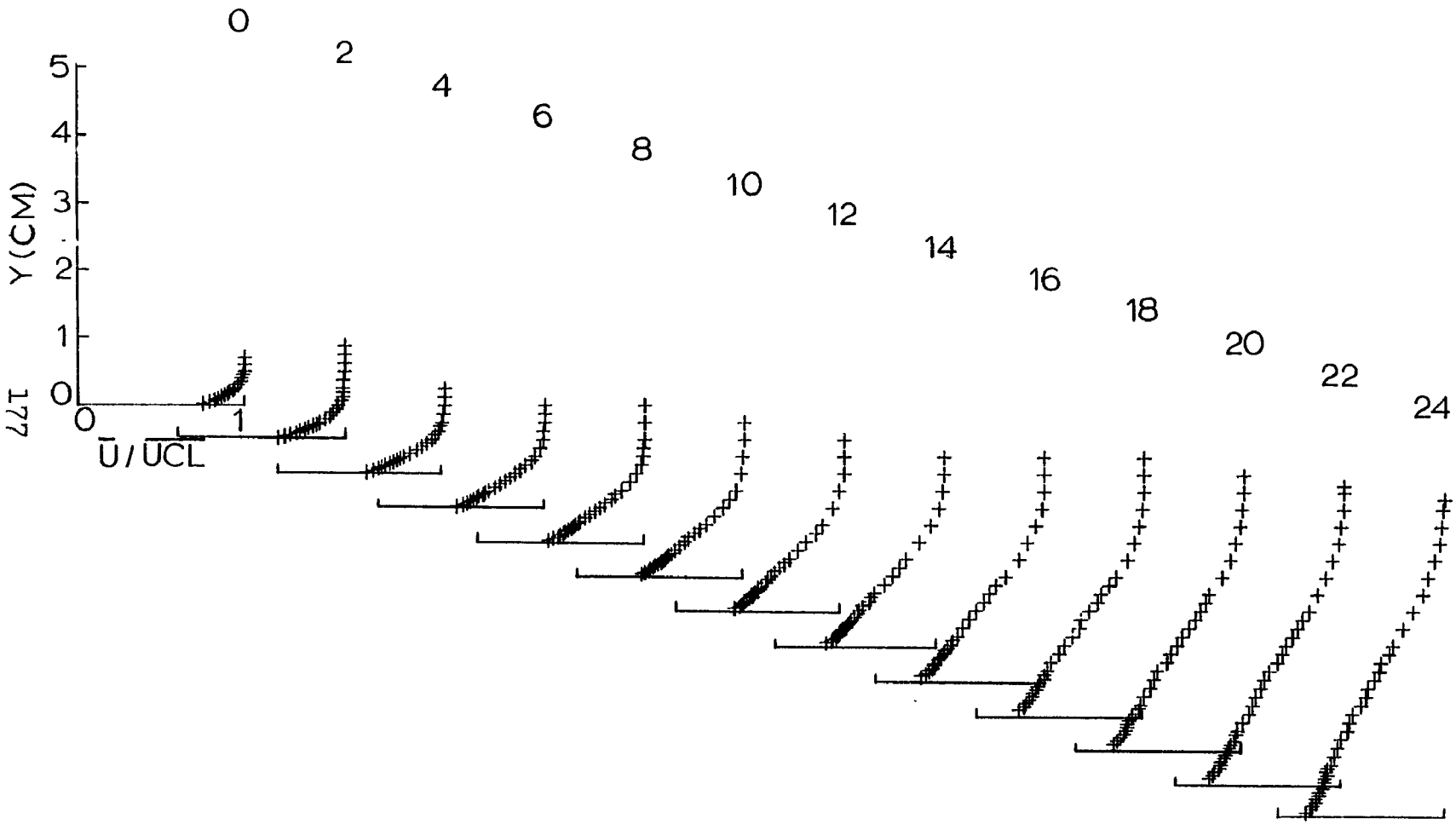

Figure 4.3 Steady Flow boundary layer velocity profiles. $\overline{UCL}(0)$ = 30.48 M/SEC

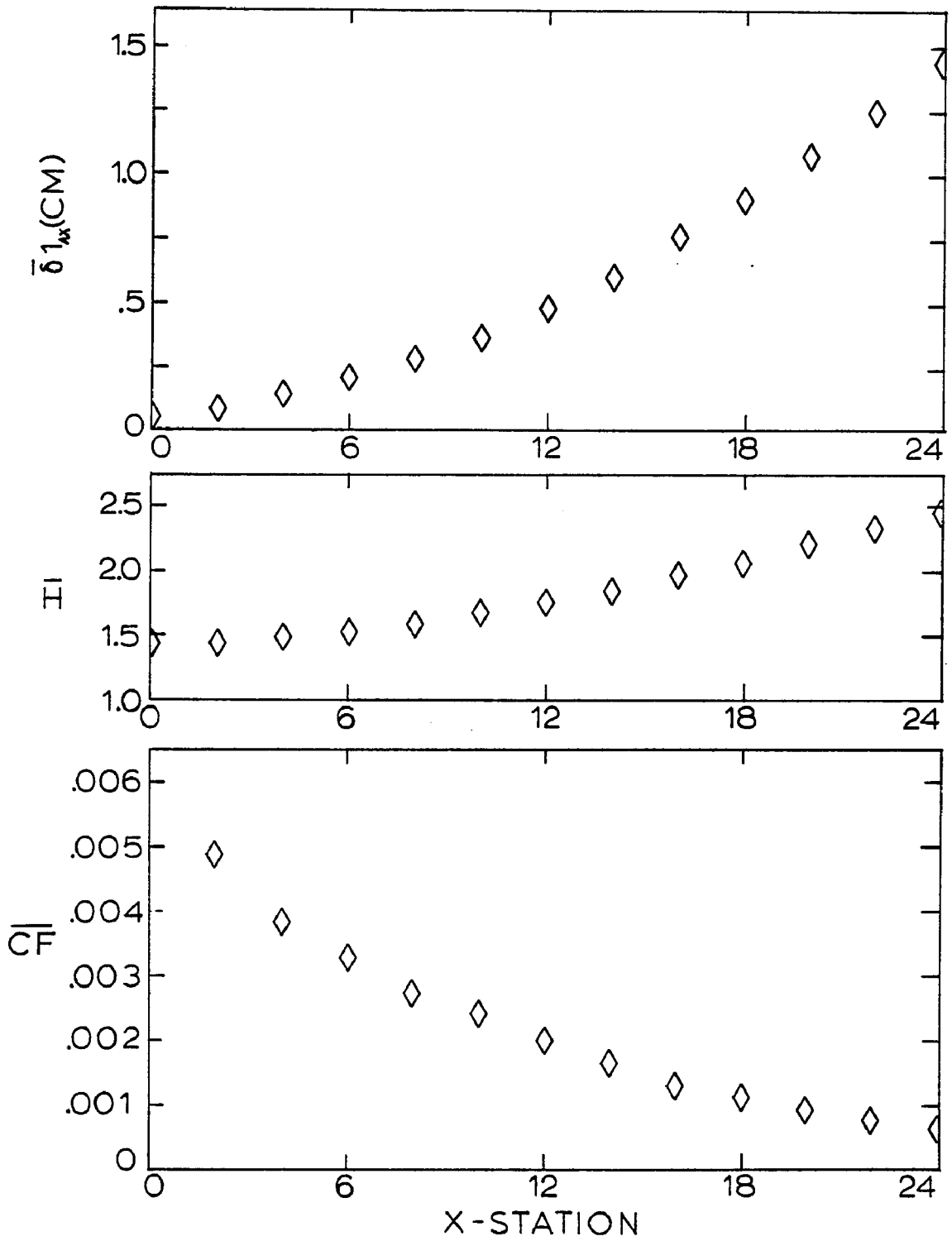

Figure 4.4 Steady flow boundary layer parameters.
DS-2/Run 1: Re_D=116667, $\overline{UCL}$(0)=18.29 m/sec.

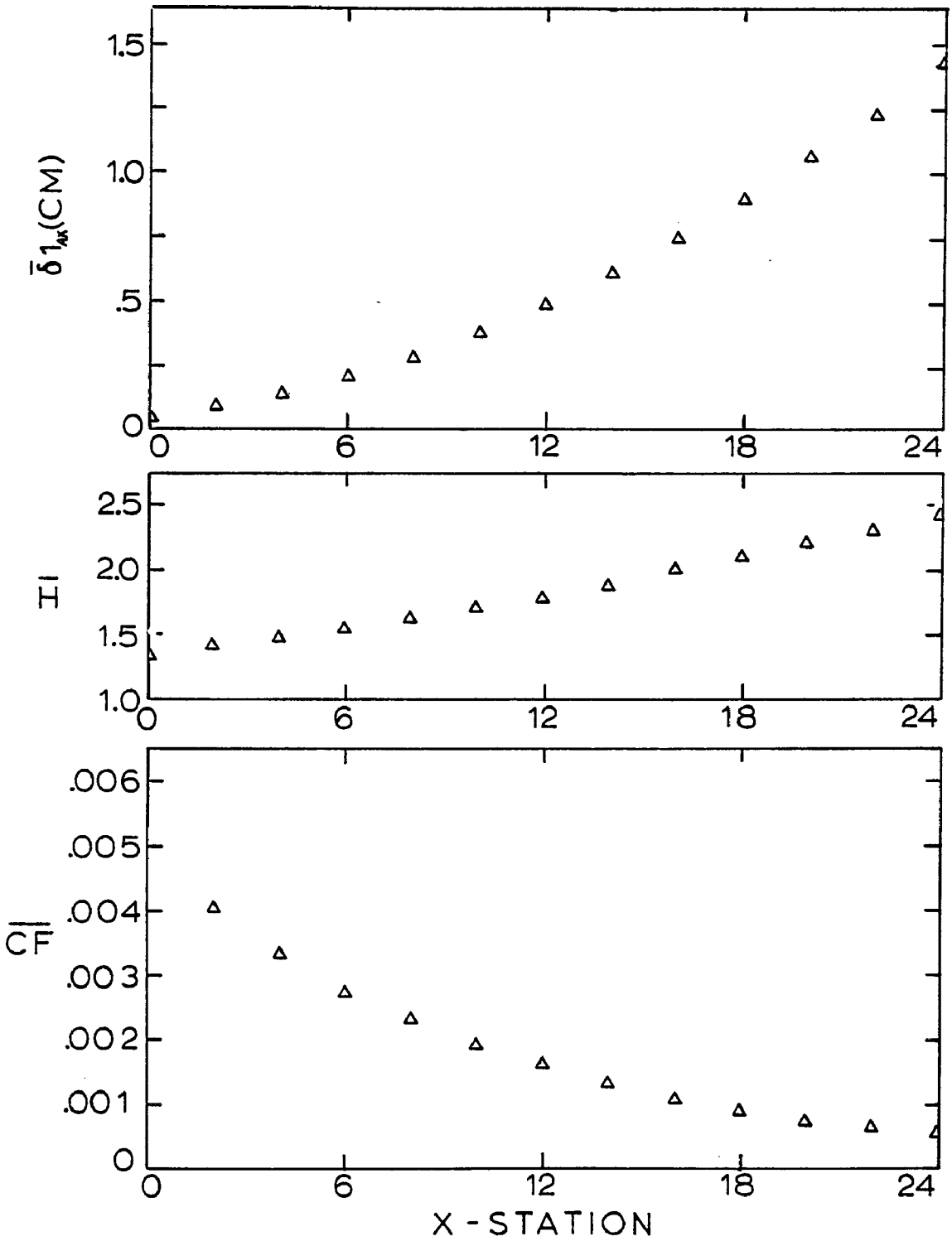

Figure 4.5 Steady flow boundary layer parameters.
DS-2/Run 2: Re_D=194931, $\overline{UCL}(0)$=30.48 m/sec.

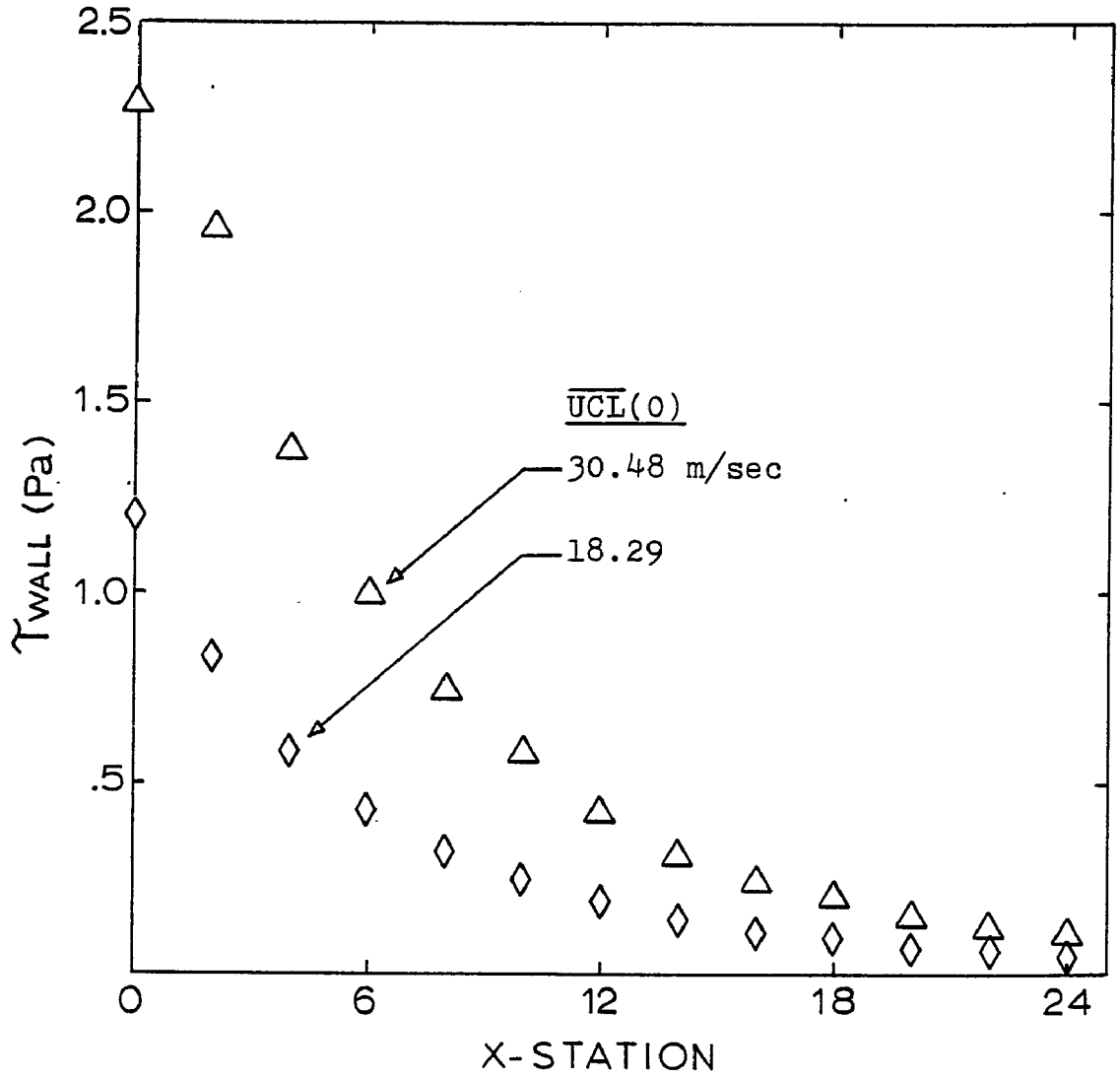

Figure 4.6 Steady flow wall shear stress.

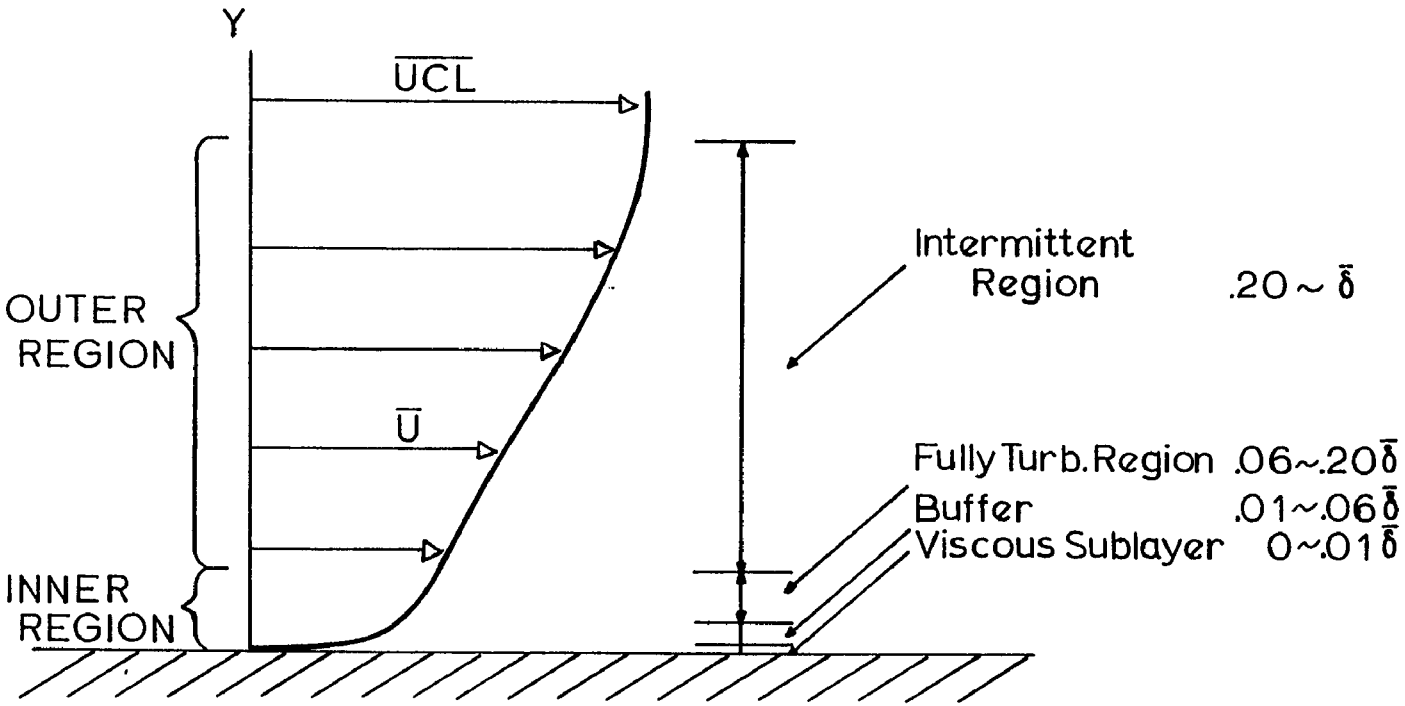

Figure 4.7 Boundary layer schematic.

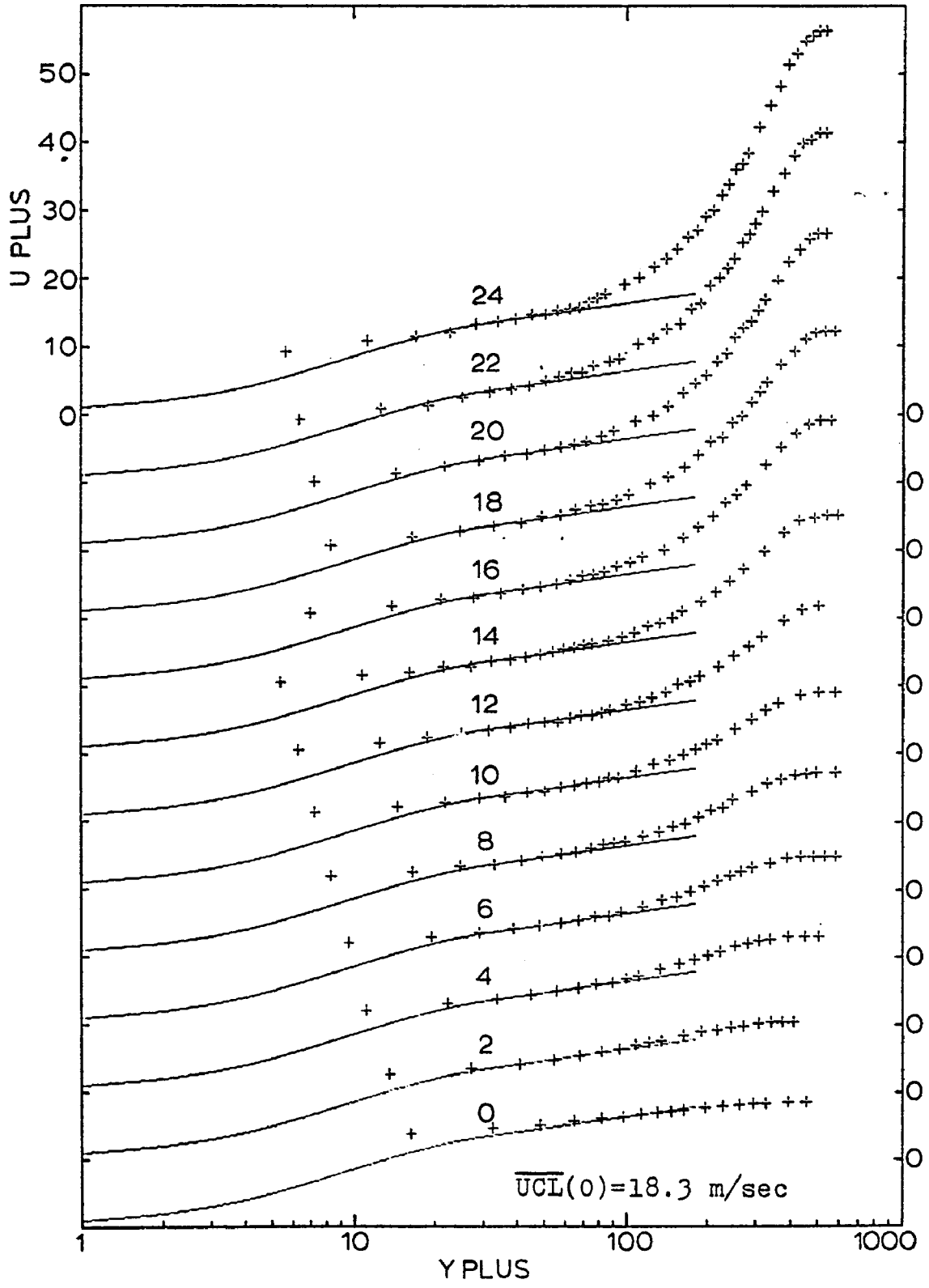

Figure 4.8 Steady flow Law-of-the-Wall profiles

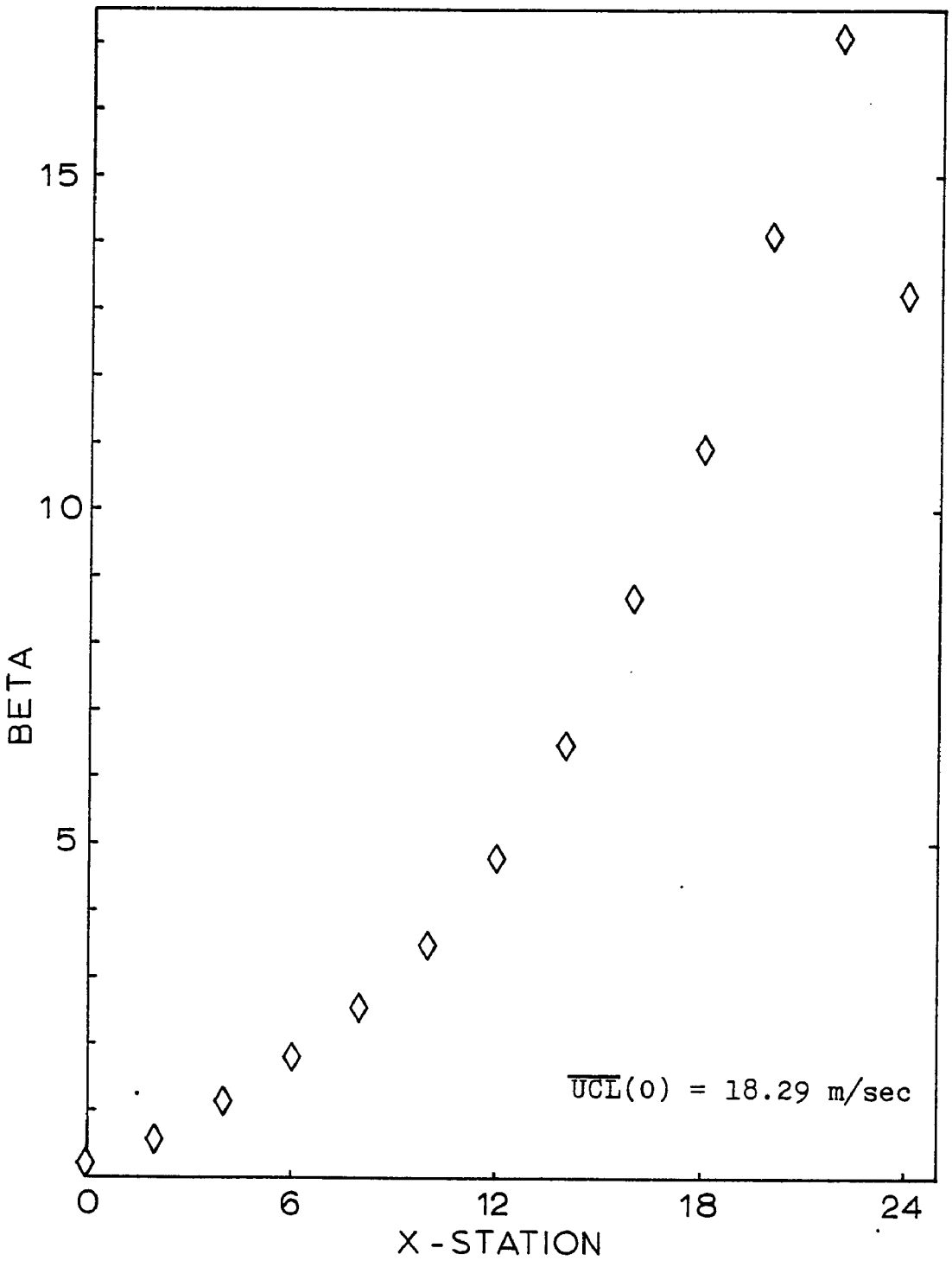

Figure 4.9 Steady flow equilibrium pressure gradient parameter.
BETA = $(\bar{\delta}1/\tau_w)(d\bar{P}/dx)$.

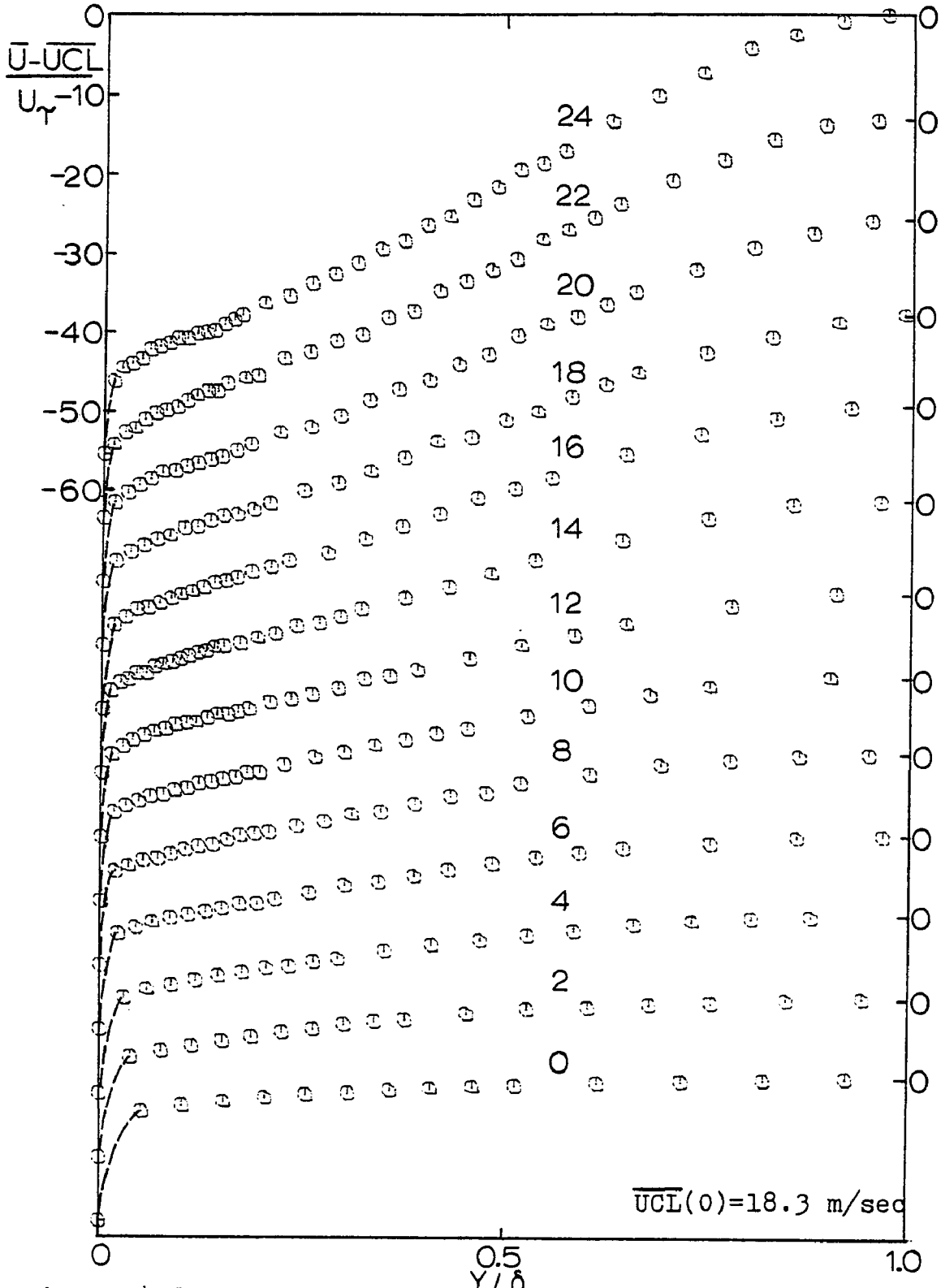

Figure 4.10 Steady flow velocity defect profiles.

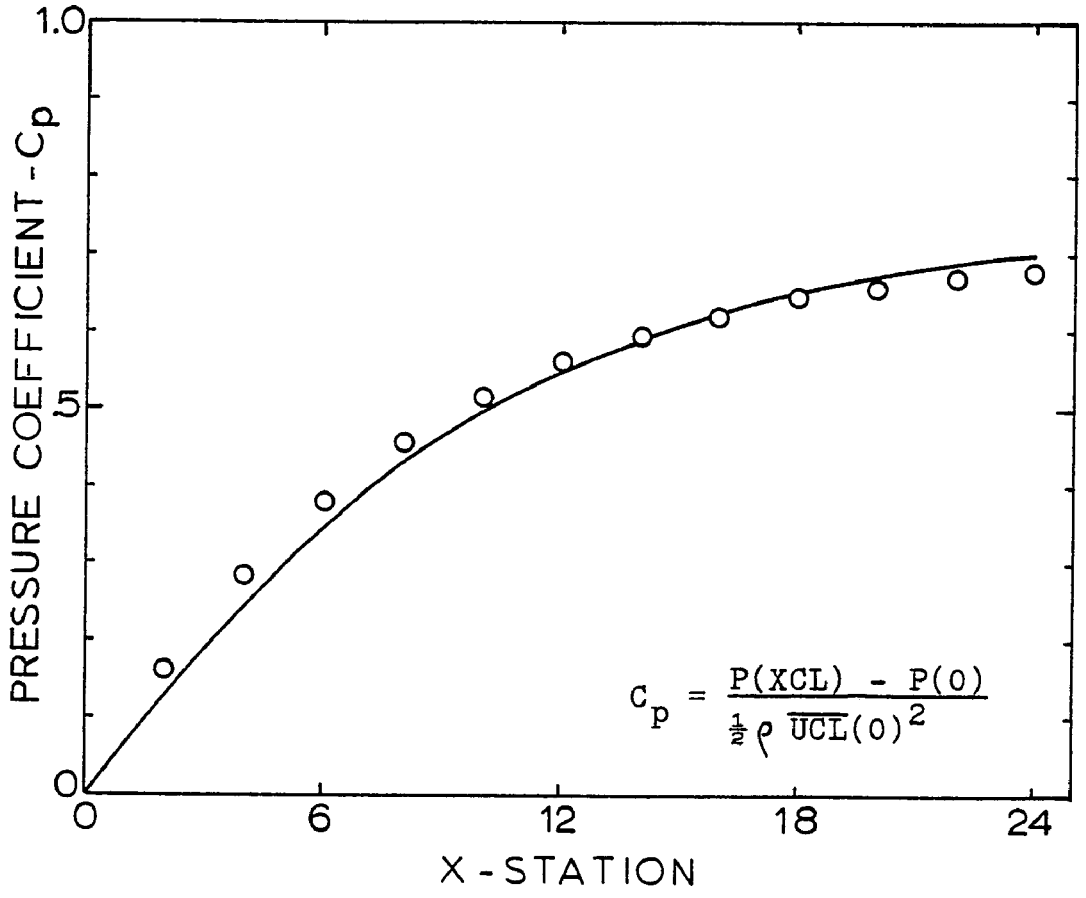

Figure 4.11 Diffuser pressure recovery.
Calculated from $\overline{UCL}$ data (——),
Calculated from $\overline{\delta}l_{AX}$ data (o).

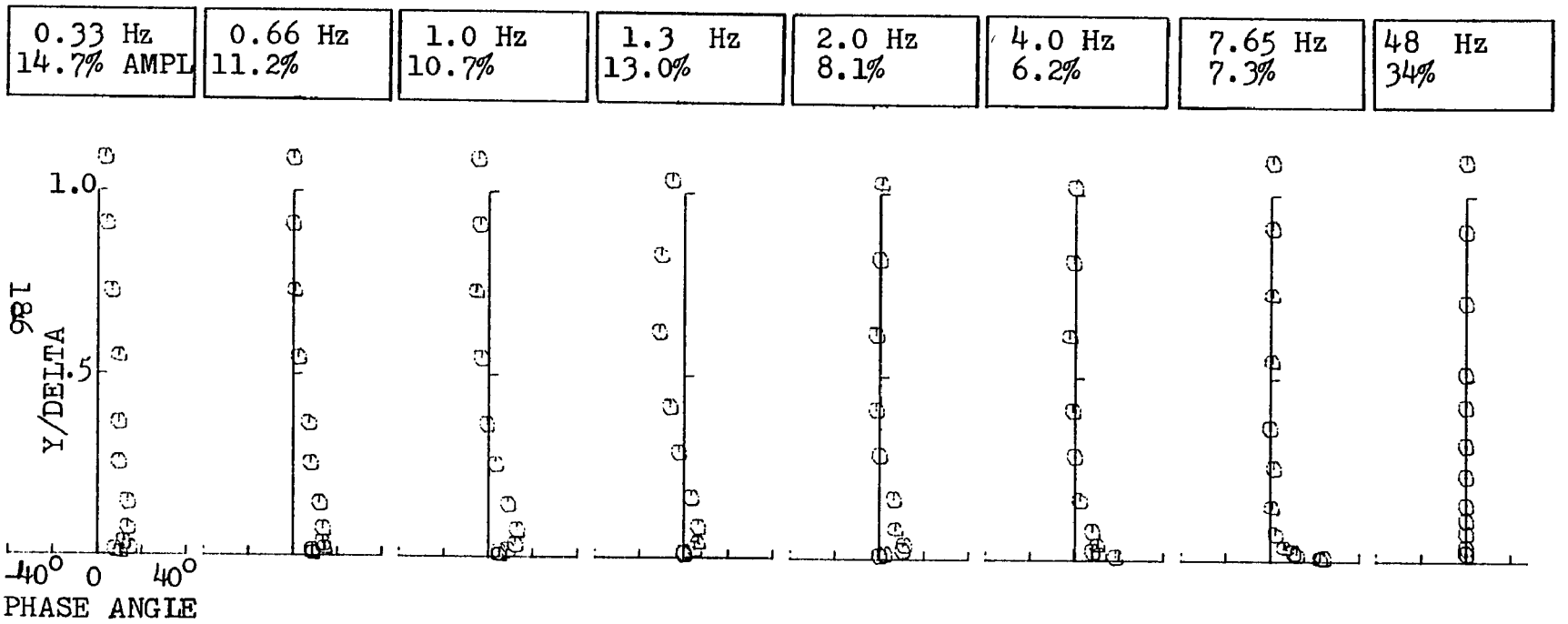

Figure 4.12 Karlsson data (1958): Amplitude Ratio
Boundary layer frequency response data
shown relative to the local free stream velocity oscillation.
$\overline{UE}$ = 5.33 m/sec (17.5 ft/sec), $\overline{\delta} \approx$ 76.0 mm (3.0 in.), AMPL=$\Delta UE/\overline{UE}$.

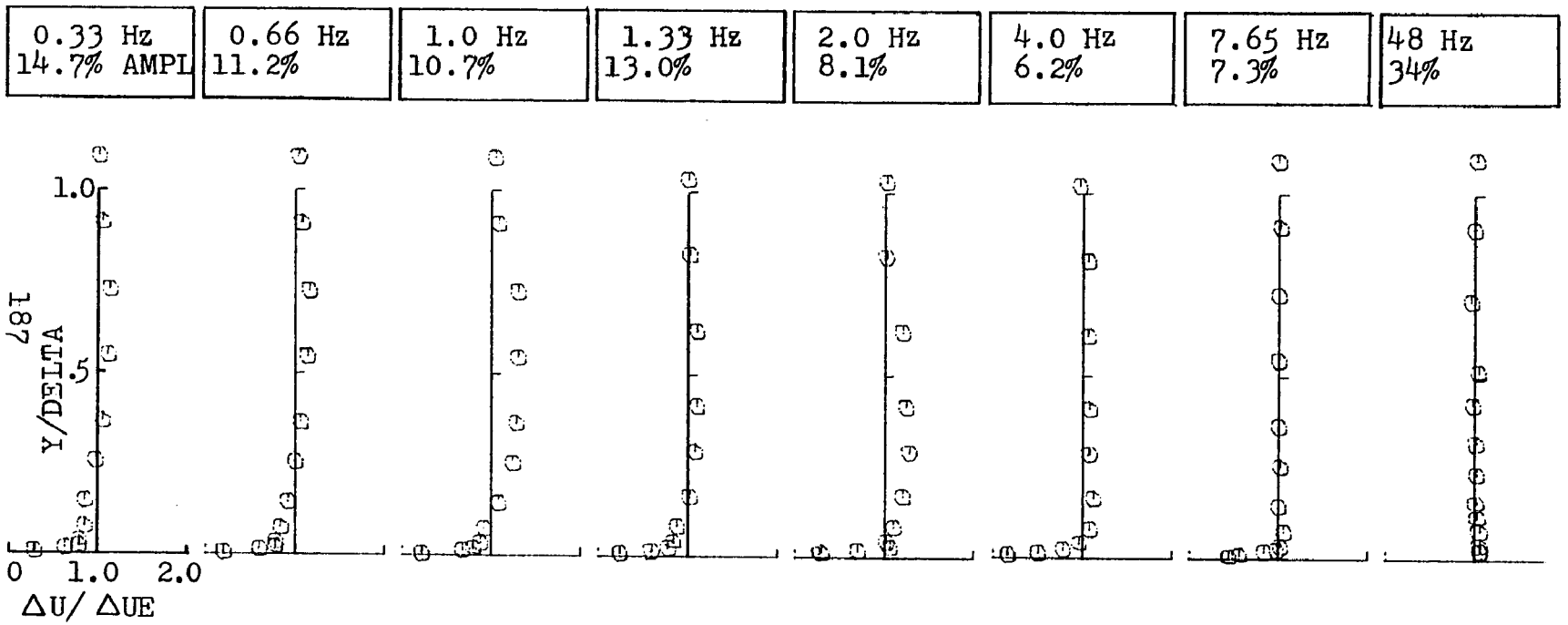

Figure 4.13 Karlsson data (1958): Phase Difference
Boundary layer frequency response data
shown relative to the local free stream velocity oscillation.
$\overline{UE}$ = 5.33 m/sec (17.5 ft/sec), $\bar{\delta} \approx$ 76.0 mm (3.0 in.), AMPL=$\Delta UE/\overline{UE}$.

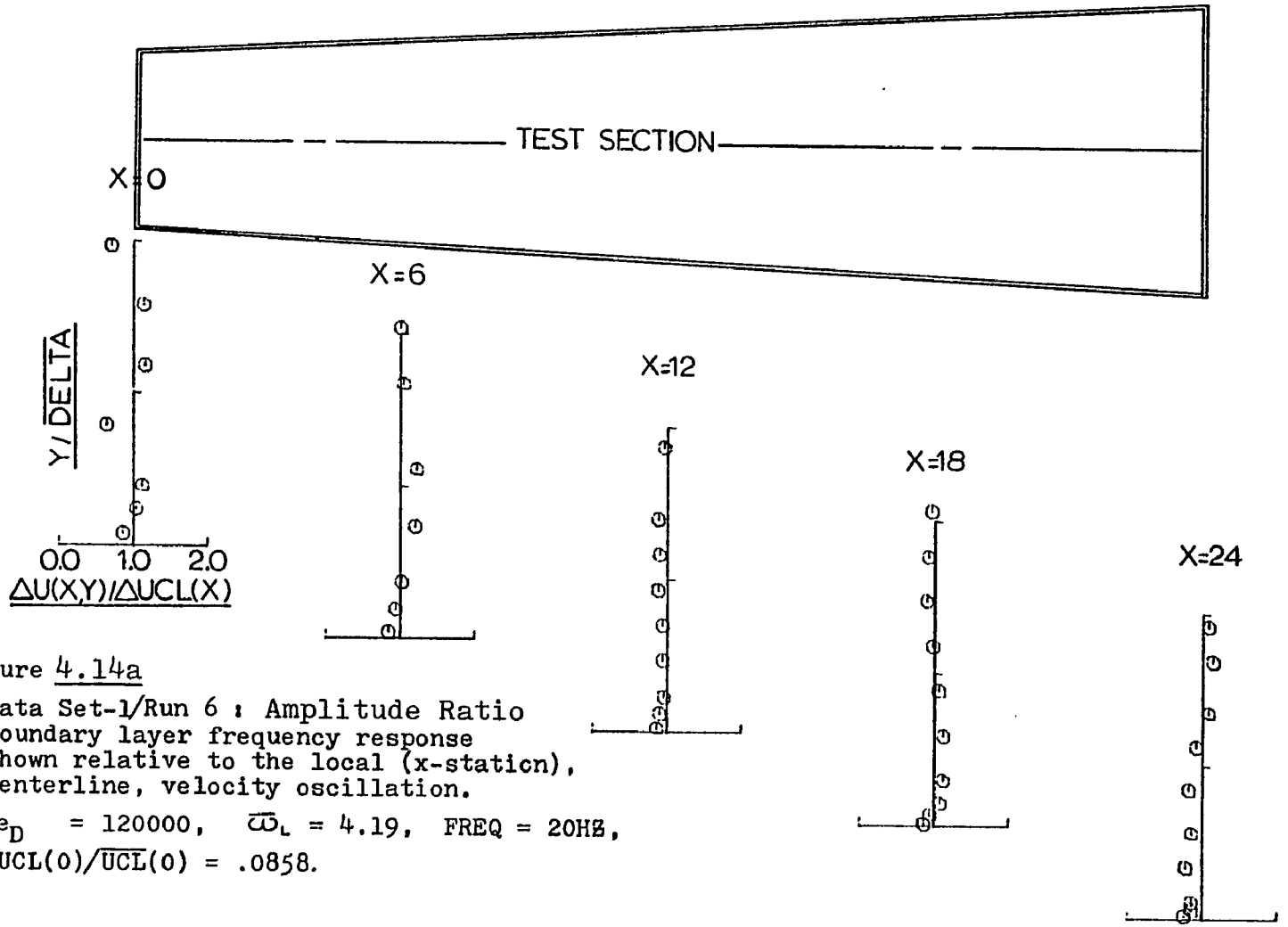

Figure 4.14a

Data Set-1/Run 6 : Amplitude Ratio
Boundary layer frequency response
shown relative to the local (x-station),
centerline, velocity oscillation.

Re_D = 120000, $\overline{\omega}_L$ = 4.19, FREQ = 20HZ,
$\Delta UCL(0)/\overline{UCL}(0)$ = .0858.

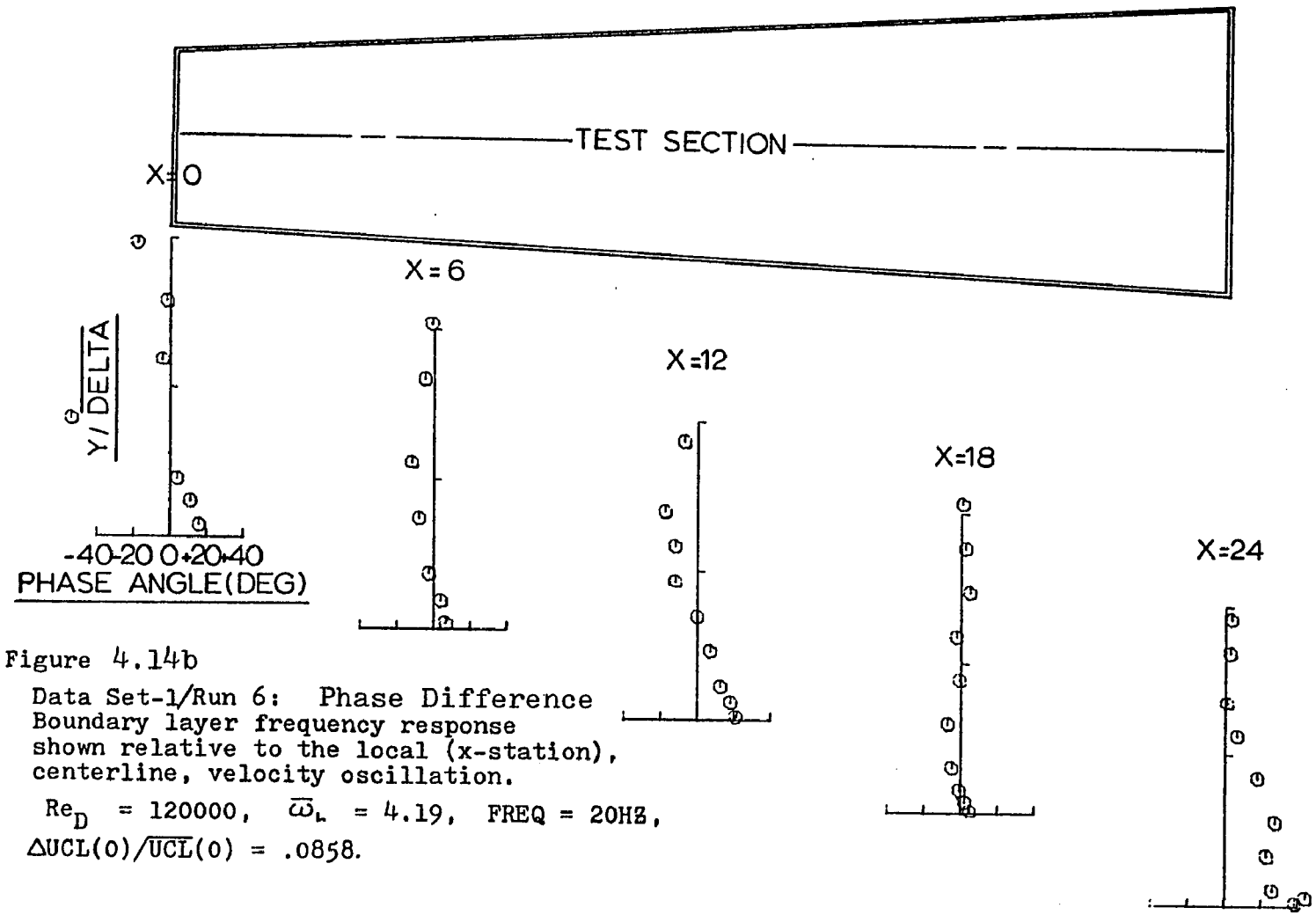

Figure 4.14b

Data Set-1/Run 6: Phase Difference
Boundary layer frequency response
shown relative to the local (x-station),
centerline, velocity oscillation.

Re_D = 120000, $\bar{\omega}_L$ = 4.19, FREQ = 20HZ,
$\Delta UCL(0)/\overline{UCL}(0)$ = .0858.

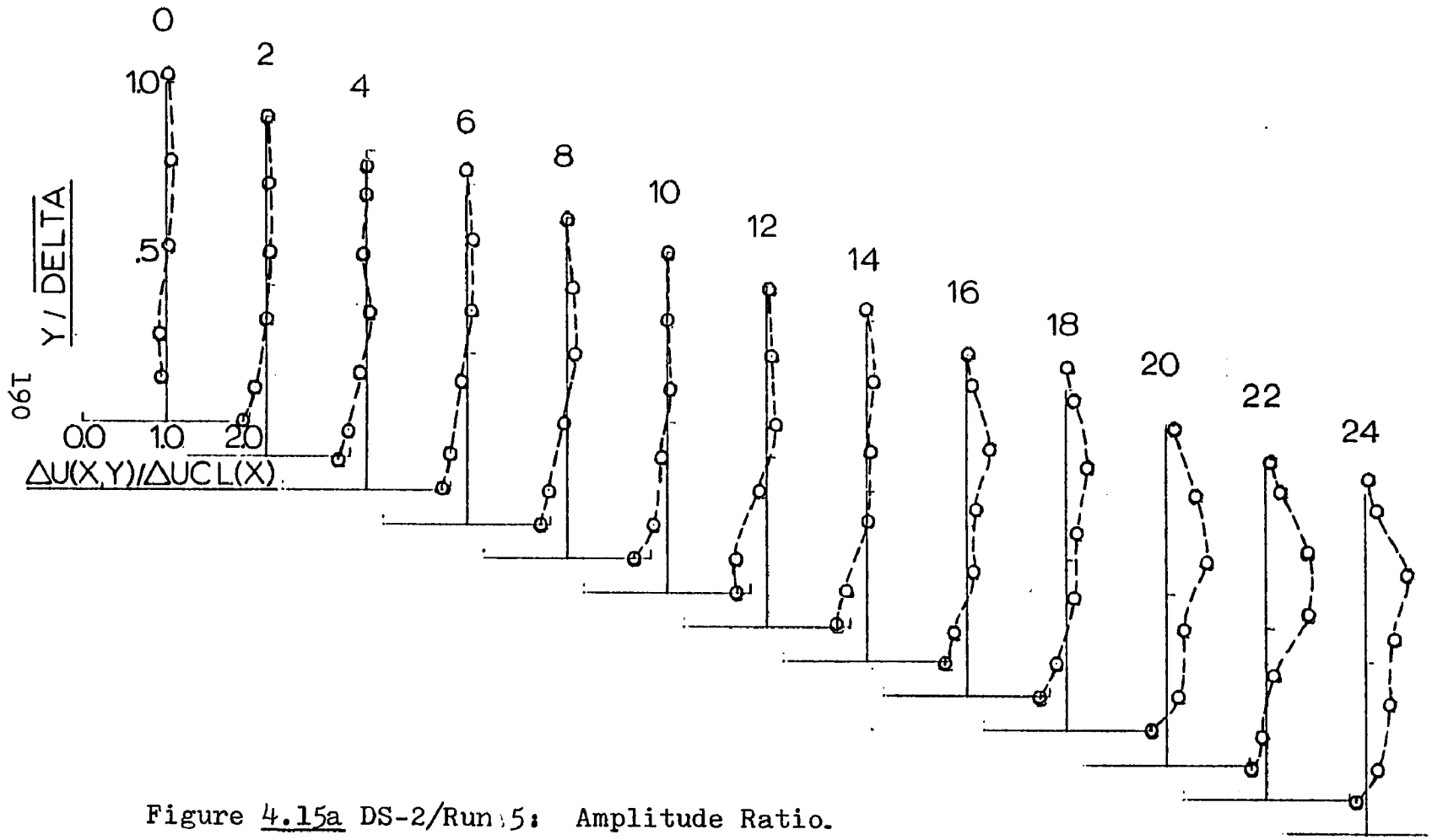

Figure 4.15a DS-2/Run 5: Amplitude Ratio.
Boundary layer frequency response shown relative to the local (x-station), centerline, velocity oscillation.
Re_D =117401, $\bar{\omega}$ =1.05, FREQ= 5HZ, $\Delta UCL(0)/\overline{UCL}(0)$= .0469

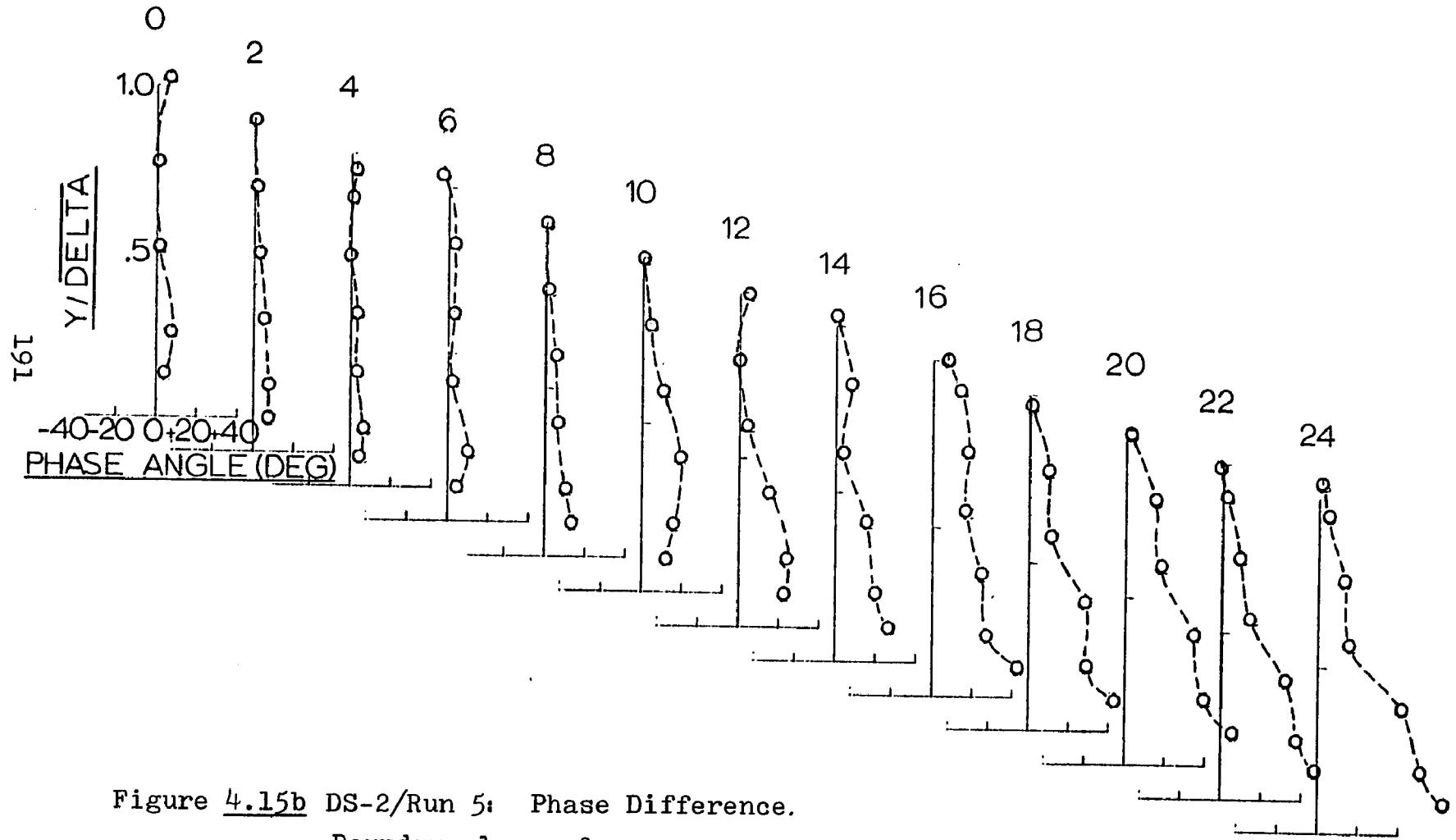

Figure 4.15b DS-2/Run 5: Phase Difference.
Boundary layer frequency response shown relative to the local (x-station), centerline, velocity oscillation.
Re_D =117401, $\overline{\omega}_L$ =1.05, FREQ= 5HZ, $\Delta UCL(0)/\overline{UCL}(0)$= .0469

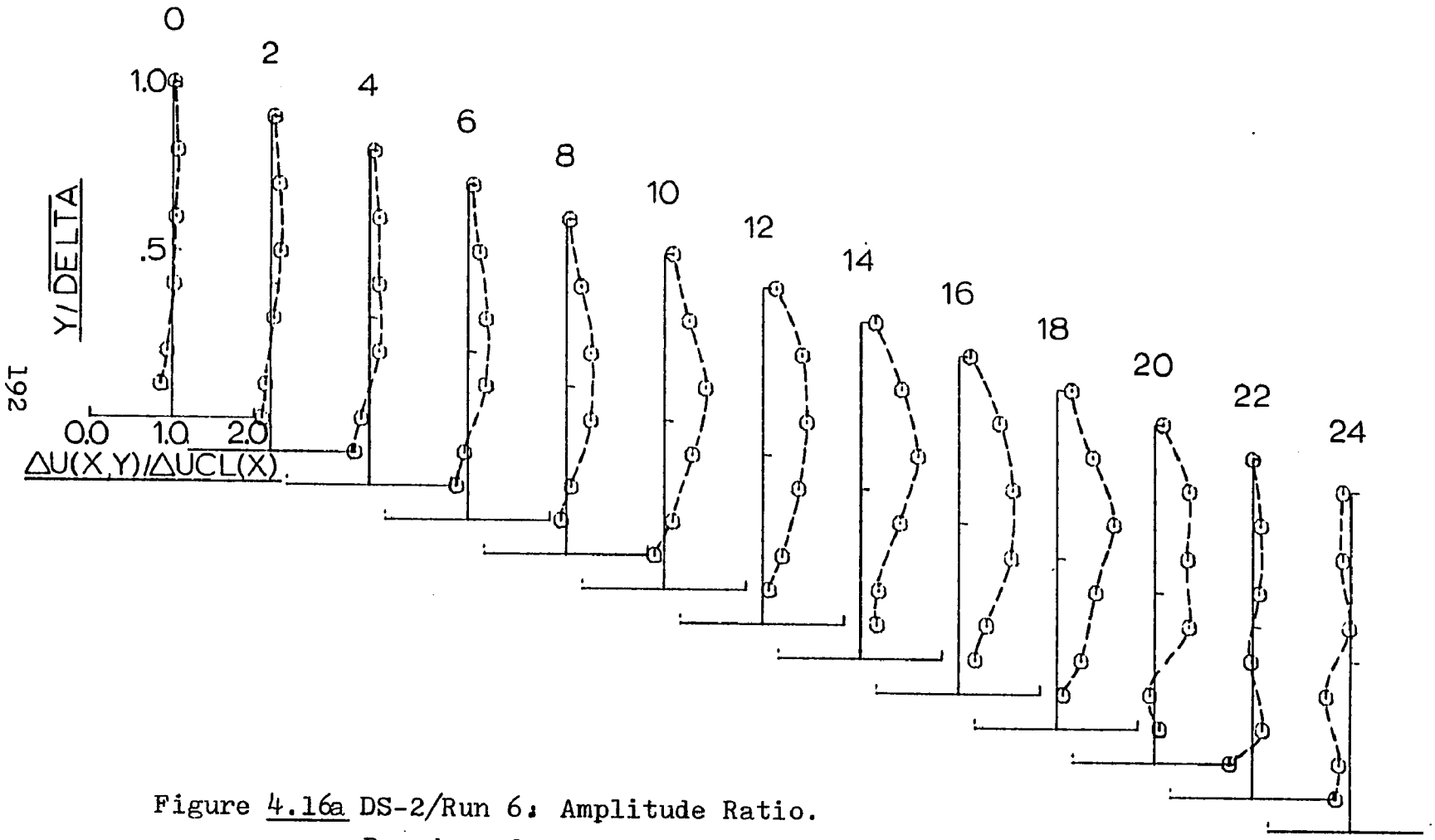

Figure 4.16a DS-2/Run 6: Amplitude Ratio.
Boundary layer frequency response shown relative to the local (x-station), centerline, velocity oscillation.
Re_D =116320, $\bar{\omega}_L$ =2.09, FREQ= 10 Hz, $\Delta UCL(0)/\overline{UCL}(0)$ = .0568

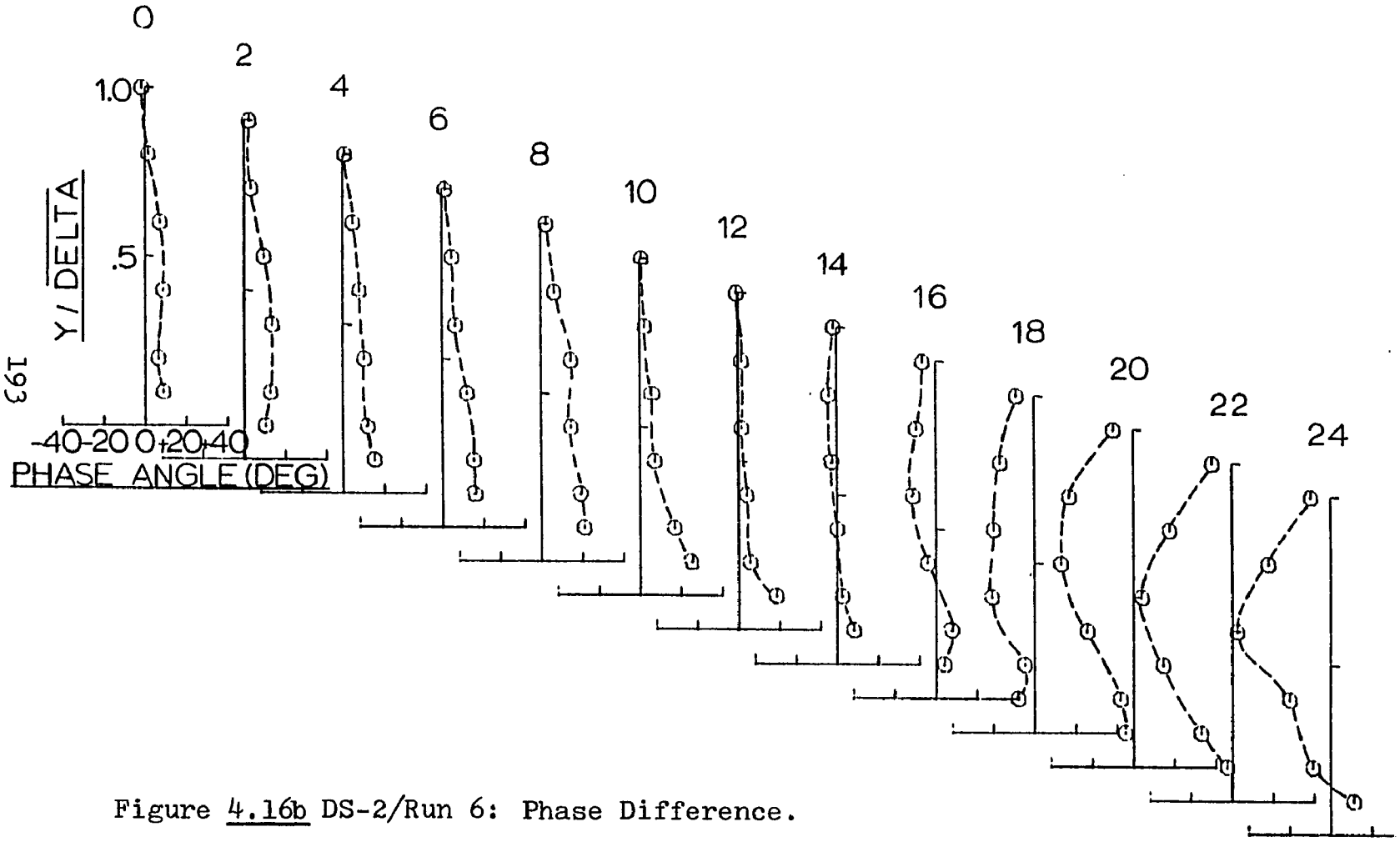

Figure 4.16b DS-2/Run 6: Phase Difference.
Boundary layer frequency response shown relative to the local (x-station), centerline, velocity oscillation.
Re_D = 116320, $\overline{\omega}_L$ = 2.09, FREQ= 10 HZ, $\Delta UCL(0)/\overline{UCL}(0)$ = .0568

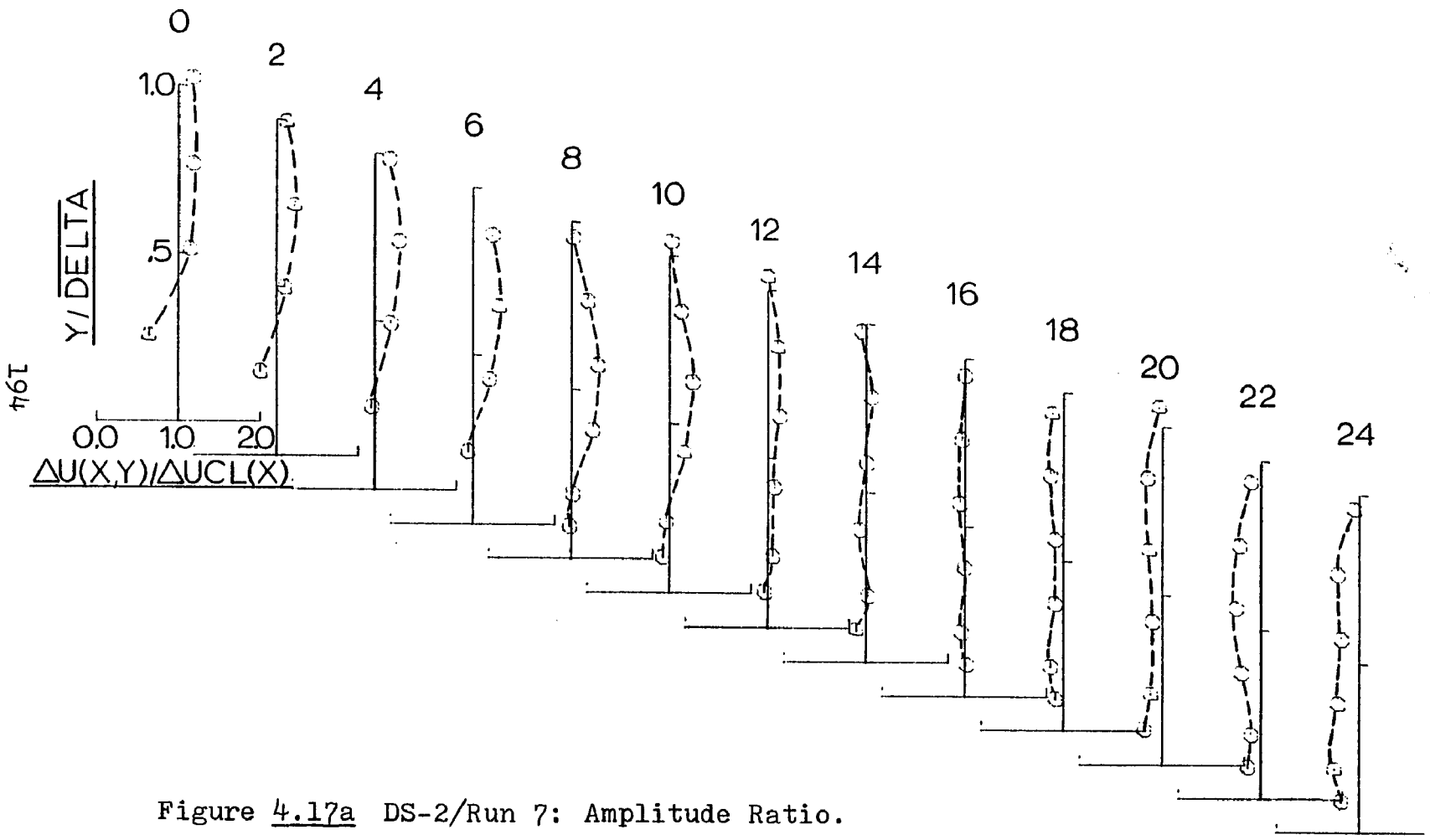

Figure 4.17a DS-2/Run 7: Amplitude Ratio.
Boundary layer frequency response shown relative to the local (x-station), centerline, velocity oscillation.
Re_D =115087, ϖ_L =3.14, FREQ =15HZ, $\Delta UCL(0)/\overline{UCL}(0)$ =.0590

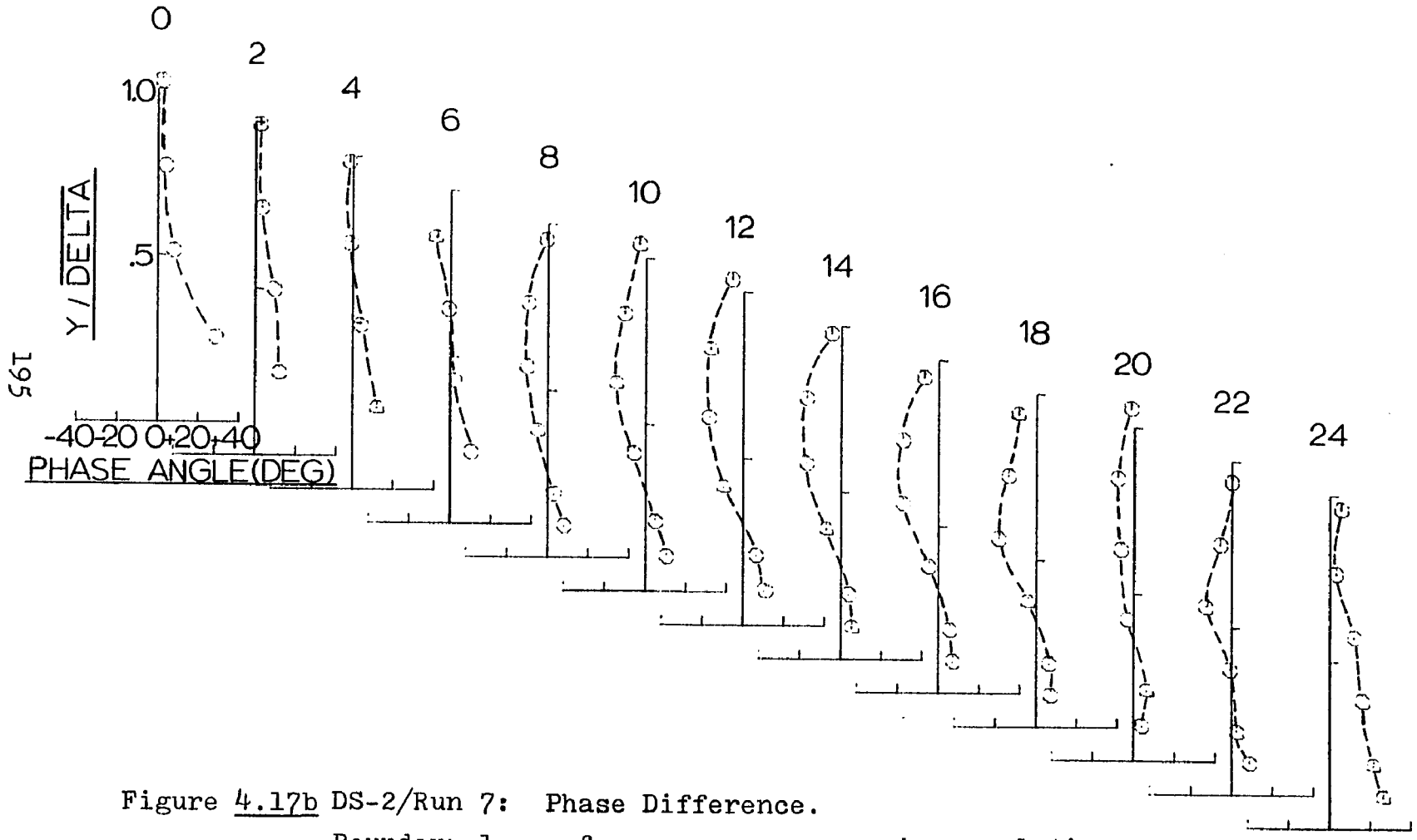

Figure 4.17b DS-2/Run 7: Phase Difference.
Boundary layer frequency response shown relative
to the local (x-station), centerline, velocity oscillation.
Re_D =115087, $\overline{\omega}_L$ = 3.14, FREQ= 15 HZ, $\Delta UCL(0)/\overline{UCL}(0)$= .0590

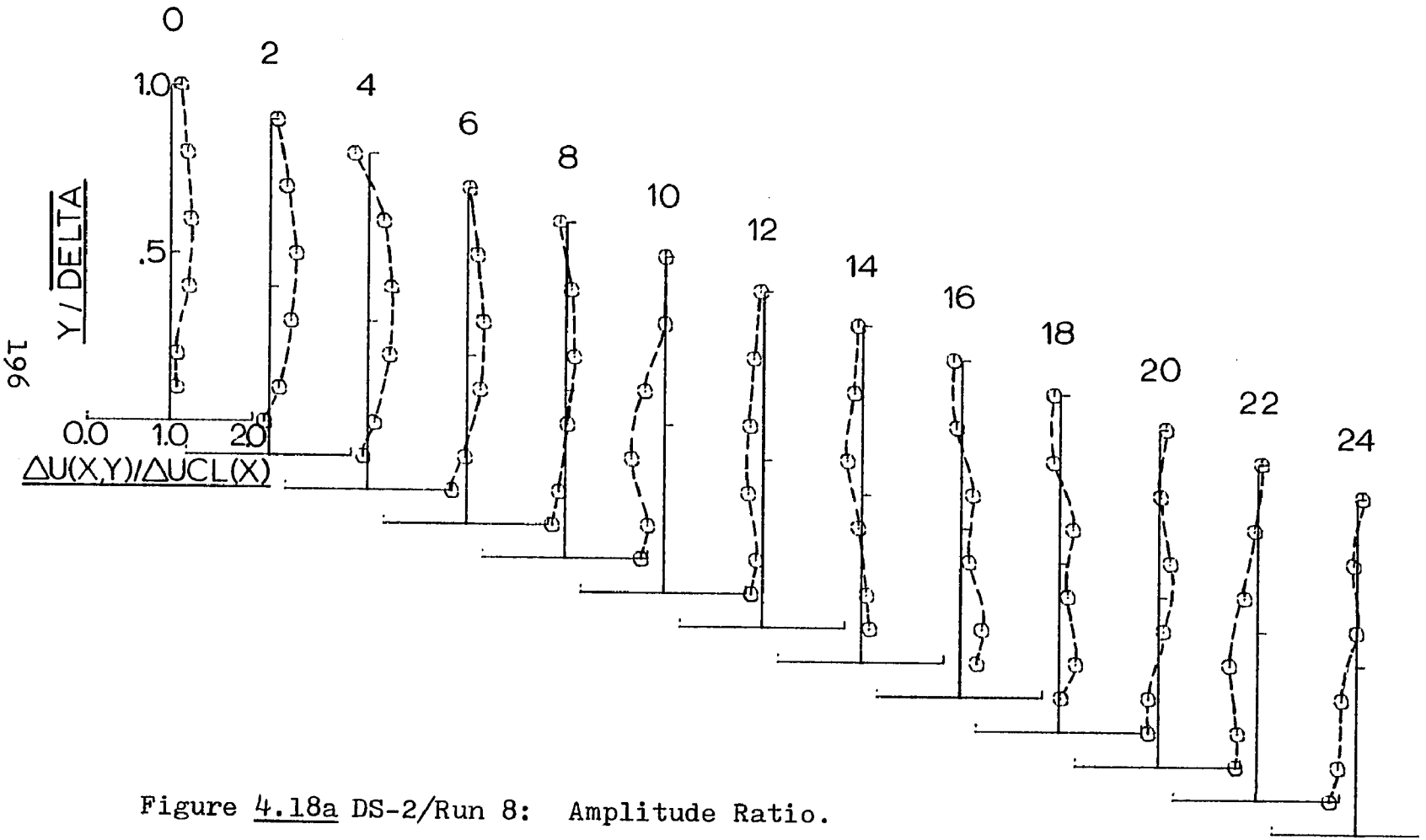

Figure 4.18a DS-2/Run 8: Amplitude Ratio.
Boundary layer frequency response shown relative to the local (x-station), centerline, velocity oscillation.
Re_D = 114768, $\overline{\omega}_L$ = 4.19, FREQ= 20 Hz, $\Delta UCL(0)/\overline{UCL}(0)$ = .0565

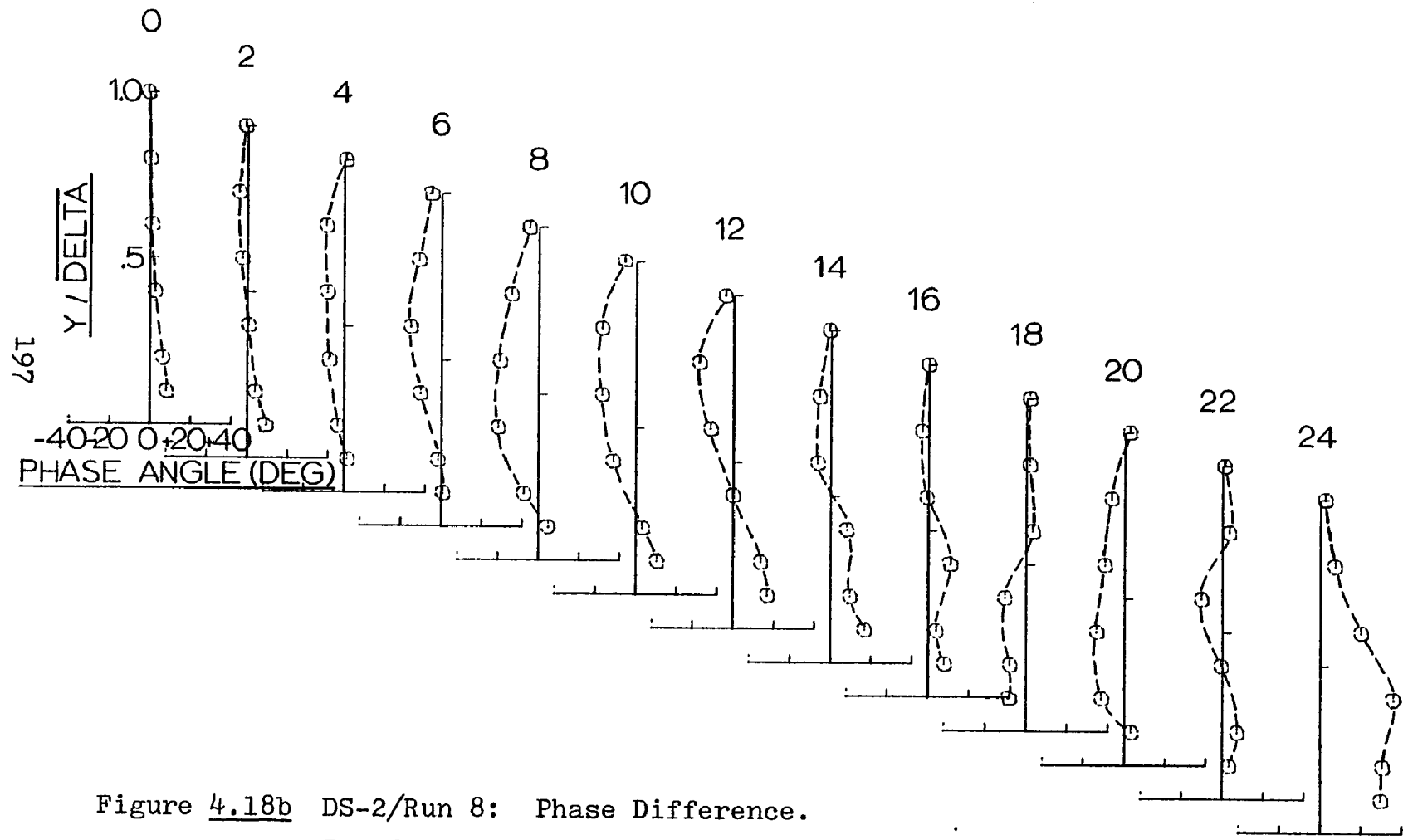

Figure 4.18b DS-2/Run 8: Phase Difference.
Boundary layer frequency response shown relative to the local (x-station), centerline, velocity oscillation.
Re_D =114768, $\bar{\omega}_L$ =4.19, FREQ= 20 HZ, $\Delta UCL(0)/\overline{UCL}(0)$= .0565

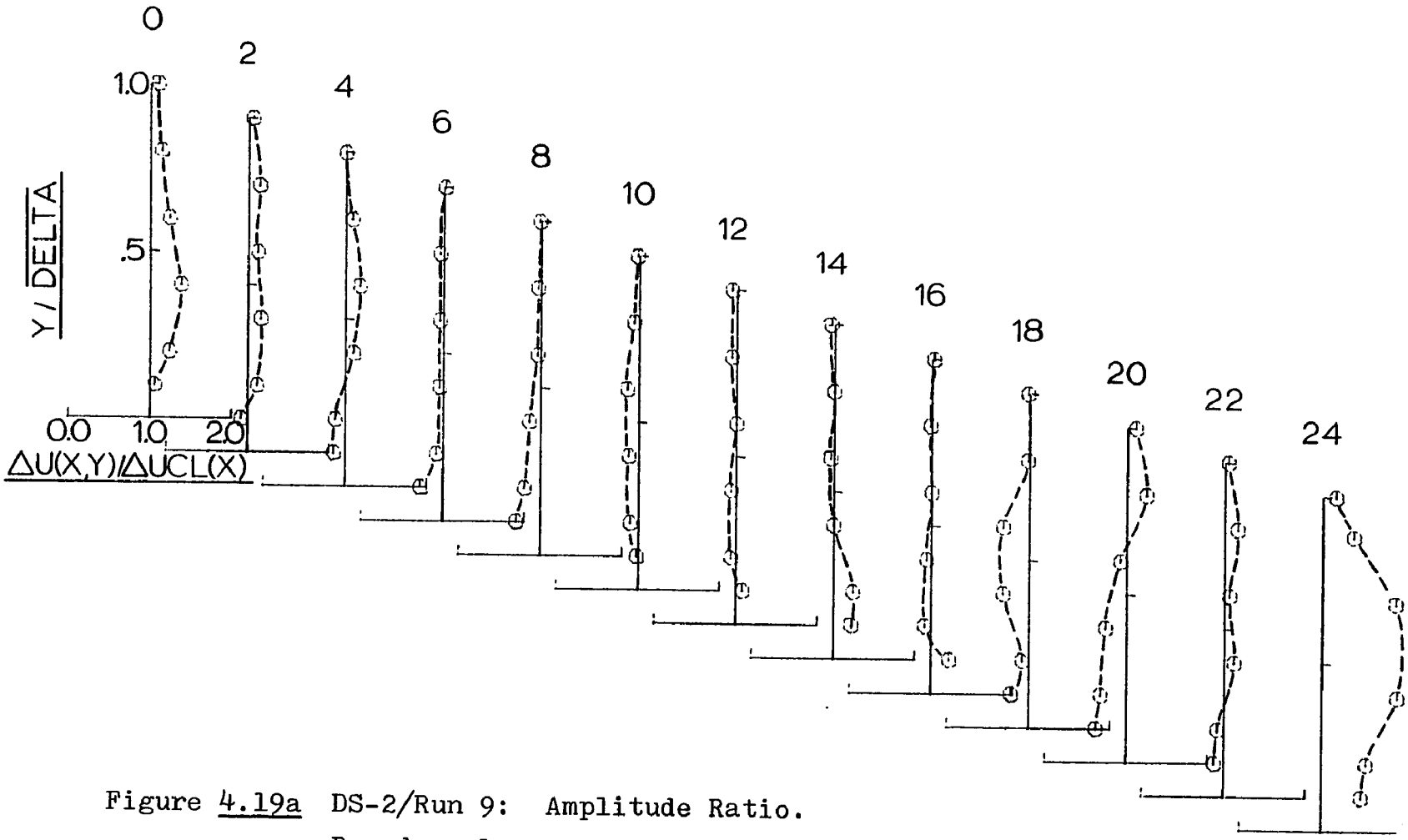

Figure 4.19a DS-2/Run 9: Amplitude Ratio.
Boundary layer frequency response shown relative to the local (x-station), centerline, velocity oscillation.
Re_D = 113402, $\overline{\omega}_L$ = 5.24 , FREQ= 25Hz, $\Delta UCL(0)/\overline{UCL}(0)$= .0457

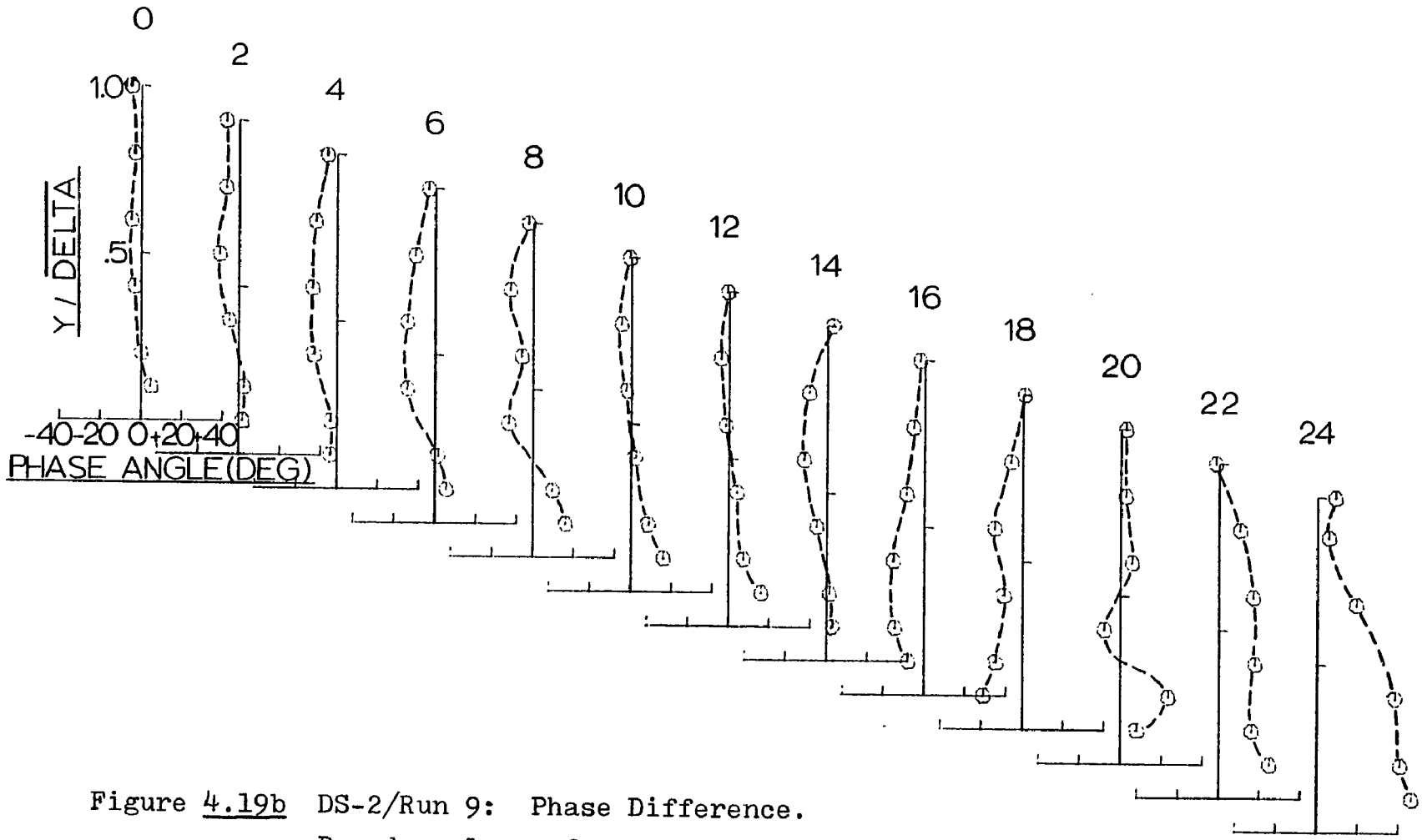

Figure 4.19b DS-2/Run 9: Phase Difference.
Boundary layer frequency response shown relative to the local (x-station), centerline, velocity oscillation.
Re_D =113402, $\overline{\omega}_L$ =5.24, FREQ= 25 Hz, $\Delta UCL(0)/\overline{UCL}(0)$= .0457

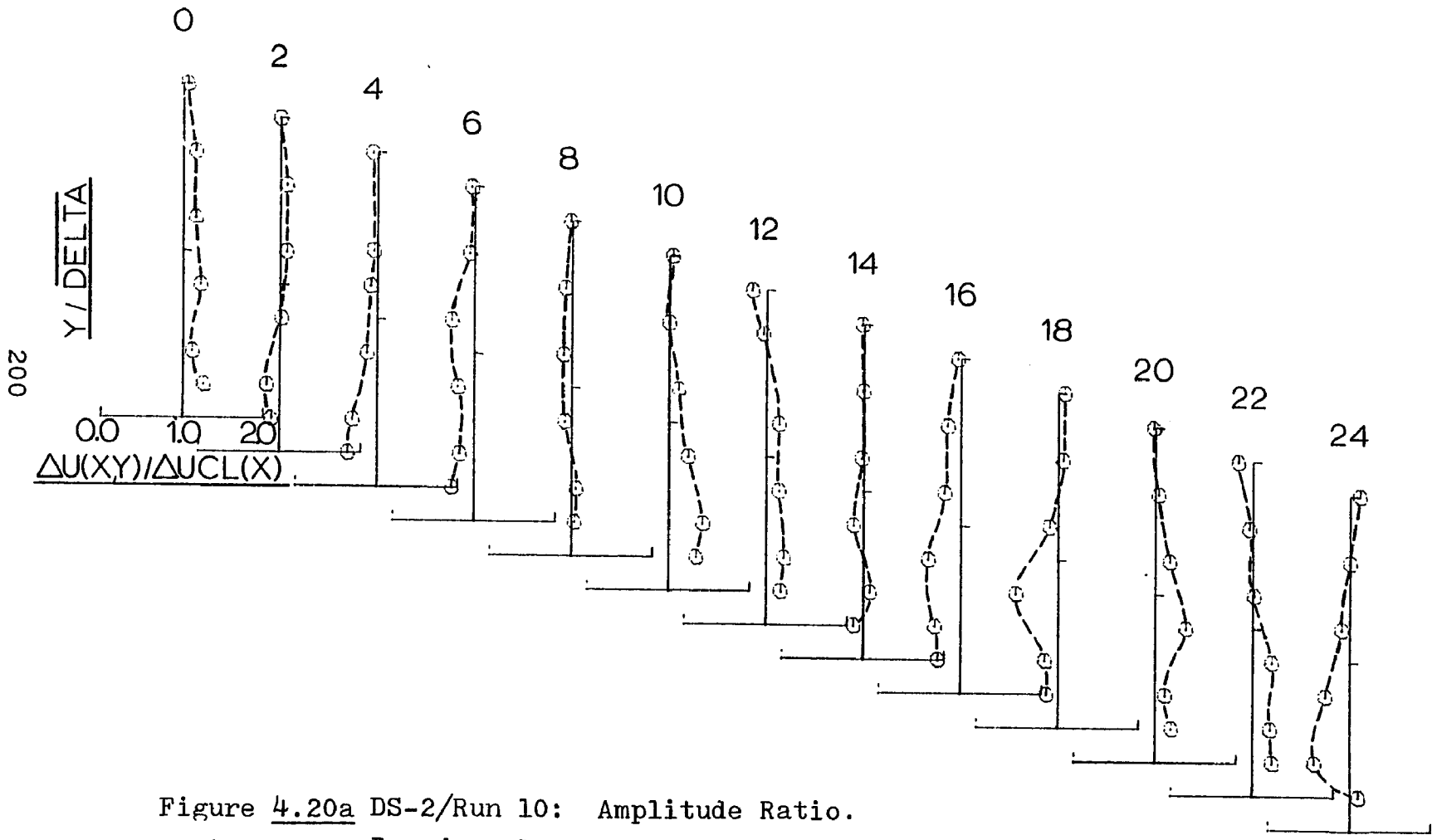

Figure 4.20a DS-2/Run 10: Amplitude Ratio.
Boundary layer frequency response shown relative to the local (x-station), centerline, velocity oscillation.
Re_D =113560, $\bar{\omega}_L$ =6.28, FREQ= 30Hz, $\Delta UCL(0)/\overline{UCL}(0)$= .0352

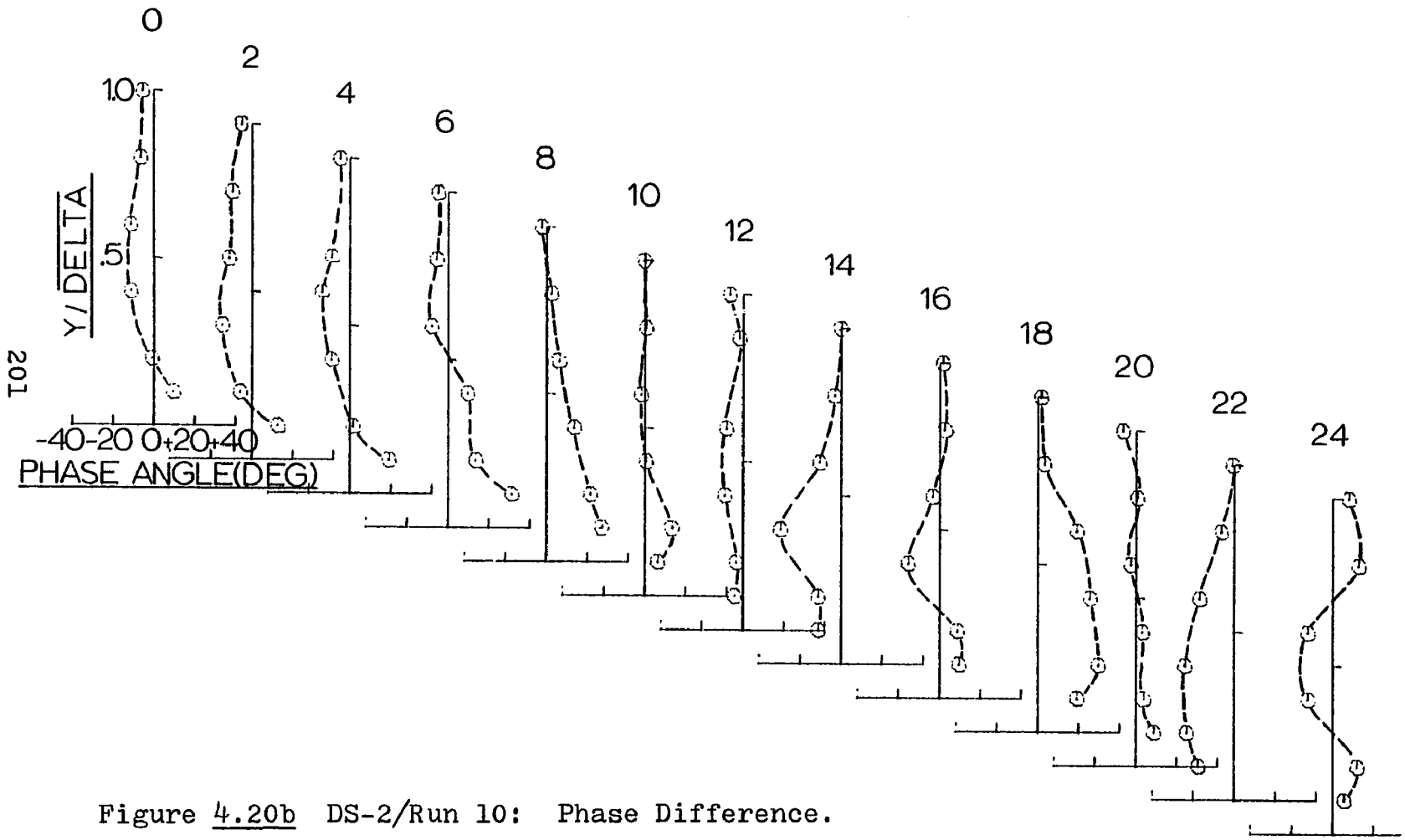

Figure 4.20b DS-2/Run 10: Phase Difference.
Boundary layer frequency response shown relative to the local (x-station), centerline, velocity oscillation.
Re_D = 113560, $\bar{\omega}_L$ = 6.28, FREQ= 30 Hz, $\Delta UCL(0)/\overline{UCL}(0)$ = .0352

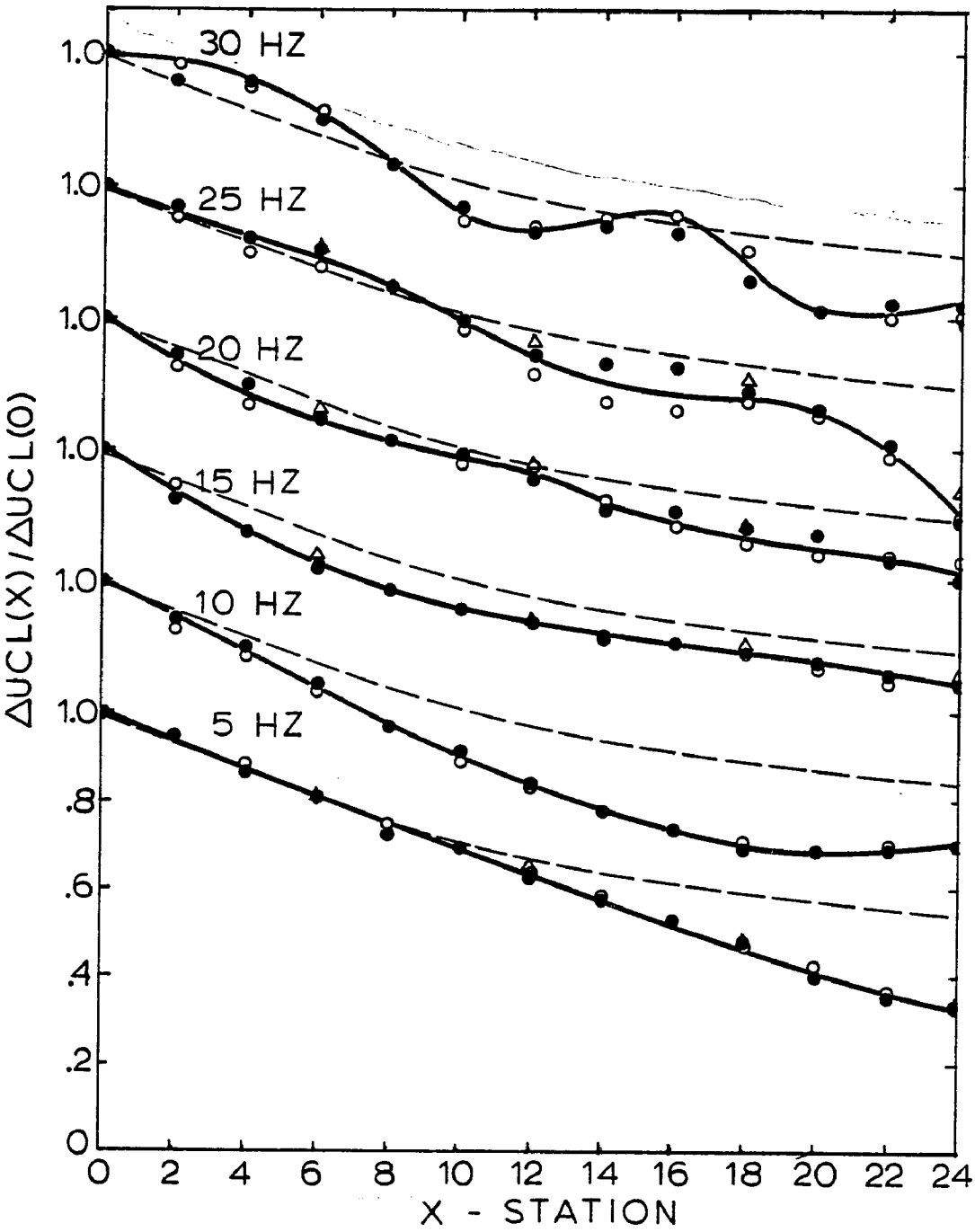

Figure 4.21a Centerline velocity response: Amplitude ratio with respect to x-station=0.
DS-2/Run 15(●); DS-2/Runs 5,6,7,8,9,10(o);
DS-1/Runs 3,4,5,7(△); Centerline, time-mean velocity decay(— —),

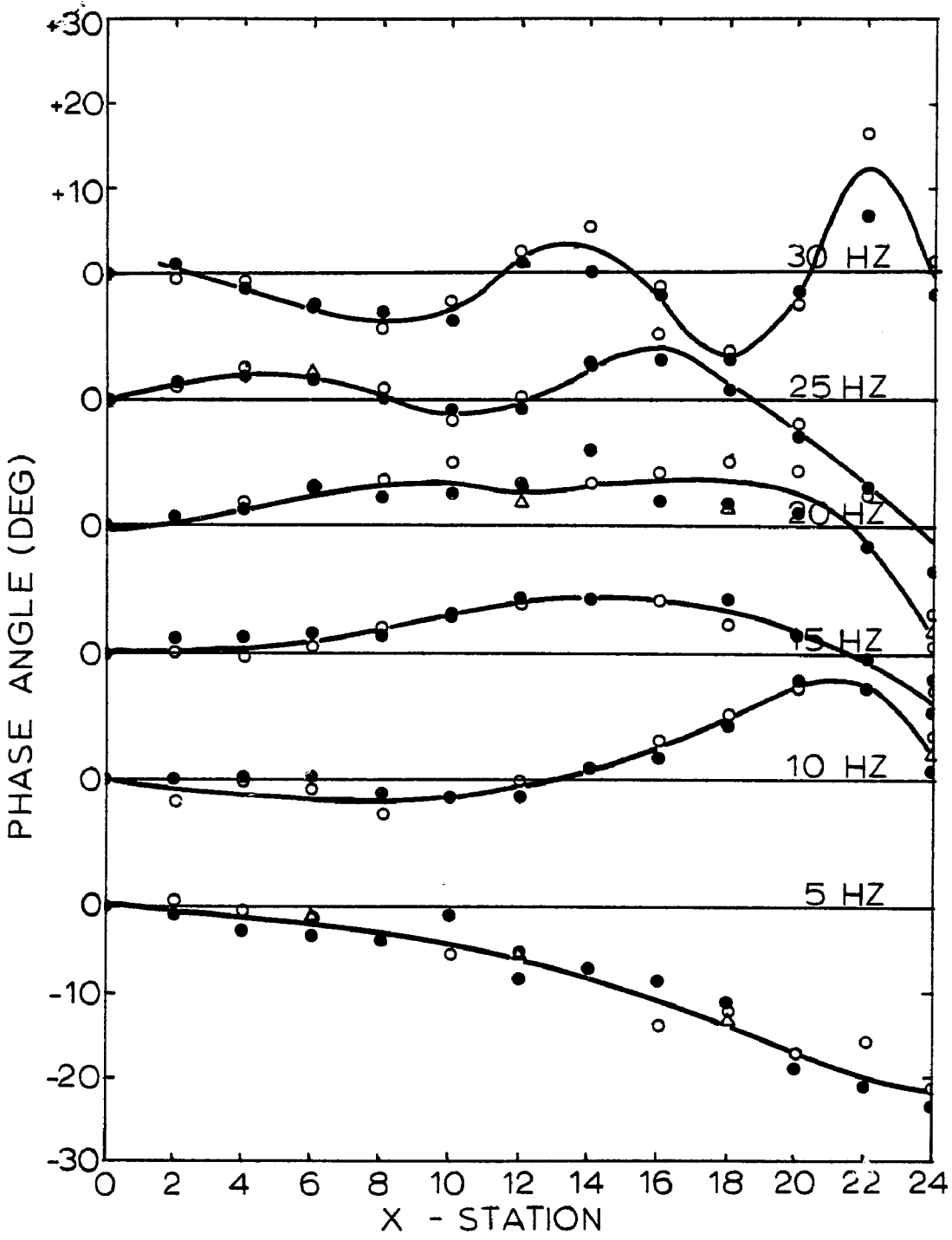

Figure 4.21b Centerline velocity response. Phase difference from x-station=0.
DS-2/Run 15(●); DS-2/Runs 5,6,7,8,9,10(○);
DS-1/Runs 3,4,5,7(△).

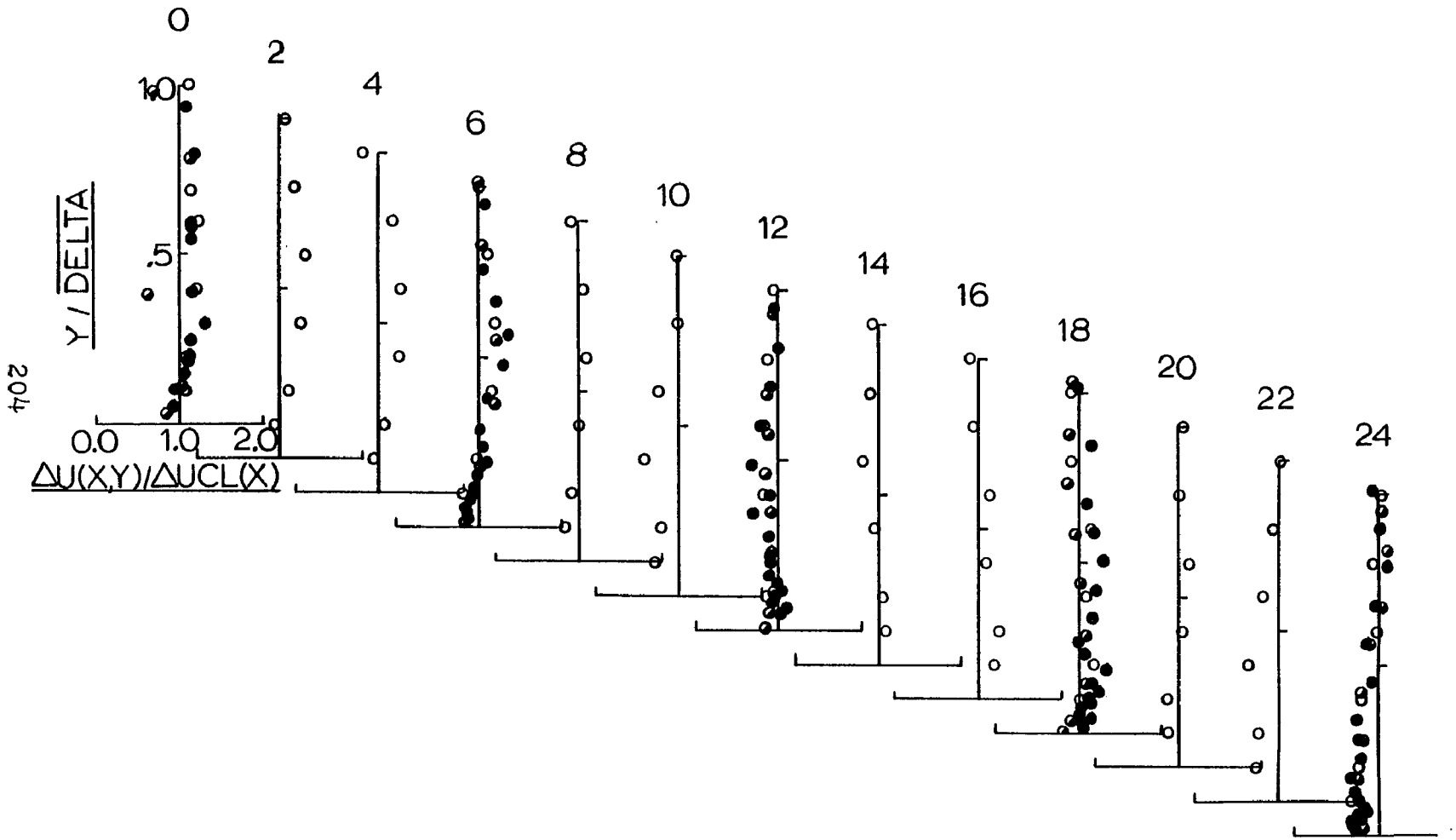

Figure 4.22a Repeatability: Amplitude Ratio.
$Re_D \approx 120{,}000$, $\overline{\omega_z}(0)=4.19$, FREQ= 20 Hz.
DS-2 / Run 8 (○); DS-2/ Run 14 (●); DS-1/ Run 6 (•).

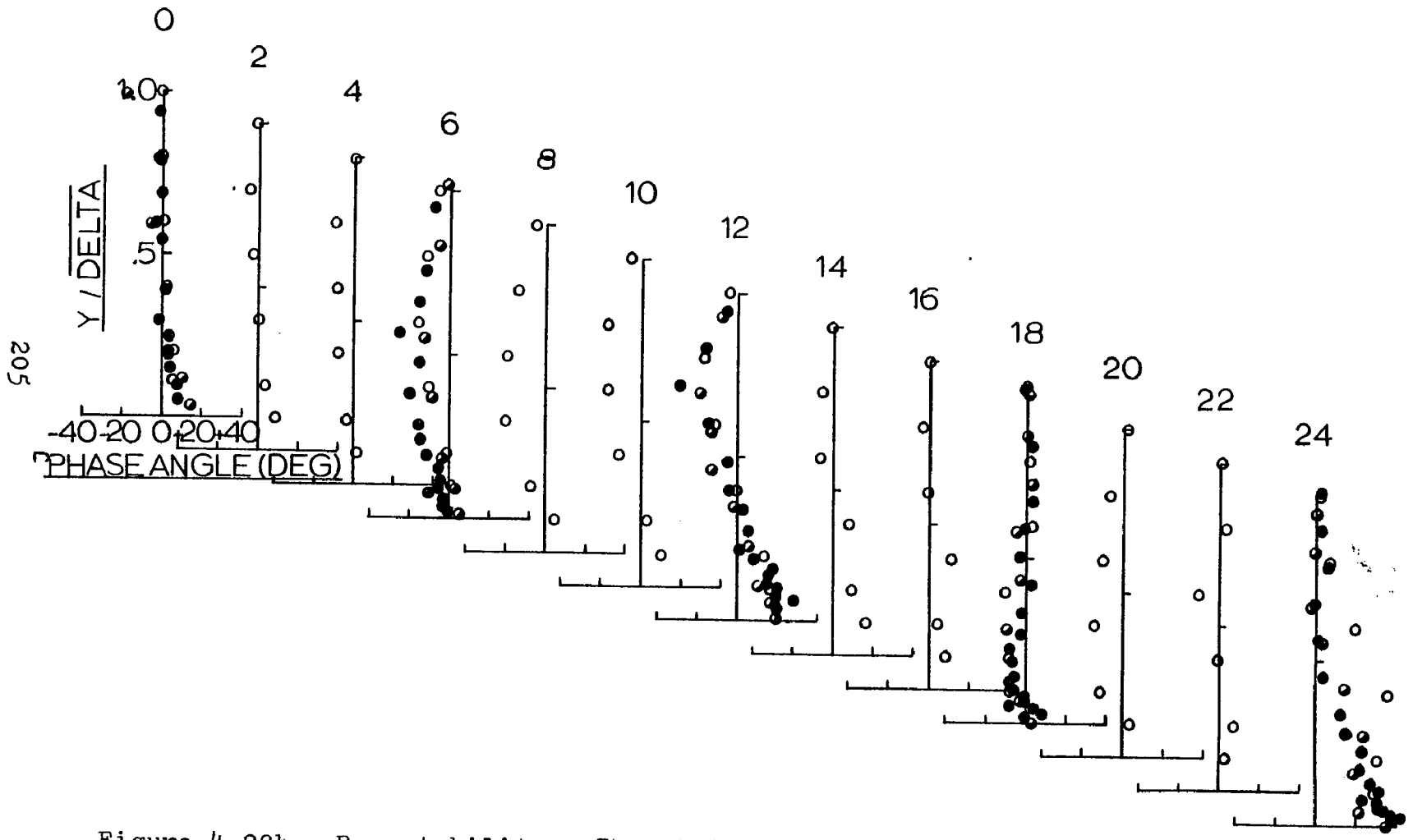

Figure 4.22b Repeatability: Phase Difference.
$Re_D \approx 120{,}000$, $\bar{\omega}_t(0)=4.19$, FREQ = 20 Hz.
DS-2 / Run 8 (o); DS-2/ Run 14 (•); DS-1 / Run 6 (•).

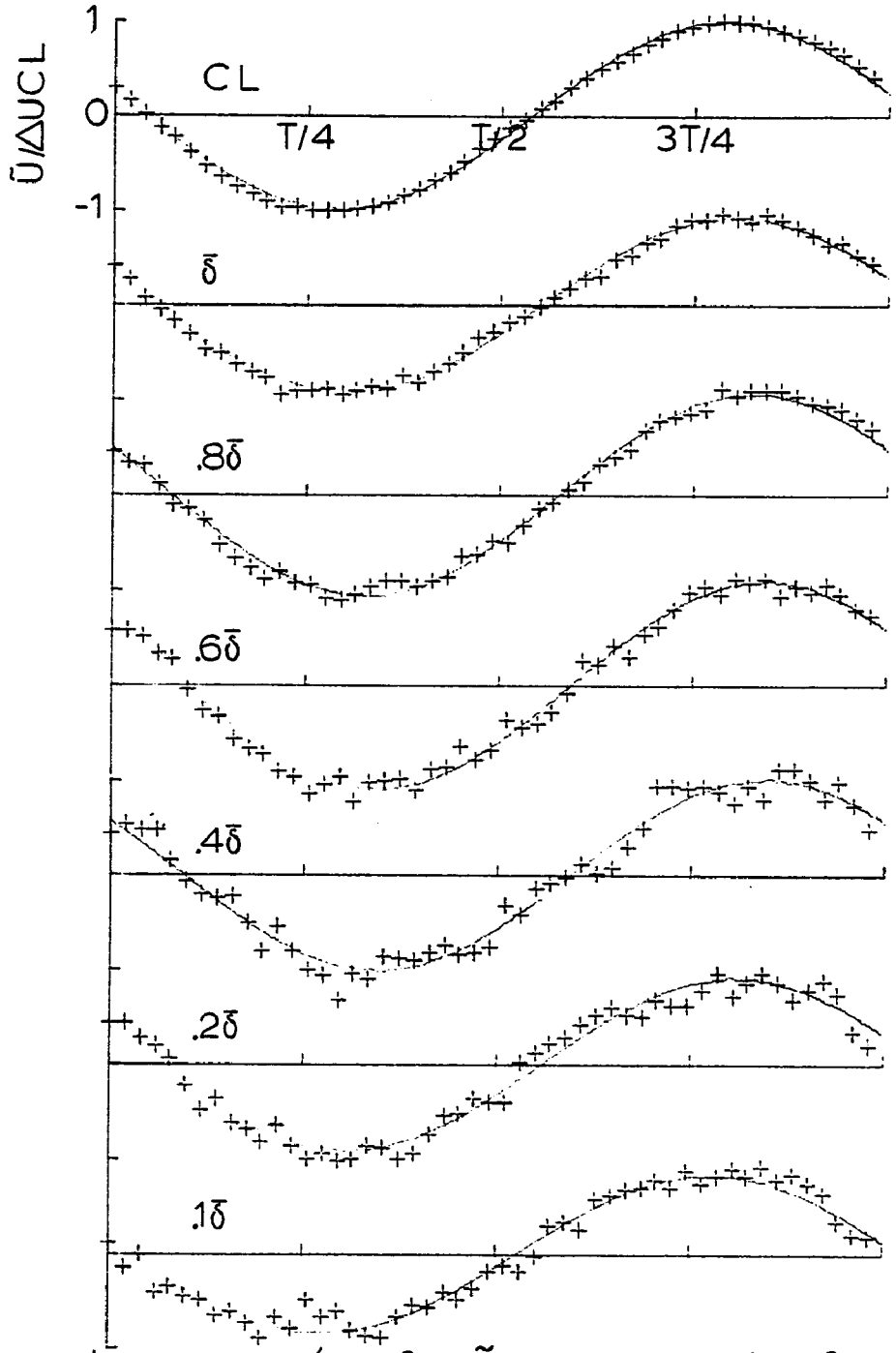

Figure 4.23a DS-2/Run 8: $\tilde{U}$ data, X-station 8. Oscillating-component velocity data at several locations through the boundary layer. Amplitudes and phases are shown relative to the centerline oscillation.

$\overline{UCL}(0)$=18.29m/sec, FREQ=20Hz, $\Delta UCL(X)/\overline{UCL}(0)$=.0407

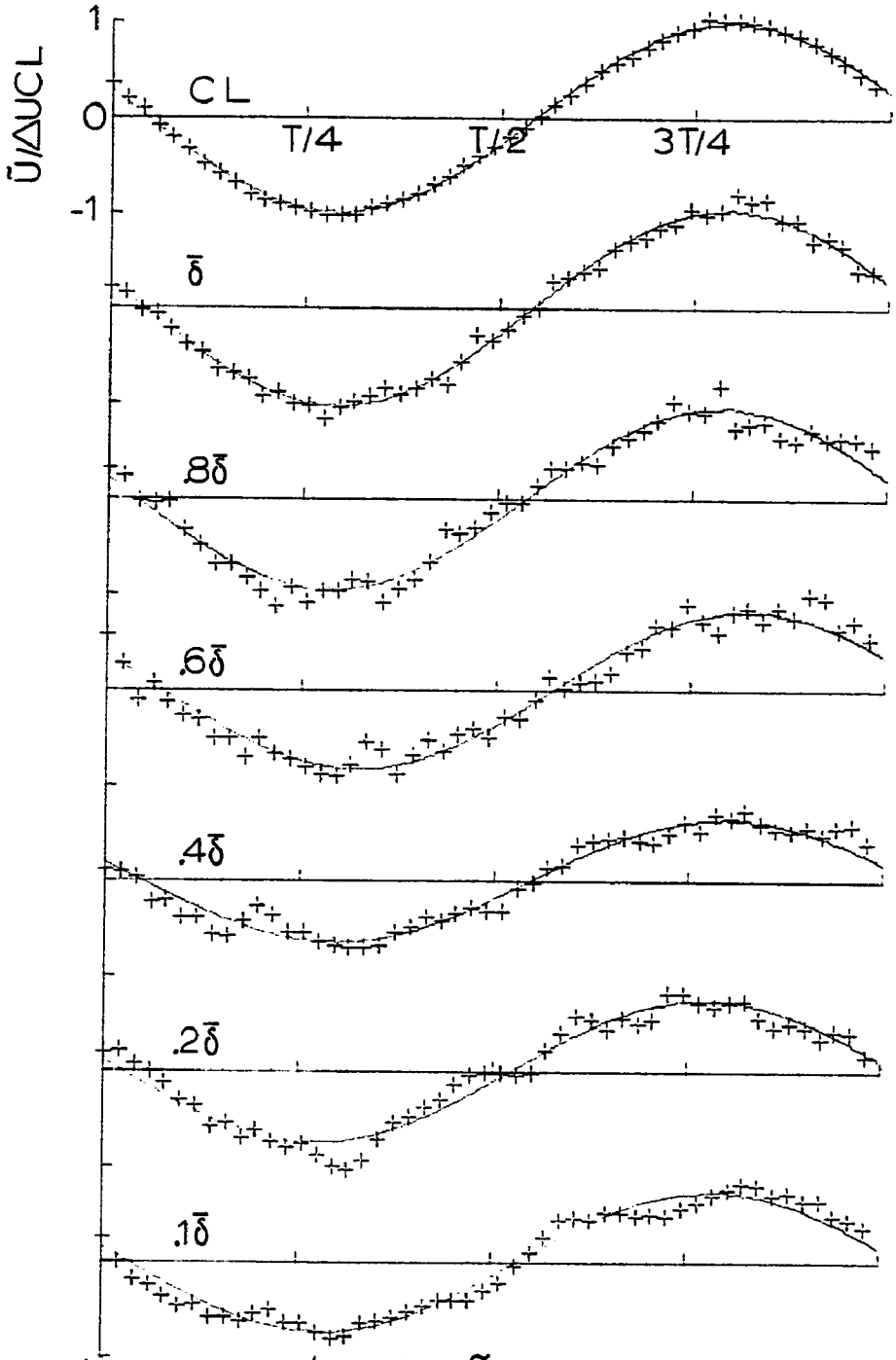

Figure 4.23b DS-2/Run 8: $\tilde{U}$ data, X-station 22. Oscillating-component velocity data at several locations through the boundary layer. Amplitudes and phases are shown relative to the centerline oscillation.

$\overline{UCL}(0)=18.29$m/sec, FREQ=20Hz, $\Delta UCL(X)/\overline{UCL}(0)=.0260$

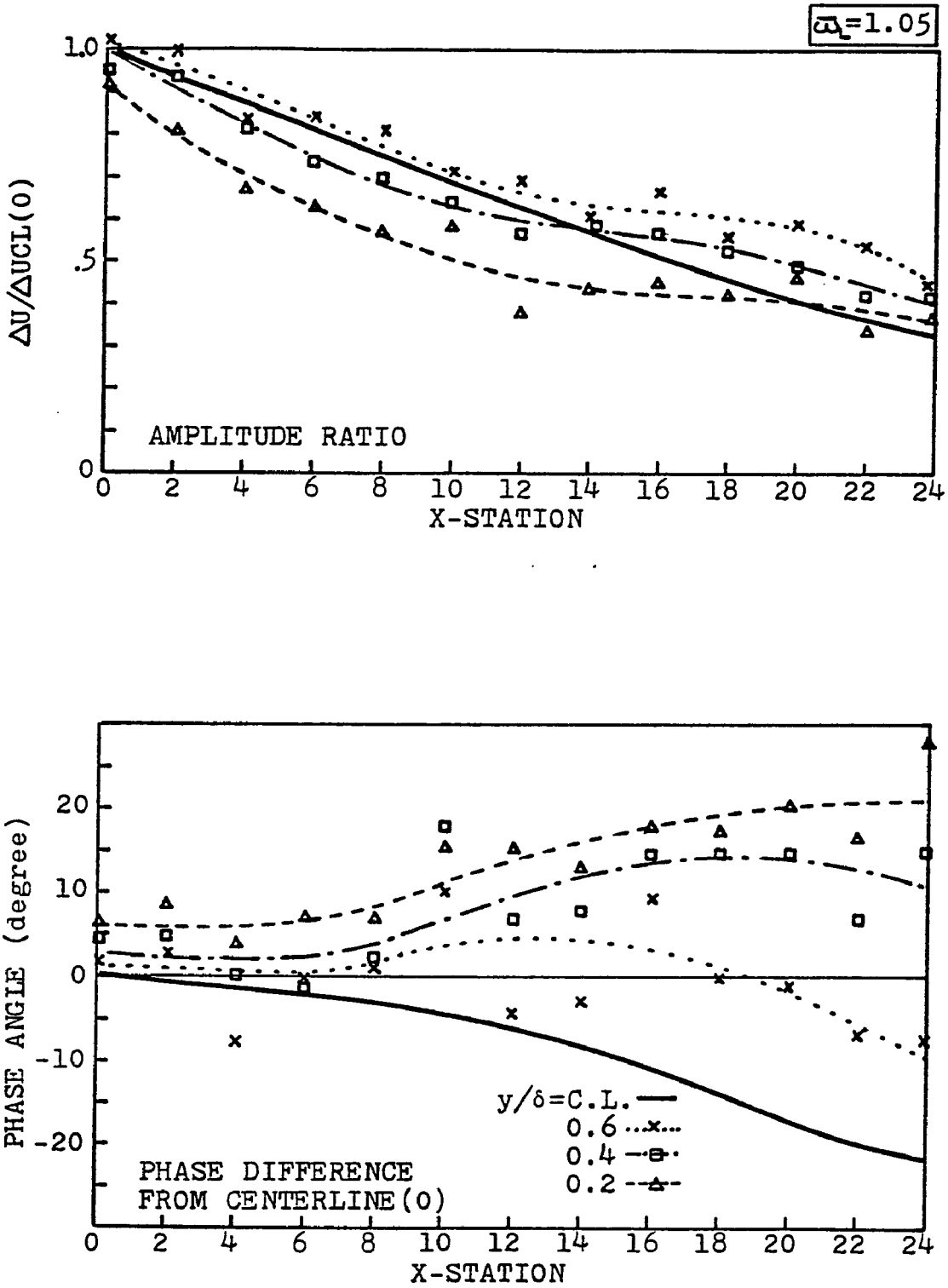

Figure 4.24a Boundary layer velocity response pattern with respect to the x-station=0, centerline oscillation. DS-2/Run 5: Re_D=117401, $\bar{\omega}_L$=1.05, FREQ= 5 Hz.

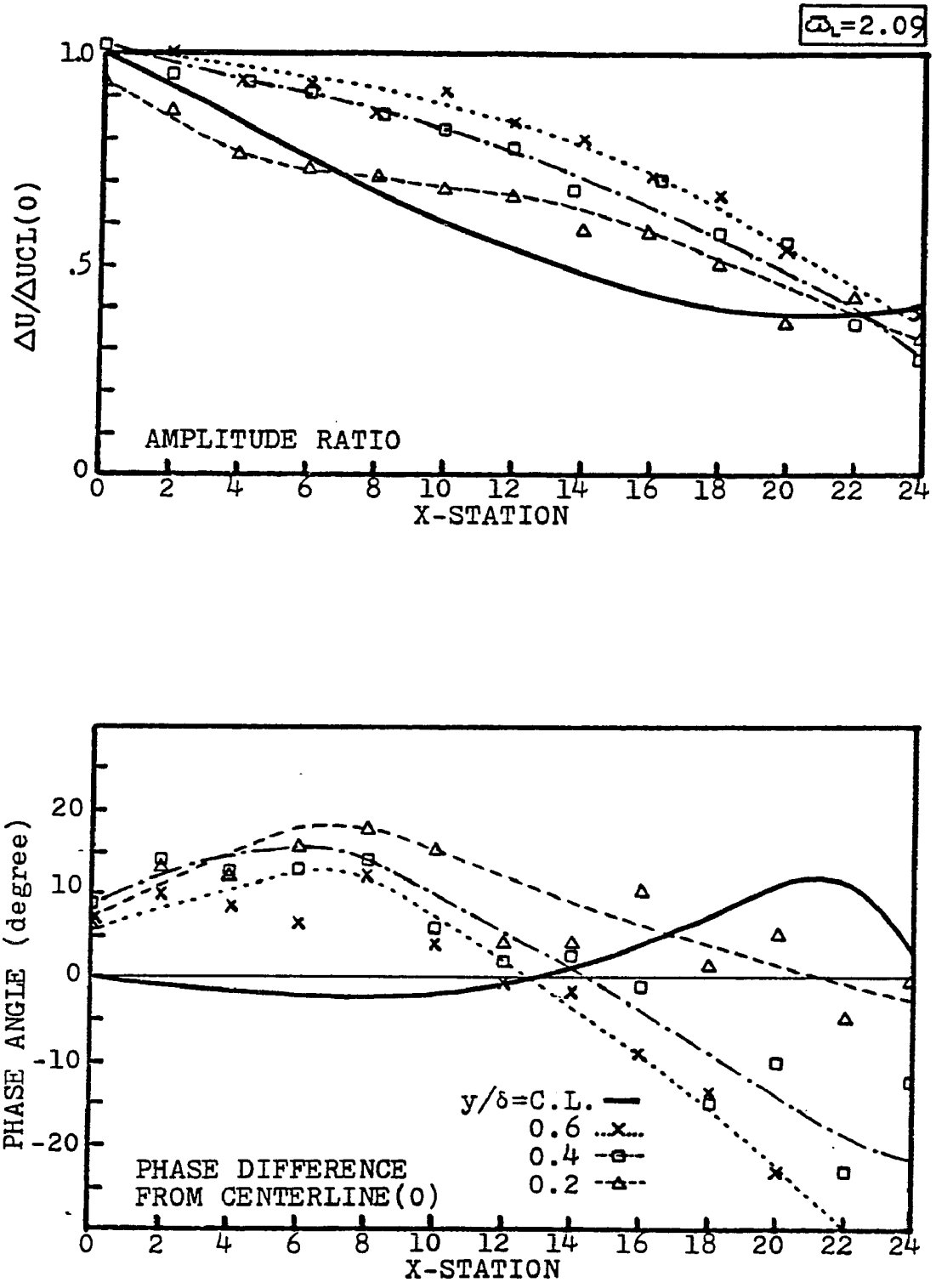

Figure 4.24b Boundary layer velocity response pattern with respect to the x-station=0, centerline oscillation. DS-2/Run 6: Re_D=116320, ω_L =2.09, FREQ=10 Hz.

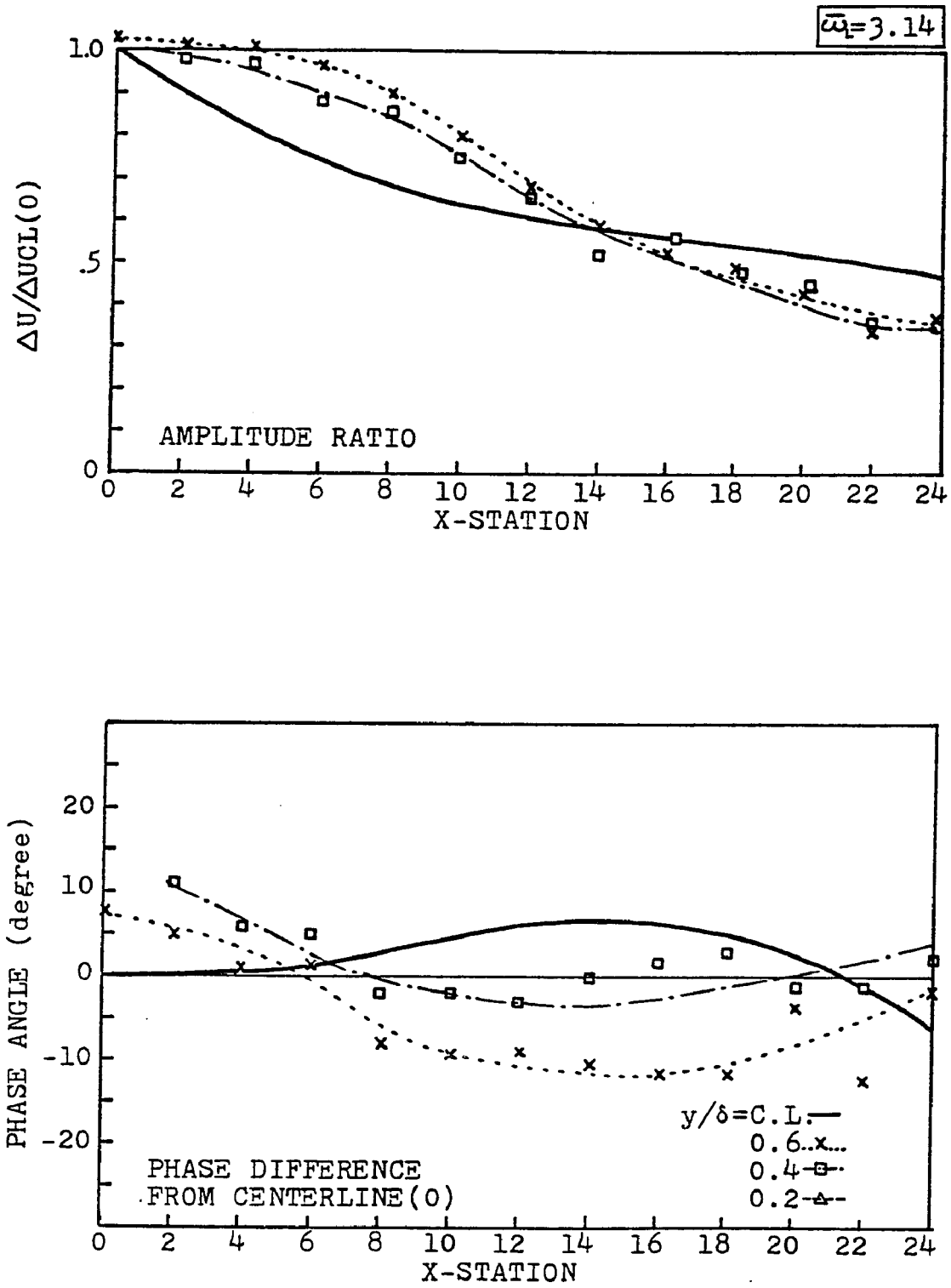

Figure 4.24c Boundary layer velocity response pattern with respect to the x-station=0, centerline oscillation. DS-2/Run 7: Re_D=115087, $\bar{\omega}_L$ =3.14, FREQ=15 Hz.

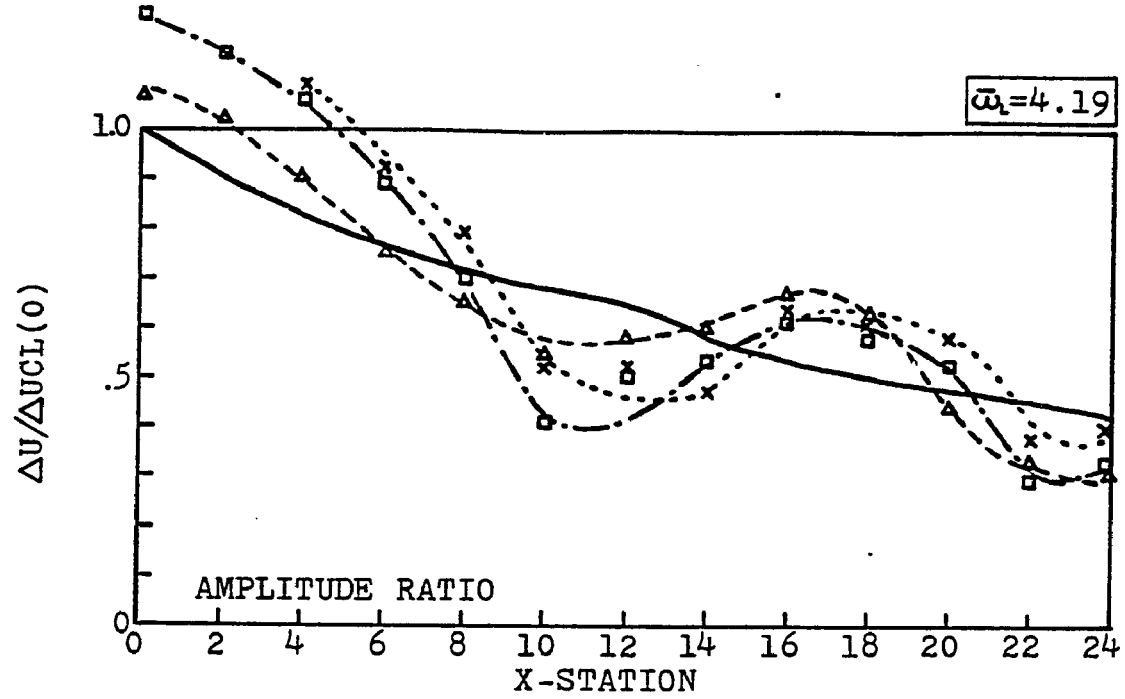

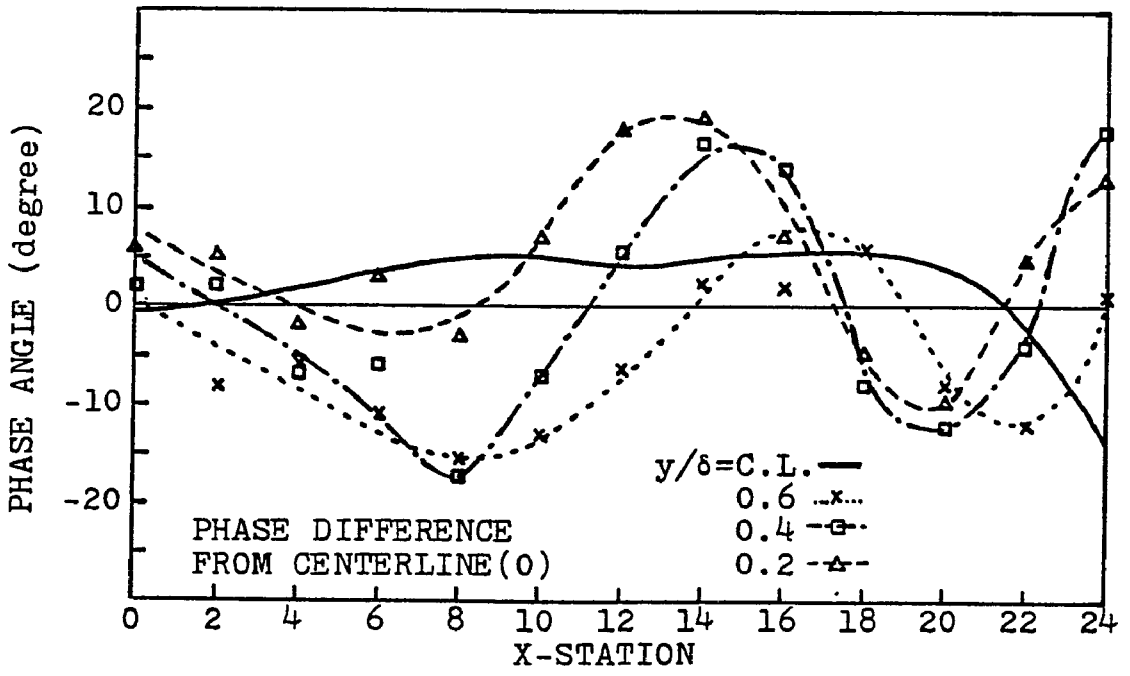

Figure 4.24d Boundary layer velocity response pattern with respect to the x-station=0, centerline oscillation. DS-2/Run 8, Re_D=114768, $\bar{\omega}_L$ =4.19, FREQ=20 Hz.

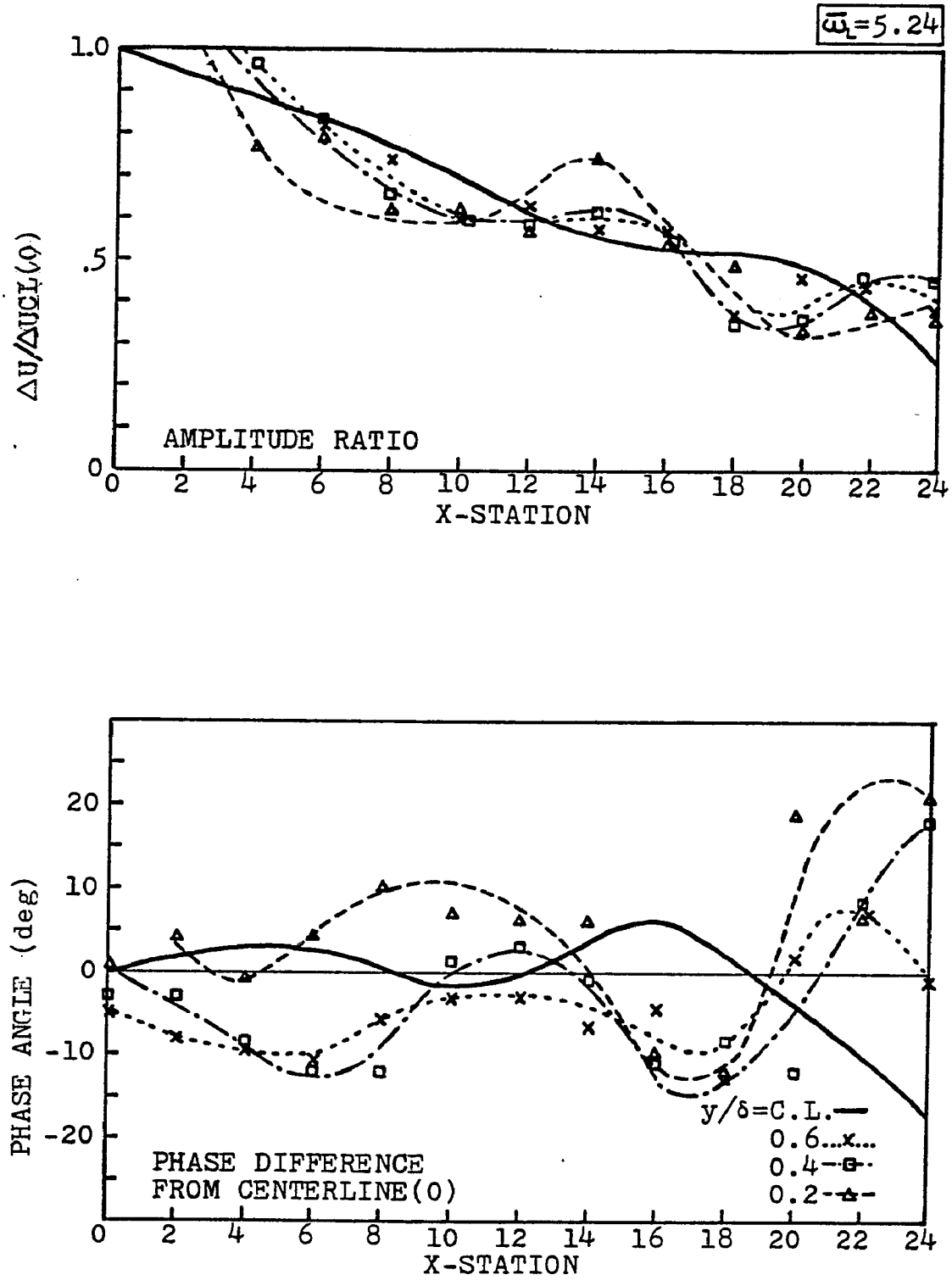

Figure 424e Boundary layer velocity response pattern with respect to the x-station=0, centerline oscillation. DS-2/Run 9: Re_D=113402, $\bar{\omega}_L$=5.24, FREQ=25 Hz.

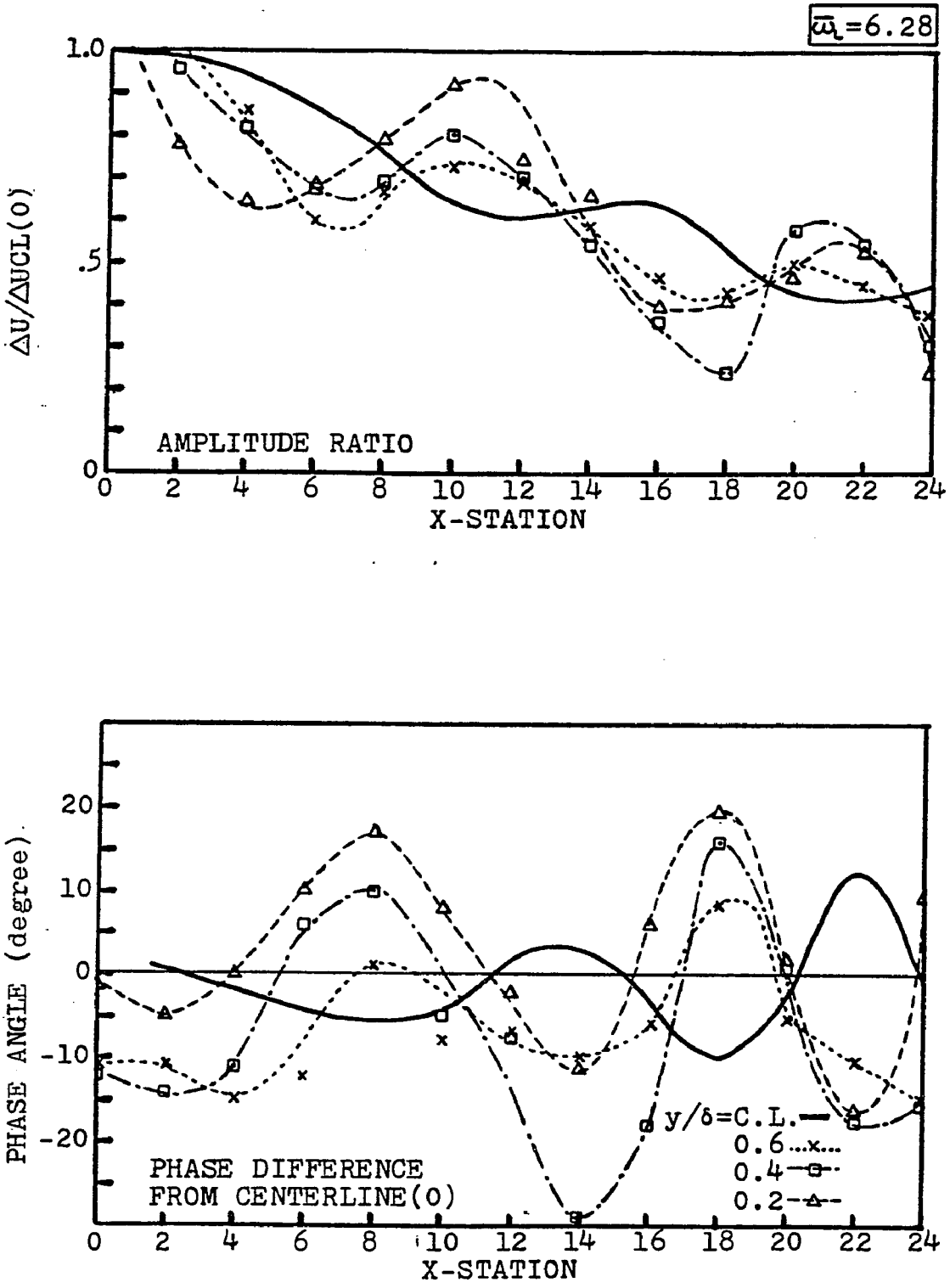

Figure 424f Boundary layer velocity response pattern with respect to the x-station=0, centerline oscillation. DS-2/Run 10: Re_D=113560, $\bar{\omega}_t$ =6.28, FREQ=30 Hz.

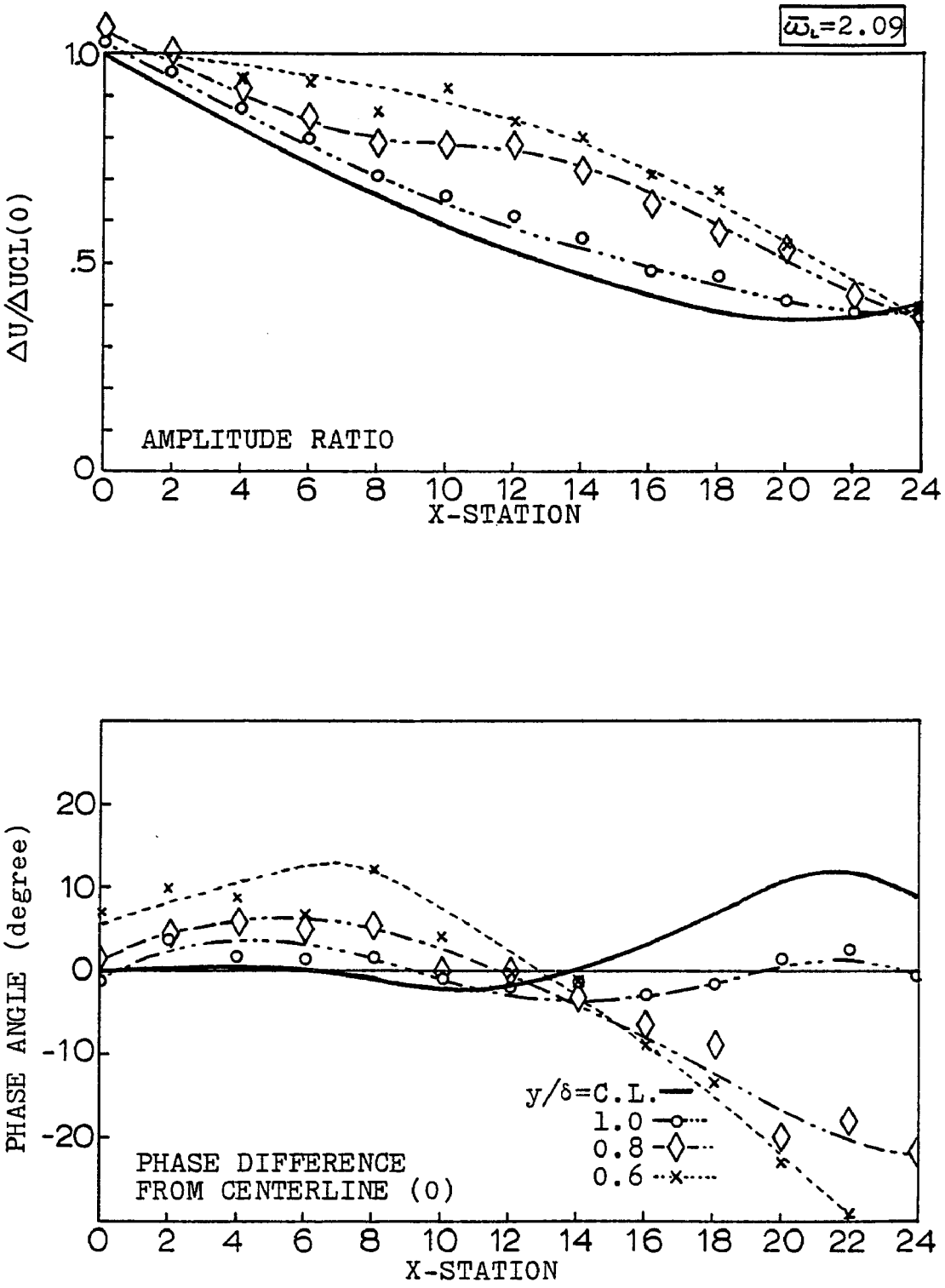

Figure 4.25a Outer-edge velocity response pattern with respect to the x-station=0, centerline oscillation. DS-2/Run 6: Re_D=116320, $\bar{\omega}_L$ =2.09, FREQ=10 Hz.

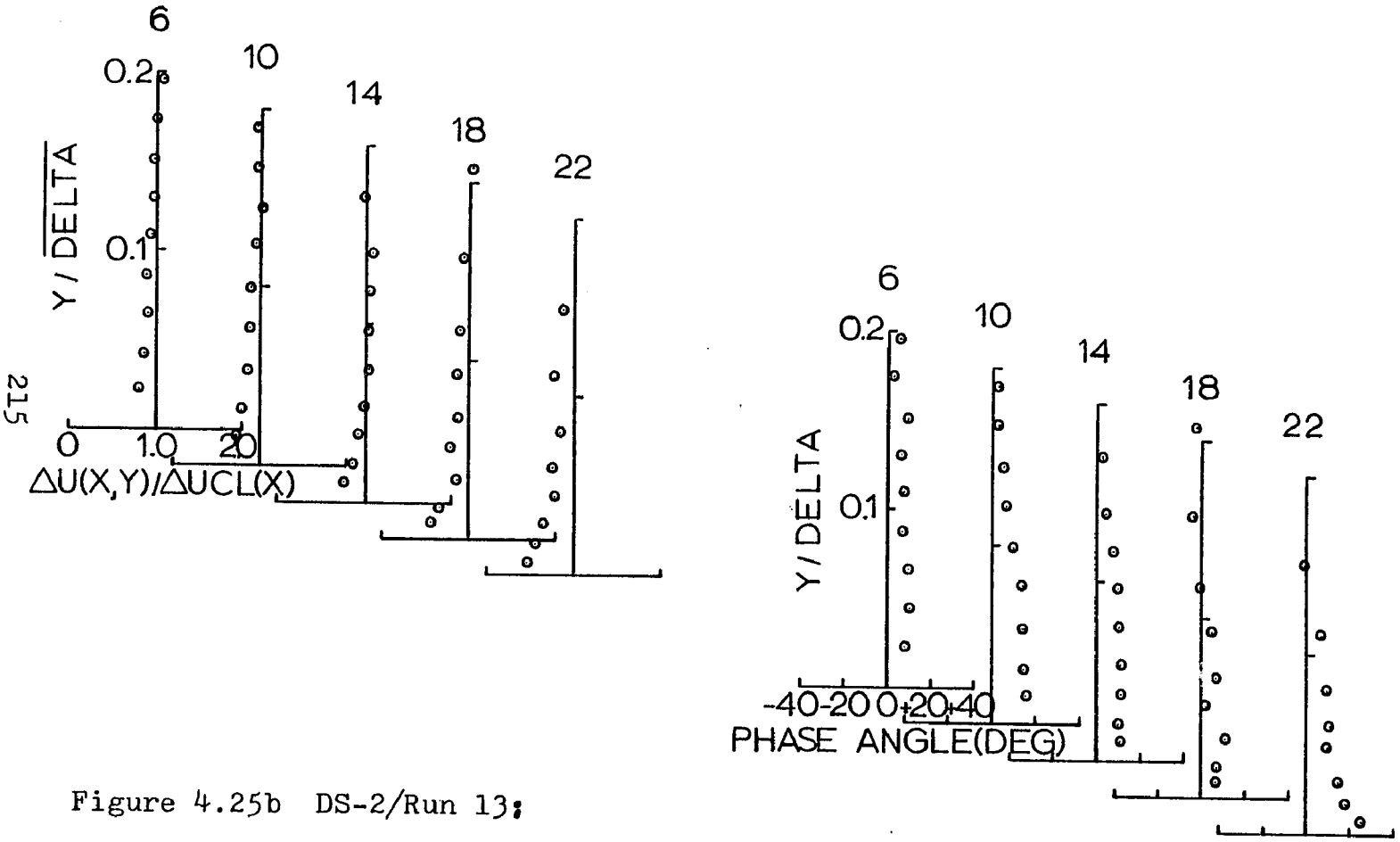

Figure 4.25b DS-2/Run 13:

Near-wall boundary layer response.

Re_D = 121,852, $\overline{\omega}_L$ = 3.14, FREQ = 15 Hz, $\Delta UCL(0)/\overline{UCL}(0)$ = .0768.

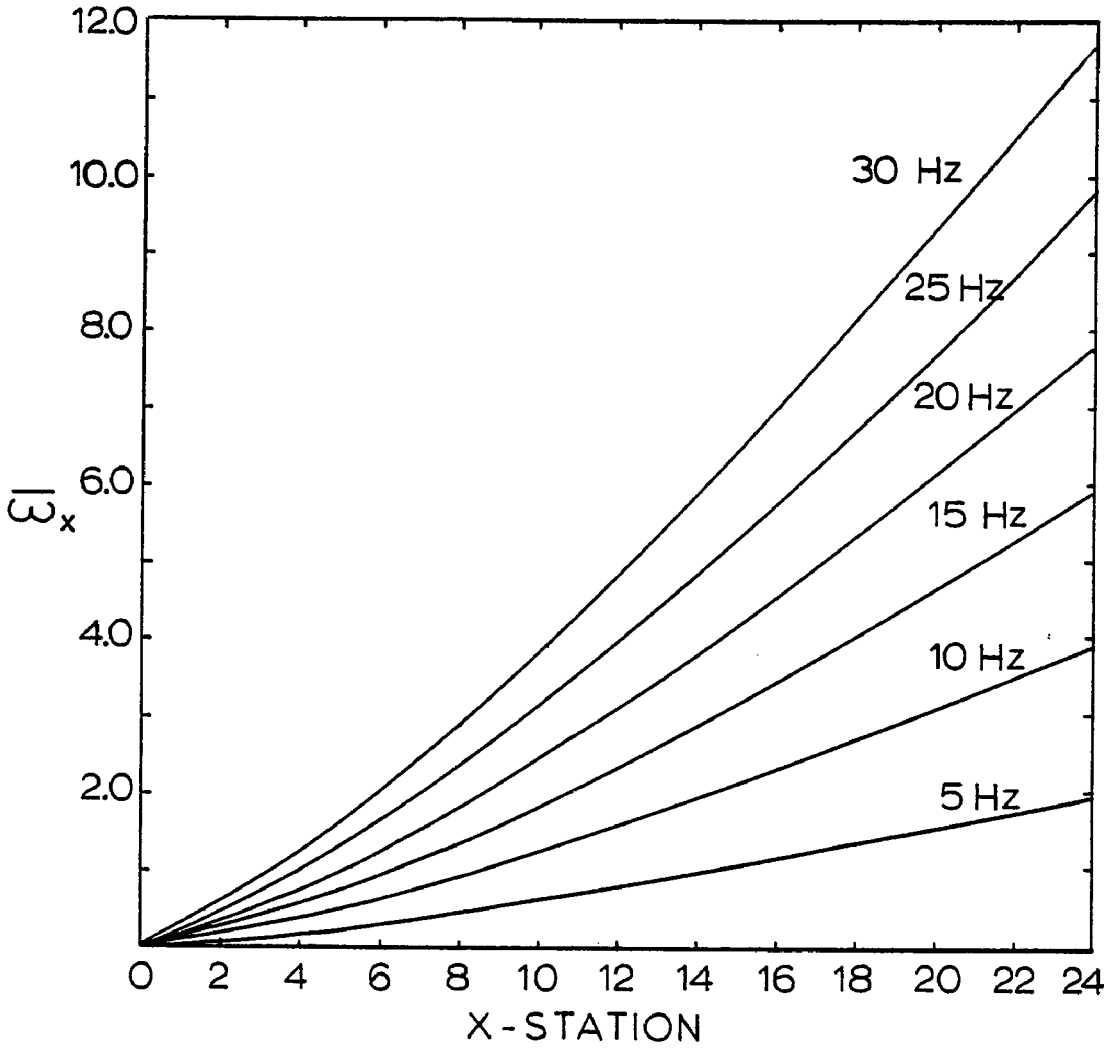

Figure 4.26 The variation of the local dimensionless frequency parameter, $\bar{\omega}_x$, with X-station for $Re_D \cong 120{,}000$ and FREQ = 5, 10, 15, 20, 25 and 30 Hz.

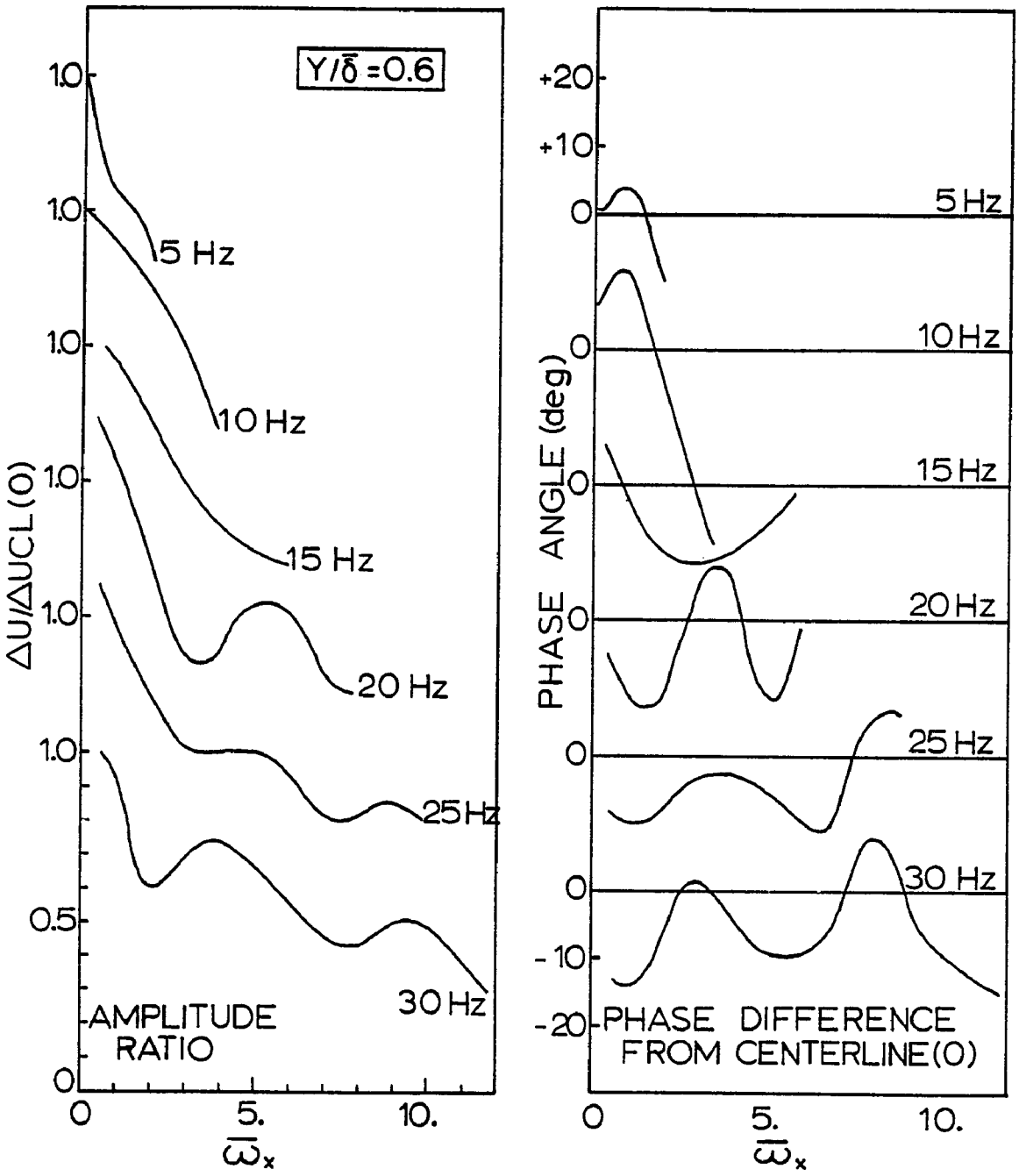

Figure 4.27 A comparison of the velocity response patterns as a function of $\bar{\omega}_x$ for $Y/\delta = 0.6$.

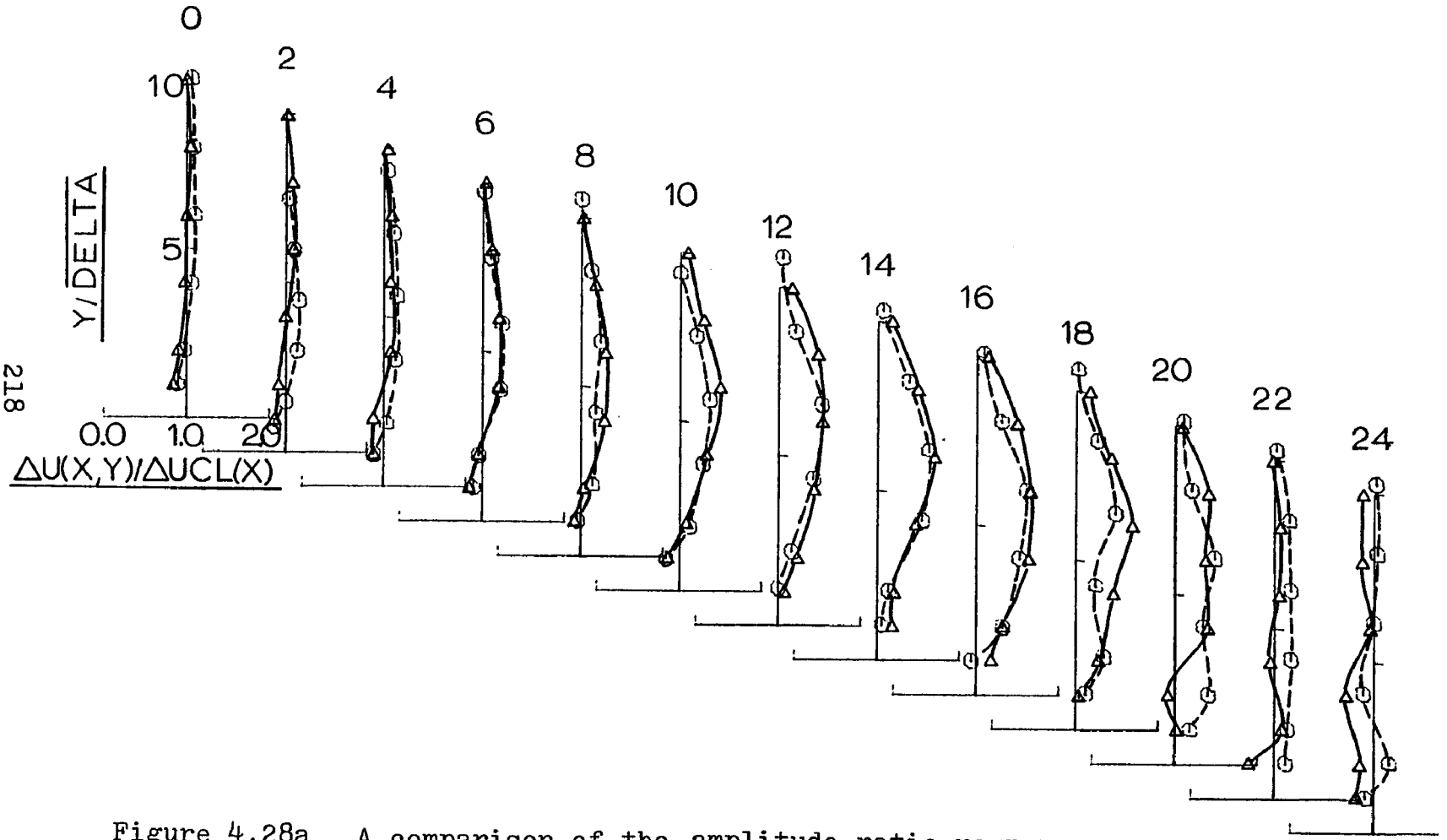

Figure 4.28a A comparison of the amplitude ratio response for two test runs with identical $\overline{\omega}_L$ = 2.09:
DS-2/Run 11 (--o--), Re_D = 198,000, FREQ = 16.6 Hz;
DS-2/Run 6 (—△—), Re_D = 116,000, FREQ = 10 Hz.

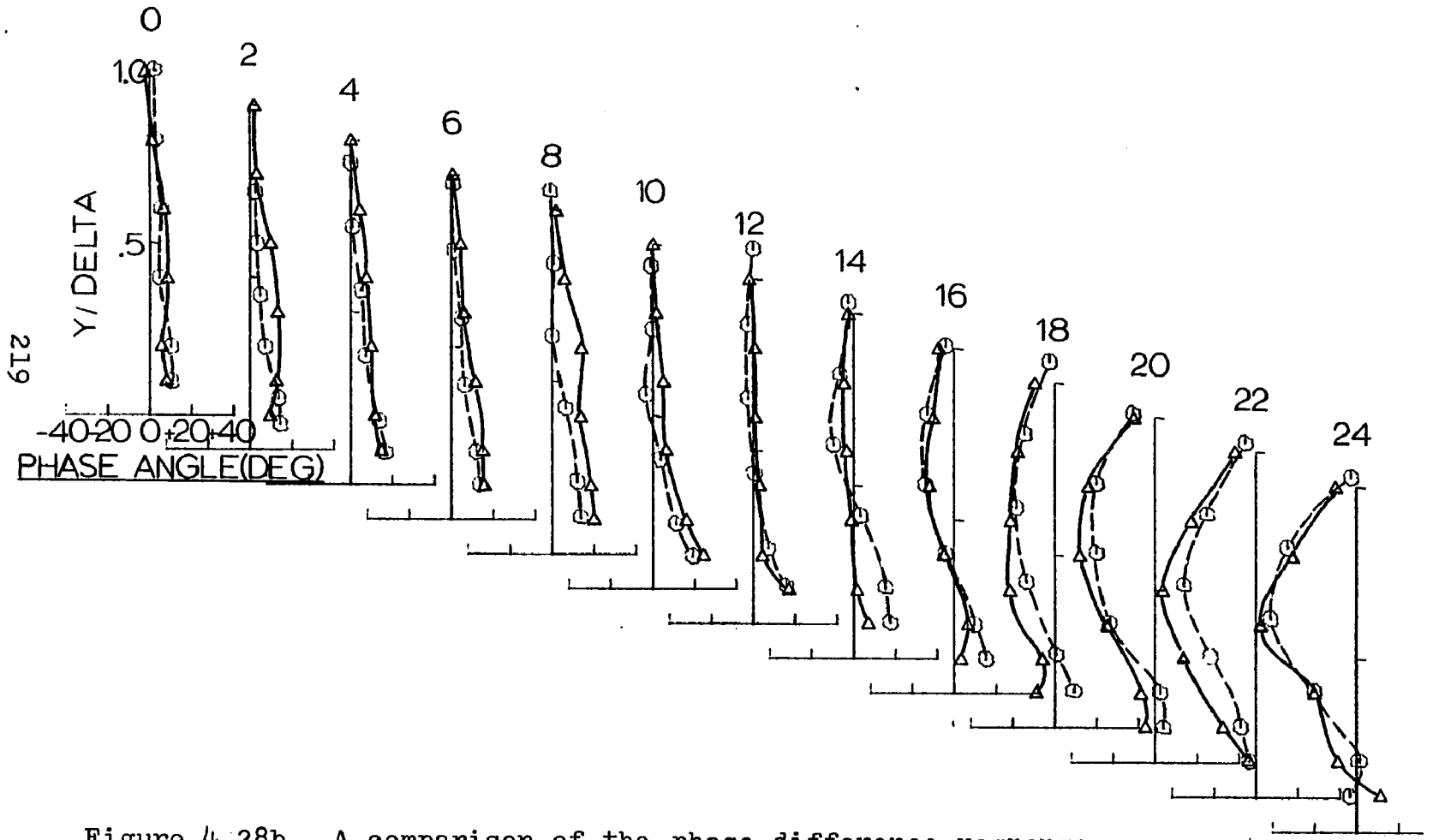

Figure 4.28b A comparison of the phase difference response for two test runs with identical $\overline{\omega}_L = 2.09$:
DS-2/Run 11 (--o--), Re_D = 198,000, FREQ = 16.6 Hz;
DS-2/Run 6 (—△—), Re_D = 116,000, FREQ = 10 Hz.

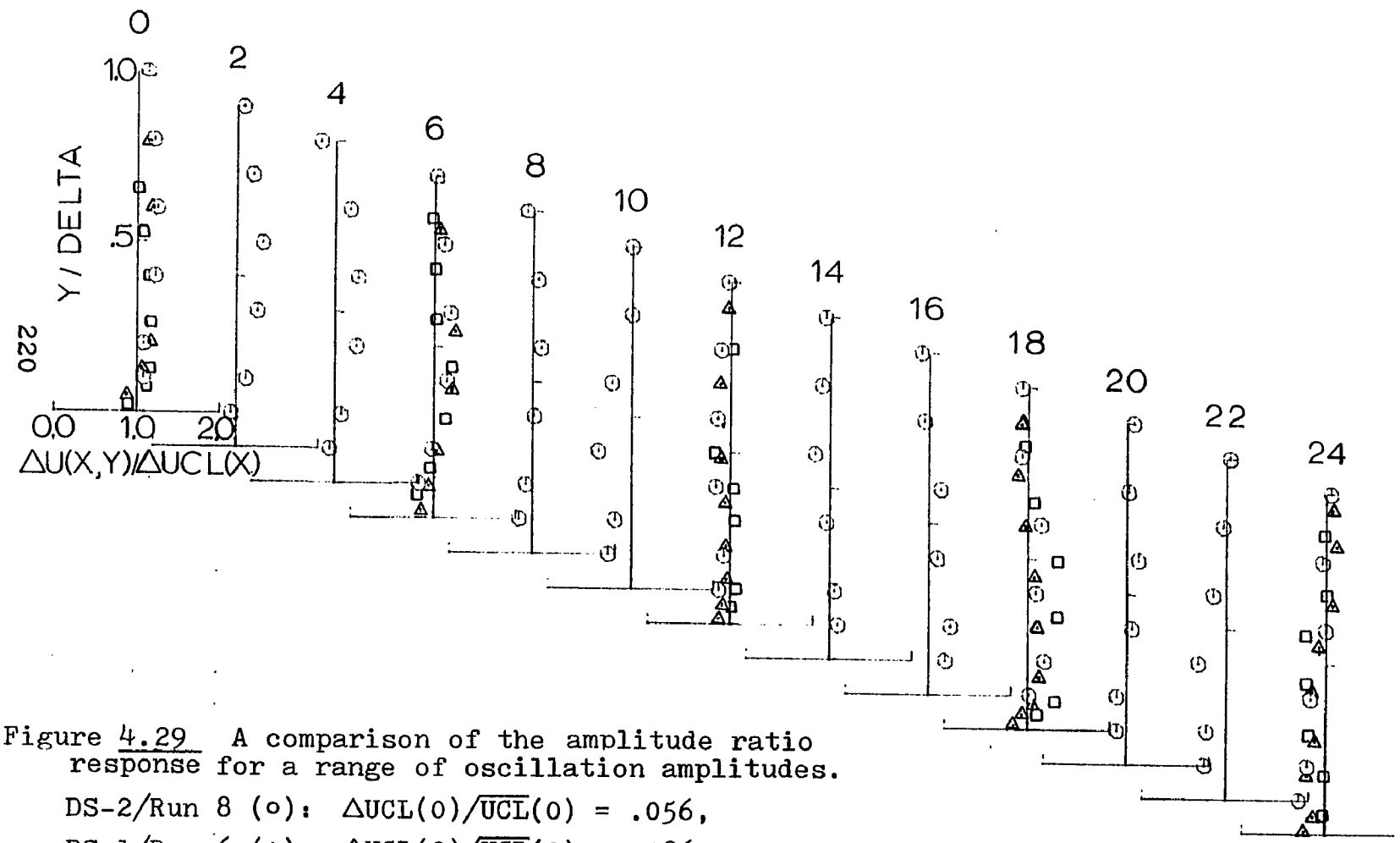

Figure 4.29 A comparison of the amplitude ratio response for a range of oscillation amplitudes.

DS-2/Run 8 (o): $\Delta UCL(0)/\overline{UCL}(0) = .056$,

DS-1/Run 6 (Δ): $\Delta UCL(0)/\overline{UCL}(0) = .086$,

DS-1/Run 5 (□): $\Delta UCL(0)/\overline{UCL}(0) = .027$.

$Re_D \cong 120{,}000$, $\bar{\omega}_L = 4.19$, FREQ = 20 Hz.

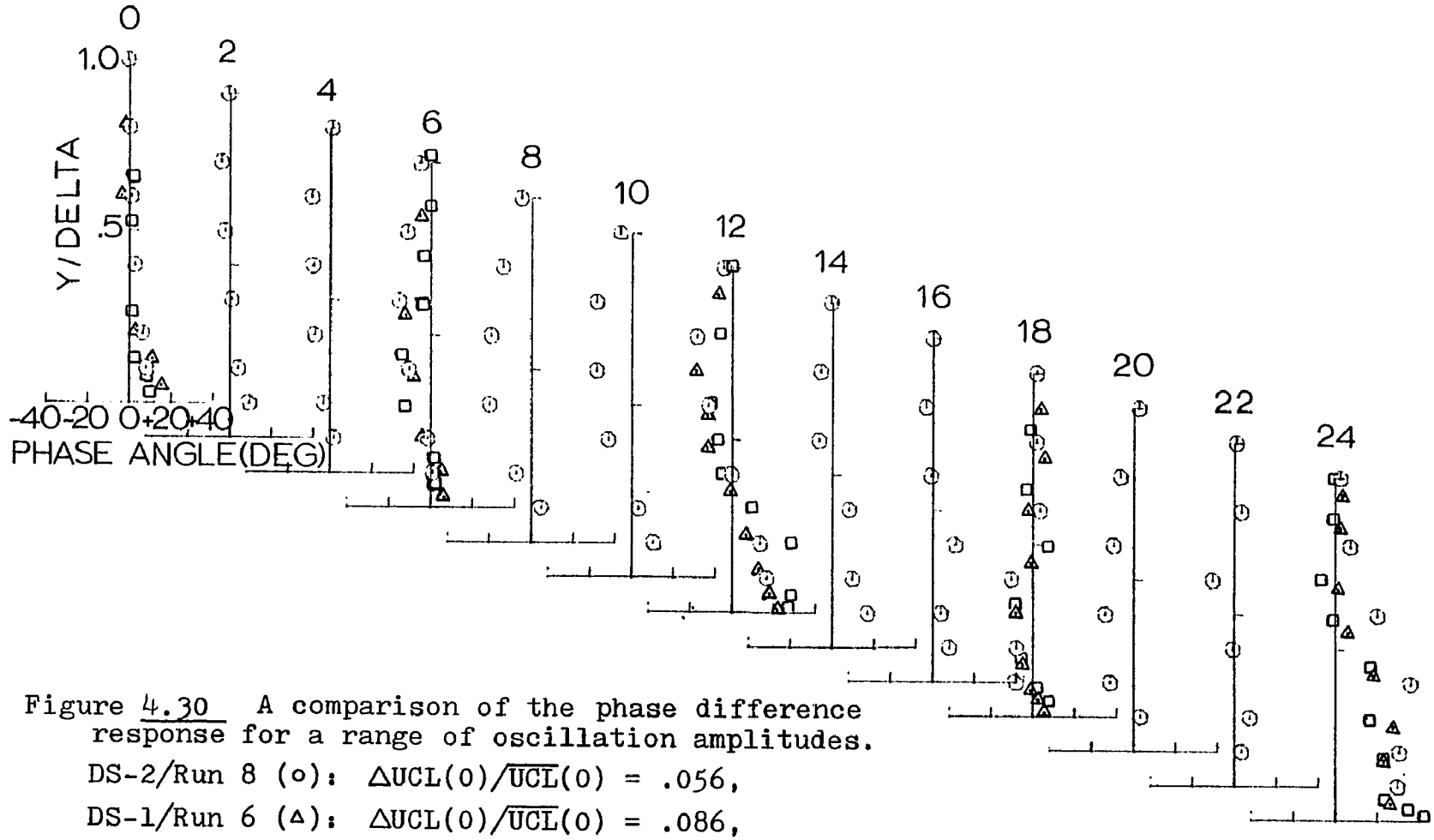

Figure 4.30 A comparison of the phase difference response for a range of oscillation amplitudes.

DS-2/Run 8 (o): $\Delta UCL(0)/\overline{UCL}(0) = .056$,

DS-1/Run 6 (△): $\Delta UCL(0)/\overline{UCL}(0) = .086$,

DS-1/Run 5 (□): $\Delta UCL(0)/\overline{UCL}(0) = .027$.

$Re_D \cong 120{,}000$, $\bar{\omega}_L = 4.19$, FREQ = 20 Hz.

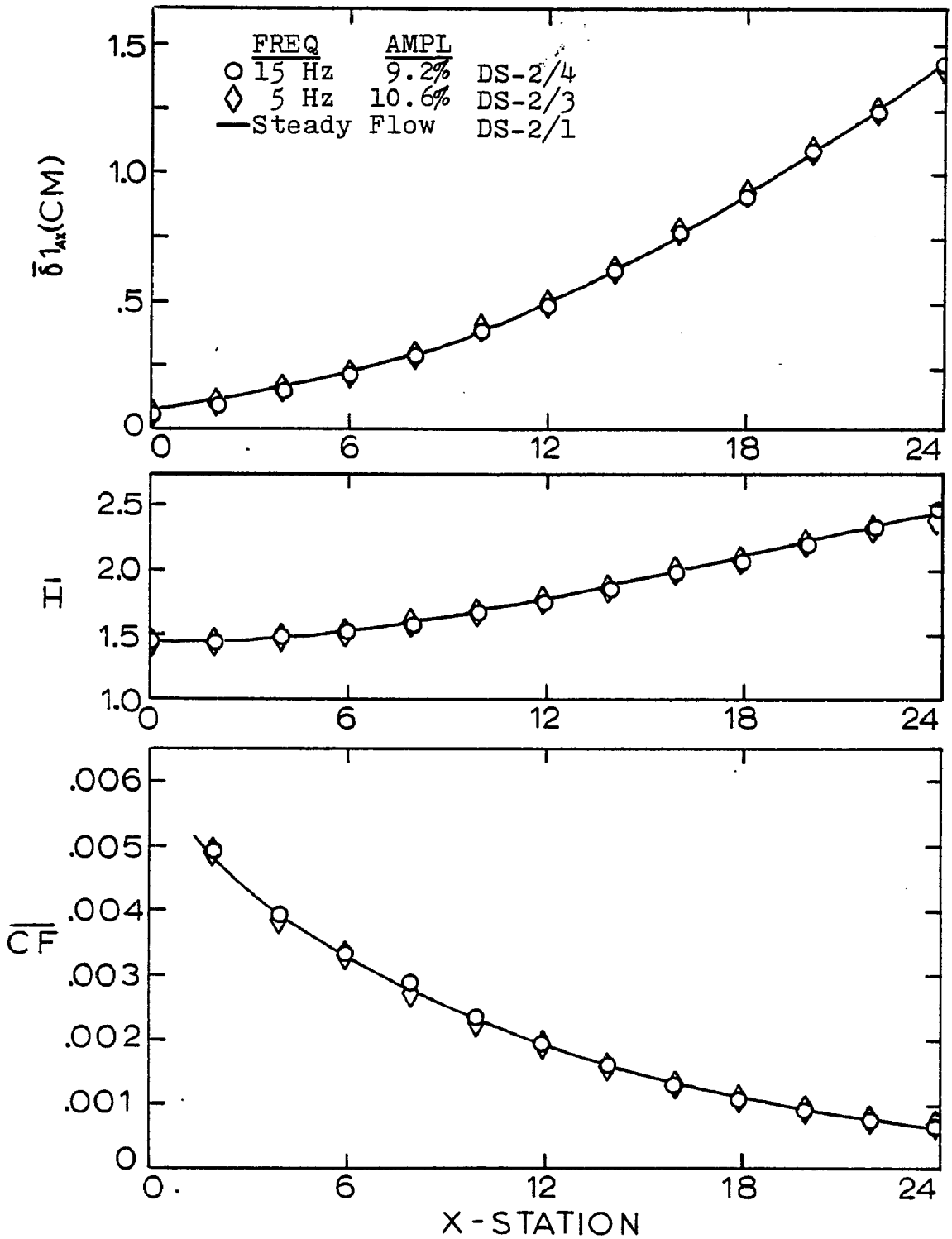

Figure 431 Comparison of steady-flow and time-mean boundary layer parameters for $Re_D \approx 120{,}000$, $\overline{UCL}(0) = 18.29$ m/sec.

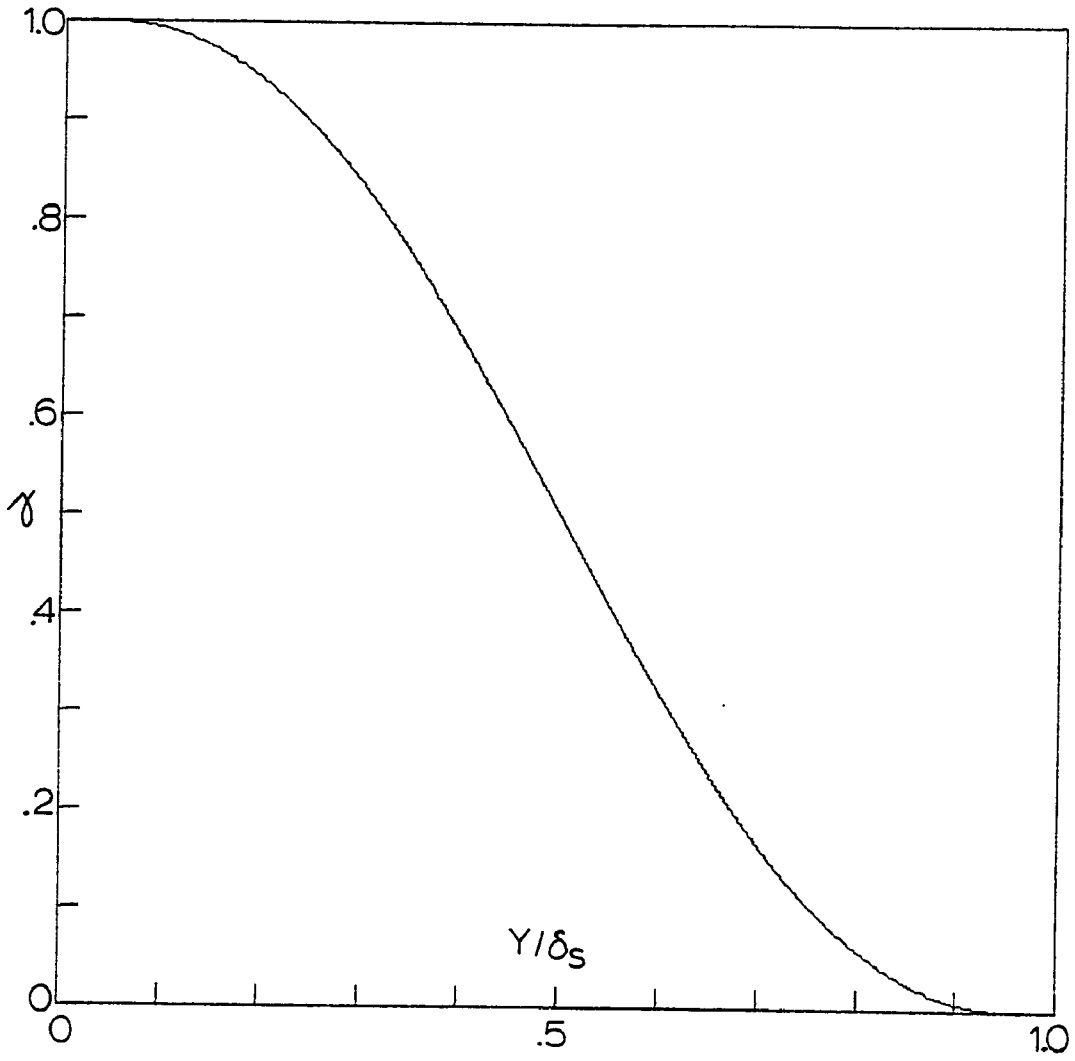

Figure 5.1 Turbulent boundary layer intermittency function, γ, taken from the work of McD Galbraith and Head (40). (The δ_s is a correlating parameter which is not related to the boundary layer thickness. $\delta = Y$ where $\frac{\overline{U}}{UCL} = 0.995$.)

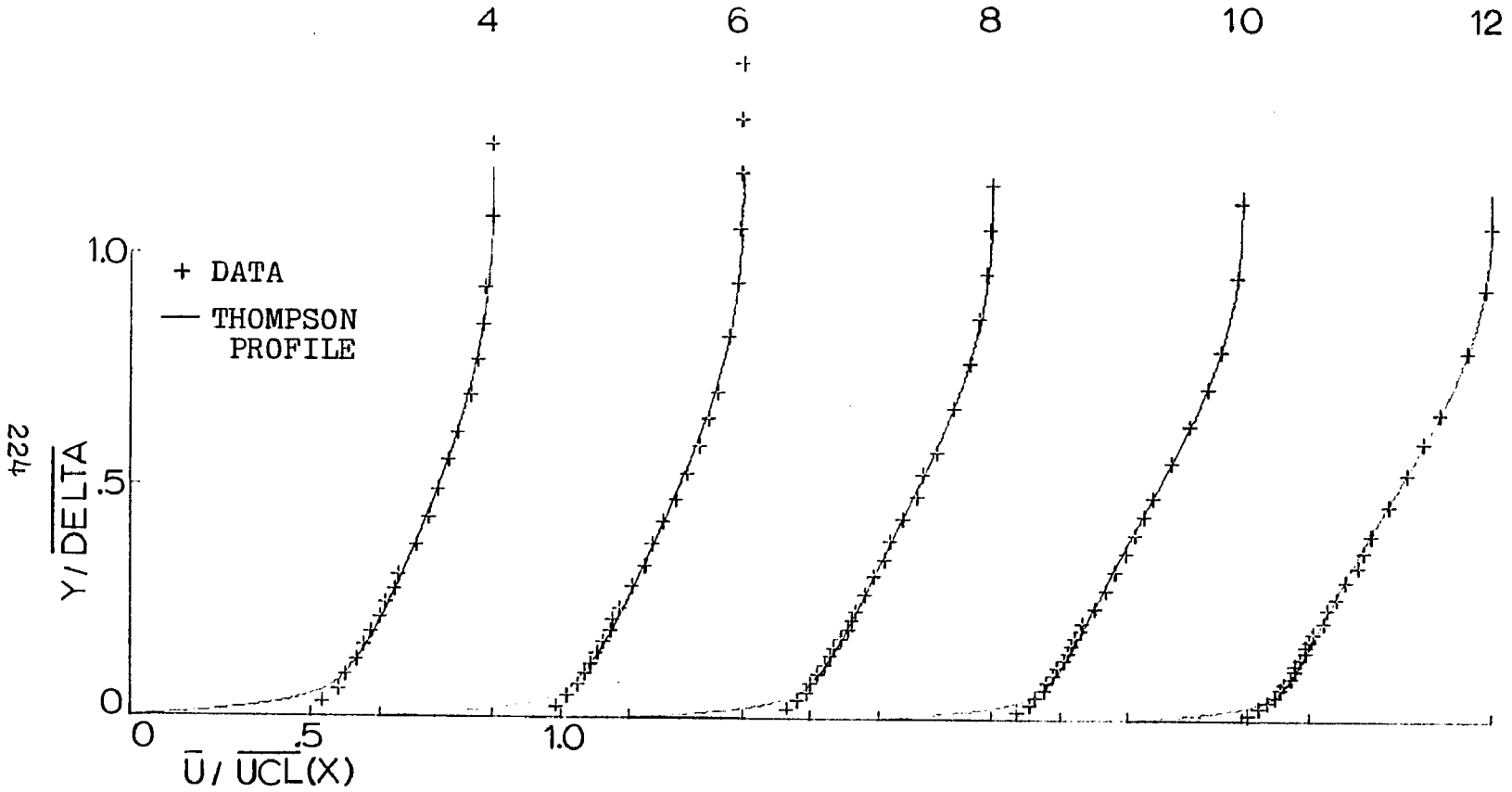

Figure 5.2 Thompson profile fit to the base flow boundary layer velocity data. $\overline{UCL}(0)$ = 18.29 m/sec

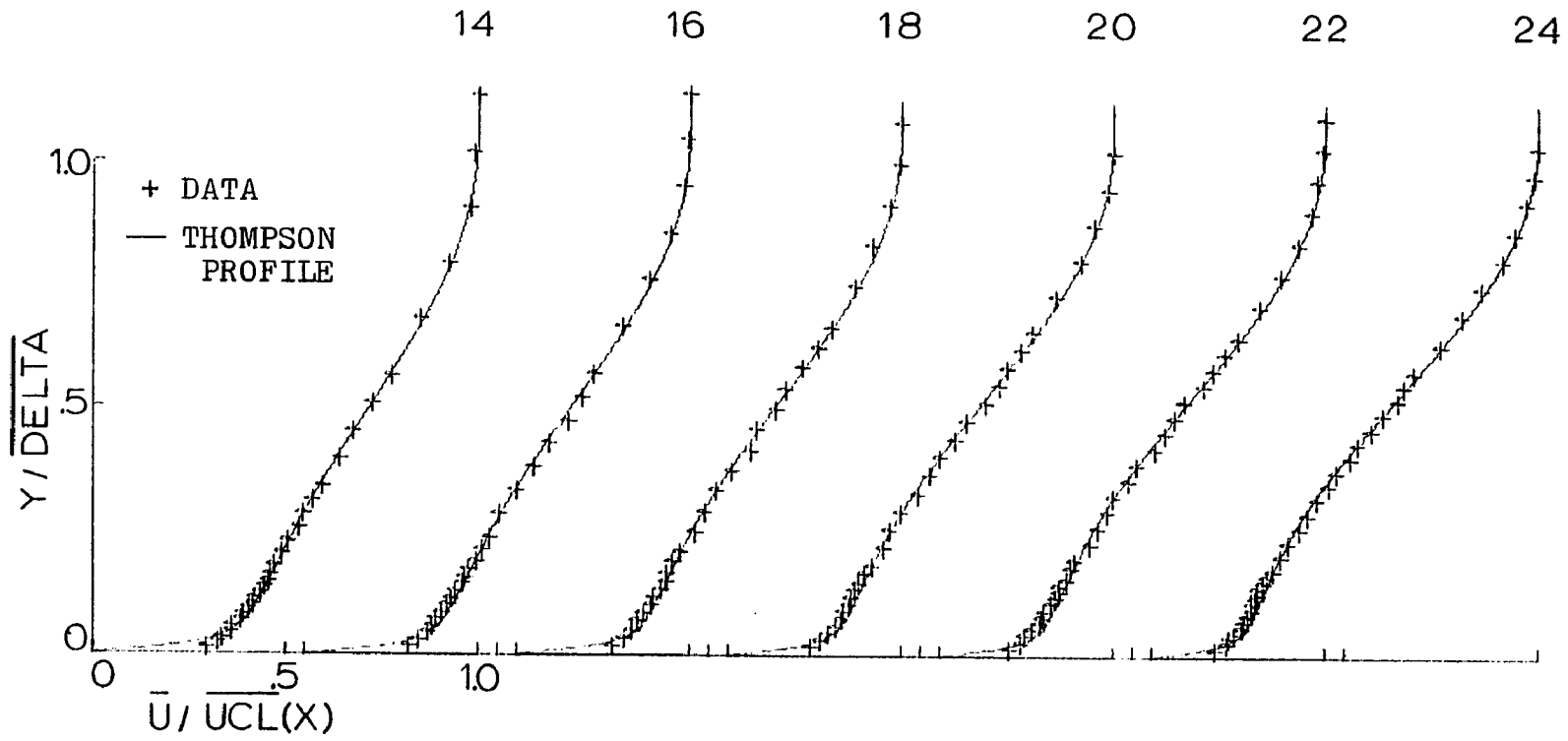

Figure 5.3 Thompson profile fit to the base flow boundary layer velocity data. $\overline{UCL}(0)$ = 18.29 m/sec

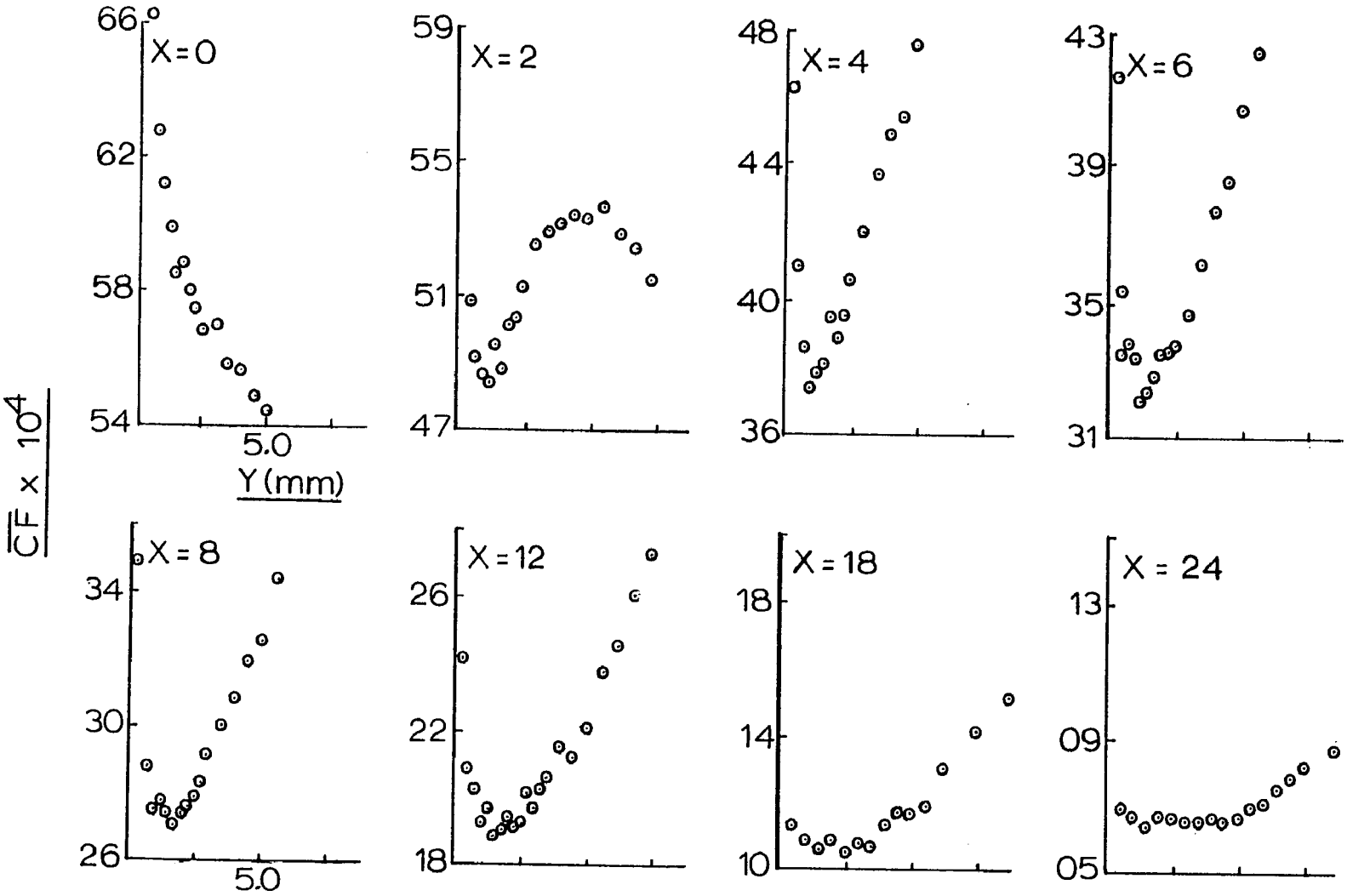

Figure 5.4 Law-of-the-wall solution for the time-mean skin friction coefficient. $\overline{UCL}(0)$ = 18.3 m/sec.

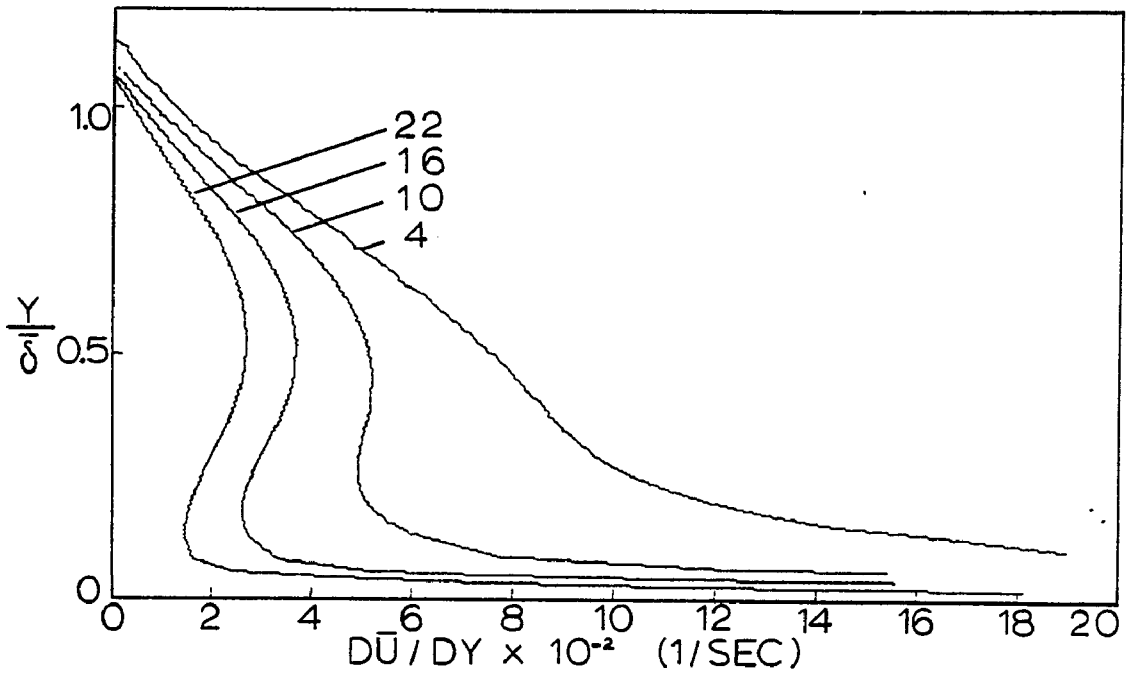

Figure 5.5 Transverse gradient of the streamwise velocity. Based on a Thompson profile representation of time-averaged velocity data.
$\overline{UCL}(0)$ = 18.29 m/sec.

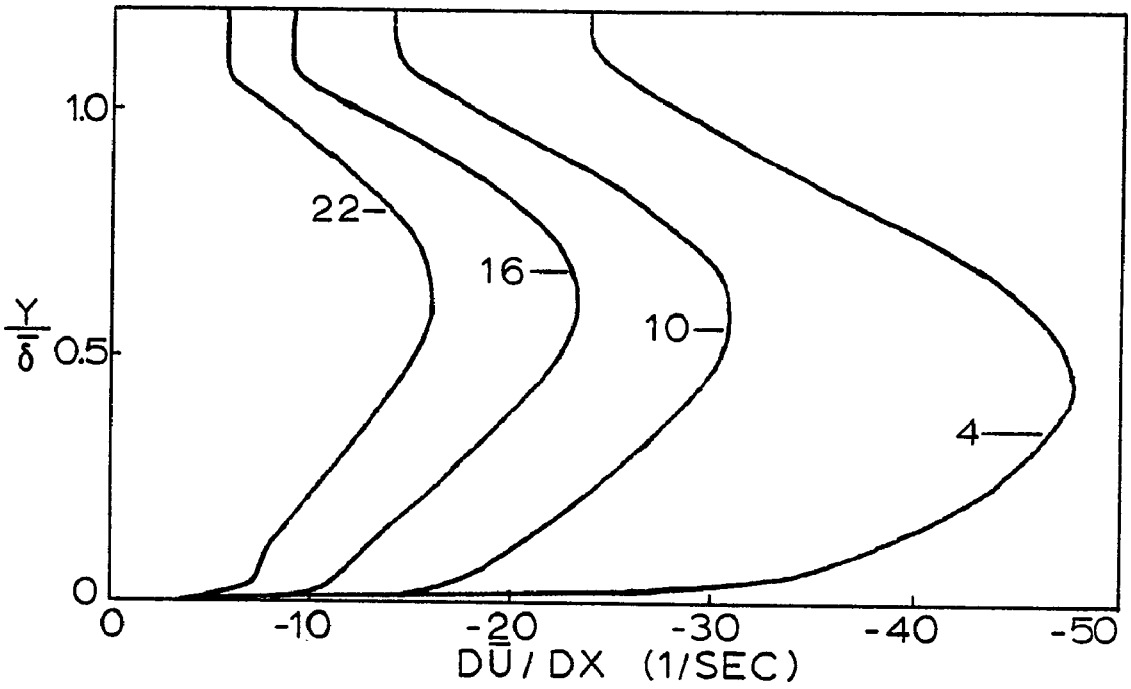

Figure 5.6 Streamwise gradient of the streamwise velocity. Based on a Thompson profile representation of time-averaged velocity data.
$\overline{UCL}(0)$ = 18.29 m/sec.

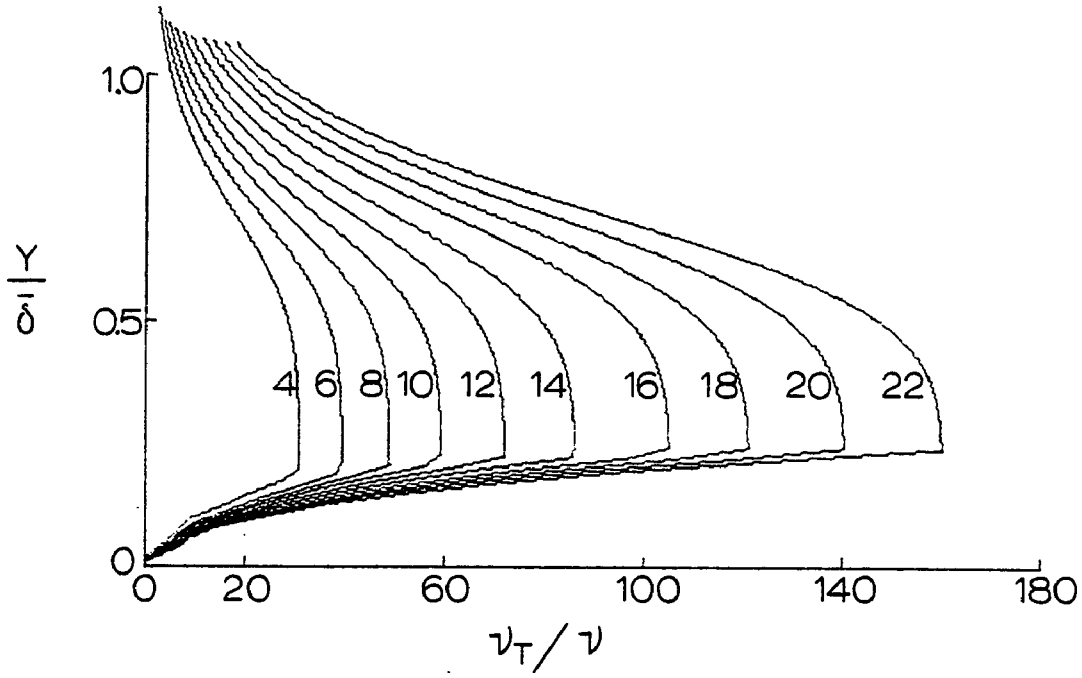

Figure 5.7 Eddy viscosity. Cebeci and Smith (1974) model based on a Thompson profile representation of time-averaged velocity data.

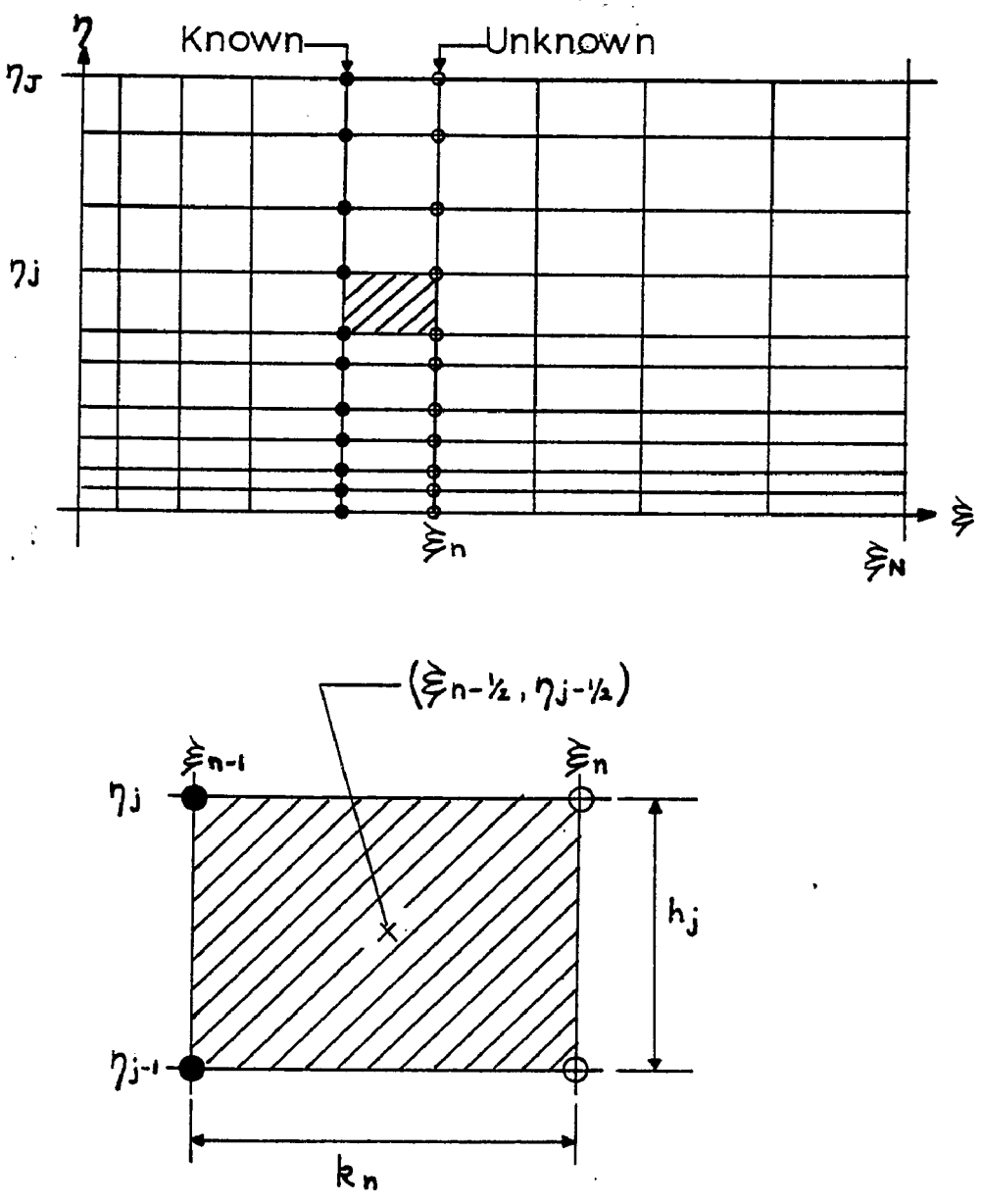

Figure 5.8 Finite difference net for the Keller Box scheme. (Taken from reference (49)).

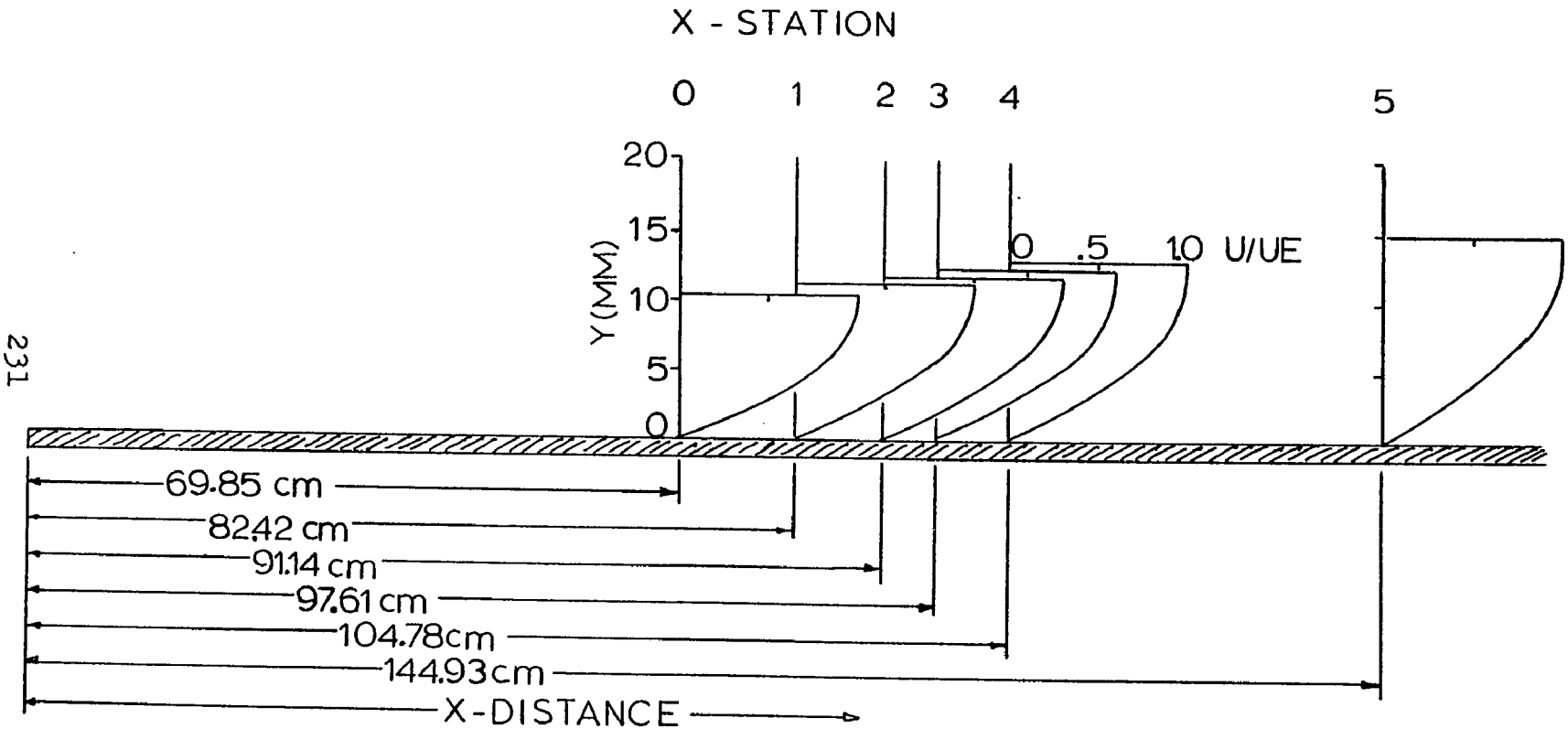

Figure 6.1 Base flow velocity profile development for laminar, Blasius flow, $\overline{UE}$ = 3.0 m/sec, X-stations correspond to case for FREQ = 0.28 Hz.

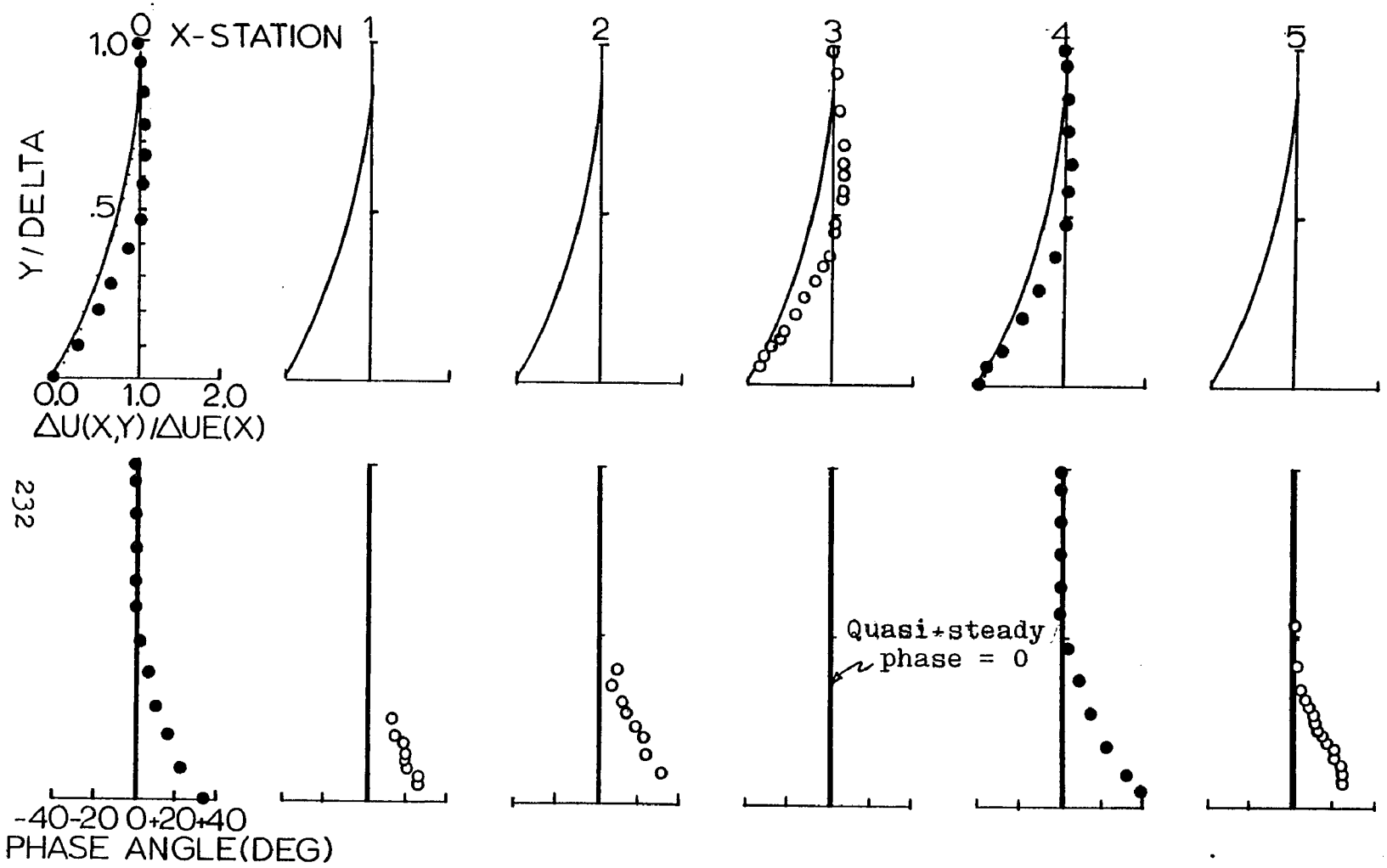

Figure 6.2 Oscillating laminar boundary layer. Comparison of the quasi-steady response (solid line) to the data of Hill and Stenning (∘), and the solution of Lighthill (•).
X-station/$\bar{\omega}x$: 0/.40, 1/.47, 2/.52, 3/.56, 4/.60, 5/.83; FREQ=0.28Hz.

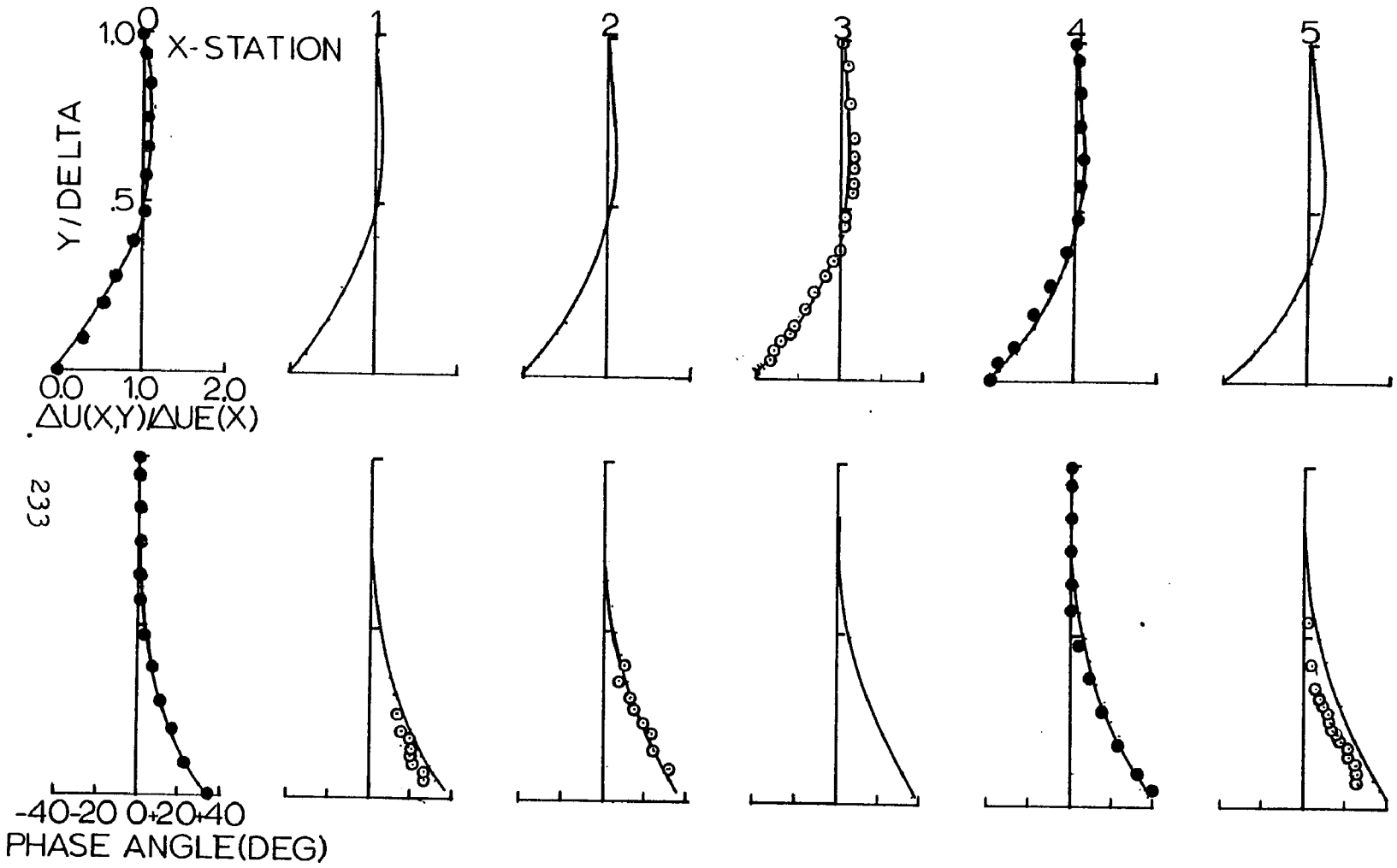

Figure 6.3 Oscillating laminar boundary layer. Comparison of the theory (solid line) to the data of Hill and Stenning (°) and the solution of Lighthill (•).
X-station/$\bar{\omega}$x: 9/.40, 1/.47, 2/.52, 3/.56, 4/.60, 5/.83; FREQ=0.28Hz.

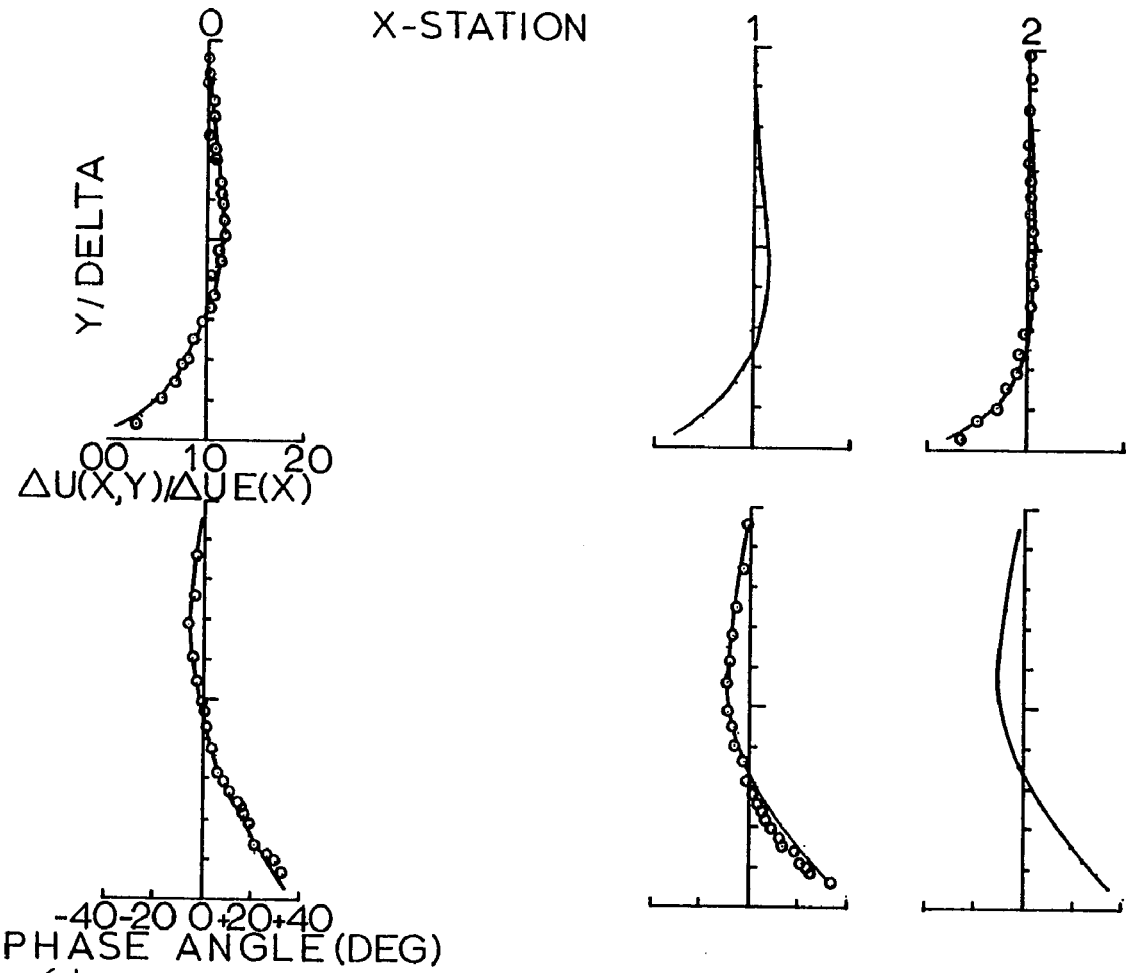

Figure 6.4 Oscillating laminar boundary layer.
Comparison of the theory (solid line) to the data of Hill and Stenning (o). $\overline{UE}$ = 3.0 m/sec, FREQ = 1.02 Hz.
X-station/x(mm)/$\bar{\omega}_x$ 0/699/1.48, 1/1184/2.48, 2/1260/2.65

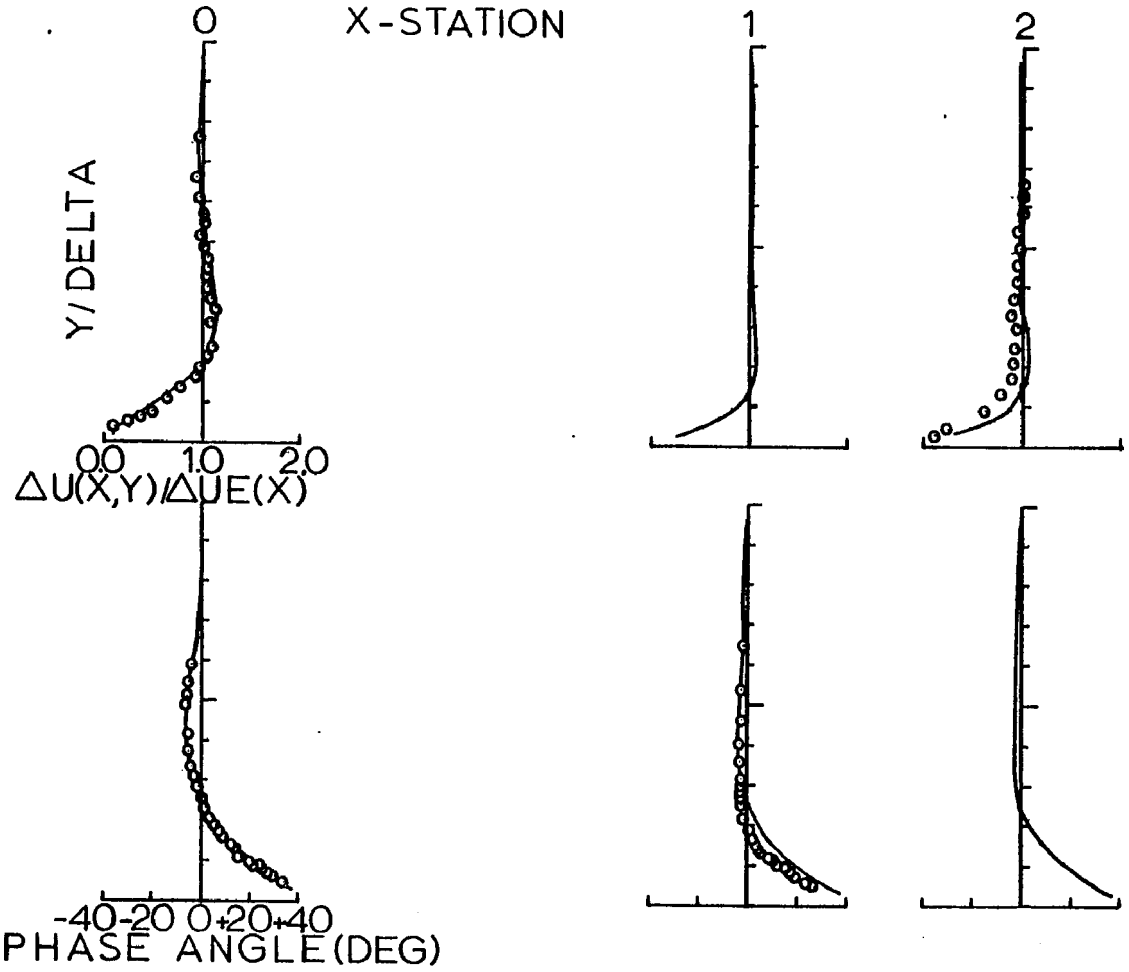

Figure 6.5 Oscillatory laminar boundary layer.
Comparison of the theory (solid line) to the data of Hill and Stenning (o). $\overline{UE}$ = 3.0 m/sec, FREQ = 3.5 Hz.
X-station/x(mm)/$\bar{\omega}_x$ 0/699/4.98 1/1082/7.72 2/1298/9.26

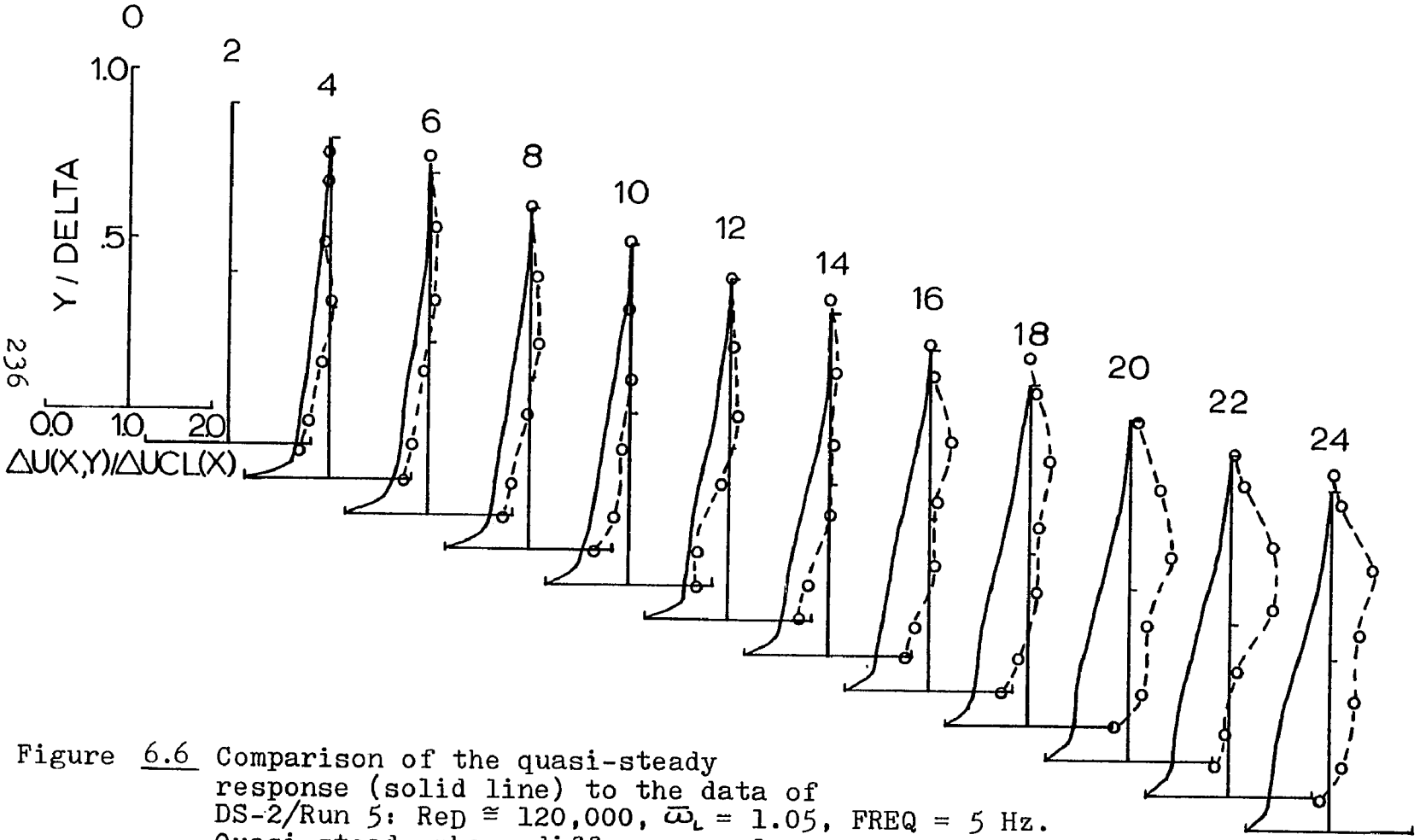

Figure 6.6 Comparison of the quasi-steady response (solid line) to the data of DS-2/Run 5: $Re_D \cong 120{,}000$, $\bar{\omega}_L = 1.05$, FREQ = 5 Hz. Quasi-steady phase difference = 0.

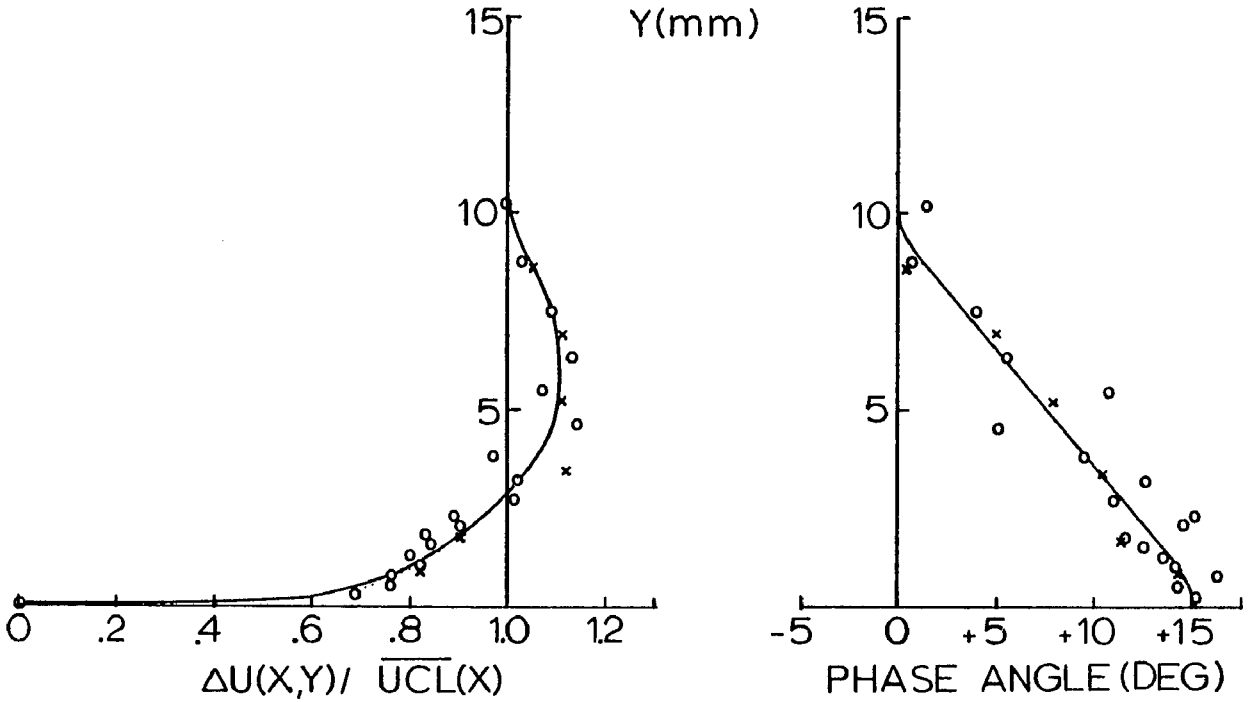

Figure 6.7 Initial Conditions. $Re_D \cong 120{,}000$, $\omega_L = 2.09$, FREQ = 10 Hz. Curve fit (——), DS-2/Run 16 (∘), DS-2/Run 6 (×).

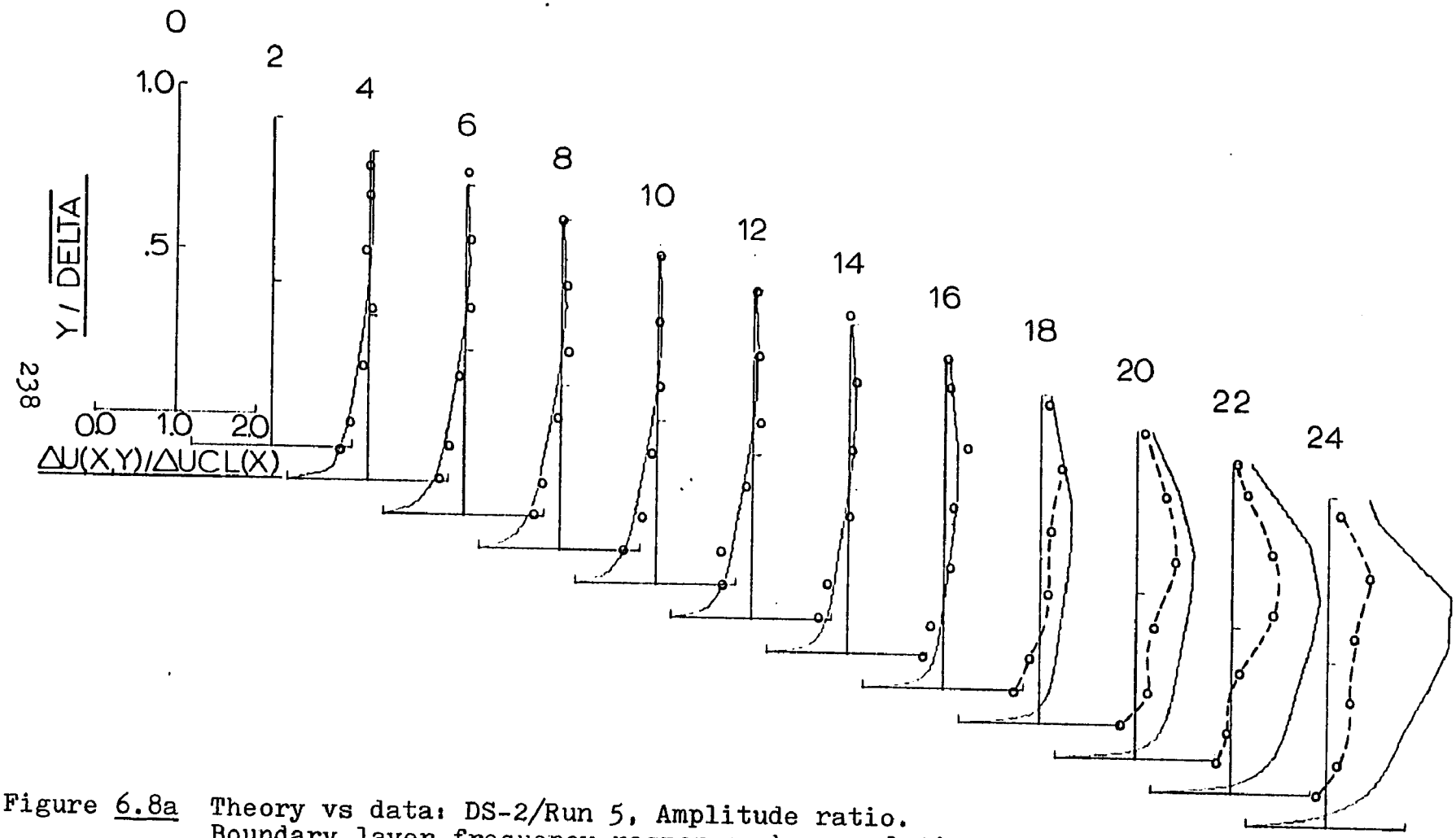

Figure 6.8a Theory vs data: DS-2/Run 5, Amplitude ratio.
Boundary layer frequency response shown relative to the local (x-station), centerline, velocity oscillation.
Data (---o--), DS-2/Run 5: $Re_D \cong 120{,}000$, $\bar{\omega}_L = 1.05$, FREQ= 5 Hz.
Theory(———).

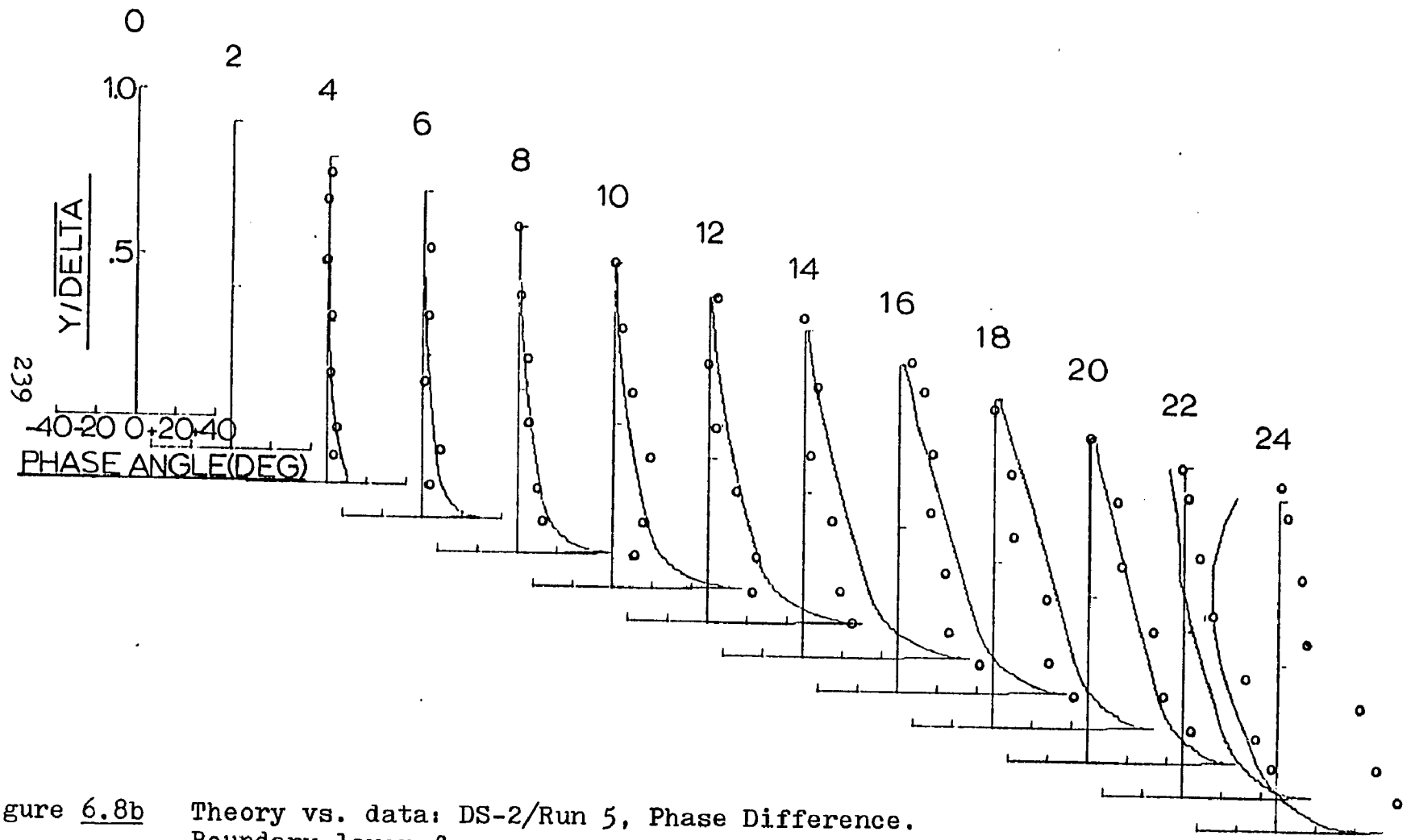

Figure 6.8b Theory vs. data: DS-2/Run 5, Phase Difference.
Boundary layer frequency response shown relative to the local (x-station), centerline, velocity oscillation.
Data (---o--), DS-2/Run 5, $Re_D \cong 120{,}000$, $\bar{\omega}_t = 1.05$, FREQ= 5 Hz.
Theory(———).

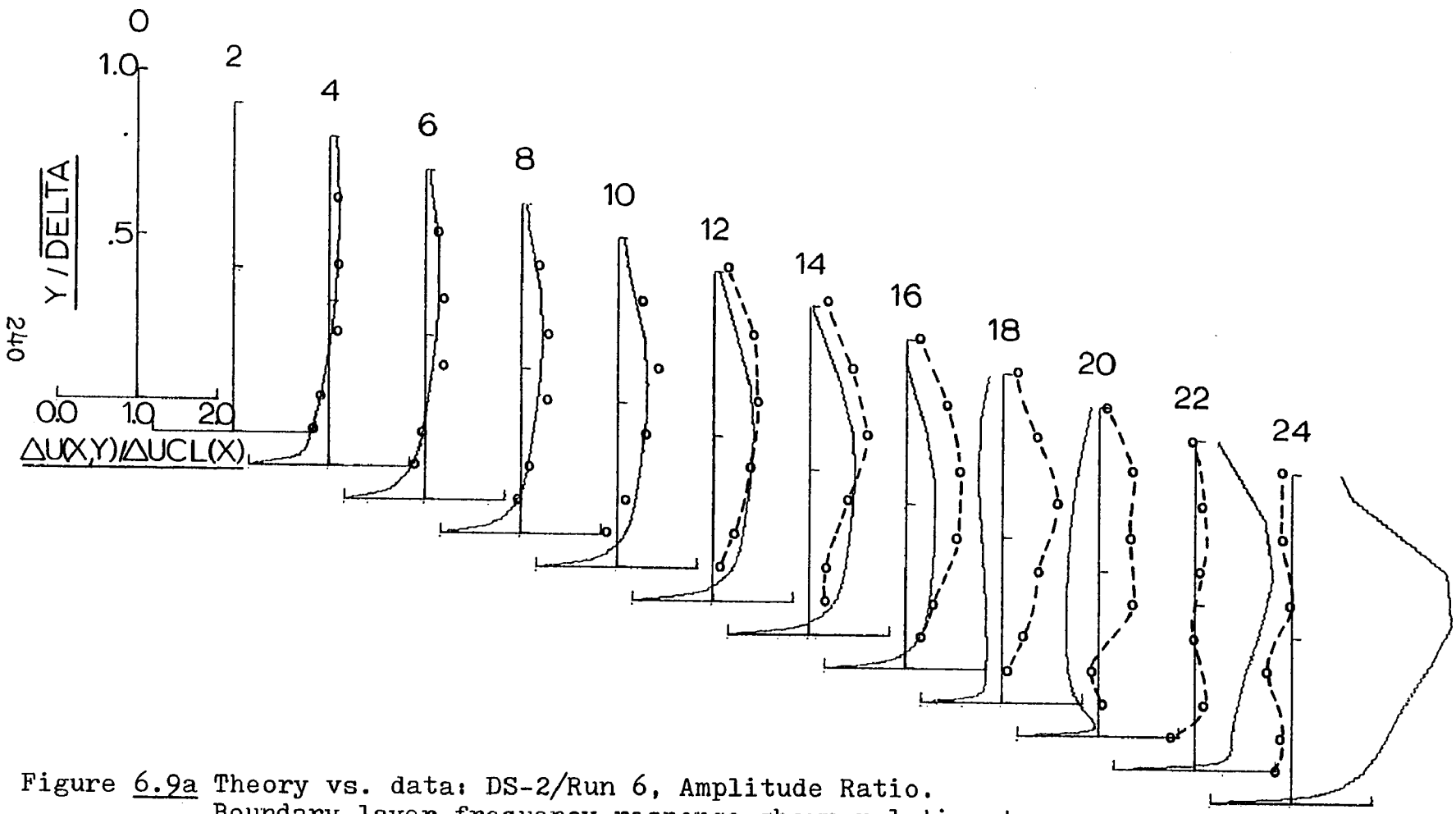

Figure 6.9a Theory vs. data: DS-2/Run 6, Amplitude Ratio.
Boundary layer frequency response shown relative to the local (x-station), centerline, velocity oscillation.
Data (---o--), DS-2/Run 6: Re_D=116320, $\bar{\omega}_L$ =2.09, FREQ=10 Hz.
Theory(———).

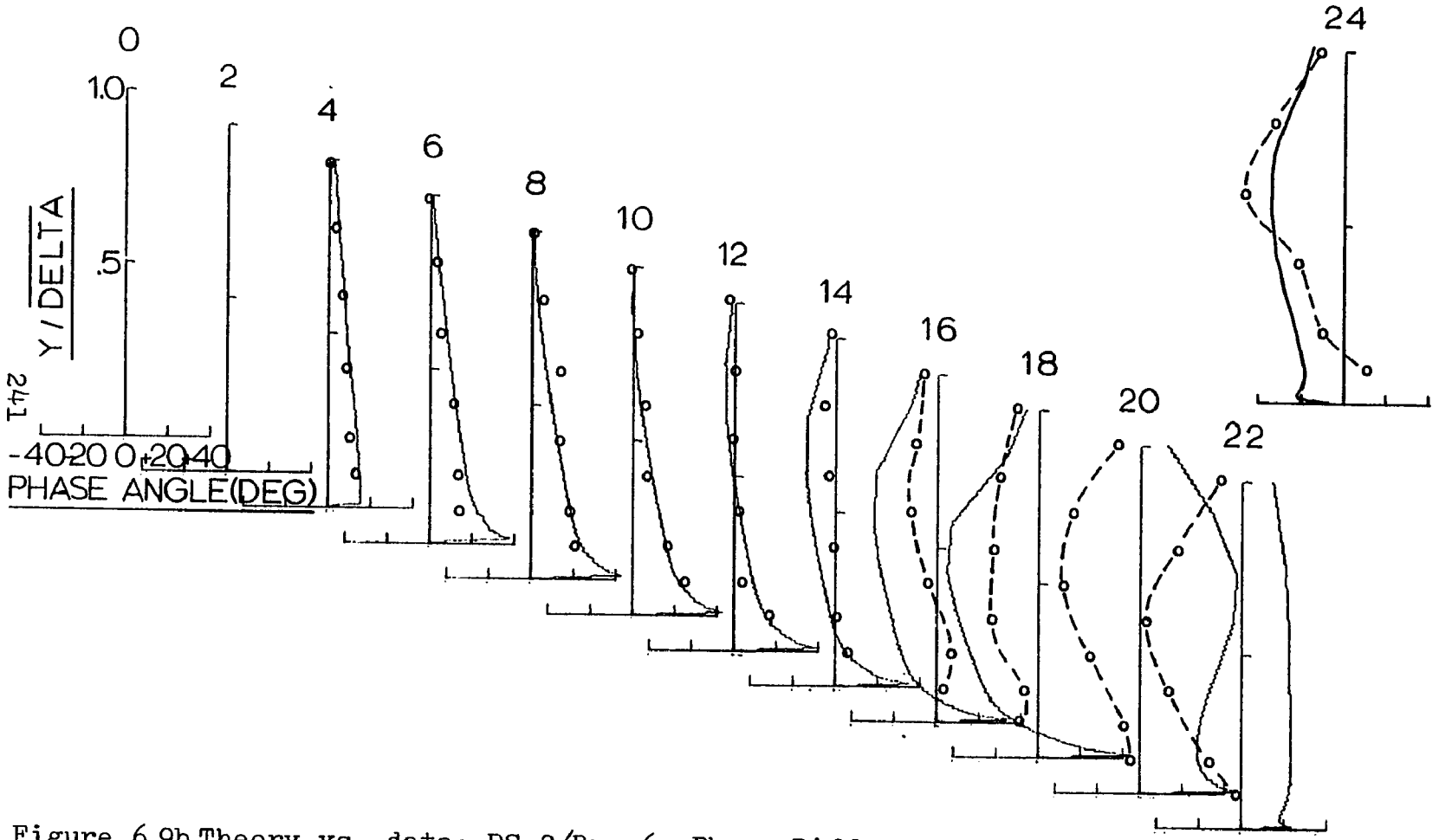

Figure 6.9b Theory vs. data: DS-2/Run 6, Phase Difference.
Boundary layer frequency response shown relative to the local (x-station), centerline, velocity oscillation.
Data (---o--), DS-2/Run 6: Re_D=116320, $\bar{\omega}_L$ =2.09, FREQ=10 Hz.
Theory (———).

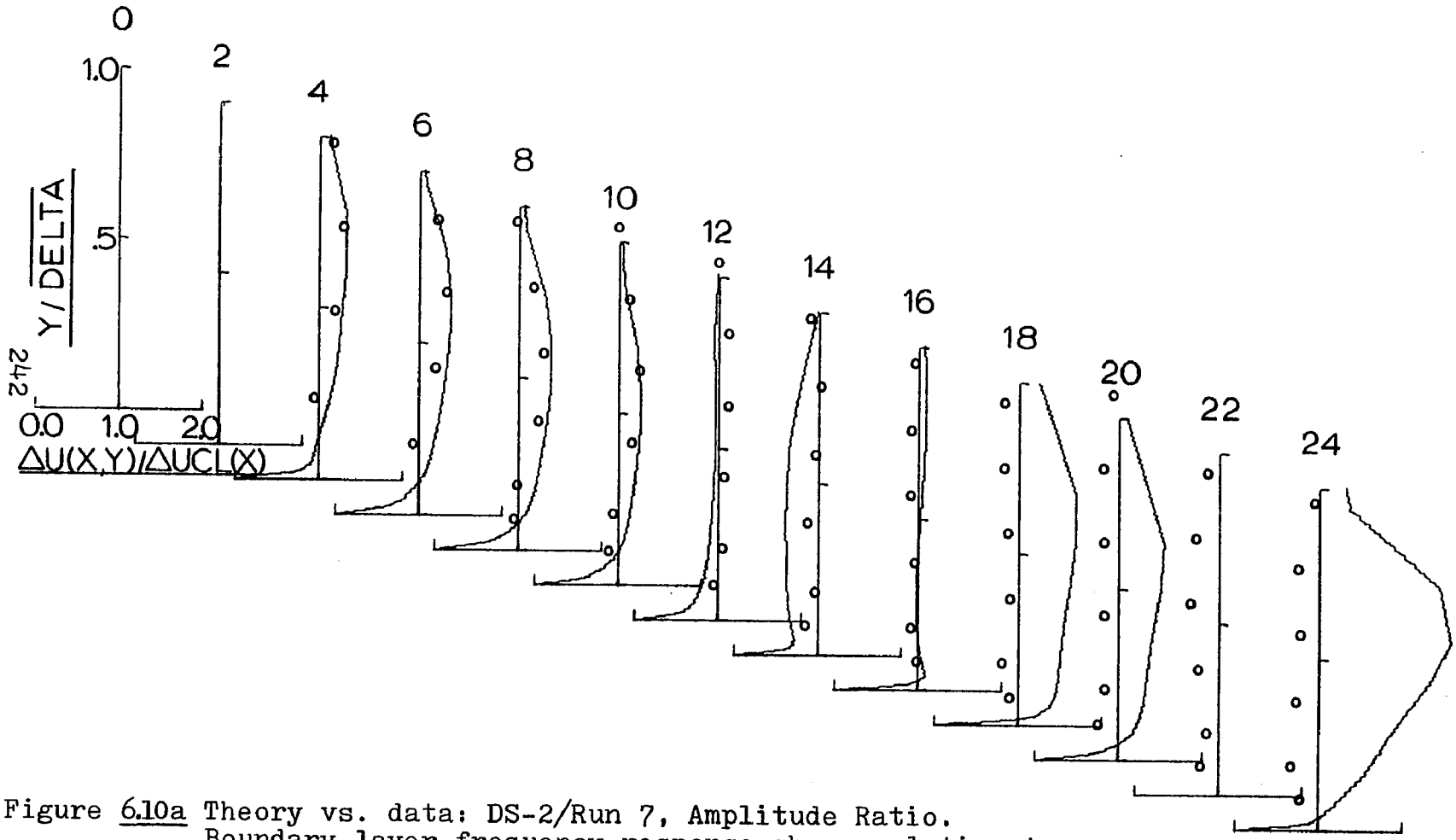

Figure 6.10a Theory vs. data: DS-2/Run 7, Amplitude Ratio.
Boundary layer frequency response shown relative to the local (x-station), centerline, velocity oscillation.
Data (---o--), DS-2/Run 7: Re_D=115087, $\bar{\omega}_L$ =3.14, FREQ=15 Hz.
Theory(———).

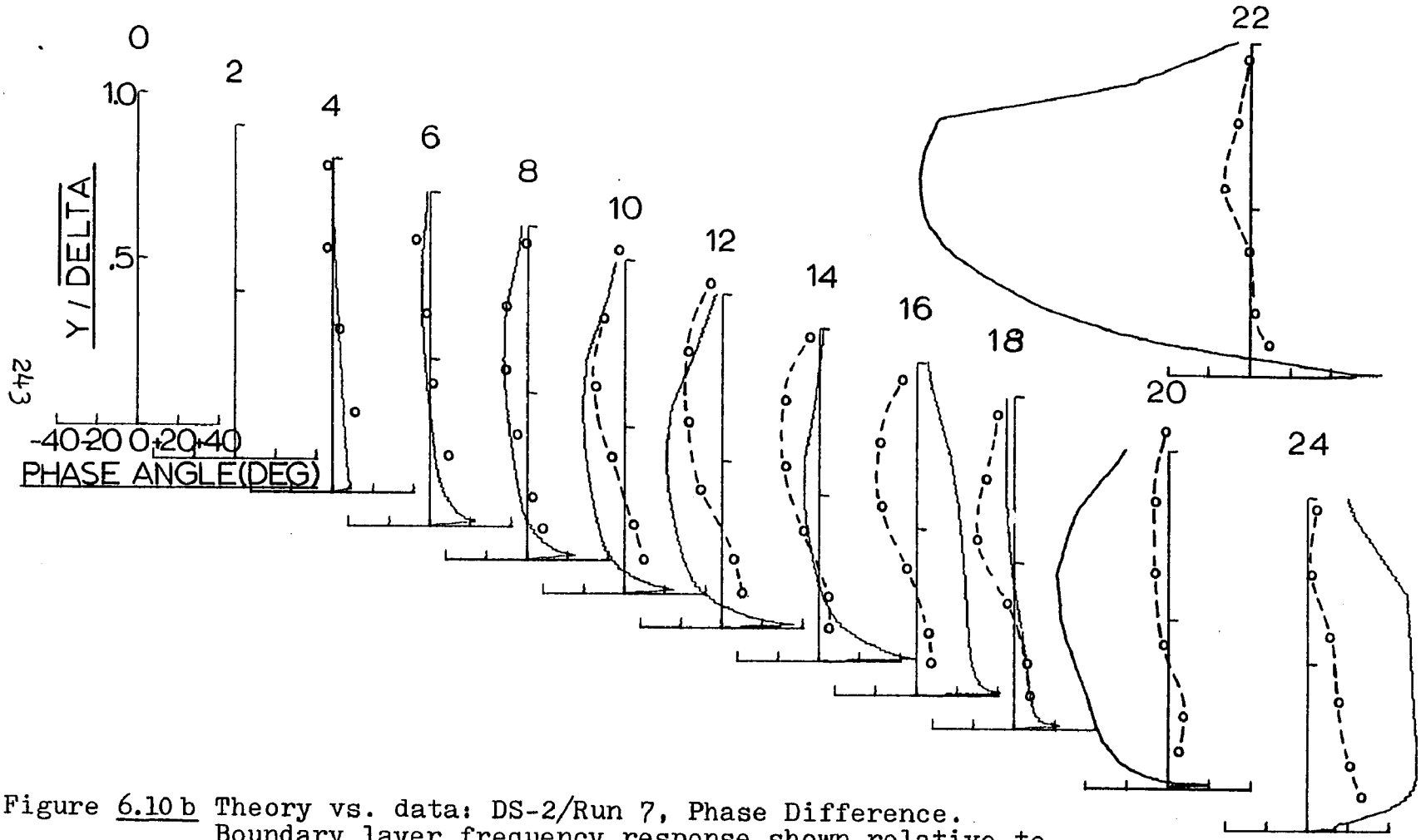

Figure 6.10 b Theory vs. data: DS-2/Run 7, Phase Difference.
Boundary layer frequency response shown relative to the local (x-station), centerline, velocity oscillation.
Data (---o--), DS-2/Run 7: Re_D=115087, $\bar{\omega}_L$ =3.14, FREQ=15 Hz.
Theory(———).

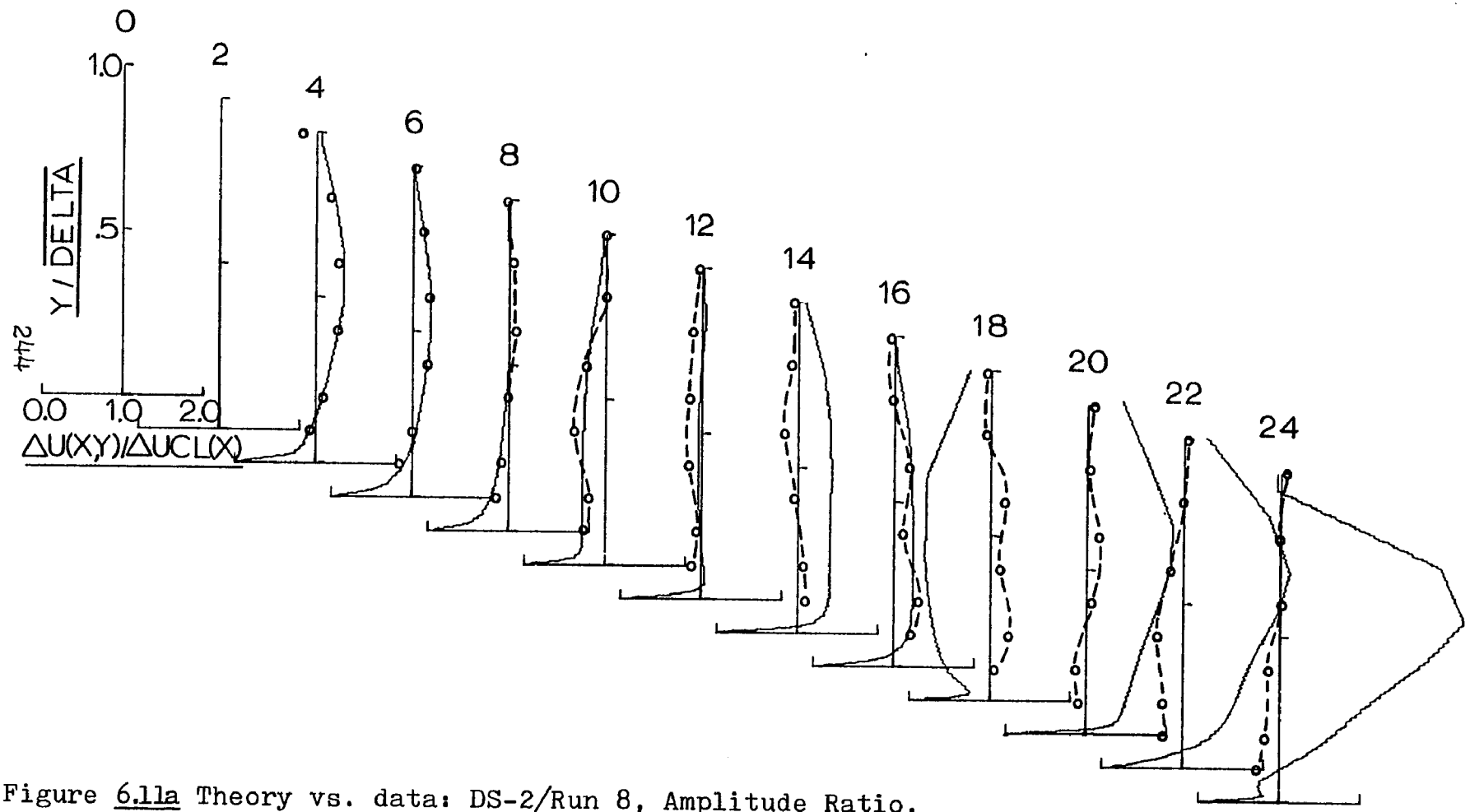

Figure 6.11a Theory vs. data: DS-2/Run 8, Amplitude Ratio.
Boundary layer frequency response shown relative to the local (x-station), centerline, velocity oscillation.
Data (---o--), DS-2/Run 8: Re_D=114768, $\bar{\omega}_L$ =4.19, FREQ=20 Hz.
Theory(———).

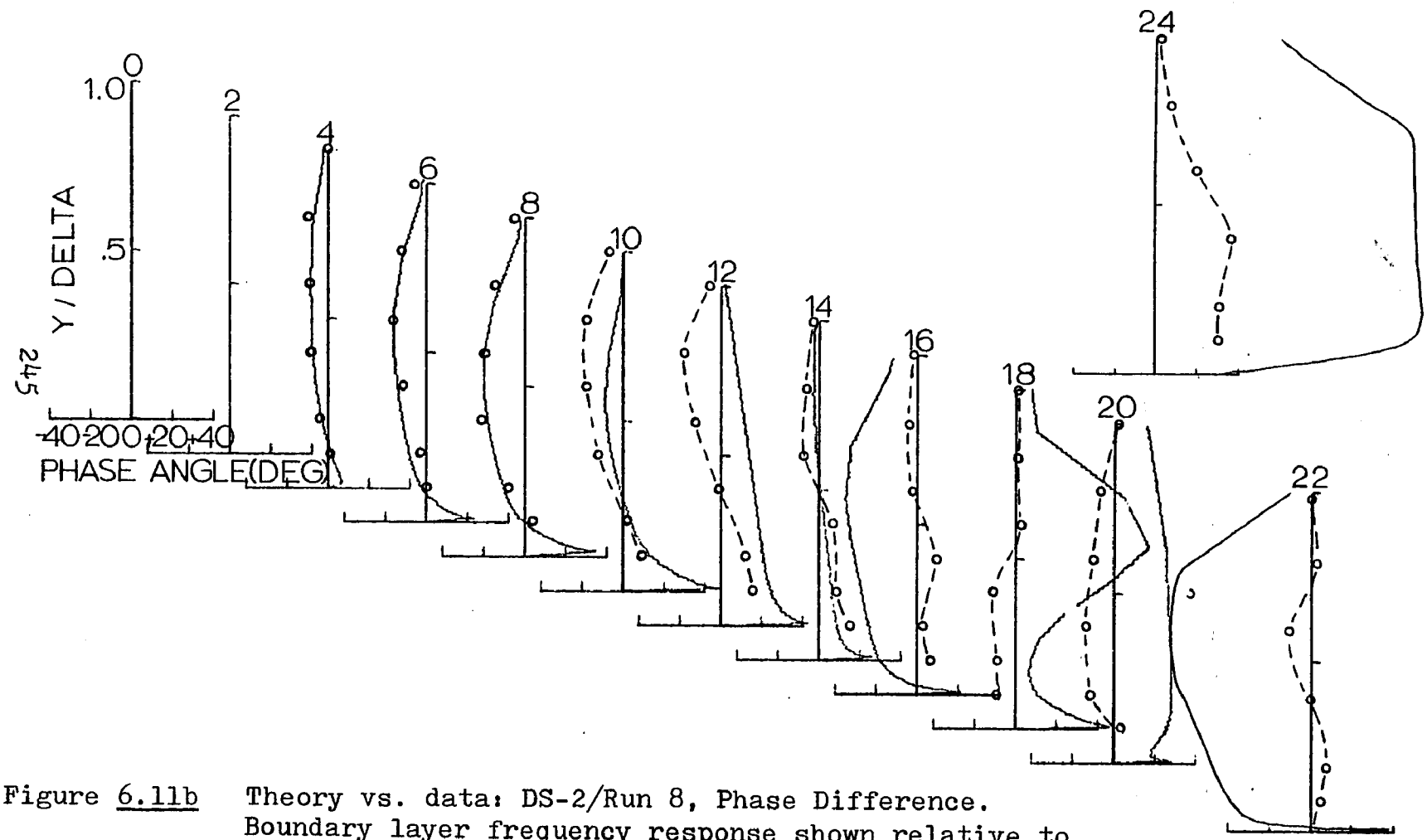

Figure 6.11b Theory vs. data: DS-2/Run 8, Phase Difference.
Boundary layer frequency response shown relative to the local (x-station), centerline, velocity oscillation.
Data (---o---), DS-2/Run 8: Re_D=114768, $\bar{\omega}_t$ =4.19, FREQ=20 Hz.
Theory(———).

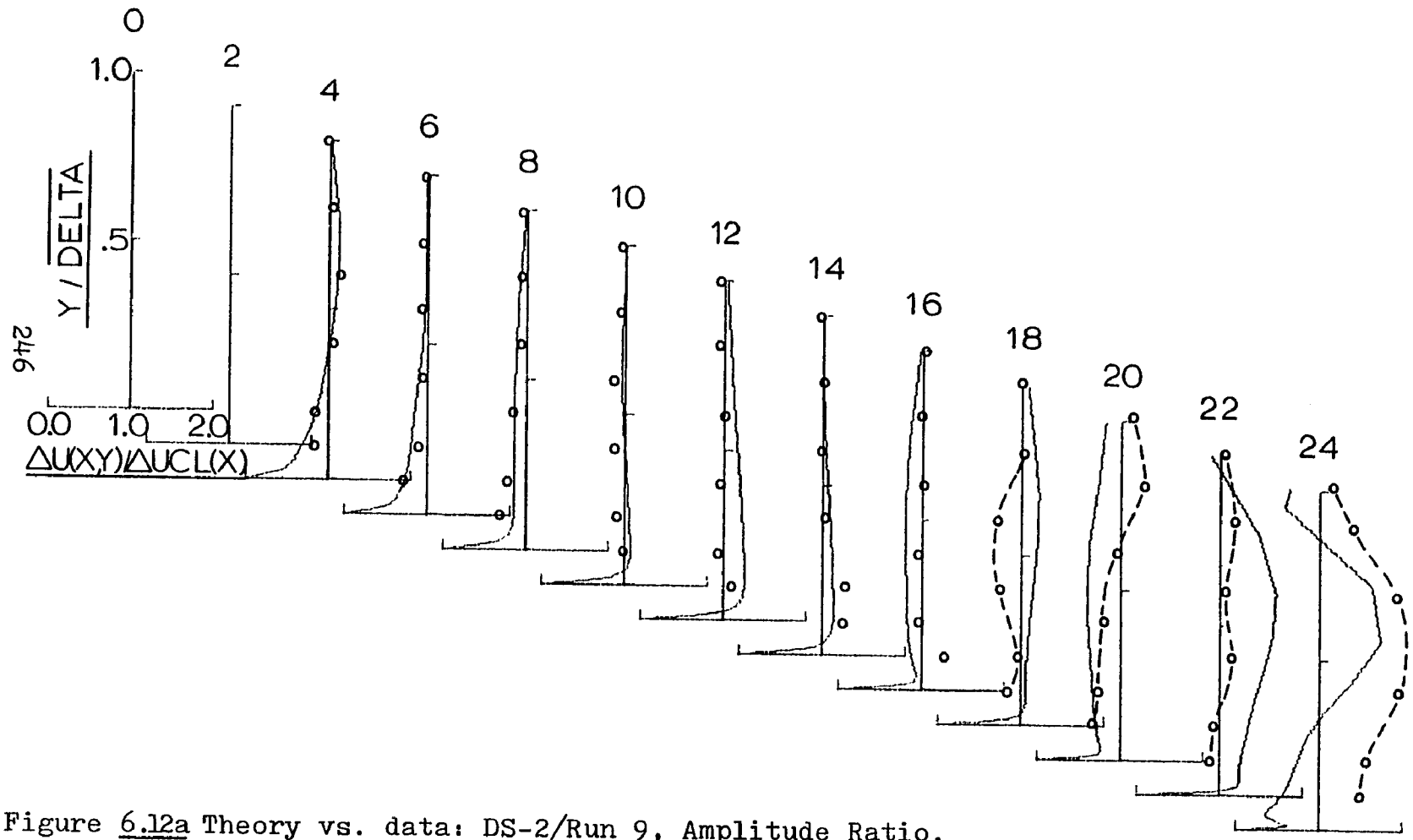

Figure 6.12a Theory vs. data: DS-2/Run 9, Amplitude Ratio.
Boundary layer frequency response shown relative to the local (x-station), centerline, velocity oscillation.
Data (---o---), DS-2/Run 9: Re_D=113402, $\bar{\omega}_L$ =5.24, FREQ=25 Hz.
Theory(———).

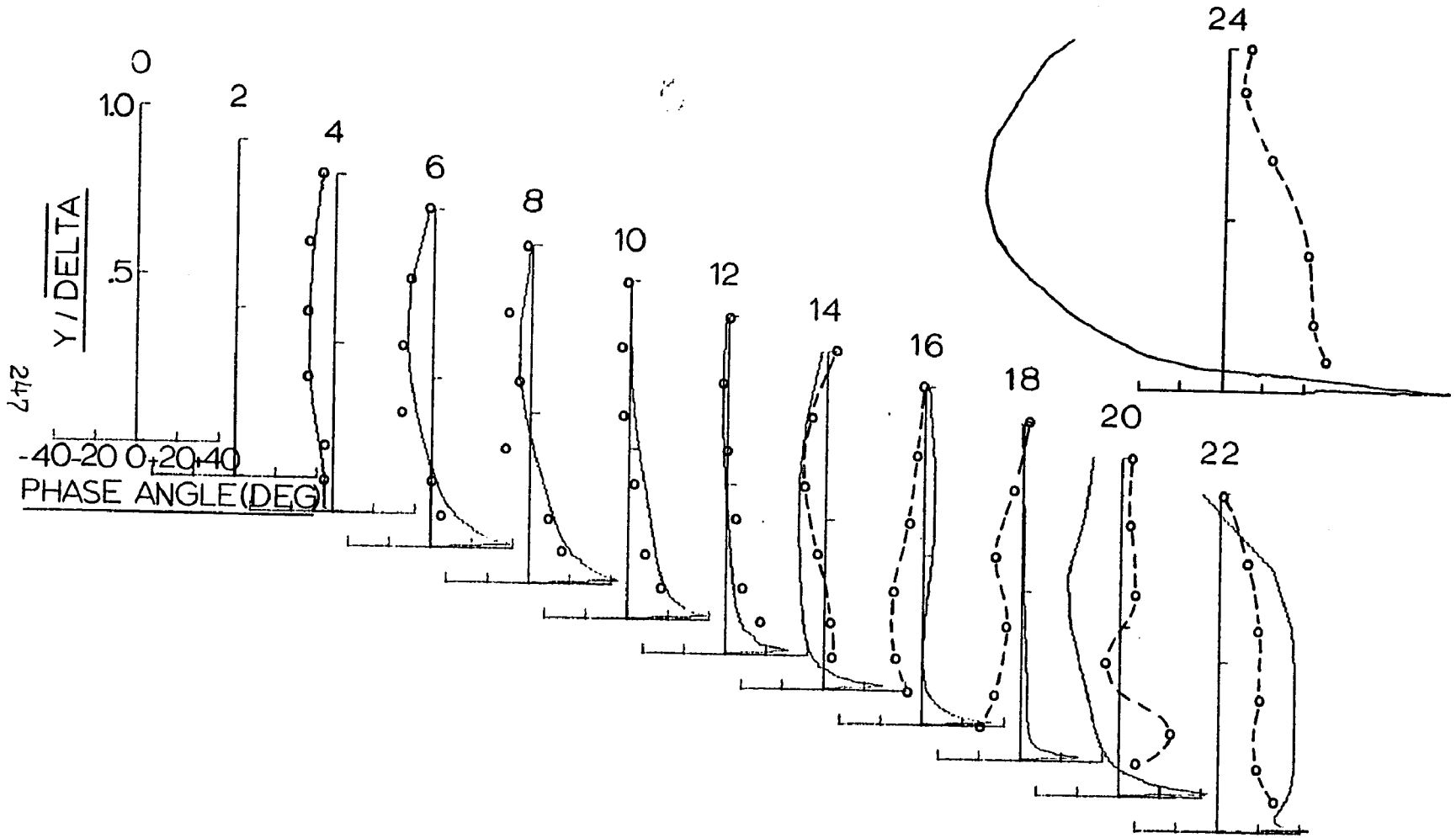

Figure 6.12b Theory vs. data: DS-2/Run 9, Phase Difference.
Boundary layer frequency response shown relative to the local (x-station), centerline, velocity oscillation.
Data (--- --), DS-2/Run 9: Re_D=113402, $\bar{\omega}_L$ =5.24, FREQ=25 Hz.
Theory(———).

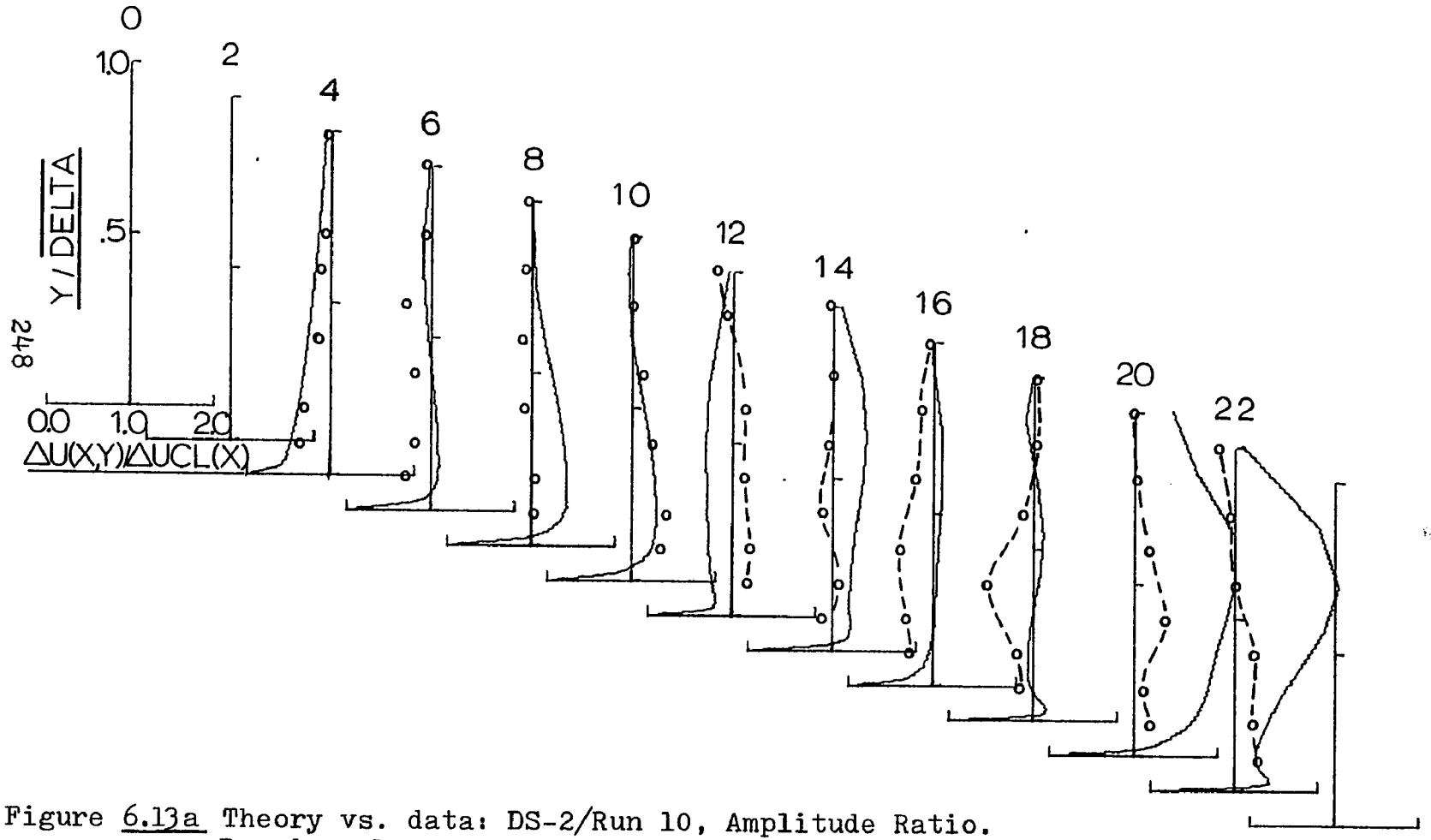

Figure 6.13a Theory vs. data: DS-2/Run 10, Amplitude Ratio.
Boundary layer frequency response shown relative to the local (x-station), centerline, velocity oscillation.
Data (---o---), DS-2/Run 10: Re_D=113560, $\bar{\omega}$ =6.28, FREQ=30 Hz.
Theory(———).

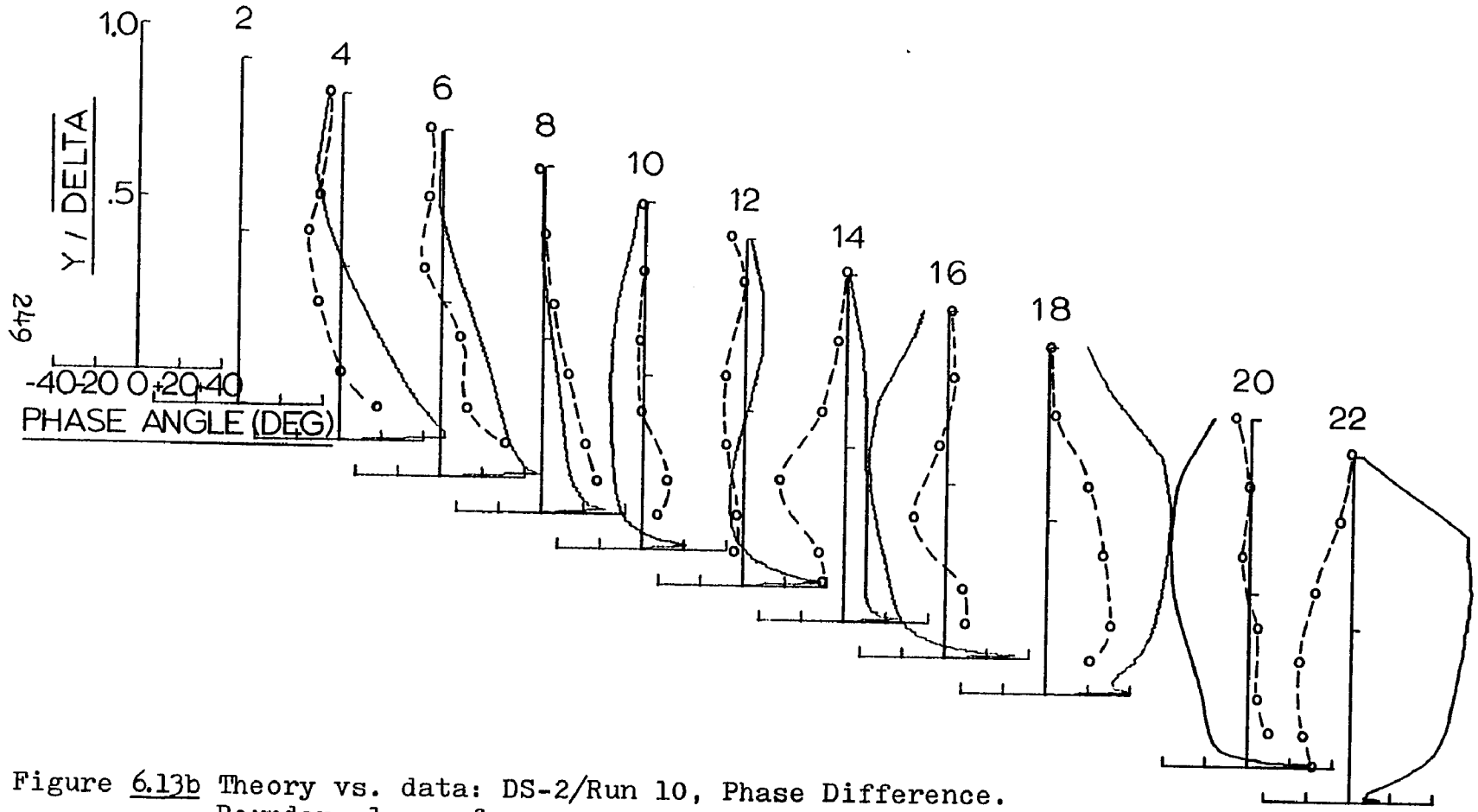

Figure 6.13b Theory vs. data: DS-2/Run 10, Phase Difference.
Boundary layer frequency response shown relative to the local (x-station), centerline, velocity oscillation.
Data (---o---), DS-2/Run 10: Re_D=113560, $\bar{\omega}_L$ =6.28, FREQ=30 Hz.
Theory(———).

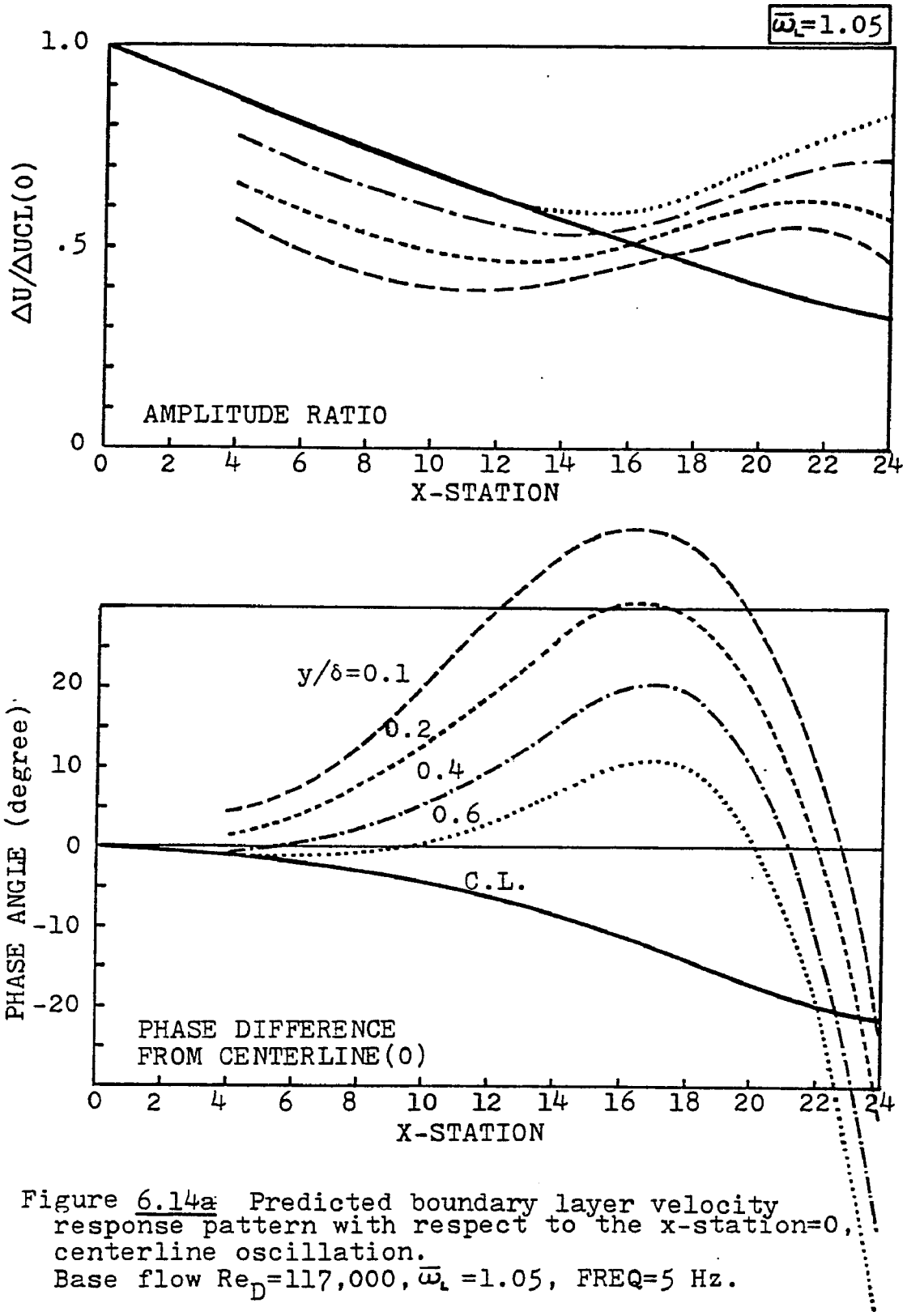

Figure 6.14a Predicted boundary layer velocity response pattern with respect to the x-station=0, centerline oscillation.
Base flow Re_D=117,000, $\bar{\omega}_L$ =1.05, FREQ=5 Hz.

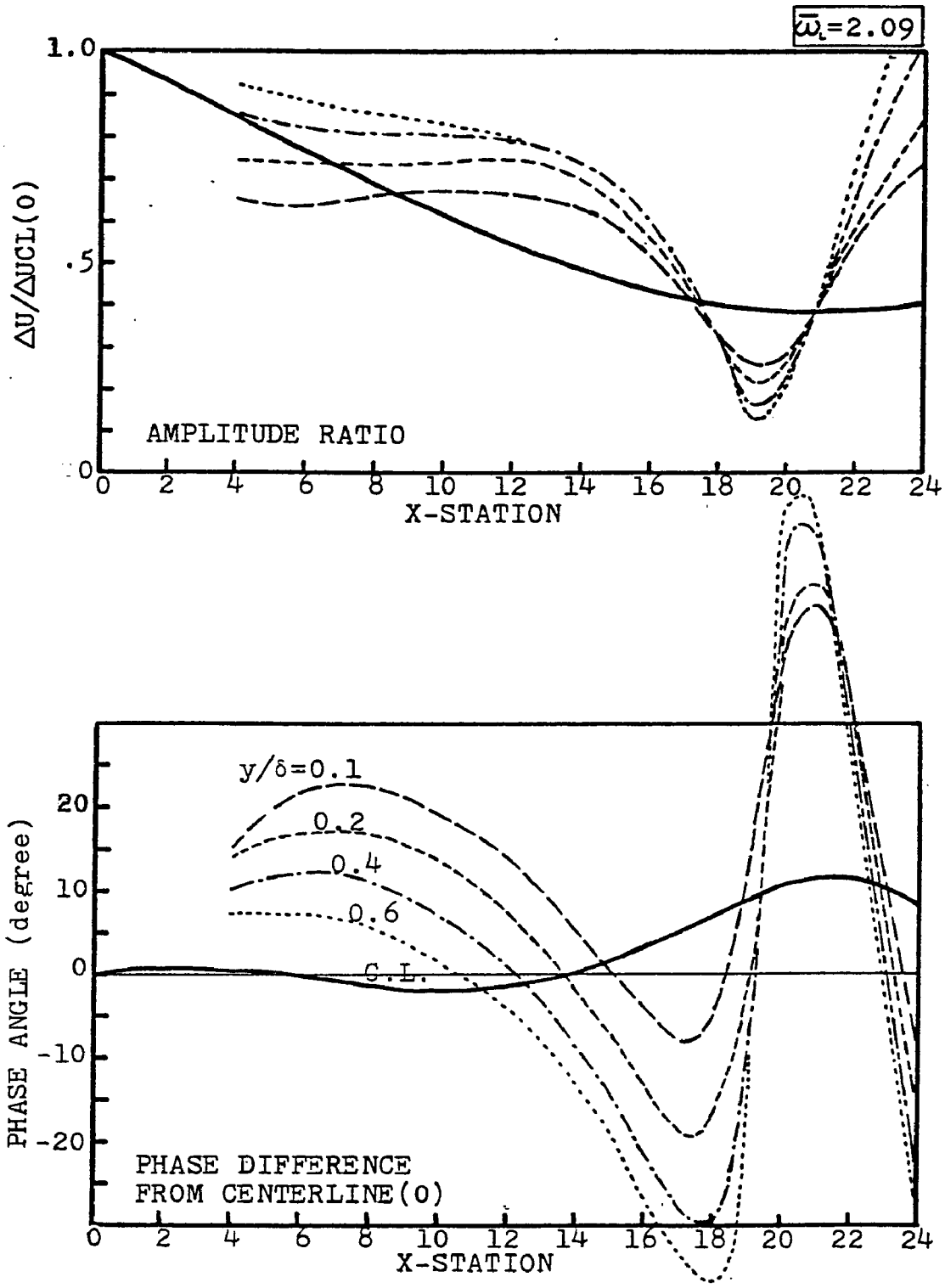

Figure 6.14b Predicted boundary layer velocity response pattern with respect to the x-station=0, centerline oscillation.
Base flow Re_D=117,000, $\bar{\omega}_t$ =2.09, FREQ=10 Hz.

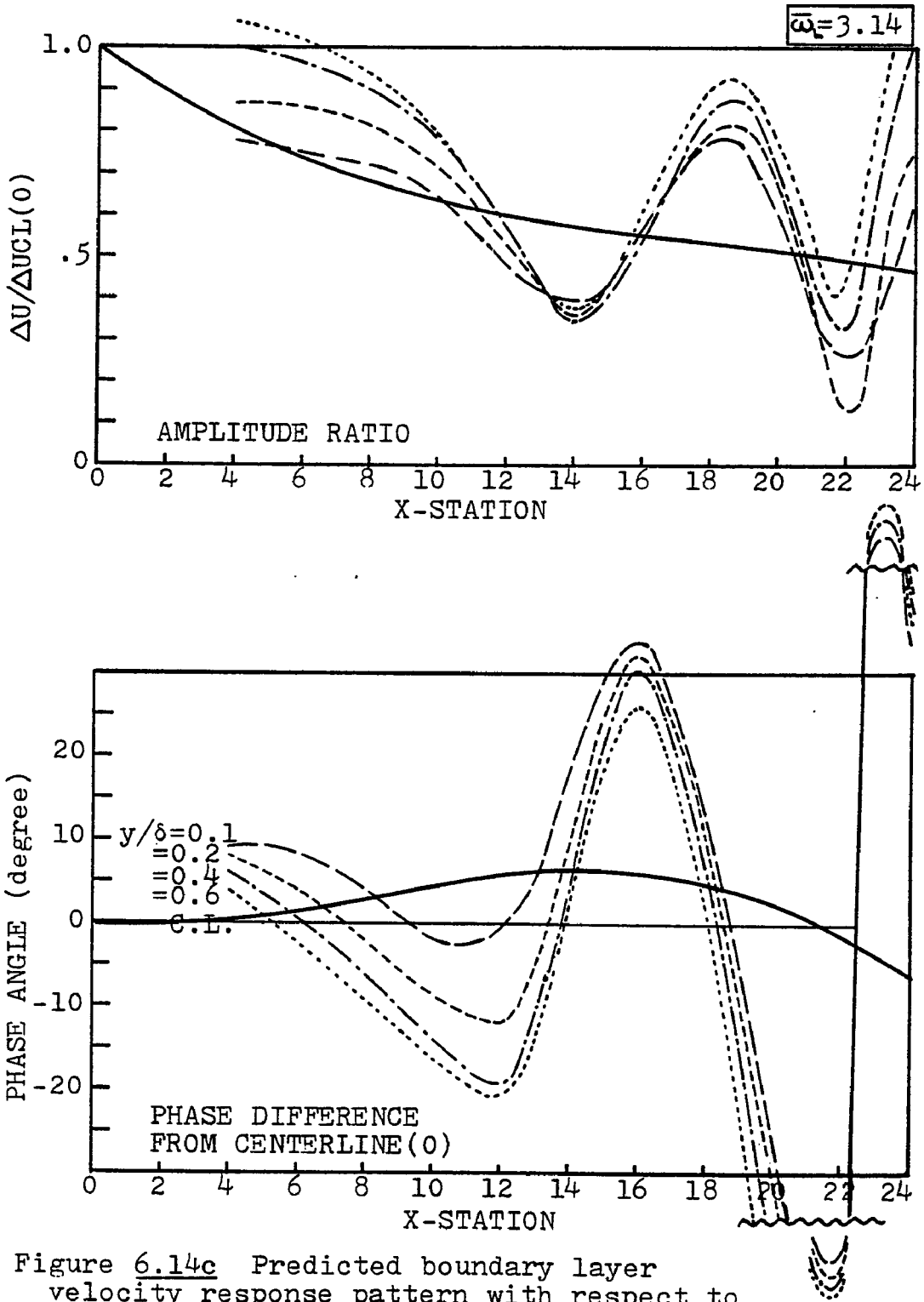

Figure 6.14c Predicted boundary layer velocity response pattern with respect to the x-station=0, centerline oscillation. Base flow Re_D=117,000, $\bar{\omega}_L$=3.14, FREQ=15 Hz.

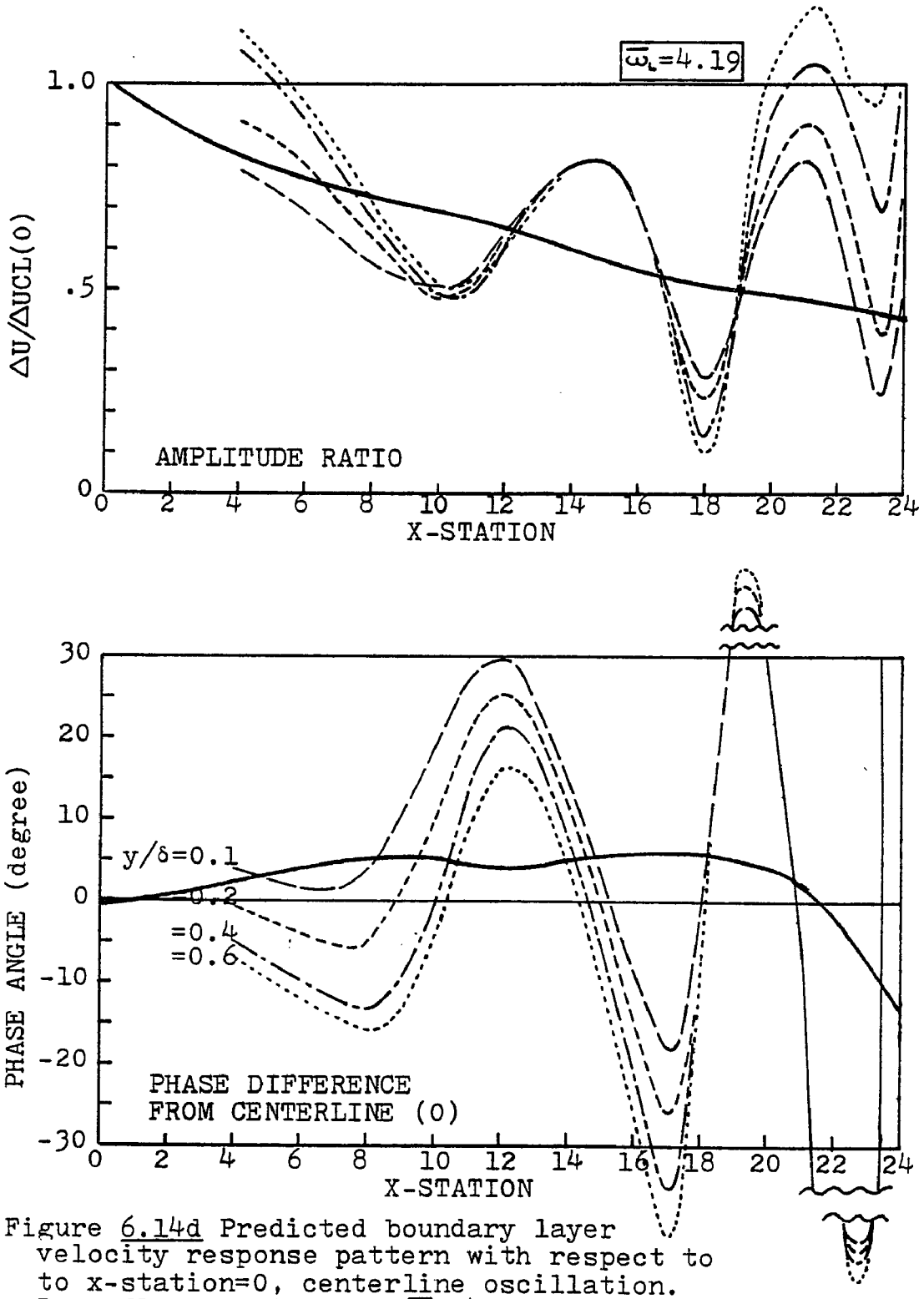

Figure 6.14d Predicted boundary layer velocity response pattern with respect to to x-station=0, centerline oscillation. Base flow Re_D=117,000, $\bar{\omega}_L$=4.19, FREQ=20 Hz.

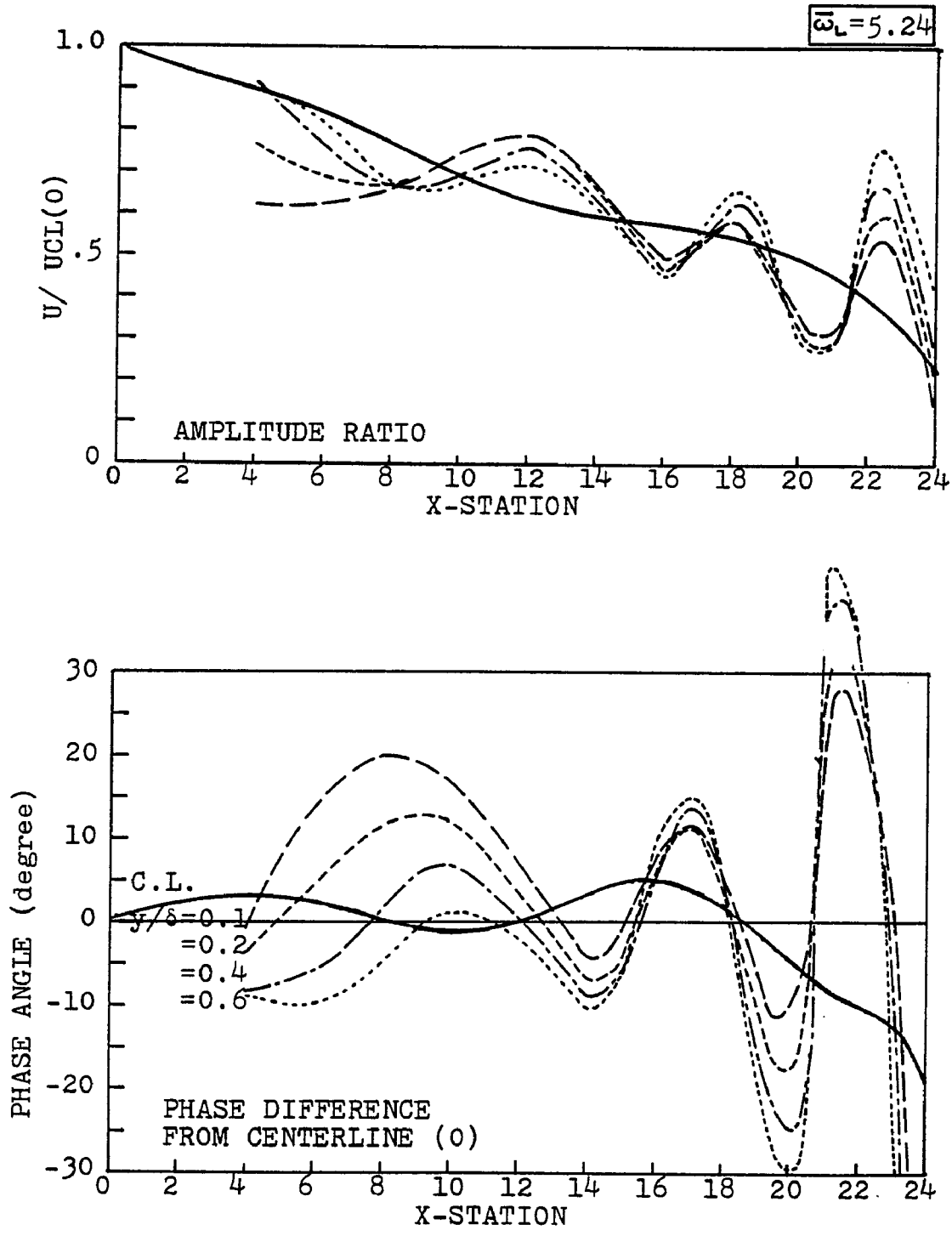

Figure 6.14e Predicted boundary layer velocity response pattern with respect to the x-station=0, centerline oscillation. Base flow Re_D=117,000, $\bar{\omega}_L$=5.24, FREQ=25 Hz.

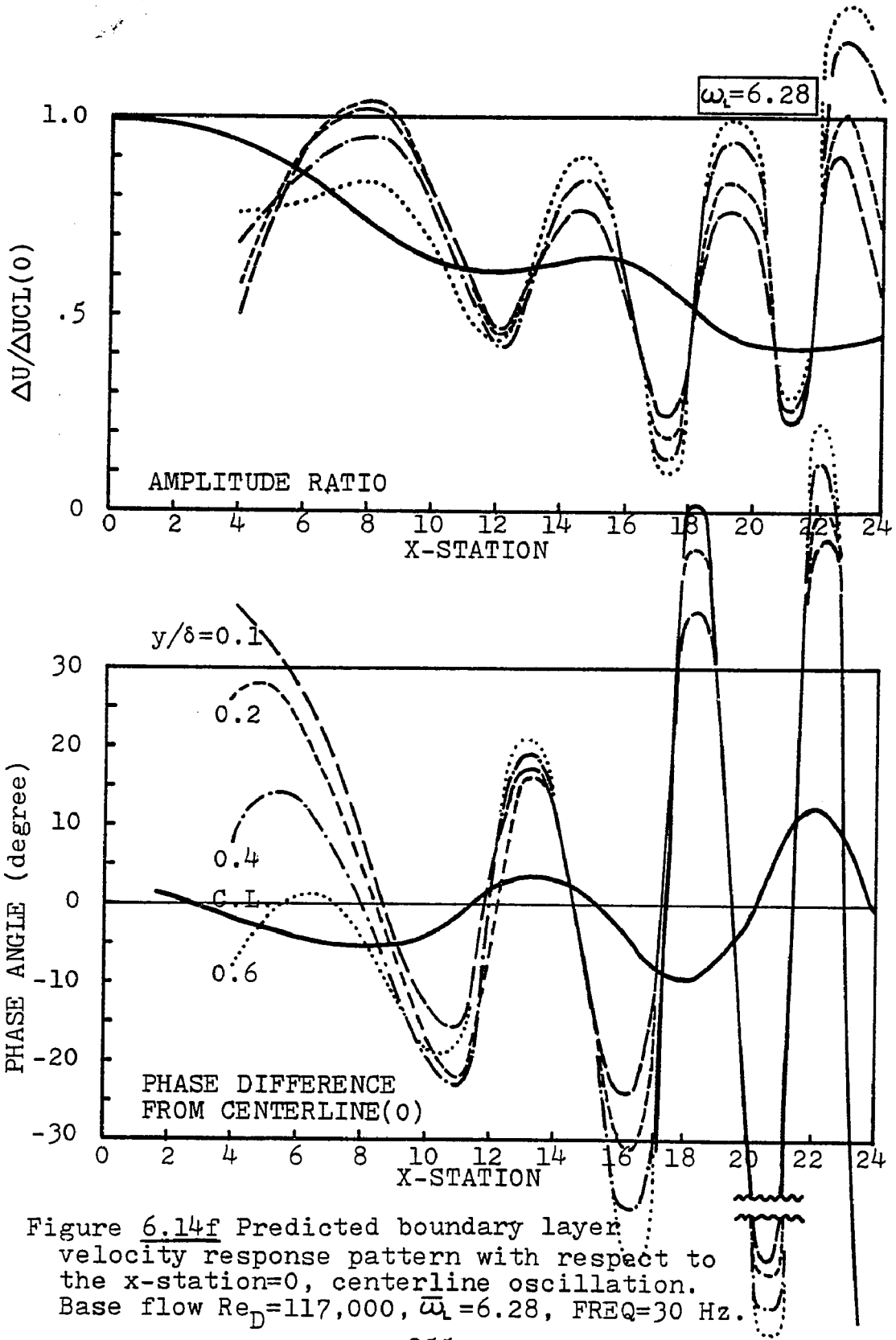

Figure 6.14f Predicted boundary layer velocity response pattern with respect to the x-station=0, centerline oscillation. Base flow Re_D=117,000, $\bar{\omega}_L$=6.28, FREQ=30 Hz.

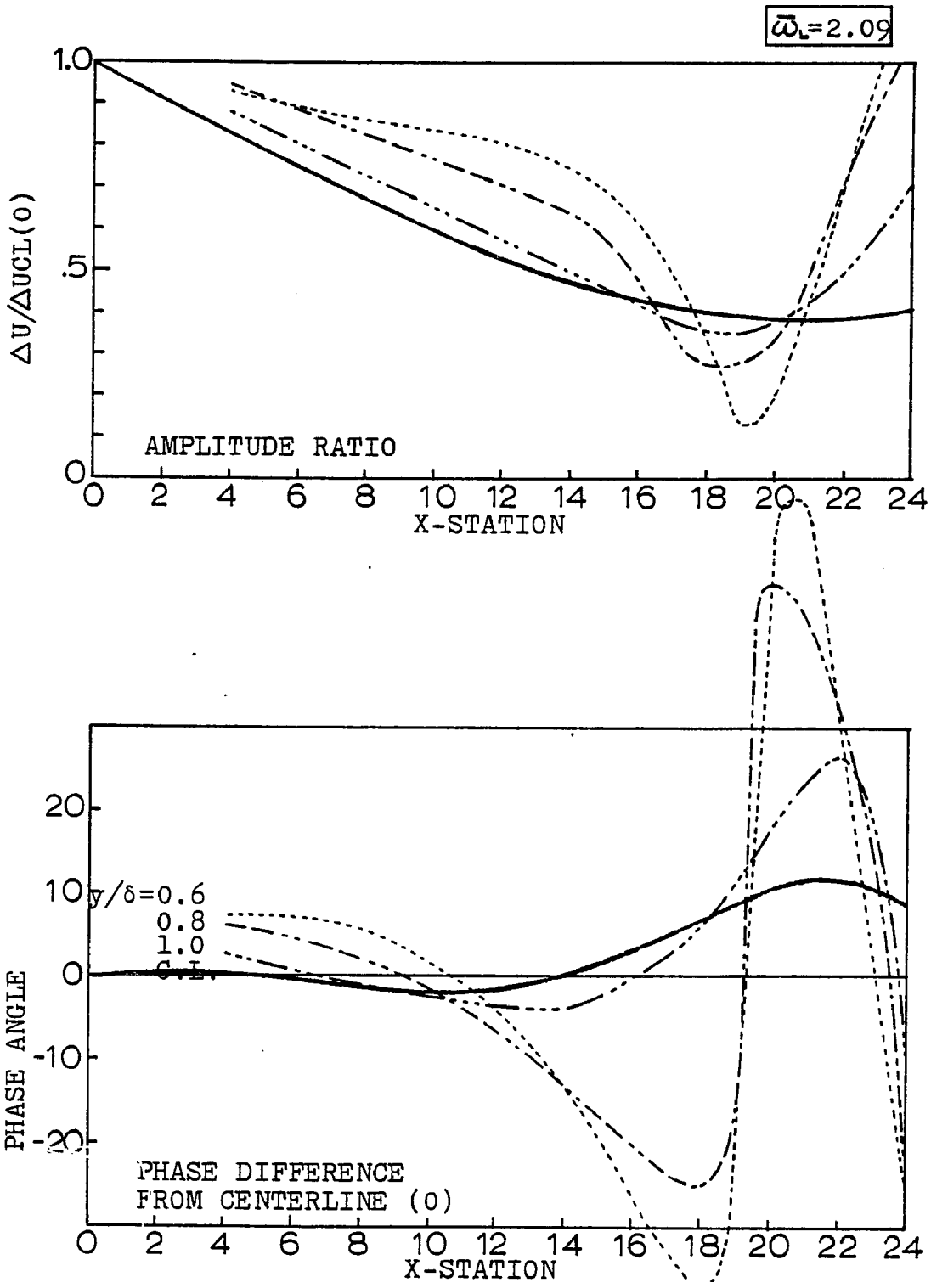

Figure 6.15 Predicted outer-edge velocity response pattern with respect to the x-station=0, centerline oscillation.

Base flow Re_D=117,000, $\bar{\omega}_L$ =2.09, FREQ=10 Hz.

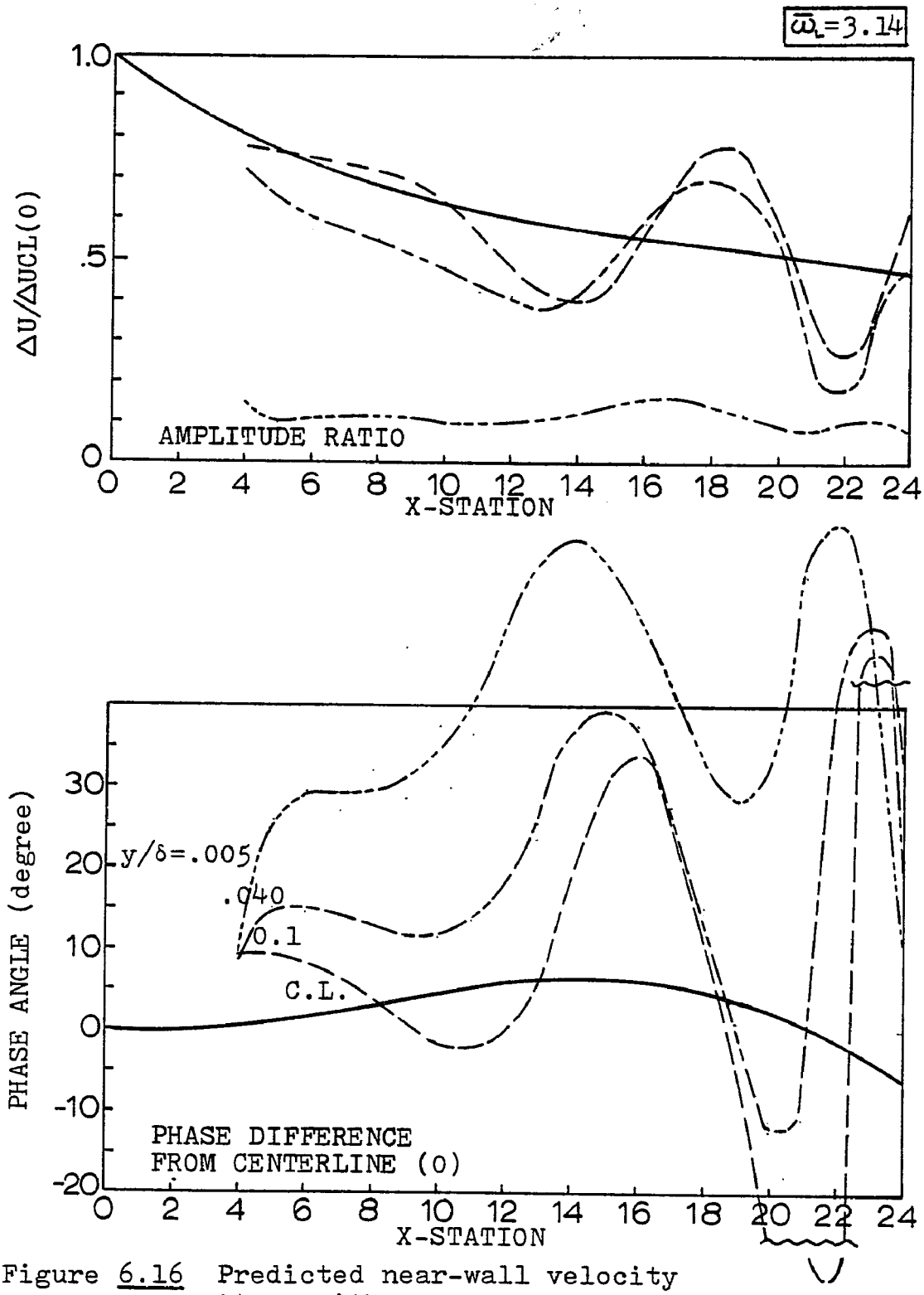

Figure 6.16 Predicted near-wall velocity response pattern with respect to the x-station=0, centerline oscillation.
Base flow Re_D=117,000, $\bar{\omega}_L$=3.14, FREQ=15 Hz.

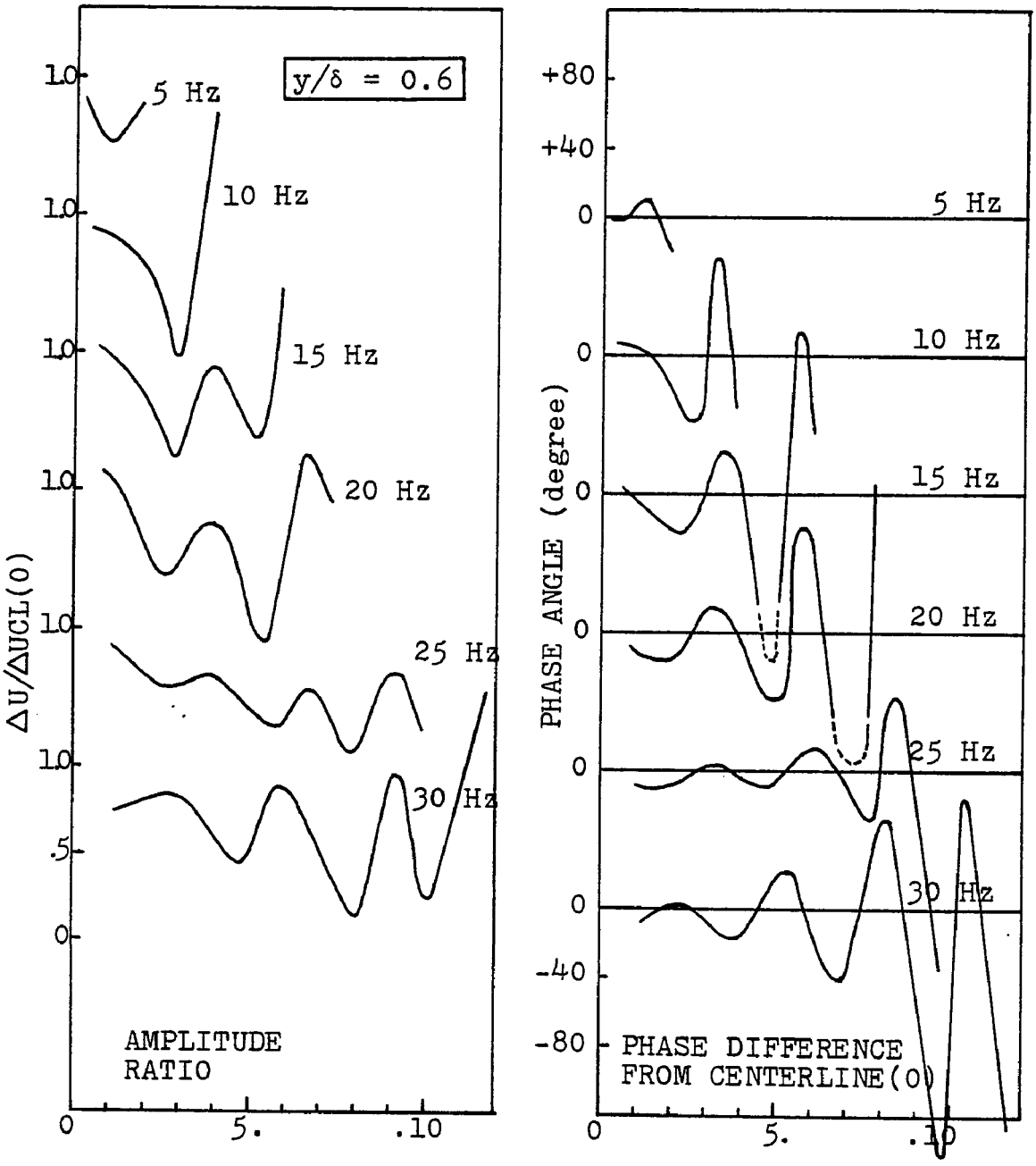

Figure 6.17 A comparison of the theoretical response patterns as a function of $\bar{\omega}_x$ for $y/\delta = 0.6$.

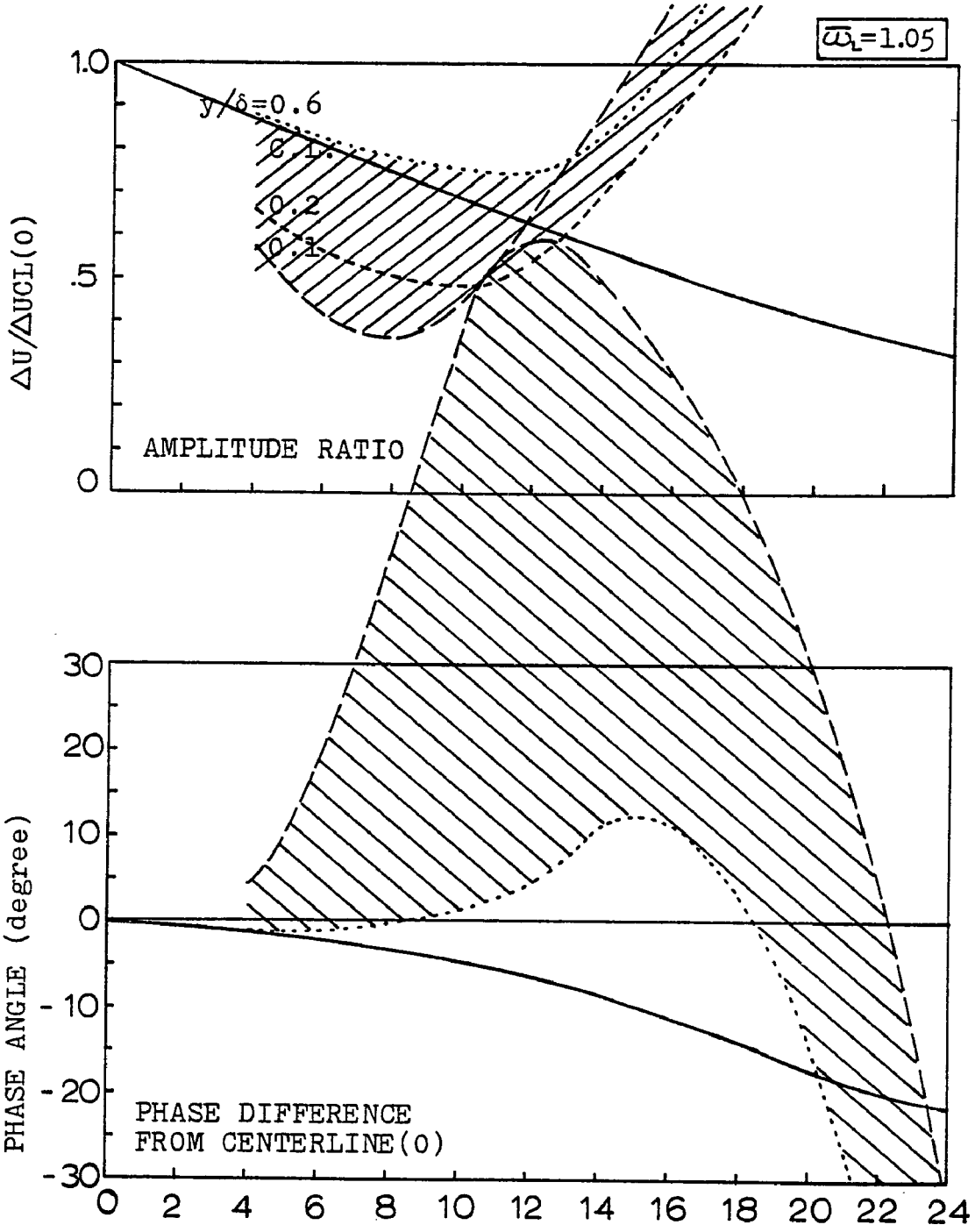

Figure 6.18 Quasi-laminar response pattern prediction: FREQ=5 Hz.

REFERENCES

1. Evans, R. L., "Turbulence and Unsteadiness Measurements Downstream of a Moving Blade Row," Trans. ASME, Journal of Engineering for Power, Jan., 1975.

2. Evans, R. L., "Boundary-Layer Development on an Axial-Flow Compressor Stator Blade," Trans. ASME, Journal of Engineering for Power, Vol. 100, Apr., 1978.

3. Gostelow, J. P., "A New Approach to the Experimental Study of Turbomachinery Flow Phenomena," Paper No. 76-GT-47, ASME Gas Turbine Conference, New Orleans, La., March, 1976.

4. Hirsch, Ch., and Kool, P., "Measurement of the Three-Dimensional Flow Field Behind an Axial Compressor Stage," Trans. ASME, Journal of Engineering for Power, April, 1977.

5. Stenning, A. H., and Schachenmann, A. A., "Oscillatory Flow Phenomena in Diffusers at Low Reynolds Numbers," ASME Paper No. 73-FE-14, 1973.

6. Schachenmann, A. A., "Oscillating Turbulent Flow in a Conical Diffuser," Ph.D. Thesis, Department of Mechanical Engineering, Lehigh University, Bethlehem, Pa., 1974.

7. Schachenmann, A. A., and Rockwell, D. O., "Oscillating Turbulent Flow in a Conical Diffuser," Trans. ASME, Journal of Fluids Engineering, Dec., 1976.

8. Schachenmann, A. A., and Rockwell, D. O., "Prediction of Diffuser Core Flow Fluctuations Caused by Oscillating Turbulent Flow," Journal of Aircraft, Vol. 15, No. 6, June, 1978.

9. Hughes, W. F., and Gaylord, E. W., Basic Engineering Equations, Schaum, New York.

10. Patel, V. C., "On the Equations of a Thick Axisymmetric Turbulent Boundary Layer," The University of Iowa Institute of Hydraulic Research, Report No. 143, Jan., 1973.

11. Tennekes, H., and Lumley, J. L., "A First Course in Turbulence," The M.I.T. Press, 1972.

12. Lighthill, M. J., "The Response of Laminar Skin Friction and Heat Transfer to Fluctuations in the Stream Velocity," Proceedings of the Royal Society, Vol. 224, Ser. A, 1954.

13. Nickerson, R. J., "The Effect of Free Stream Oscillations on the Laminar Boundary Layers on a Flat Plate," Sc.D. Thesis, M.I.T., 1957.

14. Pedley, T. J., "Two-Dimensional Boundary Layers in a Free Stream which Oscillates without Reversing," Journal of Fluid Mechanics, Vol. 55, 1972.

15. Lin, C. C., "Motion in the Boundary Layer with a Rapidly Oscillating External Flow," Proceedings of the 9th International Congress of Applied Mechanics, Sept., 1956.

16. Hill, P. G., and Stenning, A. H., "Laminar Boundary Layer in Oscillatory Flow," Journal of Basic Engineering, Trans., ASME, Sept., 1960.

17. Patel, M. H., "On Laminar Boundary Layers in Oscillatory Flow," Proceedings of the Royal Society, Ser. A, Vol. 347, 1975.

18. Hussain, A. K. M. F., and Reynolds, W. D., "The Mechanics of a Perturbation Wave in Turbulent Shear Flow," Stanford University Report No. FM-6, May, 1970.

19. Acharya, M., and Reynolds, W. C., "Measurements and Predictions of a Fully Developed Turbulent Channel Flow with Imposed Controlled Oscillations," Stanford University, Technical Report No. TF-8, May, 1975.

20. Brown, F. T., Margolis, D. L., and Shah, R. P., "Small-Amplitude Frequency Behavior of Fluid Lines with Turbulent Flow," Trans. ASME, Journal of Basic Engineering, Dec., 1969,

21. Margolis, D. L., and Brown, F. T., "Measurement of the Propagation of Long-Wavelength Disturbances Through Turbulent Flow in Tubes," ASME Paper No. 75-FE-22, 1975.

22. McDonald, H., and Shamroth, S. J., "An Analysis and Application of the Time-Dependent Turbulent Boundary-Layer Equations," AIAA Journal, Vol. 9, No. 8, Aug., 1971.

23. Singleton, R. E., et al, "Unsteady Turbulent Boundary Layer Analysis," NASA-TM-X-62242, Feb., 1973.

24. Cebeci, T., "Calculation of Unsteady Two-Dimensional Laminar and Turbulent Boundary Layer with Fluctuations in External Velocity," Proceedings of the Royal Society, Ser. A, 355, 1977.

25. Cousteix, J., Desopper, A., and Houdeville, R., "Structure and Development of a Turbulent Boundary Layer in an Oscillatory External Flow," Symposium on Turbulent Shear Flows, April, 1977, Penn State University.

26. Patel, M. H., "On Turbulent Boundary Layers in Oscillatory Flow," Proceedings of the Royal Society, Ser. A, Vol. 353, No. 1672, Feb., 1977.

27. Karlsson, S. K. F., "An Unsteady Turbulent Boundary Layer," Journal of Fluid Mechanics, Vol. 5, Part 4, 1959.

28. Miller, J. A., "Heat Transfer in the Oscillating Turbulent Boundary Layer," Trans. ASME, Journal of for Power, Oct., 1969.

29. Loehrke, R. I., Morkovin, M. V., and Fejer, A. A., "REVIEW-Transition in Nonreversing Oscillating Boundary Layers," Trans. ASME, Journal of Fluids Engineering, Dec., 1975.

30. McCroskey, W. J., "Some Current Research in Unsteady Fluid Dynamics - The 1976 Freeman Scholar Lecture," Trans. ASME, Journal of Fluids Engineering, March, 1977.

31. Brocher, E., "Oscillatory Flows in Ducts: A Report on Euromech 73," Journal of Fluid Mechanics, Vol. 79, Part 1, 1977.

32. Bradshaw, P., "An Introduction to Turbulence and its Measurement," 1st ed., Pergamon Press, Oxford, 1971.

33. Oka, S., and Kostic, Z., "Influence of Wall Proximity on Hot-wire Velocity Measurements," DISA Information, No. 13, May, 1972.

34. Kline, S. J., et al, Computation of Turbulent Boundary Layers-1968. AFOSR-IFP-Stanford Conference, Vols. I and II, Stanford University Press, Stanford, Cal., 1968.

35. Clauser, F. H., "Turbulent Boundary Layers in Adverse Pressure Gradients," Journal of the Aeronautical Sciences, Feb., 1954.

36. Cebeci, T., and Smith, A. M. O., "Analysis of Turbulent Boundary Layers," Applied Mathematics and Mechanics, Vol. 15, Academic Press, 1974.

37. Owczarek, J. A., Introduction to Fluid Mechanics, International Textbook Co., Scranton, Pa., 1968.

38. Thompson, B. G. J., "A New Two-Parameter Family of Mean Velocity Profiles for Incompressible Boundary Layers on Smooth Walls," Aeronautical Research Council R & M No. 3463, April, 1965.

39. Sarnecki, A. J., "The Turbulent Boundary Layer on a Permeable Surface," Ph.D. dissertation, Cambridge University, 1959.

40. McD Galbraith, R. A. and Head, M. R., "Eddy Viscosity and Mixing Length from Measured Boundary Layer Development," Aeronautical Quarterly, May, 1975.

41. Simpson, R. L., "Characteristics of Turbulent Boundary Layers at Low Reynolds Numbers with and without Transpiration," Journal of Fluid Mechanics, Vol. 42, Part 4, 1970.

42. Reynolds, W. C., "Computation of Turbulent Flows," Annual Review of Fluid Mechanics, Vol. 8, 1976.

43. Patankar, S. V., and Spalding, D. B., "Heat and Mass Transfer in Boundary Layers," 2nd ed., Intertext Books, 1970.

44. Crawford, M. E., and Kays, W. M., "STAN-5, A Program for Numerical Computation of Two-dimensional Internal/External Boundary Layer Flows," Stanford University Dept. of Mechanical Engineering Report HMT-23, 1975.

45. Mellor, G. L., and Herring, H. J., "Computation of Turbulent Boundary Layers - 1968. AFOSR-IFP-Stanford Conference (S. J. Kline, et al, eds.), Vol. I, Stanford University Press, Calif., 1968.

46. Klebanoff, P. S., "Characteristics of a Turbulent Boundary Layer in Zero Pressure Gradient," NACA TN 3178, July, 1954.

47. Escudier, M. P., "The Distribution of Mixing-Length in Turbulent Flows Near Walls," Imperial College Heat Transfer Section Report TWF/TN/1, 1966.

48. Van Driest, E. R., "On Turbulent Flow Near a Wall," Journal of Aeronautical Science, 23, 1956.

49. Keller, H. B., "Numerical Methods in Boundary-Layer Theory," Annual Review of Fluid Mechanics, Vol. 10, 1978.

50. Keller, H. B., "A New Difference Scheme for Parabolic Problems," Proceedings of 2nd Symposium on the Numerical Solution of Partial Differential Equations, B. Hubbard (ed.), Academic Press, 1971.

VITA

I was born on November 1, 1940, in Hazleton, Pennsylvania. I attended high schools in Pennsylvania and Maryland, and graduated in 1958 from Mt. St. Joseph's High School in Baltimore. I received a B.S.M.E. from Rensselaer Polytechnic Institute, Troy, N. Y., in 1962. From 1962 to 1967 I served as a commissioned officer in the U. S. Navy. In 1971 I earned an M. S. in Mechanical Engineering from the Rensselaer Graduate Center, Hartford, Ct., while employed at Pratt & Whitney Aircraft of East Hartford. I came to Lehigh University in September, 1972 to begin the doctoral degree program. I left the University in February, 1976 for a position with Exxon Research and Engineering Co., Florham Park, N. J., which I presently hold.